A thesis presented for the degree of
Doctor of Philosophy

Gamma-ray bursts with MeerLICHT

Simon de Wet

Supervised by Prof. Paul J. Groot

Department of Astronomy
University of Cape Town
February 2024

Plagiarism declaration

I, Simon de Wet, know the meaning of plagiarism and declare that all of the work in this thesis, save for that which is properly acknowledged, is my own.

I confirm that I have been granted permission by the University of Cape Town's Doctoral Degrees Board to include the following publications in my thesis, and where co-authorships are involved, my co-authors have agreed that I may include the following publications:

- *The triple-peaked afterglow of GRB 210731A from X-ray to radio frequencies* (Chapter 3, published in Astronomy & Astrophysics)
  T. Laskar performed the theoretical modelling in Section 4 using his own codes. Data used in the work was provided by a number of co-authors.
- *The ultra-long GRB 220627A at* $z = 3.08$ (Chapter 4, published in Astronomy & Astrophysics)
  The spectral reduction and analysis in Section 4.3.4 was performed by L. Izzo. Data used in the work was provided by a number of co-authors.
- *A millimeter rebrightening in GRB 210702A* (Chapter 5, to be submitted to The Astrophysical Journal)
  Radio data was provided by T. Laskar. Co-authors were part of the observing programmes.

Signature:

Signed by candidate

Abstract

The subject of this thesis is the multi-wavelength observational study of gamma-ray burst (GRB) afterglows. The driving force behind this work is the fully robotic MeerLICHT optical telescope which is able to rapidly slew to the position of a GRB in the sky and obtain multi-filter follow-up observations of the early phases of the afterglow, when non-standard behaviour may occur. Following the introduction, the thesis consists of four main chapters: a chapter outlining the more than two year GRB follow-up programme undertaken with MeerLICHT in which we followed-up 29 bursts, and three chapters presenting detailed studies on individual GRBs. The first of these studies focuses on GRB 210731A. Starting 286 seconds post-trigger, MeerLICHT obtained a highly unusual light curve consisting of three peaks, which we interpreted as being due to energy injection. Through multi-wavelength theoretical modeling we found that a forward shock model within a stellar wind medium could explain all of our X-ray, optical and radio data, but not our 1.4 GHz upper limits. We suggested that a possible thermal electron population might explain the additional opacity at lower radio frequencies. The subject of the second detailed study is GRB 220627A, a rare burst consisting of two gamma-ray emission episodes separated by almost 1000 s. The discovery of the optical afterglow by MeerLICHT led to spectroscopic observations which secured the burst redshift to $z = 3.08$, making this the most distant ultra-long GRB to date. Our modelling and afterglow analysis showed that GRB 220627A does not appear to have a different progenitor compared to the wider long GRB propulation. The third detailed study encompasses GRB 210702A. This burst was unique for being the first GRB with a clear rebrightening in its millimeter light curve which we attempted to explain via energy injection or a reverse shock from a late-time shell collision. Prior to the millimeter rebrightening, we found that the X-ray, optical and millimeter data could be reconciled within a standard forward shock model in a stellar wind medium, however, similar to other bursts with extensive radio data sets, no standard model could explain all of our radio data.

I am grateful for the generous financial support provided by the Oppenheimer Memorial Trust and National Research Foundation.

Contents

Chapter 1

Introduction

1.1 Blasts from the past

Any mention of gamma-ray bursts (GRBs) will usually begin with their superlative nature - that they are the brightest, most powerful, or most relativistic explosions in the Universe; that they briefly outshine every other object in the γ-ray sky; that the energy released in γ-rays over a few seconds alone is equivalent to the rest mass energy of the Sun; that a GRB holds the record for being (briefly) the most distant object visible to the naked eye[1]; or that a GRB even held the record as the most distant object *ever* observed[2], which is even more remarkable considering that GRBs are produced on stellar scales as opposed to the scale of galaxies.

The GRB story began with the launch of the *Vela* satellites in the 1960s. These satellites were sent into space by the United States as a means of monitoring whether signatories to the Nuclear Test Ban Treaty were complying with its provisions. On board the satellites were γ-ray scintillation detectors which detected the first bursts of γ-rays which we today call GRBs. The first GRB detected was GRB 670702[3] which showed some of the features common to almost all GRBs: an erratic light curve with a duration of 10 seconds showing significant time structure and a peak energy near 1 MeV. The first paper highlighting the discovery of these bursts was published five years later in 1973 (Klebesadel et al. 1973), but not because the data was classified (as is commonly believed) but rather because the data analysis was complicated (Kouveliotou et al. 2012). The observed GRB properties were completely different to what was expected from a nuclear test, where a hard X-ray flash with little time structure was expected.

The following 24 years of GRB progress was rather slow, driven in large part by the lack of counterparts at other wavelengths and the small number of bursts detected (~ 500). However, some important trends were noticed. The first Konus GRB catalog showed some evidence for a bimodal duration distribution (Mazets et al. 1981b), while a deviation from a uniform spatial distribution of events in Euclidean space pointed towards a possible cosmological origin (Higdon & Lingenfelter 1990). Even so, the detection of low-significance spectral lines in γ-ray data from the *Venera* (Mazets et al. 1981a) and Japanese *Ginga* (Murakami et al. 1988) satellites supported magnetised Galactic neutron stars as the origins of GRBs. Many models were proposed by theorists during this era - a total of 118 were listed in a 1994 review article on the state of the field (Nemiroff 1994), though none of them turned out to be correct. The closest model was the

---

[1] The 'naked-eye' GRB 080319B reached a peak apparent visual magnitude of 5.8 and occurred at a redshift of $z = 0.937$, approximately 7.5 billion light years away. The limit for the human eye is about 6^{th} magnitude under dark skies.

[2] GRB 090423 had a spectroscopic redshift of $z = 8.2$ and held the distance record until 2015 when it was overtaken by a galaxy. The current confirmed record is held by a galaxy detected with the James Webb Space Telescope at $z = 13.2$.

[3] The naming convention for GRBs is YYMMDD, where YY refers to the year, MM to the month, and DD to the day on which the burst was detected. If more than one burst was detected on a particular day, a capital letter (A,B,C...) is added denoting the order of detection.

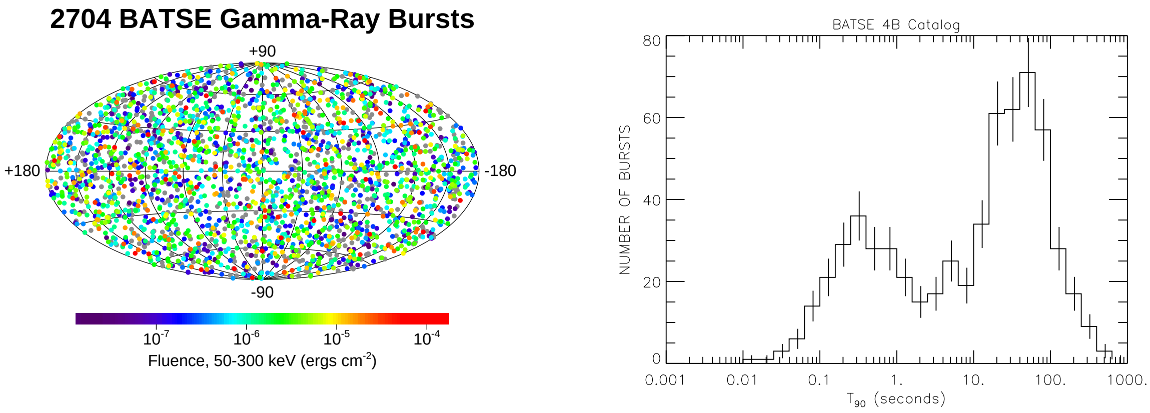

(a) (b)

Figure 1.1: Angular distribution of all GRBs detected by BATSE in Galactic coordinates (a), and the bimodal duration distribution of bursts from the 4B catalog (b). Figures are taken from the NASA National Space, Science, and Technology Center (NSSTC) Gamma-Ray Astrophysics website.

supernova shock breakout model proposed by Stirling Colgate (Colgate 1968, 1974).

The launch of NASA's *Compton Gamma Ray Observatory (CGRO)* in April 1991 led to great strides in understanding the GRB phenomenon. The Burst and Transient Source Experiment (BATSE) aboard *CGRO* was an all-sky γ-ray burst detector consisting of eight Large Area Detectors covering the energy range 20 keV to 1.9 MeV, and eight Spectroscopy Detectors covering the range 10 keV to 100 MeV. Over its nine year lifetime BATSE detected 2704 GRBs and made three key findings: (1) The angular distribution of bursts was found to be isotropic (see Figure 1.1 (a); Briggs et al. 1996) and the fluence distribution was found to deviate from the Euclidean prediction at the faint end (Meegan et al. 1992). Both these findings supported a cosmological model rather than the popular Galactic neutron star models. (2) A bimodal duration distribution was firmly established (Figure 1.1 (b)), with a duration of roughly two seconds separating the long-duration and short-duration GRBs (Kouveliotou et al. 1993). (3) The GRB spectra were found to be non-thermal and could be fitted by a smoothly-joined broken power-law 'Band function' (Band et al. 1993).

Despite the observational progress bought about by BATSE, the distance scale of GRBs was still unknown. The BATSE localisation error boxes were large, with radii ranging from approximately 0.2 to 18 degrees which made identifying a counterpart at optical wavelengths very difficult due to the lack of wide-field telescopes and the crowded nature of the optical sky. In contrast, the X-ray sky, being much less crowded than the optical sky, made it ideal for counterpart searches. *BeppoSAX* was an Italian-Dutch satellite launched in April 1996 equipped with a number of scientific instruments. Its Wide Field Instruments consisted of an all-sky Gamma-Ray Burst Monitor (GRBM, 40–700 keV) and two Wide Field Cameras (WFCs, 2–30 keV). A burst detected by BATSE or GRBM that happened to be in the field of view of the WFCs could then promptly be followed-up by the Narrow Field Instruments to obtain sub-arcminute localisations. *BeppoSAX* revolutionised the GRB field through its discovery of the first multi-wavelength counterparts to GRBs. The breakthrough came in 1997 with the identification of X-ray (Costa et al. 1997) and optical counterparts (Figure 1.2; van Paradijs et al. 1997) following GRB 970228, which was followed by the first radio counterpart (Frail et al. 1997) and redshift measurement in association with GRB 970508 (Metzger et al. 1997). With a redshift of $z = 0.835$, GRB 970508 provided conclusive evidence for the *cosmological origin* of GRBs, firmly ruling-out the Galactic models. A seminal paper predicting longer-lived broadband emission was in fact published two

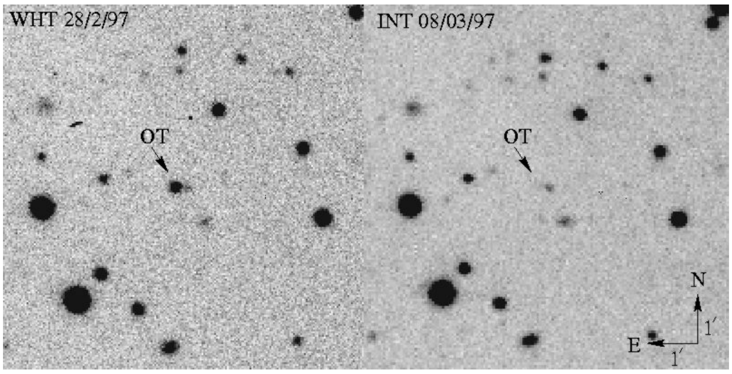

Figure 1.2: V-band images of the optical counterpart to GRB 970228, from van Paradijs et al. (1997).

weeks prior to the first counterpart discovery (Mészáros & Rees 1997) in which the authors coined the term *afterglow* to describe the longer-lived emission following the GRB. The GRB itself is commonly referred to as the *prompt emission*.

In the years following the first afterglow discoveries in 1997 up until the launch of *Swift* in 2004, *BeppoSAX* and an American satellite called the *High Energy Transient Explorer*[4]*-2 (HETE-2)* were the primary localisers of GRBs. Significant observational and theoretical progress was made in this era. The detection of the broad-lined Type Ic SN 1998bw in the error box of the long GRB 980425 hinted at a connection between the death of massive stars and long GRBs (Galama et al. 1998; Kulkarni et al. 1998), which was firmly established through the extremely-bright GRB 030329 and the accompanying SN 2003dh at $z = 0.167$ (Stanek et al. 2003; Hjorth et al. 2003). The power-law decays observed in afterglow light curves were found to be consistent with theoretical predictions of the fireball shock model (Rees & Meszaros 1992; Meszaros & Rees 1993; Mészáros & Rees 1997; Sari et al. 1998), while steepening temporal breaks in afterglow light curves were interpreted as evidence for collimation in the form of jets (Rhoads 1999; Sari et al. 1999).

The leading GRB detectors today are the *Swift* and *Fermi* missions. *Swift* was launched in November 2004 carrying three instruments: a wide-field Burst Alert Telescope (BAT, 15–350 keV) for detecting and localising GRBs with $\sim 3'$ precision; an X-Ray Telescope (XRT) which is used to search for and localise X-ray afterglows detected by BAT; and a UV-Optical Telescope (UVOT) which co-points with the XRT and can localise afterglows with subarcsecond precision. The rapid slewing capibilities of XRT and UVOT led to a massive increase in the number of X-ray and optical afterglow detections (Figure 1.3) and enabled detailed studies of the early afterglow phase. The large number of X-ray light curves resulted in a canonical X-ray light curve being established (Zhang et al. 2006), which consisted of five distinct components arising from different physical processes. The presence of X-ray flares demonstrated that the GRB central engine can remain active for longer than was previously believed. *Swift* was responsible for the detection of the first short GRB afterglows which led to the finding that the locations of short GRBs in their host galaxies was quite different to that of long GRBs and thus they were unlikely to be related to the collapse of massive stars (Gehrels et al. 2005; Bloom et al. 2006; Barthelmy et al. 2005b). The merger of two compact objects (neutron stars and black holes) was regarded as the leading model. The redshift range of GRBs was also extended by *Swift*: nearby, low-luminosity GRBs were suggested to form a distinct population compared to the high-luminosity bursts (Liang et al. 2007; Virgili et al. 2009), and the most distant GRBs were discovered such as GRB 080913 at $z = 6.7$ (Greiner et al. 2009), GRB 090423 at $z = 8.2$ (Tanvir et al. 2009; Salvaterra et al. 2009), and GRB 090429B for which a photometric redshift of $z = 9.4$ was measured (Cucchiara et al. 2011).

---

[4] The first *HETE* mission was lost during launch in November 1996. *HETE-2* was launched in October 2000.

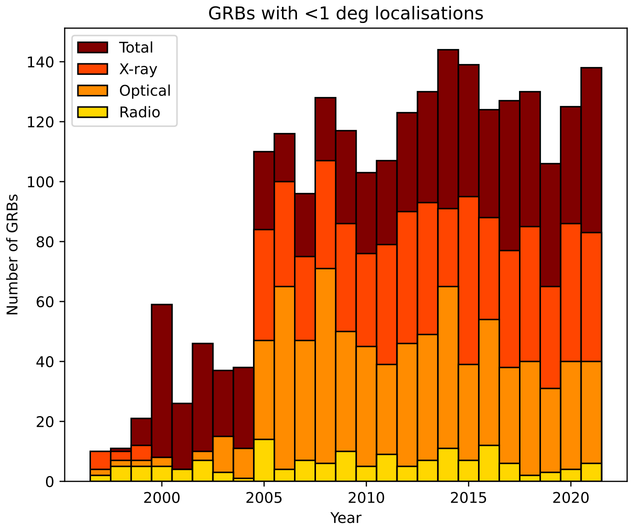

Figure 1.3: Number of GRBs with sub-degree localisations from 1997 to 2021. The rapid jump coincides with the launch of *Swift* in November 2004. Figure created using Jochen Greiner's online table of GRBs.

The *Fermi* mission was launched in June 2008 and is most notable for the substantial advances it has made in understanding the prompt GRB emission. Its two instruments span more than seven orders of magnitude in energy: the Large Area Telescope (LAT, 20 MeV–300 GeV) can observe 20% of the sky at a given time, while the Gamma-ray Burst Monitor (GBM, 8 keV–40 MeV) monitors the entire visible sky for GRBs. The LAT detections of GRBs - although infrequent[5] - showed that the emission above 100 MeV generally lasts longer and is delayed with respect to the GBM emission, pointing towards an external shock origin (Kumar & Barniol Duran 2009, 2010). This is also supported by the fact that the high-energy LAT emission is often seen to decay as a power-law. Furthermore, detailed γ-ray spectra from *Fermi* revealed additional spectral components to the Band function: a quasi-thermal component (either dominant or subdominant; Ryde et al. 2010; Zhang et al. 2011; Guiriec et al. 2011; Axelsson et al. 2012) and a third power-law component extending up to the LAT band (Abdo et al. 2009; Ackermann et al. 2010) were seen in some bursts. The disagreement of the data with the standard fireball internal shock model (Zhang & Pe'er 2009) led to an increase in theoretical efforts to understand the prompt emission. Zhang & Yan (2011) proposed the Internal-Collision-induced MAgnetic Reconnection and Turbulence (ICMART) model in which the GRB emission region consists of a moderately Poynting flux-dominated outflow where turbulent magnetic reconnection accelerates electrons to produce synchrotron radiation. Daigne et al. (2011) and Hascoët et al. (2013) proposed that photospheric emission is suppressed by a highly magnetised central engine but that magnetic energy is quickly converted to kinetic energy, which allows for internal shocks to form and thereafter produce prompt emission. Another proposal is that the entire GRB Band spectrum is quasi-thermal emission from a dissipative photosphere in which internal shock emission is suppressed (Beloborodov 2010; Lazzati & Begelman 2010; Toma et al. 2011). These competing models demonstrate that the origin of the prompt emission is still unsettled.

More recently, two important discoveries have been made related to GRBs. The first occurred in August 2017 with the detection of gravitational waves (GW) from two merging neutron stars (Abbott et al. 2017b) which was followed 1.7 s later by the detection of a short GRB by *Fermi*/GBM (Abbott et al. 2017a; Goldstein et al. 2017). Through a concerted multi-wavelength

---

[5] A total of 186 GRBs were detected by LAT over a 10 year period, compared to 2357 GRBs detected by GBM (or 8%), as presented in the Second *Fermi*/LAT GRB Catalog (Ajello et al. 2019).

follow-up campaign, a bright optical transient was discovered within the GW error box in the outskirts of the galaxy NGC 4993 at 40 Mpc. The transient faded quickly at blue wavelengths but more slowly in the red (Coulter et al. 2017; Evans et al. 2017; Nicholl et al. 2017; Shappee et al. 2017; Chornock et al. 2017; Arcavi et al. 2017), and was found to be consistent with models for a thermal transient known as a kilonova or macronova (Li & Paczyński 1998; Metzger et al. 2010; Metzger 2017; Kasen et al. 2017). Spectroscopic observations revealed the presence of lanthanide-rich ejecta produced via r-process neutron capture (Smartt et al. 2017; Pian et al. 2017; Tanvir et al. 2017). The second important discovery was the detection of TeV γ-rays by the MAGIC collaboration following GRB 190114C (MAGIC Collaboration et al. 2019a,b) - the first such detection at such high energies (> 1 TeV) by ground-based imaging atmospheric Cherenkov telescopes. These observations conclusively revealed, for the first time, the existence of a synchrotron self-compton (SSC) spectral component at high energies (Zhang 2019).

1.2 The fireball model

1.2.1 Model constraints

The fireball model for GRBs has been the most popular model for describing the GRB phenomenon. The model came about due to important constraints from observations. These are listed below, following Zhang (2018):

- Due to the vast distances to GRBs (the typical redshift is $z \approx 2$), the energy released in γ-rays alone for most bursts is equivalent to the rest-mass energy of the Sun. This requires an extremely energetic, and likely catastrophic, event.
- The GRB ejecta which produces the observed emission must be moving at *relativistic* speeds. This is necessary due to the compactness problem.
- There are at least two physical categories of GRBs: those associated with the death of massive stars and those associated with the merger of two compact objects.
- A collimated outflow, in the form of a jet, is required to explain achromatic steepenings in afterglow light curves (also known as a jet break). A beamed outflow also serves the purpose of reducing the very high isotropic γ-ray energies measured for some bursts, alleviating energy concerns.
- Afterglow radiation is likely produced via synchrotron radiation within shocks.

The compactness problem (Ruderman 1975) states the following: because photons with an energy greater than the electron rest mass energy (511 keV) are observed from GRBs, the optical depth to electron-positron pair production ($\gamma\gamma \rightarrow e^+e^-$) within the GRB emission region must be less than unity. Assuming that the pair-production cross section is close to the Thomson cross section, the pair production optical depth $\tau_{\gamma\gamma}$ is given as

$$\tau_{\gamma\gamma} \sim \sigma_{\mathrm{T}} n_{\mathrm{ph}} R, \tag{1.1}$$

where σ_{T} is the Thomson cross section, n_{ph} is the photon number density, and R is the size of the emission region. For typical GRB parameters, this value is much greater than unity, so no γ-rays are expected to escape the emission region. Relativistic motion alleviates this problem due to two reasons. If the outflow is moving with a bulk Lorentz factor Γ, photons of a particular energy received by a γ-ray detector have a lower energy in the comoving frame of the emission region - they are Doppler-deboosted by a factor Γ relative to the observer frame. The second reason is due to the increase in size of the emission region. Without considering relativistic effects, the size of the emission region is estimated via the minimum variability timescale seen in GRB light curves ($R \sim c\delta t \sim 3 \times 10^8$ cm with $\delta t \sim 10$ ms). The size of the emission region for a relativistically-moving outflow should be multiplied by a factor[6] $\sim \Gamma^2$ compared to the non-relativistic case. These two factors alleviate the compactness problem. In fact, direct evidence for relativistic motion was demonstrated through observations of the apparent motion of the size of the afterglow of GRB 030329 with Very Long Baseline Interferometry (Taylor et al. 2004).

1.2.2 Physical picture

The basic physical picture for a GRB is presented in Figure 1.4. In the case of long GRBs, the progenitor star (likely a massive Wolf-Rayet-type star) undergoes a catastrophic event which forms a black hole central engine. The central engine continuously powers a collimated outflow in which gravitational energy is converted to thermal energy or Poynting flux energy. The thermal and/or Poynting flux energy are converted to kinetic energy, which causes the outflow to reach relativistic speeds. Some of the thermal energy is released in the form of photons at a photosphere (see Figure 1.5), the signature of which may be a thermal blackbody component in the GRB spectrum. The remaining kinetic energy of the jet is converted into the random internal energy of particles within internal shocks (for kinetic energy) or magnetic dissipation (for a Poynting flux). A fraction of the internal energy within the internal shocks is partitioned to electrons and magnetic fields, which gives rise to non-thermal radiation - the GRB prompt emission. Once the jet is decelerated by the surrounding medium, a relativistic forward shock is formed along with a reverse shock which propagates back into the jet. The emission produced within the forward and reverse shocks is synchrotron radiation, both of which form part of the *afterglow* phase.

Following Section 7.2.2 in Zhang (2018), we provide a brief quantitative description of the central engine. The central engine can be defined by a parameter

$$\mu_0(t) = \frac{L_{w,0}(t)}{\dot{M}(t)c^2} = \frac{L_{m,0}(t) + L_{\mathrm{P},0}(t)}{\dot{M}(t)c^2} = \eta(t)\left[1 + \sigma_0(t)\right]. \tag{1.2}$$

Here, $L_{w,0}(t)$ is the initial central engine 'wind' luminosity (which may vary with time) consisting of a matter luminosity, $L_{m,0}(t)$, and Poynting flux luminosity, $L_{\mathrm{P},0}(t)$, and $\dot{M}(t)$ is the baryon loading rate. The parameter $\eta(t)$ is the energy per baryon:

$$\eta(t) \equiv \frac{L_{m,0}(t)}{\dot{M}(t)c^2}, \tag{1.3}$$

while $\sigma_0(t)$ is a magnetisation parameter defined as

$$\sigma_0(t) \equiv \frac{L_{\mathrm{P},0}(t)}{\eta(t)\dot{M}(t)c^2}. \tag{1.4}$$

Averaging Equation 1.2 over a period of time (for instance the burst duration) results in

$$\mu_0 = \frac{E_{\mathrm{tot},0}}{Mc^2} = \eta(1 + \sigma_0). \tag{1.5}$$

The total energy of the system decreases with time due to magnetic dissipation or energy dissipation at the photosphere. Besides these losses, energy is conserved and converted from one form to another. While the jet is accelerating (at early times) the thermal energy and Poynting flux energy are converted into kinetic energy of the outflow. Without radiative losses, we have

$$\mu = \mu_0 = \eta(1 + \sigma_0) = \Gamma\Theta(1 + \sigma_0), \tag{1.6}$$

where Γ is the bulk Lorentz factor of the outflow and Θ is the comoving energy per baryon. This equation demonstrates how energy is converted from the internal energy of the outflow (equal to

---

[6] See Section 3.2.2 of Zhang (2018) for an excellent discussion on the different timescales - and how they are

$\Theta - 1$) to kinetic energy (which is represented by Γ). The fireball regime corresponds to $\sigma_0 \ll 1$, whereas the Poynting flux dominated regime has $\sigma_0 \gg 1$. In reality, a hybrid jet consisting of both components is likely. We choose to focus on the fireball case henceforth, though both the hybrid and Poynting flux dominated cases have been studied extensively in the literature (Tchekhovskoy et al. 2009; Mészáros & Rees 2011; Metzger et al. 2011; Granot et al. 2011; Zhang & Yan 2011; Gao & Zhang 2015). The fireball regime is much simpler than the Poynting flux regime, since relativistic hydrodynamics can be used rather than relativistic magneto-hydrodynamics.

In the fireball regime we have $\sigma_0 \ll 1$. From Equation 1.6 the asymptotic maximum Lorentz factor that can be achieved is therefore

$$\Gamma_{\max} = \mu_0 \simeq \eta. \tag{1.7}$$

The evolution of the fireball and a number of important characteristic radii are depicted in Figure 1.5. During the earliest phases the fireball accelerates. This phase was studied in detail by Meszaros & Rees (1993), Piran et al. (1993), and Kobayashi et al. (1999), and the main result is that the bulk Lorentz factor increases linearly ($\Gamma \propto R$) until reaching the coasting radius R_c. At this point the outflow will move with a constant Lorentz factor equivalent to its maximum achievable value ($\Gamma_{\max} = \eta$, Equation 1.7). This quantity is often called the *initial Lorentz factor* of the jet, and is usually denoted by Γ_0 in the literature. There are means of constraining this value through observations. One of these methods - the opacity method - involves using the highest-energy γ-ray (or a cutoff in the γ-ray spectrum) to set a lower limit on Γ_0 via a method related to the compactness problem (Baring & Harding 1997; Lithwick & Sari 2001; Gupta & Zhang 2008). Another method - the afterglow onset method - uses an observed peak in the early-time optical light curve to constrain Γ_0 (see Sari & Piran 1999b; Kobayashi & Zhang 2007, and Section 1.2.3 below). This method is used in Chapter 3 for GRB 210731A.

There are two factors that may cause the maximum Lorentz to not be reached. The first is if the outflow begins to decelerate before reaching the coasting radius, so that $R_{\rm dec} < R_c$. This can occur if there is magnetic dissipation through a Poynting flux ($\sigma_0 \gg 0$), however, for a fireball with typical GRB parameters this should not be the case. The second factor that can prevent $\Gamma_{\max}$ from being reached is if there are radiative losses from a photosphere before the outflow reaches the coasting radius (the left-hand photospheric radius in Figure 1.5). Emission from a fireball photosphere was studied in detail by Mészáros & Rees (2000). The internal shock radius, $R_{\rm IS}$ (Figure 1.5), is where the prompt GRB emission is produced. The explanation for internal shocks developing is that the outflow produced by an erratic central engine - as seen in GRB light curves - is likely non-uniform in density. Two shells ejected at different times and with different bulk Lorentz factors will eventually 'catch-up' with each other, forming a shock wave in which the non-thermal GRB emission is produced (Rees & Meszaros 1994; Daigne & Mochkovitch 1998).

1.2.3 Deceleration

The afterglow phase within the fireball model occurs once the outflow begins to decelerate at the deceleration radius, $R_{\rm dec}$ (Figure 1.5). Since the focus of this thesis is the afterglow phase, we present a more complete discussion here, following Section 7.3.4 of Zhang (2018). Most of the energy in the fireball is in the form of kinetic energy at the deceleration radius. We assume an impulsive, isotropic fireball with a total kinetic energy E, initial mass M_0, and initial Lorentz factor Γ_0. In terms of nomenclature, $E = E_{\rm K,iso}$ is often adopted in afterglow theory. Prior to shock crossing, the total energy in the system is the fireball energy plus the rest mass energy of the ambient medium that will be swept-up, which has mass m:

$$E = \Gamma_0 M_0 c^2 + mc^2. \tag{1.8}$$

---

related via various factors of Γ - in the GRB problem.

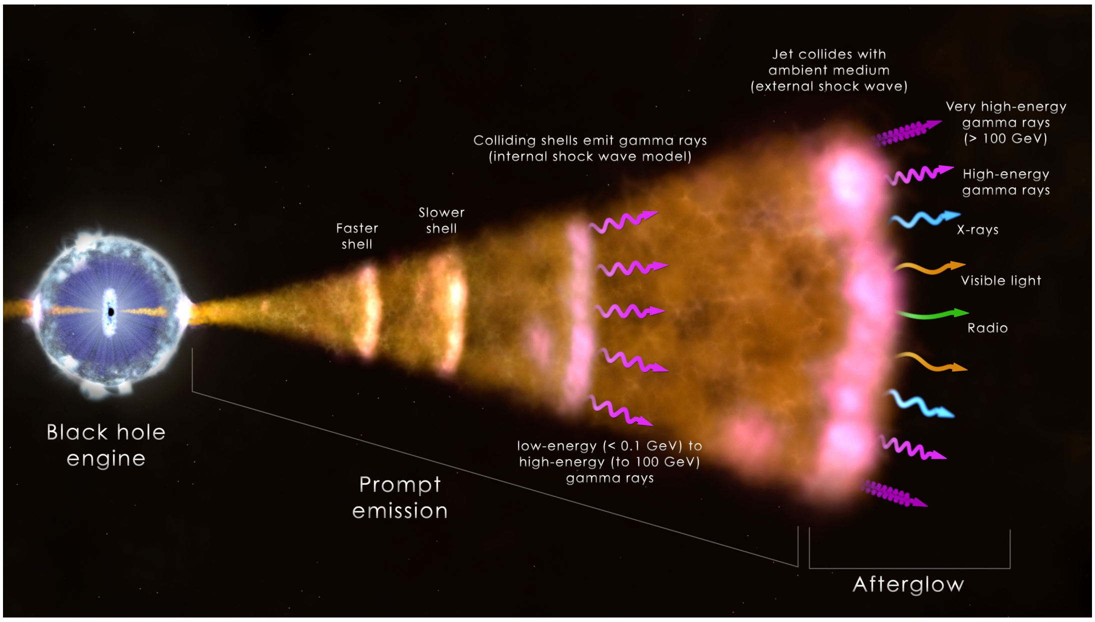

Figure 1.4: Physical model of a GRB. A collimated outflow is launched by the central engine. Internal shocks within the ejecta gives rise to the prompt emission, while the external forward shock produces the afterglow emission. Credit: NASA's Goddard Space Flight Center

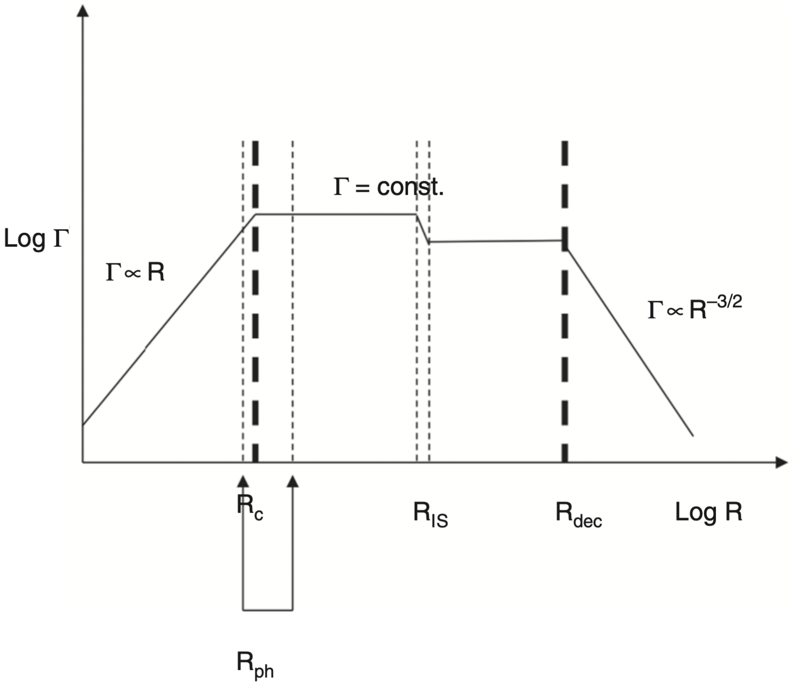

Figure 1.5: Cartoon picture depicting the evolution of the bulk Lorentz factor of a GRB fireball. Important radii are the coasting radius R_c, photospheric radius R_{ph}, internal shock radius R_{IS} where the prompt emission is produced, and deceleration radius R_{dec}. Adapted from Figure 7.6 of Zhang (2018).

After shock crossing, the total energy is

$$E = \Gamma(M_0c^2 + hV), \tag{1.9}$$

where Γ is the bulk Lorentz factor of the ejecta after sweeping up m, V is the volume enclosing the swept-up mass, and h is the enthalpy density of the shocked region. The enthalpy density $h = e+p+\rho c^2$ is the relevant quantity in relativistic hydrodynamics, where e is the internal energy density and p the pressure, both measured in the comoving frame of the shock. Requiring energy conservation before and after sweeping up m, along with relativistic shock jump conditions[7] $p = (\hat{\gamma} - 1)e$ and $e = (\Gamma - 1)\rho c^2$, results in

$$\Gamma_0 M_0 + m = \Gamma\left[M_0 + \hat{\gamma}(\Gamma - 1)m + m\right] \simeq \Gamma(M_0 + \hat{\gamma}\Gamma m), \tag{1.10}$$

where $m \ll M_0$ has been assumed. Here, $\hat{\gamma}$ is the adiabatic index, which is usually taken as $\frac{4}{3}$ in the relativistic case. Deceleration starts once the two terms in the right-hand brackets become comparable, so that

$$m_{\mathrm{dec}} = \frac{M_0}{\hat{\gamma}\Gamma}. \tag{1.11}$$

Assuming deceleration becomes important when $\Gamma = \Gamma_0/2$ and that the ambient medium consists purely of hydrogen with a constant number density n, Equation 1.11 can be written as

$$\frac{4\pi}{3} R_{\mathrm{dec}}^3 n m_p c^2 = \frac{2M_0}{\hat{\gamma}\Gamma_0} = \frac{2E}{\hat{\gamma}\Gamma_0^2}, \tag{1.12}$$

where $E = \Gamma_0 M_0 c^2$ has been used. Rearranging this expression gives the deceleration radius for a constant density ISM-like medium:

$$R_{\mathrm{dec}} = \left(\frac{3E}{2\pi\hat{\gamma}\Gamma_0^2 n m_p c^2}\right)^{1/3}. \tag{1.13}$$

From this expression it is clear that the dependence of Γ on radius during the deceleration phase is $\Gamma \propto R^{-3/2}$ in a constant-density medium, as depicted in Figure 1.5. The observed deceleration time itself can be calculated via the following logic. If a relativistically moving outflow emits two signals separated by an interval δt_e in the lab frame, an observer looking down into the moving outflow will register an interval $\delta t_{\mathrm{obs}} = \delta t_e/(2\Gamma^2)$. This follows from relativistic light propagation effects, and physically it tells us that any signal from the jet arrives at the observer in a strongly time-compressed manner. A small change in radius of the outflow is related to the emission time via $dt_e = dr/c$, and the outflow's bulk Lorentz factor is changing with radius, that is, $\Gamma(r)$. The observed deceleration time can therefore be calculated via the integral

$$t_{\mathrm{dec}} = \int_0^{R_{\mathrm{dec}}} \frac{(1+z)dr}{2\Gamma(r)^2 c} \simeq (370\,\mathrm{s}) E_{52}^{1/3} \Gamma_{0,2}^{-8/3} n^{-1/3} \left(\frac{1+z}{2}\right) \tag{1.14}$$

where the $(1 + z)$ factor comes from cosmological time dilation. The subscript in E_{52}, and in expressions that follow, indicate that the variable is in units of 10^{52}. Inverting this equation yields an expression for the initial Lorentz factor as a function of the deceleration time:

$$\Gamma_0 \simeq 0.9^{3/8} \left(\frac{3E(1+z)^3}{2\pi\hat{\gamma} n m_p c^5 t_{\mathrm{dec}}^3}\right)^{1/8} \simeq 170\, t_{\mathrm{dec},2}^{-3/8} \left(\frac{1+z}{2}\right)^{3/8} E_{52}^{1/8} n^{-1/8}. \tag{1.15}$$

As mentioned previously, a peak observed in an early optical afterglow light curve can thus be used to constrain Γ_0. It is also clear from this expression that the bulk Lorentz factor is related to the observer time as $\Gamma \propto t_{\mathrm{obs}}^{-3/8}$.

---

[7] These are derived based on mass, momentum and energy conservation and are also known as the Rankine-

One further radius of interest is the Sedov radius, which signifies the transition from a relativistic to non-relativistic (or Newtonian) outflow. This occurs when the rest mass energy of the swept-up medium is equivalent to the fireball energy:

$$\frac{4\pi}{3}R_{\rm Sedov}^3 n m_p c^2 = E. \tag{1.16}$$

Inverting Equation 1.16 yields the Sedov radius

$$R_{\rm Sedov} = \left(\frac{3E}{4\pi n m_p c^2}\right)^{1/3} \simeq (1.2\times10^{18}\,{\rm cm})(E_{52}/n)^{1/3}. \tag{1.17}$$

This occurs when the 4-speed $\Gamma\beta = \sqrt{\Gamma^2-1}$ drops below 1. Thereafter, times measured in the lab frame and observer frame are equivalent, so the non-relativistic (NR) transition occurs when

$$t_{\rm NR} \simeq R_{\rm Sedov}/c \simeq (450\,{\rm days})(E_{52}/n)^{1/3}. \tag{1.18}$$

The dynamics of the blast wave in the non-relativistic regime have been studied by Wijers et al. (1997); Dai & Lu (1999); Huang & Cheng (2003). A simple scaling law can be derived by using the fact that the kinetic energy, $mv^2/2$, is constant:

$$\frac{1}{2}mv^2 = \frac{1}{2}\left(\frac{4\pi}{3}r^3 n m_p c^2\right)v^2 = {\rm constant}. \tag{1.19}$$

Using $r = vt$ we get $v \propto r^{-3/2} \propto (vt)^{-3/2}$, so that $v \propto t^{-3/5}$. We show this scaling, along with the asymptotic relativistic scalings in Figure 1.6.

1.3 Afterglow

We presented the dynamics of a fireball in the previous Section. We now turn to the subject of afterglow emission, with the key aim of demonstrating why most afterglow emission is modelled as a power-law in both time and frequency, i.e. $F_\nu \propto t^\alpha \nu^\beta$.

1.3.1 Synchrotron spectrum

The external forward shock formed as the GRB outflow is decelerated by the ambient medium is an ideal site for accelerating charged particles. It is believed that electrons are accelerated to relativistic speeds in shocks via first-order Fermi acceleration (for a review see Blandford & Eichler 1987). The basic principle is that an electron crosses the shock front multiple times and gains energy each time, such that relativistic speeds are achieved. These electrons form a power-law distribution in energies or Lorentz factors (in the comoving frame of the shock), so that $N(E) \propto E^{-p}$ or $N(\gamma) \propto \gamma^{-p}$, where p is the power-law index of the distribution. Semi-analytical studies based on shock theory have shown $p \simeq 2.2 - 2.3$ (Achterberg et al. 2001), while particle-in-cell (PIC) simulations have shown $p = 2.4 \pm 0.1$ (Spitkovsky 2008). In afterglow modelling, shocks are usually parameterised by four microphysics parameters which reflect our ignorance of the detailed physics at the plasma level. These are the power-law index of the electron population, p; the fraction of shock internal energy partitioned to electrons, ϵ_e; the fraction of shock internal energy partitioned to magnetic fields, ϵ_B; and the fraction of electrons within the shock that are accelerated into the power-law distribution, ξ_e. Usually, $\xi_e = 1$ is assumed.

A relativistic charged particle in the presence of a magnetic field will experience an acceleration and produce synchrotron radiation. For a detailed treatment of synchrotron radiation, see Rybicki

---

Hugoniot conditions (in the non-relativistic case). We do not derive them here. See Blandford & McKee (1976) and Zhang & Kobayashi (2005).

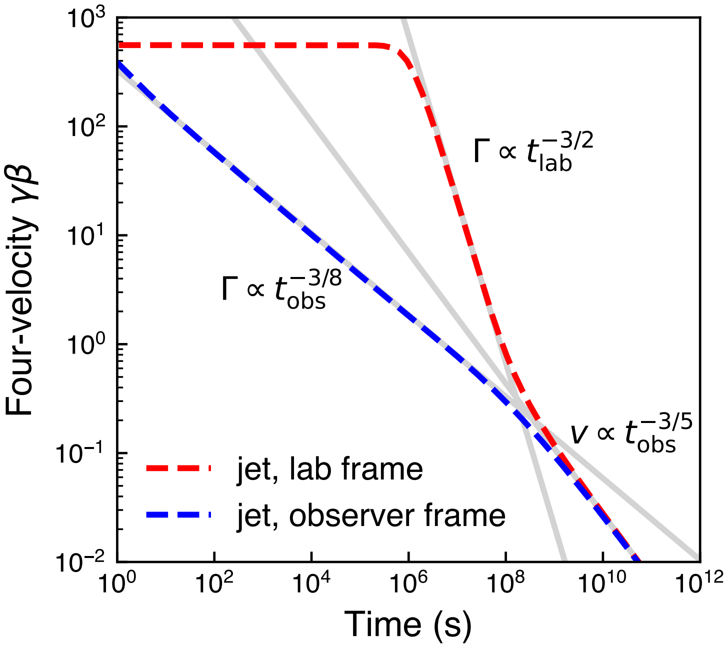

Figure 1.6: Dynamics of a fireball in the lab frame and the observer frame. We show the evolution of the four-velocity for a fireball with an explosion energy of $E = 10^{53}$ erg and ejecta mass of $10^{-4} M_{\odot}$. The circumburst medium is homogeneous with a density of $n = 1\,\mathrm{cm}^{-3}$. The fireball coasts with a Lorentz factor of ≈ 560 before it begins to decelerate. We show the asymptotic evolution of the bulk Lorentz factor in the lab frame and observer frame, and the asymptotic velocity evolution following the NR transition.

& Lightman (1979). We present the main results necessary for deriving afterglow radiation here. The spectrum of a *single* relativistic electron (top left of Figure 1.7) has a peak at a characteristic frequency with a dependence $\nu_{\rm ch} \propto \gamma^2 B'_\perp$, where γ is the electron Lorentz factor and $B'_\perp$ is the perpendicular magnetic field strength, both in the comoving frame of the shock. A larger Lorentz factor results in a higher $\nu_{\rm ch}$. Below $\nu_{\rm ch}$, the spectrum is characterised by a $\nu^{1/3}$ slope, while above $\nu_{\rm ch}$ the spectrum has an exponential cutoff.

A *population* of relativistic electrons with a power-law distribution in Lorentz factors ($N(\gamma) \propto \gamma^{-p}$) with upper and lower bounds of γ_m and γ_M will form an additional spectral segment with a slope of $\nu^{(1-p)/2}$ (top right of Figure 1.7). This can be derived by integrating the spectrum of individual electrons over the energy distribution of the electrons. There is an exponential cutoff in the spectrum which corresponds to the maximum Lorentz factor in the distribution, γ_M. In a constant magnetic field, the peak of the spectrum depends only on the Lorentz factor of the electrons with the lowest Lorentz factor in the distribution, with $\nu_m \propto \gamma_m^2$. Synchrotron electrons with a Lorentz factor γ in a random magnetic field will radiate their energy (or cool) with a power

$$P(\gamma) = \frac{4}{3}\sigma_T c \gamma^2 \beta^2 U_B, \tag{1.20}$$

where σ_T is the Thomson cross section, β is the dimensionless velocity (v/c) averaged over all pitch angles, and $U_B = B'^2/8\pi$ is the magnetic field energy density. The cooling time for an electron with energy $\gamma m_e c^2$ is therefore (Zhang 2018)

$$\tau(\gamma) = \frac{\gamma m_e c^2}{\frac{4}{3}\sigma_T c \gamma^2 \beta^2 U_B} = \frac{6\pi m_e c}{\gamma \sigma_T \beta^2 B'^2}. \tag{1.21}$$

More energetic electrons cool more quickly, since $\tau(\gamma) \propto \gamma^{-1}$. Inverting this expression yields the cooling Lorentz factor at a particular time t

$$\gamma_c(t) \simeq \frac{6\pi m_e c}{\sigma_T B'^2 t}. \tag{1.22}$$

A population of impulsively accelerated electrons will therefore have a maximum energy $\gamma_M \simeq \gamma_c$ that declines as t^{-1}. The exponential cutoff in the spectrum will move to lower frequencies over time (top right of Figure 1.7).

In GRB shocks, fresh particles are constantly being accelerated into the power-law distribution. To accurately determine the electron energy distribution as a function of time, $N(\gamma, t)$, it is necessary to account for fresh injection of particles, cooling, heating, and diffusive losses. To properly account for all of these effects, a continuity equation in energy space should be used. Here we summarise the main results. A more detailed explanation can be found in Section 5.1.5 of Zhang (2018). Fast cooling corresponds to the case when $\gamma_c < \gamma_m$, which means that all injected particles cool quickly. Slow cooling refers to the case when $\gamma_m < \gamma_c$. For electrons below γ_c, the electron distribution will have a γ^{-p} dependence - same as for the impulsive population - whereas above γ_c the distribution will follow a γ^{1-p} dependence. The result is that an additional spectral segment is formed in the emission spectrum (bottom right of Figure 1.7) with a slope of $\nu^{-p/2}$ above the cooling break, which is denoted as ν_c. An intuitive explanation is that electrons with different 'ages' - and therefore cutoff frequencies - will emit simultaneously, as depicted in the bottom left panel of Figure 1.7. There is one more spectral break that is important. This is the self-absorption break ν_a, below which the synchrotron flux is absorbed by the synchrotron-radiating electrons themselves. A detailed treatment of synchrotron self-absorption requires solving the equation of radiative transfer (Rybicki & Lightman 1979). For the standard ordering of spectral breaks ($\nu_a < \nu_m < \nu_c$) the spectrum below ν_a rises steeply as ν^2. There are two means of estimating the self-absorption frequency: the optical depth method, and the blackbody method. The blackbody method is the most widely used due to its simplicity (Sari & Piran 1999a; Kobayashi & Zhang 2003a), and involves computing the intersection point between the

Rayleigh-Jeans approximation to a blackbody function (which rises as ν^2) and the synchrotron spectrum:

$$I_\nu^{\rm bb}(\nu_a) \simeq 2kT\frac{\nu_a^2}{c^2} \simeq I_\nu^{\rm syn}(\nu_a), \tag{1.23}$$

where I_ν is the specific intensity. The temperature of the blackbody is estimated via $kT = \gamma_m m_e c^2$ when $\gamma_a \ll \gamma_m$. Altogether, the synchrotron spectrum consists of three spectral breaks (ν_a, ν_m, ν_c) with six possible different orderings. The most commonly used ordering is for $\nu_a < \nu_m < \nu_c$. If $F_{\nu,\rm max}$ is the flux at ν_m, the *broken power-law* spectrum can be written as

$$F_\nu = F_{\nu,\rm max}\begin{cases} \left(\frac{\nu_a}{\nu_m}\right)^{1/3}\left(\frac{\nu}{\nu_a}\right)^2, & \nu \le \nu_a, \\ \left(\frac{\nu}{\nu_m}\right)^{1/3}, & \nu_a < \nu \le \nu_m, \\ \left(\frac{\nu}{\nu_m}\right)^{(1-p)/2}, & \nu_m < \nu \le \nu_c, \\ \left(\frac{\nu_c}{\nu_m}\right)^{(1-p)/2}\left(\frac{\nu}{\nu_c}\right)^{-p/2}, & \nu_c < \nu. \end{cases} \tag{1.24}$$

This expression is valid in the comoving frame of the shock. To an observer, the whole spectrum will be Doppler-boosted due to the relativistic motion of the shock front, though the spectral indices will remain unchanged.

1.3.2 Dynamics

The basic blast wave dynamics during deceleration were presented in Section 1.2.3 above. Here we focus on scaling laws. After reverse shock crossing the blast wave enters a self-similar regime in which the dynamics depend only on the blast wave energy and density. The simplest case is an adiabatic fireball with constant energy and constant circumburst density (Mészáros & Rees 1997; Sari et al. 1998). Following Zhang (2018), energy conservation may be written as

$$E \simeq V\rho c^2\hat{\gamma}\Gamma^2 \simeq \frac{4\pi}{3}r^3 n m_p c^2\hat{\gamma}\Gamma^2 = \text{constant}. \tag{1.25}$$

The volume the fireball sweeps is $V = (4\pi/3)r^3$, the mass energy density in the shocked region is $\sim \rho c^2\hat{\gamma}\Gamma$, and another factor of Γ is the Lorentz boost in energy from the comoving frame of the shock to the lab frame. From Equation 1.25 we have $r^3\Gamma^2 = $ constant, from which the scaling law $r \propto \Gamma^{-2/3}$ is derived. The observer time is therefore

$$t_{\rm obs} \sim \frac{r}{2\Gamma^2 c} \propto r\Gamma^{-2} \propto \Gamma^{-2/3}\cdot\Gamma^{-2} \propto \Gamma^{-8/3}. \tag{1.26}$$

Inverting this expression yields $\Gamma \propto t_{\rm obs}^{-3/8}$, as shown in Section 1.2.3 above. A stellar wind medium is often considered in afterglow modelling, since long GRBs are known to be associated with massive star progenitors which may have ejected mass via stellar winds in the years leading up to their deaths. In this case, the density of the circumburst medium is no longer constant, but is assumed to decline as r^{-2} (Chevalier & Li 2000). A more general density profile with a power-law index k can be written as

$$n = n_0\left(\frac{r}{r_0}\right)^{-k}. \tag{1.27}$$

The energy conservation condition is therefore

$$E \sim \int 4\pi r^2 n_0\left(\frac{r}{r_0}\right)^{-k} m_p c^2\hat{\gamma}\Gamma^2 dr = \text{constant}, \tag{1.28}$$

from which it is apparent that $r^{3-k}\Gamma^2 = $ constant. Similarly to Equation 1.26, we derive the scaling law for Γ with the observer time as

$$\Gamma \propto t_{\rm obs}^{\frac{k-3}{8-2k}}, \tag{1.29}$$

which reduces to $\Gamma \propto t_{\rm obs}^{-1/4}$ when $k = 2$, as in a stellar wind medium.

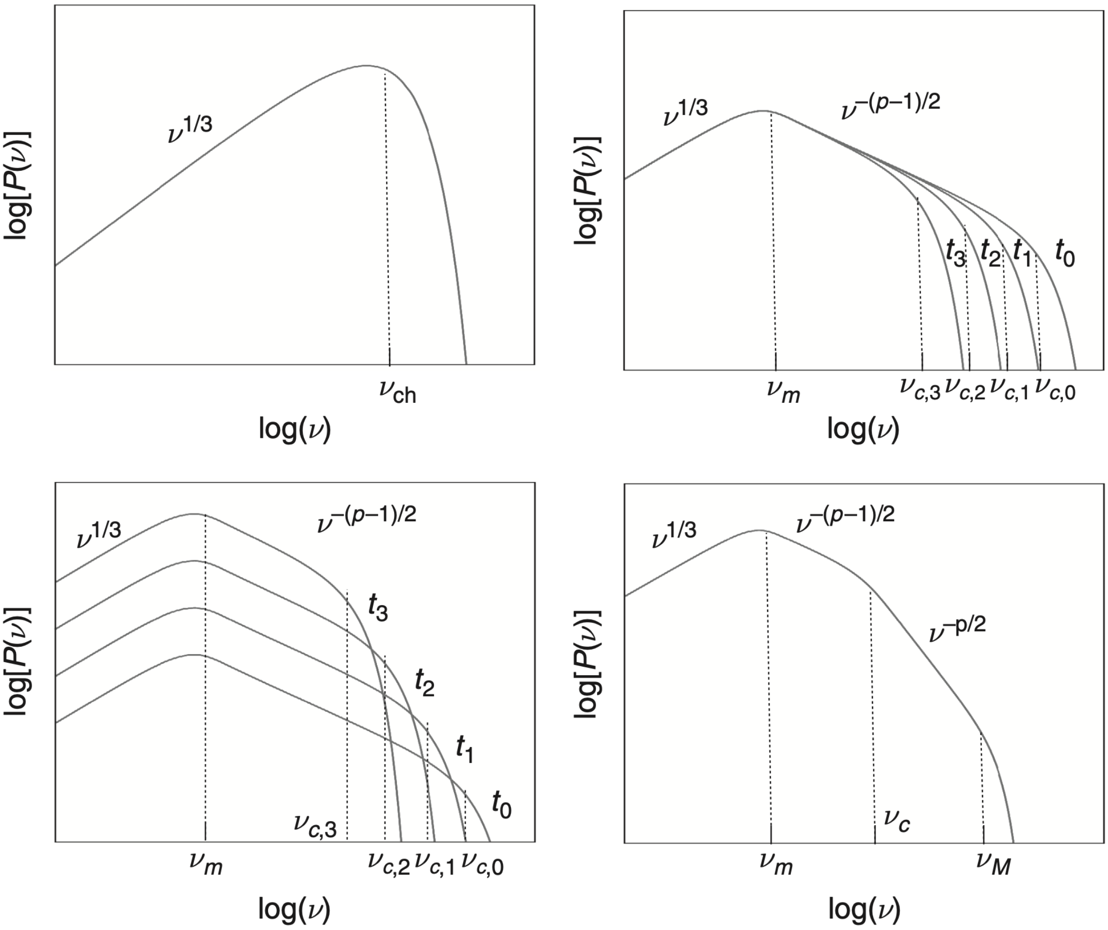

Figure 1.7: *Top left*: The synchrotron spectrum of a single electron in a uniform magnetic field. *Top right*: The spectrum formed by a population of electrons has an additional spectral segment with a high-end cutoff that moves to lower frequencies as electrons cool. *Bottom left*: When new particles are injected, they will each have different cutoffs in their electron distributions - therefore spectra - due to cooling. *Bottom right*: The combined effect of a continuously injected electron population undergoing cooling. An additional spectral segment is formed. Figure adapted from Figure 5.1 in Zhang (2018).

1.3.3 Power-law light curves

If the evolution of the three break frequencies (ν_a, ν_m, ν_c) and $F_{\nu,\max}$ is known, the temporal behaviour within each spectral segment can be calculated. A relativistic electron moving with Lorentz factor γ in the comoving frame of the shock will emit synchrotron radiation with a spectrum peaking at an observed frequency of

$$\nu_{\rm obs} \simeq \frac{3}{4\pi}\Gamma\gamma^2\frac{eB'}{m_e c}, \tag{1.30}$$

where the factor Γ comes from the Doppler boost in frequency from the comoving frame to the observer's frame, and B' is the comoving magnetic field strength. The evolution of the three parameters Γ, γ, and B' can all be derived based on the previously-mentioned dynamics. Following Section 8.2.1 of Zhang (2018), the evolution of γ_m is determined by calculating the average electron Lorentz factor:

$$\overline{\gamma} = \frac{\int_{\gamma_m}^{\gamma_M} \gamma N(\gamma)d\gamma}{\int_{\gamma_m}^{\gamma_M} N(\gamma)d\gamma}. \tag{1.31}$$

For a power-law with $N(\gamma) \propto \gamma^{-p}$ and $p > 2$ (relevant in most cases, though $p \leq 2$ has been studied), we have

$$\overline{\gamma} = \frac{p-1}{p-2}\gamma_m, \tag{1.32}$$

which can be inverted to yield

$$\gamma_m = g(p)\overline{\gamma}, \tag{1.33}$$

where the pre-factor $g(p) = \frac{p-2}{p-1}$. The internal energy within the shock is $(\Gamma-1)n_p m_p c^2$. If a fraction ϵ_e of this internal energy is partitioned to electrons, we can write

$$\epsilon_e(\Gamma-1)n_p m_p c^2 = \overline{\gamma} n_e m_e c^2, \tag{1.34}$$

which can be re-arranged to yield

$$\gamma_m = g(p)\epsilon_e(\Gamma-1)\frac{m_p}{m_e}\frac{n_p}{n_e}. \tag{1.35}$$

Usually, it is assumed that the shocked gas is hydrogen containing an equal number of electrons and protons, i.e. $n_p/n_e = 1$. From this equation it is apparent that $\gamma_m \propto \Gamma$ when $\Gamma \gg 1$. The comoving magnetic field strength is derived by assuming that a fraction ϵ_B of the shock internal energy is partitioned to magnetic fields:

$$\frac{B'^2}{8\pi} = \epsilon_B(\Gamma-1)n_2 m_p c^2 \simeq \epsilon_B \Gamma n_2 m_p c^2 \tag{1.36}$$

From relativistic shock-jump conditions, the density n_2 in the shocked region is a factor 4Γ larger than in the unshocked upstream with density n. This results in

$$B' = (32\pi m_p \epsilon_B n)^{1/2}\Gamma c, \tag{1.37}$$

from which it is evident that $B' \propto \Gamma$. For the cooling Lorentz factor, we use Equation 1.22, though the time t in this expression is actually the comoving time. To convert this to the observer's time, we must multiply t by a factor of Γ as a result of relativistic time dilation:

$$\gamma_c = \frac{6\pi m_e c}{\sigma_T B'^2 \Gamma t_{\rm obs}}. \tag{1.38}$$

The cooling Lorentz factor scales as $\gamma_c \propto B'^{-2}\Gamma^{-1}t_{\rm obs}^{-1}$. The peak observed flux of the synchrotron spectrum, $F_{\nu,\max}$, is given by (Wijers & Galama 1999)

$$F_{\nu,\max} = \frac{N_e \Gamma P'_{\nu_m}(1+z)}{4\pi d_L^2}, \tag{1.39}$$

where $N_e \propto r^3$ is the total number of electrons in the shocked region, P'_{ν_m} is the peak specific emission power of a single electron, d_L is the luminosity distance and z is the redshift. The factor of Γ comes from the relativistic transformation of P'_{ν_m} from the comoving frame to the observer frame. The peak specific emission power is given by (Wijers & Galama 1999)

$$P'_{\nu_{\rm m}} = \phi_p \frac{\sqrt{3}e^3 B'}{m_e c^2} \propto B', \tag{1.40}$$

where ϕ_p is a factor of order unity. From Equations 1.39 and 1.40 it is clear that $F_{\nu,\max} \propto r^3 \Gamma B'$. To derive the temporal behaviour of each spectral break, we employ a scaling-law analysis using the scalings calculated above. The key scalings are

$$\Gamma \propto t_{\rm obs}^{-3/8}, \quad \gamma_m \propto \Gamma, \quad B' \propto \Gamma, \quad \gamma_c \propto B'^{-2} \Gamma t_{\rm obs}^{-1}, \quad F_{\nu,\max} \propto r^3 \Gamma B'. \tag{1.41}$$

From Equation 1.30 we know that any break frequency ν_b depends on three of these parameters as $\nu_b \propto \Gamma \gamma^2 B'$. For example, we calculate the time-dependence of ν_m as

$$\nu_m \propto \Gamma \gamma_m^2 B' \propto \Gamma^4 \propto t_{\rm obs}^{-3/2}, \tag{1.42}$$

while for $F_{\nu,\max}$ we have

$$F_{\nu,\max} \propto r^3 \Gamma B' \propto r^3 \Gamma^2 \propto t^0 \sim \text{constant}. \tag{1.43}$$

Using the broken power-law spectrum from Equation 1.24, along with the scaling of $F_{\nu,\max}$ and each spectral break, the time dependence of the flux in each spectral segment can be derived. For example, in the regime with $\nu_a < \nu \leq \nu_m$ we have $F_\nu = F_{\nu,\max} \left(\frac{\nu}{\nu_m}\right)^{1/3}$. The time dependence in this regime is therefore

$$F_\nu \propto F_{\nu,\max} \nu^{1/3} \nu_m^{-1/3} \propto \text{constant} \cdot \nu^{1/3} \left(t_{\rm obs}^{-3/2}\right)^{-1/3} \propto \nu^{1/3} t_{\rm obs}^{1/2}. \tag{1.44}$$

The afterglow flux is both a power-law in time and frequency[8], $F_\nu \propto t^\alpha \nu^\beta$, with the spectral and temporal indices within a particular spectral segment forming a *closure relation* which can be used to test whether observational data are compatible with an afterglow model. Figure 1.8 presents the temporal dependencies of the spectral breaks and power-law segments for the ordering $\nu_a < \nu_m < \nu_c$. Many more orderings of the spectral breaks are possible. For a comprehensive collection of closure relations including reverse shock emission, see Gao et al. (2013).

It is possible to precisely determine physical parameters of the GRB external shock via theoretical modelling of the afterglow emission. In such a case it is necessary to take into account the detailed structure of the blast wave. Granot & Sari (2002) make use of the Blandford & McKee (1976) self-similar solution for a relativistic explosion which describes the detailed internal structure of the shock front, such as the density, Lorentz factor and internal energy density. The equal-arrival-time surface (EATS) effect and the detailed cooling history of electrons accelerated at different times should also be taken into account. We do not discuss these effects further here, but refer the reader to Waxman (1997); Panaitescu & Mészáros (1998); Sari (1998); Granot et al. (1999); Granot & Sari (2002); Uhm & Zhang (2014).

1.3.4 Phenomenology

The afterglow phase has been studied extensively via observations from across the electromagnetic spectrum. At X-ray energies, *Swift* has been prolific in obtaining X-ray light curves starting very soon after a GRB trigger. Taken as a population, these light curves have been shown to

---

[8] Beware that some authors adopt the convention with $F_\nu \propto t^{-\alpha} \nu^{-\beta}$.

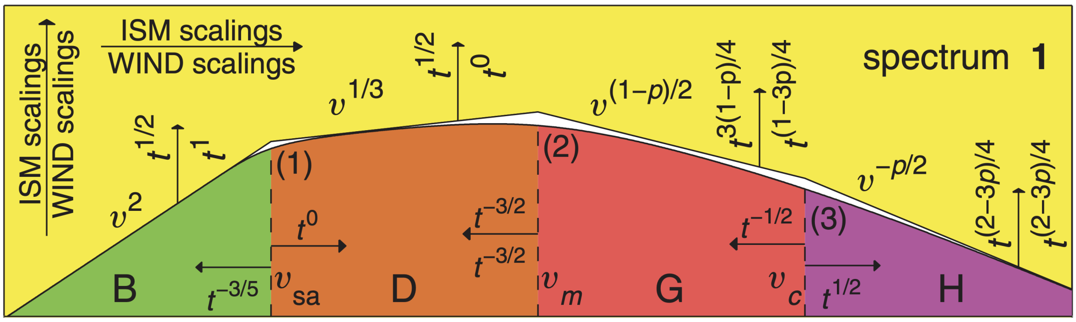

Figure 1.8: Broken power-law synchrotron spectrum with temporal dependencies of the spectral breaks and power-laws segments. The scalings in both a constant density (ISM) medium and stellar wind (WIND) medium are presented for the spectral-break ordering $\nu_a < \nu_m < \nu_c$. Figure adapted from Granot & Sari (2002).

exhibit up to five distinct components (Figure 1.10), with each component arising from a different physical origin (Zhang et al. 2006; Nousek et al. 2006). The first (I) is a steep decay segment with a temporal index of $\alpha \sim -3$ to ~ -10. This segment is usually smoothly connected to the end of the prompt emission (Barthelmy et al. 2005a), and therefore likely related to the prompt emission. The explanation for the steep decay is that once the GRB central engine stops, radiation from higher and higher latitudes with respect to the observer's line of sight is observed - the so-called 'curvature effect', with a predicted evolution of $F_\nu \propto t^{-2+\beta}\nu^\beta$ (Kumar & Panaitescu 2000; Dermer 2004). The second component (II) is a shallow decay segment with a slope of $\alpha \sim 0 - 0.7$, which if very shallow ($\alpha \approx 0$) is called a plateau. Continuous energy injection into the forward shock is the leading explanation, which can either result from a long-lasting central engine (Dai & Lu 1998; Zhang & Mészáros 2001) or an impulsive ejection of ejecta with a stratified Lorentz factor (Rees & Mészáros 1998; Sari & Mészáros 2000; Uhm et al. 2012). The third segment (III) is the 'normal' decay phase which has a slope of $\alpha \sim -1.2$. The origin of this emission is the external forward shock, and should therefore follow the closure relations as outlined in Section 1.3.3 above. If the normal decay segment breaks to a steeper decay with a slope of $\alpha \sim 2$ (segment IV), this likely signifies a *jet break*. Such a jet break in afterglow light curves should be achromatic, and is caused by a deficit in observed flux which occurs when the relativistic beaming angle $\sim 1/\Gamma$ of the emission becomes larger than the opening angle of the jet, θ_j (Figure 1.9). Jet breaks have been widely observed and are regarded as strong evidence for GRB collimation. Wang et al. (2018) used X-ray and optical light curves to constrain the opening angles from jet breaks and found a typical angle of $\theta_j = (2.5 \pm 1.0)^\circ$. The fifth observed component (V) in X-ray light curves are flares showing a rapid rise and fall with steep ($|\alpha| \sim 3$) temporal indices (Burrows et al. 2005; Chincarini et al. 2007). The fact that they are often superposed over a power-law component suggests that they have an internal rather than external origin, with many also being detected by *Swift*/BAT. It is strongly believed that they are directly powered by the central engine, and are therefore the delayed extension of the prompt emission but with reduced amplitudes (Zhang et al. 2006; Fan & Wei 2005).

Optical afterglow light curves show many similar features to those seen in X-ray light curves, but with more complex behaviour at early times (see Figure 1.11). Within the standard external shock framework, some optical light curves show a smooth peak at early times which is regarded as the onset of afterglow, as discussed in Section 1.2.3. A small number of bursts show a steeper decay at early times with $\alpha \sim -2$, sometimes with a steep rise beforehand. Such a feature is regarded as emission from a reverse shock (Mészáros & Rees 1997; Sari & Piran 1999b; Zhang et al. 2003). Optical flares have also been observed which may be related to X-ray flares, though in general they tend to be less significant than X-ray flares (Swenson et al. 2013). Some light curves show re-brightenings which are likely caused by energy injection, while at times after about

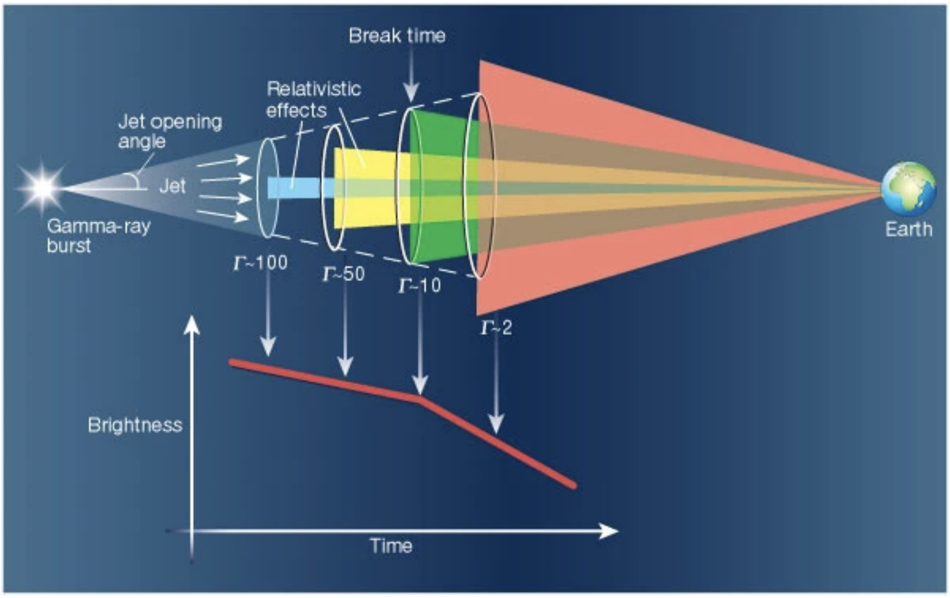

Figure 1.9: Demonstration of the jet break effect. The GRB jet is pointed directly towards an observer on Earth. Due to relativistic beaming, only emission from within a $\sim 1/\Gamma$ cone is visible to the observer. Over time, the jet slows down and the relativistic beaming angle grows larger. Eventually, it will exceed the opening angle of the jet, leading to a deficit in flux and a steepening in the light curve known as a jet break. Figure from Woosley (2001).

a week the light curves of nearby GRBs may show a red 'bump' from an associated supernova.

Radio follow-up of GRBs has been much less frequent than at X-ray and optical frequencies (see Figure 1.3). For GRBs which are followed-up in the radio, the detection rate has been roughly one third (Chandra & Frail 2012). In contrast to X-ray and optical light curves which are usually declining from early times, radio light curves are often rising, and peak on timescales of a few days to weeks after the GRB trigger. This is because the radio bands lie below ν_m (and possibly also ν_a) where the light curves are expected to rise before ν_m crosses the observing band (Figure 1.8). Sampling these parts of the synchrotron spectrum are in fact crucial for determining true physical blast wave parameters, as optical and X-ray observations do not usually constrain $F_{\nu,\max}$ or ν_m. In more recent years, there has been a small but growing sample of GRBs in which an additional spectral component from a *reverse shock* has been detected (Laskar et al. 2013; Perley et al. 2014; Laskar et al. 2016, 2019). Detection of such a component can be used to constrain the jet's magnetisation and initial bulk Lorentz factor (Sari & Piran 1999b; Kobayashi & Zhang 2003b).

1.3.5 Afterglow modelling via MCMC techniques

Markov chain Monte Carlo (MCMC) techniques are currently the most popular method for determining physical parameters related to afterglow emission (see Sharma 2017, for a review on MCMC methods for Bayesian data analysis in astronomy). There are six fundamental parameters for standard forward shock emission in a constant density medium: blast wave parameters including the isotropic-equivalent kinetic energy ($E_{\rm K,iso}$), circumburst density (n) and the opening angle of the jet (θ_j); and shock microphysics parameters (ϵ_e, ϵ_B, p). For a given afterglow model which may be analytic (as in Granot & Sari (2002)) or based on simulations (as for `ScaleFit`, Chapter 4), a particular set of afterglow parameters will produce synchrotron spectra that evolve as a function of time. Afterglow observations at a variety of times and frequencies can then be used to determine the best-fit model parameters. In practice, however, it is often the case that afterglow observations fall within a single spectrum regime. For instance, X-ray and optical observations

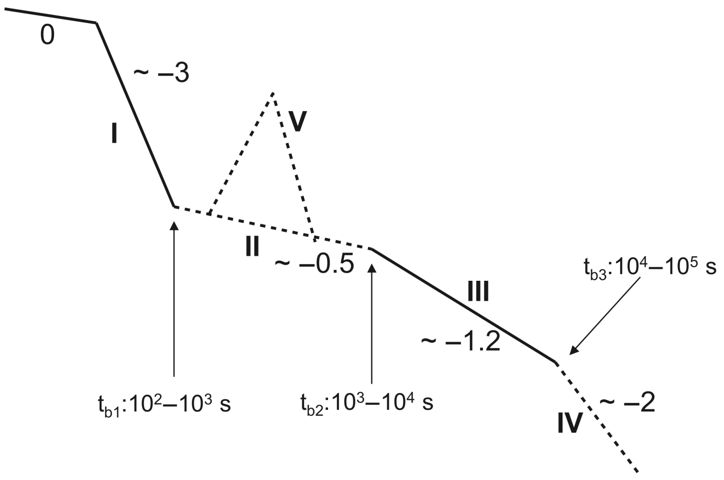

Figure 1.10: Canonical X-ray light curve from Zhang et al. (2006), consisting of five components: (I) steep decay phase; (II) shallow decay/plateau phase; (III) normal decay phase; (IV) post-jet break phase; (V) X-ray flares. Phase '0' indicates the prompt emission. Segments I and III (solid lines) are seen in most X-ray light curves, while Segments II, IV and V (dotted lines) are only seen in a fraction of GRBs.

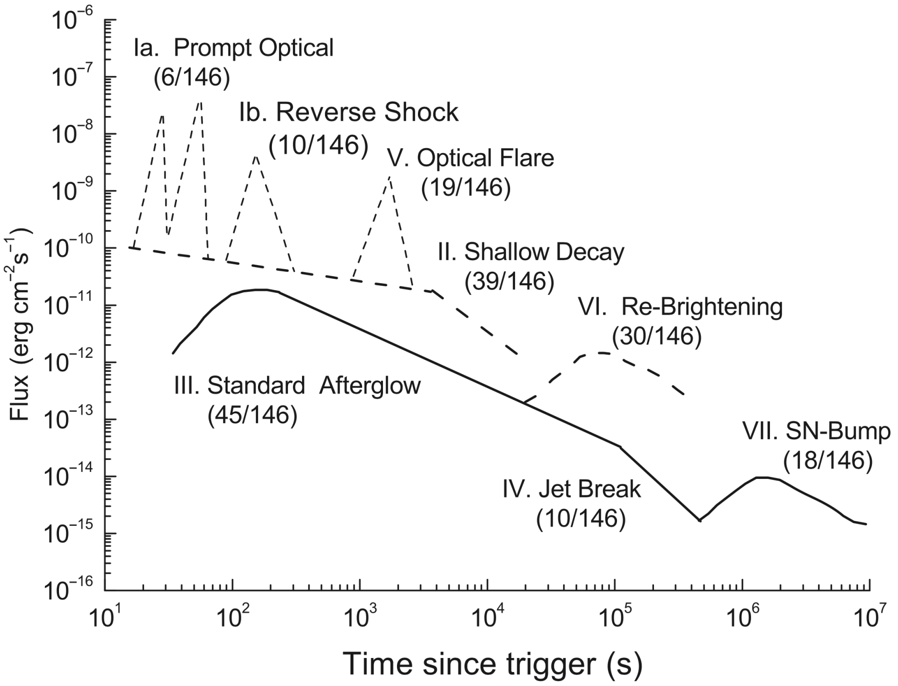

Figure 1.11: Synthetic optical light curve from Li et al. (2012). Components I through V are the same as those in 1.10, though component I is subdivided into optical flares related to the prompt emission (Ia) and flares from a reverse shock (Ib). Unlike the standard X-ray light curve, the standard optical afterglow (III) may exhibit a smooth peak at early times which is regarded as the onset of afterglow. Segment (VI) is a late-time rebrightening which may be due to a refreshed shock, among other causes. Segment VII is a late-time red bump from an emerging supernova.

are the most frequently obtained and do not usually constrain ν_a or $F_{\nu,\mathrm{max}}$. As a result, there are likely to be strong degeneracies and correlations between model parameters. MCMC methods are an effective way of sampling such a large parameter space and uncovering correlations and degeneracies between parameters. In particular, the `emcee` Python package (Foreman-Mackey et al. 2013) offers advantages over traditional MCMC samplers because its multiple 'walkers' make it affine-invariant. Section 4.1 in Chapter 4 provides a detailed implementation of such methods.

1.4 MeerLICHT

The driving force behind this thesis is the MeerLICHT optical telescope (Bloemen et al. 2016). MeerLICHT is a wide-field, fully robotic optical telescope located at the South African Astronomical Observatory (SAAO) site near Sutherland[9] in South Africa. The telescope was built as a prototype for the BlackGEM array (Groot et al., 2024, in prep.) and its primary science goal is to provide a simultaneous optical view of the radio sky as seen by the MeerKAT radio telescope. The optical design consists of a modified Dall-Kirkham Cassegrain system with a parabolic primary mirror and a spherical convex secondary mirror (see Figure 1.12). The telescope aperture is 60 cm with a focal length of 330 cm which results in a focal ratio of F/5.5, while the filter wheel houses five SDSS filters (u,g,r,i,z) along with a wider (440–720 nm) q filter (see Figure 1.13). A set of three lenses in the lens barrel correct for atmospheric dispersion and an off-axis coma. The STA1600 CCD detector consists of 10560×10560 square pixels with 9 μm sides resulting in a 2.7 deg^2 field of view sampled at $0.56''$/pixel.

The telescope is mounted on an equatorial mount with hour angle (HA) limits of -3 hours in the East and +4.5 hours in the West. Additionally, there is a 20 degree altitude limit with respect to the horizon. The telescope has a slew speed of 90 degrees per minute for both the declination and right ascension axes which allows for rapid slewing between sky positions. In order to simplify image reduction and transient identification, MeerLICHT observes using a predefined sky grid of 15946 grid points that tile the sky from the South celestial pole to a declination of $+62°$. There are an additional 140 specially-defined fields that encompass specific objects of interest and baryonic mass overdensities. There is currently a $\sim$15 s overhead between ending an exposure and starting the next exposure, with the primary contributors being the CCD readout time (7 s), download to local computer (5 s), and filter change (3 s). Since MeerLICHT is sky background limited for 60 s exposures, we employ a nominal exposure time of 60 s for all science observations. Although longer exposures would result in greater image depth, this would result in a reduction in sky coverage when observing multiple fields. For special cases when greater depth is required, we have the option to coadd 60 s exposures or increase the exposure time. The historical median limiting AB magnitudes achieved for 60 second exposures are 20.6 in q, 19.0 in u, 20.2 in g, 19.9 in r, 19.4 in i, and 18.4 in z. The wide field of view and six filters spanning the entire optical range were specifically chosen to enable the MeerLICHT and BlackGEM telescopes to rapidly tile the large error boxes of gravitational wave events and determine optical colours for young transients.

The custom-made data reduction pipeline (Vreeswijk et al., in prep.) consists of two components: the first is called BlackBOX which performs standard CCD reduction tasks on the raw images, including gain, crosstalk, bias, and flatfield corrections; the second is known as ZOGY which is used for source identification, astrometry, photometry, and image subtraction for transient identification. The astrometric calibration is tied to the Gaia Data Release 2 (DR2) astrometric catalogue with a reference epoch of J2015.5 in the International Celestial Reference System (ICRS) frame. Photometric calibration is performed using a calibration catalogue of Gaia DR2 stars with magnitudes in the MeerLICHT filters. These magnitudes are obtained by fitting spectral models to photometry from survey data (such as Gaia, PanSTARRS, GALEX,

---

[9] The median q-band image quality at Sutherland is $2.81''$. This value is derived directly from the almost 100 000 q-band images MeerLICHT has taken between 2017 and 2024.

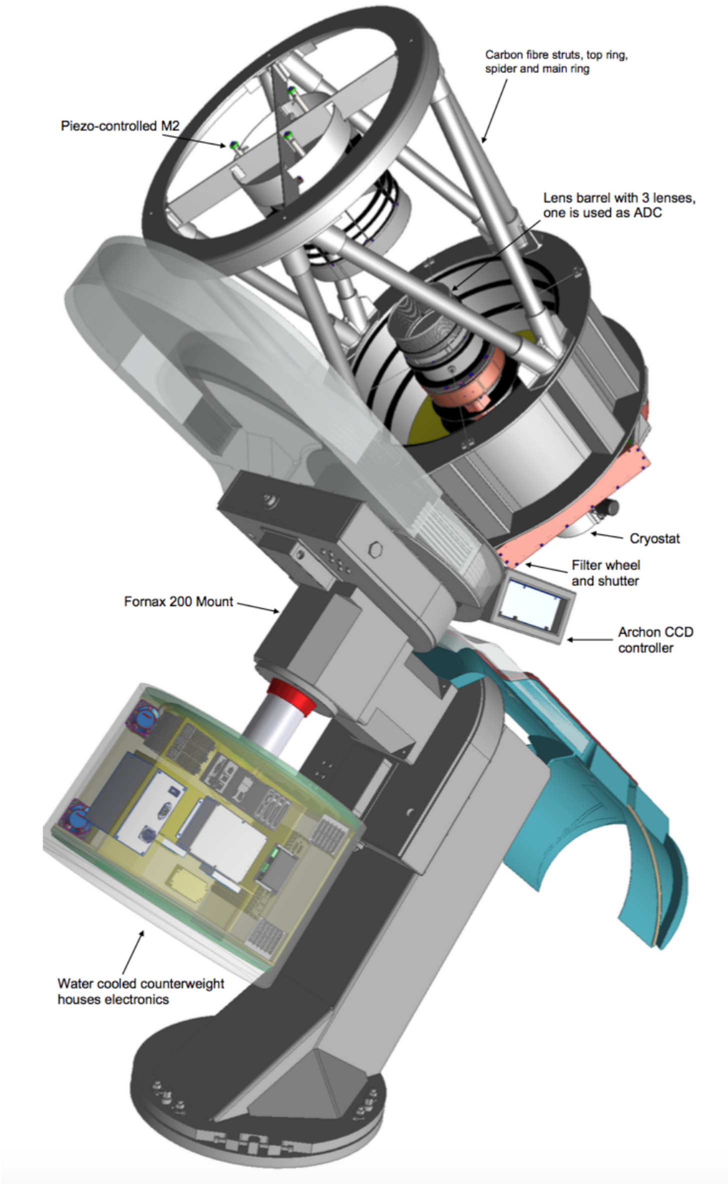

Figure 1.12: Schematic of the MeerLICHT optical telescope, the driving force behind this thesis. Figure from Bloemen et al. (2016).

2MASS and SkyMapper) and deriving AB magnitudes from the fitted spectra taking into account the MeerLICHT filter transmission curves. Transients are identified by subtracting an archival reference image from the reduced image following the ZOGY formalism (Zackay et al. 2016), and identifying sources from the corrected significance image (S_{corr}), which is derived from the difference image. The primary data products are available within 15 minutes after each exposure and consist of a reduced image and source catalogue file containing all 5σ source detections identified by SExtractor, and a transient catalogue file containing all objects with |`SNR_ZOGY`|> 6, meaning that they have a signal-to-noise ratio of greater than $+6$ in the S_{corr} image (or less than -6, for negative transients).

1.5 This thesis

In this thesis I will present the results of a GRB follow-up campaign we implemented with the MeerLICHT optical telescope. In Chapter 2 I describe the GRB follow-up programme we began

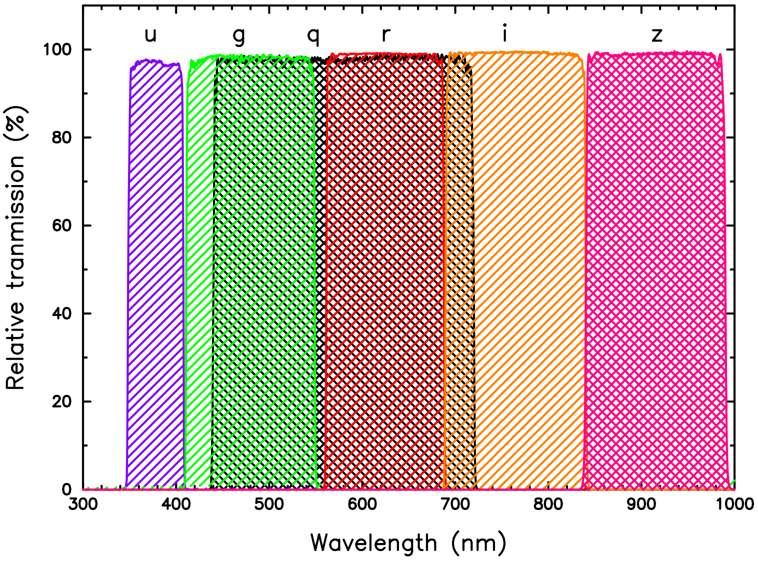

Figure 1.13: MeerLICHT filter transmission curves, from Groot et al. (2004, in prep.).

with MeerLICHT in June 2021. Starting with the scientific justification for the programme, I will move onto an investigation into the observability and detection rates which we might have expected for *Swift* and *Fermi* GRBs before beginning the programme. I will then detail our follow-up strategy and present the results of our observing campaign. The next three chapters provide detailed accounts of three individual bursts, allowing us to perform detailed tests of afterglow models on comprehensive multi-wavelength datasets and thereby elucidate the physics of the afterglow phenomenon.

In Chapter 3 I present the most striking MeerLICHT dataset from our follow-up campaign. MeerLICHT began observing GRB 210731A a mere 286 seconds after the *Swift* trigger time and obtained a light curve showing three peaks of similar brightness within the first four hours - unusual but not unprecedented behaviour for an optical afterglow. Following this discovery we quickly put together proposals to acquire radio observations of the burst with the Very Large Array (VLA) and MeerKAT radio telescopes, which enabled broadband theoretical modelling of the afterglow. Our multi-filter MeerLICHT observations were crucial for showing that the complex optical light curve behaviour was achromatic, and that energy injection into the forward shock was the favoured mechanism to explain the rebrightenings.

In Chapter 4 I detail our follow-up campaign of an *ultra-long* GRB - a GRB whose duration of γ-ray activity is longer than 1000 seconds. GRB 220627A was noteworthy for having two distinct emission episodes that triggered the *Fermi* Gamma-ray Burst Monitor twice. Initial speculation was that the burst may have been gravitationally-lensed, which was quickly rescinded once it was found that the two episodes had quite different γ-ray spectra. MeerLICHT observations were pivotal for discovering and localising the optical afterglow, which led to spectroscopic observations that pinned-down the burst redshift to $z = 3.08$, making this the most distant ultra-long GRB to date. The observations and analysis presented here were not suggestive of the burst having a different progenitor to other, normal long GRBs, contrary to claims made by other authors.

In Chapter 5 I study GRB 210702A, where the main focus is in fact *radio* observations, though MeerLICHT did obtain important early-time optical data starting only 15 minutes after the burst trigger. The ALMA 97.5 GHz light curve for this burst shows a remarkable rebrightening beginning at 8.2 days - the first such rebrightening seen in a millimeter afterglow light curve. A number of mechanisms to explain the rebrightening are explored, with energy injection and a reverse shock from a late-time shell collision ending up as the preferred scenarios. Another key finding is that a standard forward shock model cannot explain much of the radio data, particularly at frequencies lower than 40 GHz. The thesis concludes with a summary of the work completed and a look forward towards future work.

A very strong component of this thesis is its multi-wavelength character, which is naturally driven by the multi-wavelength nature of the afterglow phenomenon. A significant time-investment was spent becoming acquainted with the techniques of X-ray and radio data calibration, in addition to optical data from MeerLICHT. A second strong component is the use of theoretical modelling using MCMC statistical methods to derive intrinsic blast wave parameters. The use of these various techniques was stimulated by three workshops I attended over the course of my PhD: the European Radio Interferometry School in September 2022, the X-Vision X-ray astronomy workshop in February 2023, and a small GRB afterglow modelling workshop hosted at the University of Bath in October 2022. I am grateful for these experiences and for the enlightening conversations with experts in each respective field.

Bibliography

Abbott, B. P., Abbott, R., Abbott, T. D., & Acernese, F. 2017a, ApJ, 848, L13

Abbott, B. P., Abbott, R., Abbott, T. D., & Acernese, F. 2017b, Phys. Rev. Lett., 119, 161101

Abdo, A. A., Ackermann, M., Ajello, M., et al. 2009, ApJ, 706, L138

Achterberg, A., Gallant, Y. A., Kirk, J. G., & Guthmann, A. W. 2001, MNRAS, 328, 393

Ackermann, M., Asano, K., Atwood, W. B., et al. 2010, ApJ, 716, 1178

Ajello, M., Arimoto, M., Axelsson, M., et al. 2019, ApJ, 878, 52

Arcavi, I., Hosseinzadeh, G., Howell, D. A., et al. 2017, Nature, 551, 64

Axelsson, M., Baldini, L., Barbiellini, G., et al. 2012, ApJ, 757, L31

Band, D., Matteson, J., Ford, L., et al. 1993, ApJ, 413, 281

Baring, M. G. & Harding, A. K. 1997, ApJ, 491, 663

Barthelmy, S. D., Cannizzo, J. K., Gehrels, N., et al. 2005a, ApJ, 635, L133

Barthelmy, S. D., Chincarini, G., Burrows, D. N., et al. 2005b, Nature, 438, 994

Beloborodov, A. M. 2010, MNRAS, 407, 1033

Blandford, R. & Eichler, D. 1987, Phys. Rep., 154, 1

Blandford, R. D. & McKee, C. F. 1976, Physics of Fluids, 19, 1130

Bloemen, S., Groot, P., Woudt, P., et al. 2016, in Society of Photo-Optical Instrumentation Engineers (SPIE) Conference Series, Vol. 9906, Ground-based and Airborne Telescopes VI, ed. H. J. Hall, R. Gilmozzi, & H. K. Marshall, 990664

Bloom, J. S., Prochaska, J. X., Pooley, D., et al. 2006, ApJ, 638, 354

Briggs, M. S., Paciesas, W. S., Pendleton, G. N., et al. 1996, ApJ, 459, 40

Burrows, D. N., Romano, P., Falcone, A., et al. 2005, Science, 309, 1833

Chandra, P. & Frail, D. A. 2012, ApJ, 746, 156

Chevalier, R. A. & Li, Z.-Y. 2000, ApJ, 536, 195

Chincarini, G., Moretti, A., Romano, P., et al. 2007, ApJ, 671, 1903

Chornock, R., Berger, E., Kasen, D., et al. 2017, ApJ, 848, L19

Colgate, S. A. 1968, Canadian Journal of Physics Supplement, 46, 476

Colgate, S. A. 1974, ApJ, 187, 333

Costa, E., Frontera, F., Heise, J., et al. 1997, Nature, 387, 783

Coulter, D. A., Foley, R. J., Kilpatrick, C. D., et al. 2017, Science, 358, 1556

Cucchiara, A., Levan, A. J., Fox, D. B., et al. 2011, ApJ, 736, 7

Dai, Z. G. & Lu, T. 1998, Phys. Rev. Lett., 81, 4301

Dai, Z. G. & Lu, T. 1999, ApJ, 519, L155

Daigne, F., Bošnjak, Ž., & Dubus, G. 2011, A&A, 526, A110

Daigne, F. & Mochkovitch, R. 1998, MNRAS, 296, 275

Dermer, C. D. 2004, ApJ, 614, 284

Evans, P. A., Cenko, S. B., Kennea, J. A., et al. 2017, Science, 358, 1565

Fan, Y. Z. & Wei, D. M. 2005, MNRAS, 364, L42

Foreman-Mackey, D., Hogg, D. W., Lang, D., & Goodman, J. 2013, PASP, 125, 306

Frail, D. A., Kulkarni, S. R., Nicastro, L., Feroci, M., & Taylor, G. B. 1997, Nature, 389, 261

Galama, T. J., Vreeswijk, P. M., van Paradijs, J., et al. 1998, Nature, 395, 670

Gao, H., Lei, W.-H., Zou, Y.-C., Wu, X.-F., & Zhang, B. 2013, New A Rev., 57, 141

Gao, H. & Zhang, B. 2015, ApJ, 801, 103

Gehrels, N., Sarazin, C. L., O'Brien, P. T., et al. 2005, Nature, 437, 851

Goldstein, A., Veres, P., Burns, E., et al. 2017, ApJ, 848, L14

Granot, J., Komissarov, S. S., & Spitkovsky, A. 2011, MNRAS, 411, 1323

Granot, J., Piran, T., & Sari, R. 1999, ApJ, 513, 679

Granot, J. & Sari, R. 2002, ApJ, 568, 820

Greiner, J., Krühler, T., Fynbo, J. P. U., et al. 2009, ApJ, 693, 1610

Guiriec, S., Connaughton, V., Briggs, M. S., et al. 2011, ApJ, 727, L33

Gupta, N. & Zhang, B. 2008, MNRAS, 384, L11

Hascoët, R., Daigne, F., & Mochkovitch, R. 2013, A&A, 551, A124

Higdon, J. C. & Lingenfelter, R. E. 1990, ARA&A, 28, 401

Hjorth, J., Sollerman, J., Møller, P., et al. 2003, Nature, 423, 847

Huang, Y. F. & Cheng, K. S. 2003, MNRAS, 341, 263

Kasen, D., Metzger, B., Barnes, J., Quataert, E., & Ramirez-Ruiz, E. 2017, Nature, 551, 80

Klebesadel, R. W., Strong, I. B., & Olson, R. A. 1973, ApJ, 182, L85

Kobayashi, S., Piran, T., & Sari, R. 1999, ApJ, 513, 669

Kobayashi, S. & Zhang, B. 2003a, ApJ, 582, L75

Kobayashi, S. & Zhang, B. 2003b, ApJ, 582, L75

Kobayashi, S. & Zhang, B. 2007, ApJ, 655, 973

Kouveliotou, C., Meegan, C. A., Fishman, G. J., et al. 1993, ApJ, 413, L101

Kouveliotou, C., Wijers, R. A. M. J., & Woosley, S. 2012, Gamma-ray Bursts

Kulkarni, S. R., Frail, D. A., Wieringa, M. H., et al. 1998, Nature, 395, 663

Kumar, P. & Barniol Duran, R. 2009, MNRAS, 400, L75

Kumar, P. & Barniol Duran, R. 2010, MNRAS, 409, 226

Kumar, P. & Panaitescu, A. 2000, ApJ, 541, L51

Laskar, T., Alexander, K. D., Berger, E., et al. 2016, ApJ, 833, 88

Laskar, T., Berger, E., Zauderer, B. A., et al. 2013, ApJ, 776, 119

Laskar, T., van Eerten, H., Schady, P., et al. 2019, ApJ, 884, 121

Lazzati, D. & Begelman, M. C. 2010, ApJ, 725, 1137

Li, L., Liang, E.-W., Tang, Q.-W., et al. 2012, ApJ, 758, 27

Li, L.-X. & Paczyński, B. 1998, ApJ, 507, L59

Liang, E., Zhang, B., Virgili, F., & Dai, Z. G. 2007, ApJ, 662, 1111

Lithwick, Y. & Sari, R. 2001, ApJ, 555, 540

MAGIC Collaboration, Acciari, V. A., Ansoldi, S., et al. 2019a, Nature, 575, 455

MAGIC Collaboration, Acciari, V. A., Ansoldi, S., et al. 2019b, Nature, 575, 459

Mazets, E. P., Golenetskii, S. V., Aptekar, R. L., Gurian, I. A., & Ilinskii, V. N. 1981a, Nature, 290, 378

Mazets, E. P., Golenetskii, S. V., Ilinskii, V. N., et al. 1981b, Ap&SS, 80, 3

Meegan, C. A., Fishman, G. J., Wilson, R. B., et al. 1992, Nature, 355, 143

Meszaros, P. & Rees, M. J. 1993, ApJ, 405, 278

Mészáros, P. & Rees, M. J. 1997, ApJ, 476, 232

Mészáros, P. & Rees, M. J. 2000, ApJ, 530, 292

Mészáros, P. & Rees, M. J. 2011, ApJ, 733, L40

Metzger, B. D. 2017, Living Reviews in Relativity, 20, 3

Metzger, B. D., Giannios, D., Thompson, T. A., Bucciantini, N., & Quataert, E. 2011, MNRAS, 413, 2031

Metzger, B. D., Martínez-Pinedo, G., Darbha, S., et al. 2010, MNRAS, 406, 2650

Metzger, M. R., Djorgovski, S. G., Kulkarni, S. R., et al. 1997, Nature, 387, 878

Murakami, T., Fujii, M., Hayashida, K., Itoh, M., & Nishimura, J. 1988, Nature, 335, 234

Nemiroff, R. J. 1994, Comments on Astrophysics, 17, 189

Nicholl, M., Berger, E., Kasen, D., et al. 2017, ApJ, 848, L18

Nousek, J. A., Kouveliotou, C., Grupe, D., et al. 2006, ApJ, 642, 389

Panaitescu, A. & Mészáros, P. 1998, ApJ, 493, L31

Perley, D. A., Cenko, S. B., Corsi, A., et al. 2014, ApJ, 781, 37

Pian, E., D'Avanzo, P., Benetti, S., et al. 2017, Nature, 551, 67

Piran, T., Shemi, A., & Narayan, R. 1993, MNRAS, 263, 861

Rees, M. J. & Meszaros, P. 1992, MNRAS, 258, 41

Rees, M. J. & Meszaros, P. 1994, ApJ, 430, L93

Rees, M. J. & Mészáros, P. 1998, ApJ, 496, L1

Rhoads, J. E. 1999, ApJ, 525, 737

Ruderman, M. 1975, in Seventh Texas Symposium on Relativistic Astrophysics, ed. P. G. Bergman, E. J. Fenyves, & L. Motz, Vol. 262, 164–180

Rybicki, G. B. & Lightman, A. P. 1979, Radiative processes in astrophysics

Ryde, F., Axelsson, M., Zhang, B. B., et al. 2010, ApJ, 709, L172

Salvaterra, R., Della Valle, M., Campana, S., et al. 2009, Nature, 461, 1258

Sari, R. 1998, ApJ, 494, L49

Sari, R. & Mészáros, P. 2000, ApJ, 535, L33

Sari, R. & Piran, T. 1999a, ApJ, 517, L109

Sari, R. & Piran, T. 1999b, ApJ, 520, 641

Sari, R., Piran, T., & Halpern, J. P. 1999, ApJ, 519, L17

Sari, R., Piran, T., & Narayan, R. 1998, ApJ, 497, L17

Shappee, B. J., Simon, J. D., Drout, M. R., et al. 2017, Science, 358, 1574

Sharma, S. 2017, ARA&A, 55, 213

Smartt, S. J., Chen, T. W., Jerkstrand, A., et al. 2017, Nature, 551, 75

Spitkovsky, A. 2008, ApJ, 682, L5

Stanek, K. Z., Matheson, T., Garnavich, P. M., et al. 2003, ApJ, 591, L17

Swenson, C. A., Roming, P. W. A., De Pasquale, M., & Oates, S. R. 2013, ApJ, 774, 2

Tanvir, N. R., Fox, D. B., Levan, A. J., et al. 2009, Nature, 461, 1254

Tanvir, N. R., Levan, A. J., González-Fernández, C., et al. 2017, ApJ, 848, L27

Taylor, G. B., Frail, D. A., Berger, E., & Kulkarni, S. R. 2004, ApJ, 609, L1

Tchekhovskoy, A., McKinney, J. C., & Narayan, R. 2009, ApJ, 699, 1789

Toma, K., Wu, X. F., & Mészáros, P. 2011, MNRAS, 415, 1663

Uhm, Z. L. & Zhang, B. 2014, ApJ, 780, 82

Uhm, Z. L., Zhang, B., Hascoët, R., et al. 2012, ApJ, 761, 147

van Paradijs, J., Groot, P. J., Galama, T., et al. 1997, Nature, 386, 686

Virgili, F. J., Liang, E.-W., & Zhang, B. 2009, MNRAS, 392, 91

Wang, X.-G., Zhang, B., Liang, E.-W., et al. 2018, ApJ, 859, 160

Waxman, E. 1997, ApJ, 491, L19

Wijers, R. A. M. J. & Galama, T. J. 1999, ApJ, 523, 177

Wijers, R. A. M. J., Rees, M. J., & Meszaros, P. 1997, MNRAS, 288, L51

Woosley, S. 2001, Nature, 414, 853

Zackay, B., Ofek, E. O., & Gal-Yam, A. 2016, ApJ, 830, 27

Zhang, B. 2018, The Physics of Gamma-Ray Bursts

Zhang, B. 2019, Nature, 575, 448

Zhang, B., Fan, Y. Z., Dyks, J., et al. 2006, ApJ, 642, 354

Zhang, B. & Kobayashi, S. 2005, ApJ, 628, 315

Zhang, B., Kobayashi, S., & Mészáros, P. 2003, ApJ, 595, 950

Zhang, B. & Mészáros, P. 2001, ApJ, 552, L35

Zhang, B. & Pe'er, A. 2009, ApJ, 700, L65

Zhang, B. & Yan, H. 2011, ApJ, 726, 90

Zhang, B.-B., Zhang, B., Liang, E.-W., et al. 2011, ApJ, 730, 141

Chapter 2

GRB follow-up with MeerLICHT

In preparation for the fourth LIGO/Virgo observing run, we made the decision in early 2021 to begin a GRB follow-up program with the MeerLICHT optical telescope, with the intention of including the BlackGEM array once operational. Our rationale for starting such a programme was the following:

- GRBs are fast transients requiring rapid follow-up by electromagnetic (EM) facilities, particularly at higher energies (optical to γ-rays) where they evolve most quickly at early times.
- The progenitors of some GRBs - mainly of a short-duration - are compact binaries consisting of neutron stars and/or black holes which are strong candidates for producing gravitational waves (GW) detectable by LIGO/Virgo. This was confirmed through the joint EM/GW detection of GRB 170817A and GW 170817 (Abbott et al. 2017a,b).
- During previous observing runs, GW alerts and their EM follow-up were coordinated through the Gamma-ray Coordinates Network (GCN), which is the primary platform for coordinating GRB follow-up within the EM community.
- *Fermi*/GBM GRBs have large sky error boxes much like GW alerts (Goldstein et al. 2020), requiring a large number of telescope pointings to cover a sizeable probability region. This makes them an ideal testing-ground for GW follow-up.
- The science returns of GRB follow-up can be high. Nearby GRBs offer the possibility of detecting a supernova (e.g. GRB 030329; Stanek et al. 2003; Hjorth et al. 2003) or kilonova in a host galaxy (e.g. GRB 130603B; Tanvir et al. 2013; Berger et al. 2013), while some GRBs are detected at very high redshifts (e.g. GRB 090429B at $z = 9.4$; Cucchiara et al. 2011) making them some of the most distant objects observed in the Universe. Very early afterglow observations can provide insight into the complex interplay between the afterglow and prompt emission, with the added possibility of detecting a rare reverse shock signature at optical to radio frequencies (e.g. GRB 130427A; Laskar et al. 2013; Perley et al. 2014).
- It is valuable to 'make our presence known' within the GRB community due to the significant overlap between the GW and GRB communities.

Before starting the program, we undertook an initial investigation into the frequency we could expect to observe *Fermi* and *Swift* GRBs.

2.1 Observability of *Fermi*/GBM GRBs

The *Fermi* Gamma-Ray Space Telescope was launched on 2008 June 11 with the intention of studying the high-energy γ-ray sky. *Fermi* is equipped with two main instruments: a pair-conversion imaging detector known as the Large Area Telescope (Atwood et al. 2009, LAT) which scans the sky every three hours and detects photons in the 20 MeV - 300 GeV range; and the Gamma-ray Burst Monitor (Meegan et al. 2009, GBM) which consists of 14 scintillation detectors operating in the 8 keV - 40 MeV energy range that monitors the entire sky for GRBs. Together, both detectors cover an energy range spanning seven orders of magnitude with fine time and spectral resolution. As a result, *Fermi* has greatly enhanced our understanding of the GRB prompt emission physics.

The GBM detects ∼240 GRBs per year (von Kienlin et al. 2020) and sends out public alerts to the EM community with a latency of ∼10 minutes. The GBM cannot perform imaging or reconstruct the arrival directions of photons in the same way as the LAT or BAT onboard *Swift*, and as a consequence cannot provide sub-degree localisations. It instead uses the relative rates in the 12 NaI detectors to determine the most likely photon arrival direction, using an algorithm based on that used by BATSE (Pendleton et al. 1999). The statistical uncertainty on GBM localisations can be as small as 1° (Connaughton et al. 2015), though a study of the systematic uncertainties of the automated localisations found that the true burst locations were 1.8° from the predicted positions for 52% of GRBs and 4.1° for the remaining 48%, with the median 90% area of their localisations having a sky area of 209 deg^2 (Goldstein et al. 2020). The large sky error boxes of GBM localisations have therefore deterred follow-up by all but the largest field-of-view telescopes, with most groups waiting for smaller localisation regions from *Swift*, *INTEGRAL*, *Fermi*/LAT or the interplanetary network (IPN) before directing their follow-up efforts. The intermediate Palomar Transient Factory (iPTF) was the first instrument to discover an optical afterglow based solely on a GBM localisation through tiling 72 deg^2 of the sky in 10 telescope pointings during the follow-up of GRB 130702A (Singer et al. 2013). A further 8 afterglows were discovered by iPTF in their follow-up of 35 *Fermi* GRBs (Singer et al. 2015). Since then, GBM follow-up has been undertaken by MASTER (Lipunov et al. 2016), ZTF (Coughlin et al. 2019) and GOTO (Mong et al. 2021a).

Before starting our follow-up of GBM-detected GRBs, we decided to conduct an investigation into the feasibility of such an undertaking based on an historic sample of GBM-detected bursts. Since 2016, the `RoboBA` algorithm has been employed by the *Fermi*/GBM team to replace human-in-the-loop processing for GBM triggers while maintaining the same accuracy and reducing the latency with which localisations are provided to the EM community (Goldstein et al. 2020). From early 2018 onwards, localisations have been provided as full-sky HEALPix (Górski et al. 2005) FITS files. In September 2019 `RoboBA` was updated to produce more accurate localisations with a smaller incorporated systematic uncertainty (Fermi GBM Team 2019). We downloaded the HEALPix fits files from the HEASARC[1] archive for GRBs detected between September 2019 and April 2021 with a declination $< 10°$. For each file we employed our ranked-tiling method (Ghosh et al. 2016) scheduling script to tile the GBM error boxes to encompass a cumulative probability of at least 90% according to MeerLICHT's fixed sky-grid. The ranked tiling method calculates the probability contained in each field of the fixed sky-grid and ranks them in order of contained probability. The fields which cumulatively encompass a given probability (90% in this case) are the fields chosen for observing. Ghosh et al. (2016) showed that this method requires fewer tiles to encompass a given probability compared to the contour-covering method. Figure 2.1 shows our tiling for a well-localised burst and a burst with a very large error box. For the entire sample of 201 bursts we calculated the 50% and 90% cumulative probability areas and calculated the number of tiles needed to cover each error box using the ranked-tiling scheduling script. In Figure 2.2 we see that for half of the GRBs in our sample we would be able to cover a probability of 90% with 167 tiles or less, which amounts to approximately 3 hours of observing time assuming 60 s exposures per pointing.

In devising a follow-up strategy, we would ideally like to cover a probability of at least 90% to give us a good chance of observing the afterglow as well as observing each field at least twice in a single night in order to rule out asteroids and check for fading behaviour. A total of 80 tiles could

---

[1] https://heasarc.gsfc.nasa.gov/FTP/fermi/data/gbm/bursts/

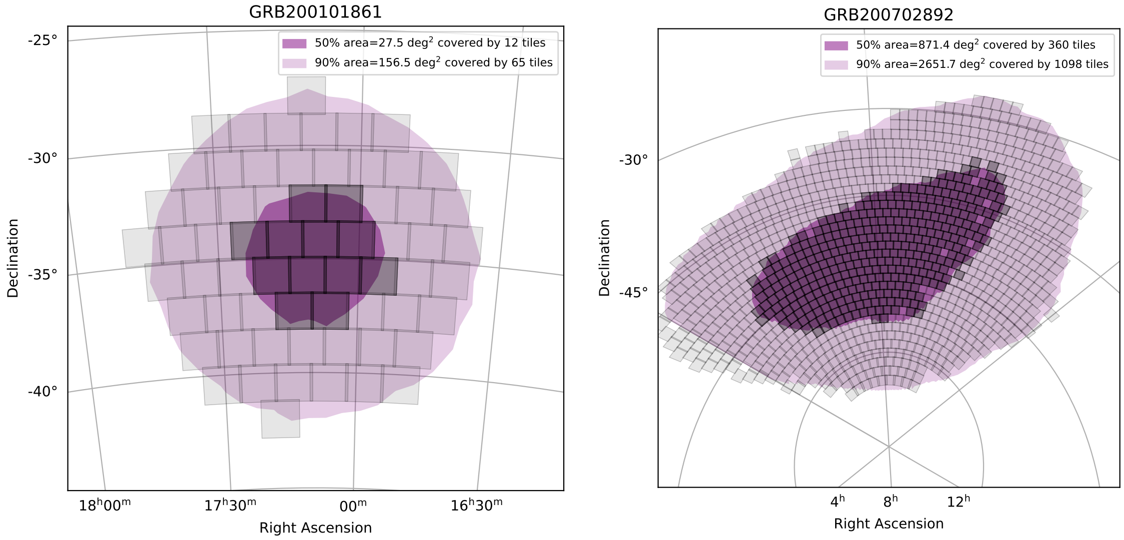

Figure 2.1: Example tilings of *Fermi*/GBM sky maps for a well-localised burst (left) and a burst with an enormous error box (right). We show the 50% and 90% probability contours along with the number of tiles required to cover a cumulative probability of 50% and 90%. Assuming each field is observed once with a 60 s exposure, it would take ∼1 hour to observe 90% of the well-localised burst's error box, while the poorly-localised burst would require an unfeasible ∼19 hours.

be observed twice in about 3 hours on a single night. We find that 42/201 bursts in our sample could be observed with 80 or fewer tiles while covering a probability of 90%, resulting in a rate of approximately one such burst every two weeks, which we take as an upper limit considering telescope observing constraints and bad weather.

2.2 Observability of *Swift* GRBs

The Neil Gehrels *Swift* Observatory (Gehrels et al. 2004) was launched on 2004 November 20 equipped with three instruments: a Burst Alert Telescope (Barthelmy et al. 2005, BAT), X-Ray Telescope (Burrows et al. 2005, XRT), and Ultra-Violet/Optical Telescope (Roming et al. 2005, UVOT). *Swift*/BAT detects hard X-rays in the 15-350 keV energy range and is able to localise bursts to an accuracy of $1'$–$4'$ by means of a coded-aperture mask situated 1 metre above the CdZnTe detector plane. The XRT has a $23.6' \times 23.6'$ field-of-view (FOV) and is able to autonomously slew to the position of a BAT-detected burst within one minute of a GRB trigger, allowing for the rapid localisation of the afterglow to positional accuracies of several arcseconds. The UVOT has a 30 cm primary mirror with a $17' \times 17'$ FOV and 6 broadband filters spanning ultra-violet to optical wavelengths (170-600 nm), allowing for sub-arcsecond localisations should an optical afterglow be detected. *Swift* rapidly disseminates the results of XRT and UVOT follow-up of BAT-detected bursts to the GCN to enable follow-up by other ground-based and space-based facilities, and has revolutionised the study of GRBs in a number of aspects.

Although the observation of optical afterglows is now fairly common due to *Swift*, it still remains the case that new and interesting discoveries are routinely made. For this reason, we decided to investigate the rates with which we could expect to observe *Swift*-detected GRBs with MeerLICHT. MeerLICHT has a $98.6' \times 98.6'$ FOV which is much larger than the $\sim 3'$-radius error circles with which BAT detects GRBs, meaning that a single telescope pointing would in almost all cases contain the BAT error circle. We obtained a table of all *Swift* GRBs from the NASA

---

[2] https://swift.gsfc.nasa.gov/archive/grb_table/

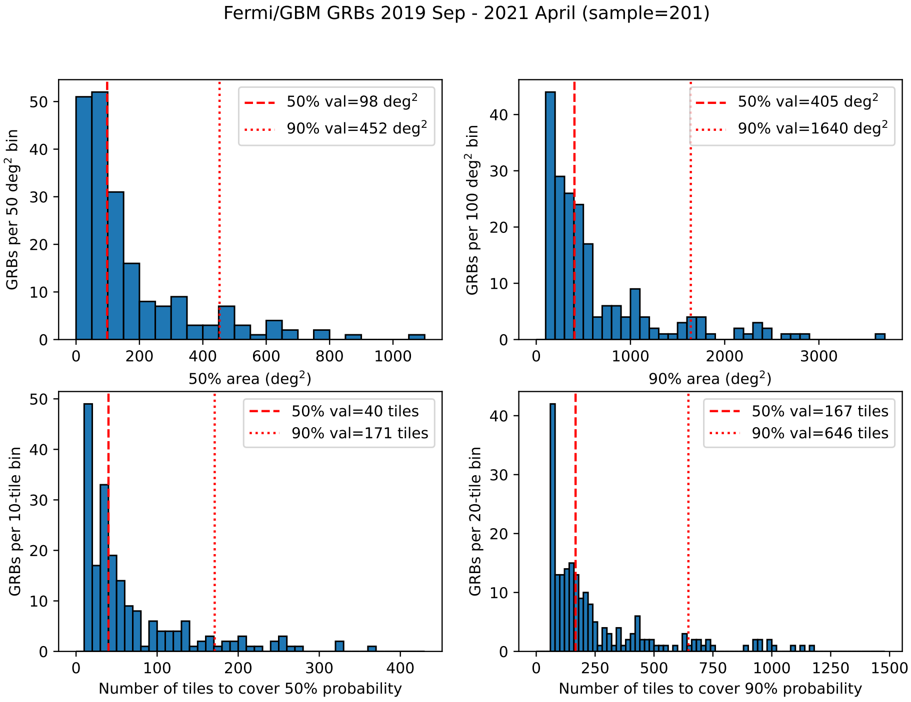

Figure 2.2: Top row: we show the distributions of the sky areas required to cover a cumulative probability of 50% and 90% of the GBM error boxes for our sample of GBM-detected GRBs. Bottom row: we show the distributions of the number of MeerLICHT tiles required to cover 50% and 90% cumulative probabilities. The red vertical lines in each figure indicate the median and 90% sample values.

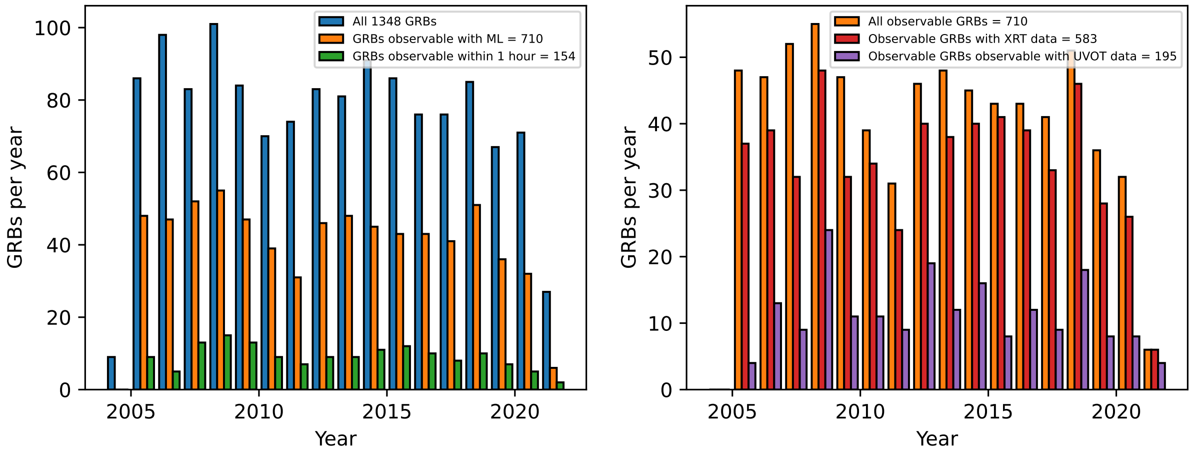

Figure 2.3: Left: roughly half of all *Swift* GRBs detected between December 2004 and April 2021 would have been observable with MeerLICHT, and just more than 10% would have been observable within 1 hour of the GRB trigger, equating to 0.8 GRBs per month, or roughly 10 per year. Right: Almost a quarter of all observable bursts had UVOT counterparts, meaning they would likely have optical afterglows observable with MeerLICHT.

GSFC archive[2] between December 2004 and April 2021 and determined how many of the bursts would have been observable with MeerLICHT based on their BAT positions. The sample consisted of 1348 GRBs after cleaning the table for GRBs with missing information. The left-hand plot in Figure 2.3 shows that 753 - or 52% - of these GRBs would have been observable with MeerLICHT, amounting to 3.8 GRBs per month. A total of 157 of these observable GRBs would have been observable within 1 hour of the *Swift* trigger time, at a rate of 0.8 GRBs per month (or ∼ 10 per year). These are the most interesting GRBs for MeerLICHT as they would make use of our ability to respond quickly to a trigger and autonomously start observing. Furthermore, early afterglows are generally brighter and show more interesting behaviour than at later times, increasing the science returns. The right panel of Figure 2.3 shows that roughly a quarter of all observable GRBs have UVOT counterparts. That does not, however, mean that the remaining GRBs do not have optical afterglows. The lower number of afterglows detected by UVOT could be due to several reasons: some GRBs may be 'dark' due to dust extinction in the GRB vicinity; a high redshift burst might not be observable at UV/optical wavelengths due to Lyman absorption; or the afterglow may simply be below the UVOT detection limits. Figure 2.4 shows the distribution of times until a GRB would be observable, and the distribution in how long each GRB would be observable on the first night since the GRB trigger. A total of 22% of all observable GRBs would have been observable within 1 hour of the trigger time (Figure 2.4 left). These are the bursts we would ideally like to target. Additionally, half of all observable GRBs would be observable for at least 3.2 hours, and 90% would be observable for 7.1 hours. Our MeerLICHT strategy is to target the bursts that can be observed as soon as possible after the GRB trigger, and observe them for as long as possible.

2.3 Follow-up strategy

2.3.1 GCN

The GCN consists of information distributed in two different formats: Notices and Circulars. Notices are automatically generated data-packets (socket- or email-based) containing positional information about an event detected by a triggering mission - in our case *Fermi* and *Swift* - and are distributed without any humans-in-the-loop resulting in time delays of 2–10 s between a

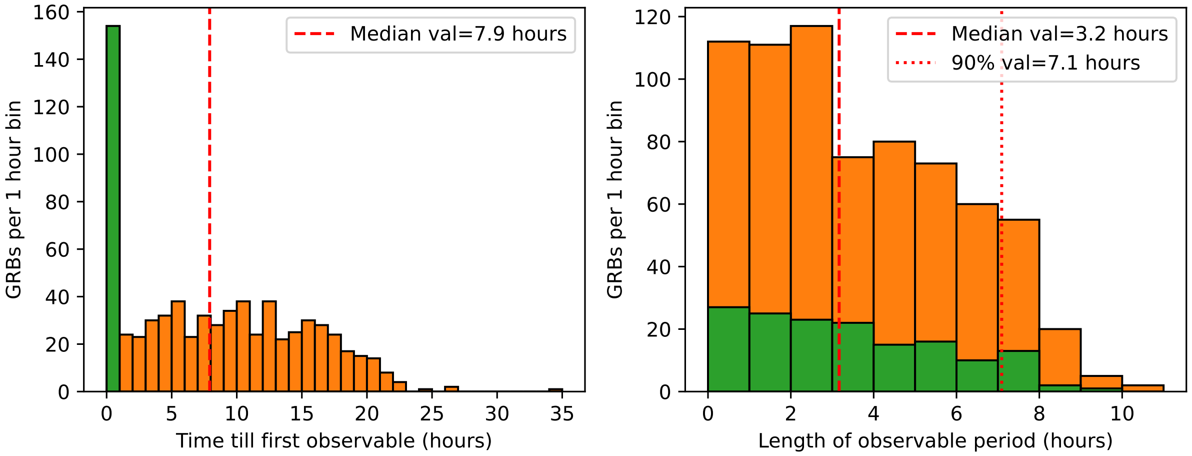

Figure 2.4: Left: the distribution of times until an observable GRB could be observed with MeerLICHT. The green colour denotes those bursts which would have been observable within 1 hour of the GRB trigger time, while the orange colour denotes all other bursts. Right: the distribution of durations for which an observable GRB could be observed in a single contiguous observing block following a GRB trigger.

GRB trigger and the Notice being sent out. Circulars are prose-style messages used to inform the community about follow-up observations that may have been conducted, and usually include preliminary results reporting detections or upper limits associated with the event.

MeerLICHT is setup to receive GCN Notices from *Fermi* and *Swift* once they are triggered by a burst. Each mission has a unique set of Notice types that it distributes when triggered by a GRB. For *Swift* bursts we use the `BAT_Position` Notices to schedule observations. These Notices contain the RA and Dec of the burst with a typical accuracy of $3'$ and are distributed with a time delay of between 7–30 s after the trigger time. Following a GBM-detected burst, we make use of the `GBM_Final_Position` Notices to schedule observations with MeerLICHT, as they usually provide more accurate positions than earlier Notices along with links to the HEALPix fits files produced by `RoboBA`. These Notices can have a delay of up to 10-minutes following a trigger, but since GBM GRBs have large error boxes requiring at least ~ 60 tiles to cover a probability of 90%, we can accept the delay in starting observations in favour of more accurate localisations.

2.3.2 Observing criteria

For *Swift* bursts our observing criteria are simple: we will observe all GRBs that are visible to MeerLICHT within five hours of the trigger time. For *Fermi*/GBM bursts, the criteria are more complex: we will observe bursts for which we can observe a cumulative probability of at least 70% with 80 or fewer tiles, and for which observing can start within 5 hours of the trigger time. We additionally require that the Galactic extinction $A_V < 5$ at the field centre in order to avoid observing fields with high extinction where it is unlikely we would be able to detect an extragalactic transient. Since the *Fermi* error boxes are so large and require a large number of telescope pointings to cover a probability of 90%, we only use the q-band as it allows us to go deeper in a single 60 s exposure than in any other band. For *Swift*-triggered bursts we follow a repeating filter sequence of *quqgqrqiqz* 60 s exposures in order to obtain a high-cadence coverage in the more sensitive q-band along with quasi-simultaneous multi-colour observations at other wavelengths. Our observing strategy is summarised in Table 2.1. Once observations of a GRB afterglow are obtained, our aim is to rapidly report our detections or upper limits to the GCN as a Circular. For *Swift* bursts the analysis is fairly trivial since the position of the GRB is normally known with $\sim 3''$ accuracy as a result of an XRT afterglow detection. We do not use

Table 2.1: MeerLICHT (ML) triggering criteria for GRBs

	Fermi/GBM	*Swift*/BAT
GRBs/year	~240	~90
90% error radius	~2°	~3′
ML fields to cover 90%	167[a]	1
Observing constraint	$\geq$ 70% prob. with $\leq$ 80 fields $<$ 5 hours post-trigger	$<$ 5 hours post-trigger
A_V limit (mag)	< 5	< 5
Moon angle limit	$> 10°$	$> 10°$
Priority[b]	4	6
Exposure time (s)	60	60
Filter sequence	q	$quqgqrqiqz$
Repeats	3	50

[a] This value is the median number of fields required to cover a cumulative probability of 90% from the sample of historic GRBs with HEALPix sky maps. All *Swift*/BAT bursts fit into a single ML field, hence we list a value of 1.

[b] Our scheduling script observing priority. *Swift* triggers receive a higher priority so that a *Fermi* trigger will not override ongoing *Swift*-triggered observations.

the pipeline catalogue files (see Chapter 1) to obtain source photometry since these only contain 5σ sources. Rather, we utilise a custom-made forced photometry routine that forms part of the MeerLICHT data reduction software. The routine requires the source position to be known: if the source is visible in our images, we determine the coordinates from our own images; otherwise, we obtain the coordinates from external sources such as GCN Circulars. A source is detected if the signal-to-noise ratio from the forced photometry routine is greater than three (3σ). For *Fermi*/GBM bursts, the analysis is more involved.

2.3.3 Identifying promising transient candidates in *Fermi*/GBM error boxes

Identifying promising transient candidates in tiled observations of an error box can be challenging - the analysis of MeerLICHT observations following GW 190814 was only completed more than a year after the event itself (de Wet et al. 2021a). This was because the MeerLICHT database was not yet set up for the fast querying of transient candidates, and also because a real-bogus machine learning classifier had not yet been implemented to run on the transient candidates (see Hosenie et al. 2021, for our implementation). This was also true during the first year or so of the GRB programme meaning that similar methods as used in the GW 190814 analysis had to be used to find transient candidates (the procedure is outlined in de Wet et al. 2021a), rather than querying for transients via the database. The result was a much slower response time in identifying promising candidates.

Once the database (called MeerZICHT) was up and running, the procedure became much simpler and faster. MeerZICHT ingests transient candidates directly from the transient catalogue files and Jupyter notebooks are then used to query the data for promising candidates satisfying the following criteria:

1. we only consider transients whose first detection is in the observations being considered. Since the database contains all transients previously detected by MeerLICHT, we filter out transients that have been 're-detected'.

2. We require that a transient has at least two detections in a single night separated by more than 10 minutes in time. Our scheduling strategy ensures this is the case since fields are only re-observed once all fields have been observed at least once (Table 2.1).

3. Each transient detection must have a real-bogus machine learning score greater than 0.8. As shown in the machine learning classifier paper (Hosenie et al. 2021), a real-bogus machine learning score of greater than 0.8 leads to a very high purity of reals.

4. We exclude candidates with matches in the Gaia DR3 catalogue within a matching radius of $1''$.

5. Known solar system objects are excluded.

6. We vet the remaining candidates by eye using thumbnail images of the reduced, reference, difference, and S_{corr} images.

Not all of these criteria could be used throughout the programme as some of the necessary features were not yet in place. For instance, the machine learning classifier had to be trained and implemented to run on every observation, and was even updated more recently; and solar system objects such as asteroids could only be easily excluded once asteroid catalogue files became a regular MeerLICHT data product. Perhaps an even greater challenge was the non-uniformity of sky coverage - often, MeerLICHT was not able to observe every scheduled field more than once in a night due to the onset of bad weather or reaching the telescope's observing limits. This meant that fields which were only observed once would not be considered in our search for transients.

2.4 Results of programme

2.4.1 *Fermi*/GBM triggers

We began actively following-up on *Fermi*/GBM triggers which satisfied our triggering criteria (Table 2.1) on 2021 November 15. For the results and statistics presented here, we consider the period from 15 November 2021 up until the end of December 2023 - a period of 25.5 months. We received a total of 489 triggers during this time. To determine which of these triggers were associated with genuine GRBs, we cross-matched our triggers with GRBs listed in the online *Fermi* GBM Burst Catalog. Only 36 (7%) of the triggers were unrelated to a catalogued GRB. We regard these as spurious triggers. For the remaining 453 real triggers, we used our scheduling scripts to tile the error boxes. For 187 of these triggers, no part of the error boxes could be observed by MeerLICHT due to the position being too far north or due to being Sun angle-constrained. For the remaining 266 triggers (59%), at least some of the error box could be observed, though in some cases the covered probability was very low. Among these observable triggers, only 15 satisfied all of our triggering criteria that more than 70% of the error box be observable with 80 or fewer fields within 5 hours of the trigger time. These are listed in Table 2.2 below. Among these 15 candidates, two thirds (10/15) were followed-up with MeerLICHT. The remaining 5 triggers were not observed due to poor weather in Sutherland (4/5) or technical/software-related errors (1/5). For GRB 230405B and GRB 231118A we also received *Swift* triggers. In these cases *Swift* follow-up observations were scheduled due to the higher priority for *Swift* bursts. For GRB 220514A, a better localisation from *INTEGRAL* led us to manually schedule observations of the *INTEGRAL* error box. The number of fields required to cover the error boxes for GRB 230808B and GRB 231129C was only 7 and 2, respectively, as listed in Table 2.2. The reason for these unusually low numbers was that the *Fermi*/GBM skymap was not immediately available upon receiving the trigger. In these cases, we used the *Fermi*-estimated position and error radius to determine which fields to observe. The *Fermi* error radius, however, does not include a systematic uncertainty inherent in the GBM localisations, which explains the much smaller number of fields scheduled.

Table 2.2: *Fermi*/GBM triggers satisfying our trigger criteria

Trigger[a]	GRB	Cumulative probability	Number of fields	Time till first observations	Observed[b] (Y/N)
GRB211130.636	211130A	0.90	72	2.92	Y
GRB211229.930	211229B	0.90	71	0.88	N (technical)
GRB220114.585	220114A	0.85	66	0.00	Y
GRB220115.709	220115A	0.90	78	1.46	N (weather)
GRB220514.517	220514A	0.90	69	4.32	Y (*INTEGRAL*)
GRB220627.890	220627A	0.71	52	0.34	Y
GRB220810.969	220810A	0.90	69	0.21	Y
GRB221016.986	221016A	0.90	78	0.34	N (weather)
GRB230405.832	230405B	0.90	69	4.38	Y (*Swift*)
GRB230808.699	230808B	0.92	7	0.66	Y
GRB230827.762	230827A	0.90	67	0.33	Y
GRB231020.790	231020A	0.90	65	0.29	N (weather)
GRB231104.966	231104B	0.83	62	0.35	Y
GRB231118.720	231118A	0.90	71	1.00	Y (*Swift*)
GRB231129.799	231129C	0.93	2	0.66	N (weather)

[a] Internal trigger name.

[b] For a number of bursts which we did follow-up, we did not observe the entire GBM error box as a result of a better-localised position being available from *Swift* or *INTEGRAL*. These are indicated in parentheses. For the bursts which were not followed up, we indicate the reason.

2.4.2 *Swift* triggers

We began actively following-up on *Swift* triggers at the beginning of June 2021. For the results presented here we consider the period from June 2021 up to the end of December 2023 – a period of 31 months in total. The number of GRB triggers over this period was 159. These are listed in Table 2.3 below. A number of the triggers were not associated with confirmed GRBs, so we regard these as spurious triggers. In order to determine which triggers were related to genuine GRBs, we cross-matched our triggers with GRBs listed in the online *Swift*/BAT GRB catalog[3]. The most recent GRB listed in this catalog was GRB231215A, so for GRBs which occurred after this time we confirmed the veracity of a trigger by inspecting *Swift* GCN circulars. A total of 39 of these triggers were spurious, with the remaining 120 triggers being related to real GRBs. Two triggers belonged to the same burst (GRB 221009A), so that the final tally of genuine GRBs is 119.

Among the 120 triggers associated with real GRBs, a total of 62 were not observable: 43 of these due to the GRB position being too far north for MeerLICHT, 17 due to Sun angle constraints, and 2 due to high Galactic extinction. The remaining 58 triggers were observable with MeerLICHT during the night of the GRB trigger. Among these 58 triggers, 35 satisfied our self-imposed 5 hour time limit constraint (Table 2.1), while 23 did not. In principle, all 35 of the triggers which fully satisfied our triggering criteria should have been observed. However, we only obtained follow-up observations for 16 of these triggers (or 15 unique GRBs, as a result of two GRB 221009A triggers), which results in an acceptance rate of 43% . These are all listed in Table 2.4. It should be noted that not every GRB for which we obtained observations was automatically triggered. For four of the 15 GRBs (210610A, 210610B, 220427A, 221202A) we had to manually submit the scheduling scripts to the telescope, due to technical or software-related issues.

Our aim at the start of the programme was to obtain follow-up observations for as many GRBs as possible which passed our triggering criteria. We were only able to follow-up on 43%

---

[3] https://swift.gsfc.nasa.gov/results/batgrbcat/

(or 15) of these GRBs. The remaining 57% (or 19) of GRBs were not observed due to three reasons: by far the dominant reason for not observing was due to poor weather conditions in Sutherland (15/19); the second reason was due to technical or software-related problems (3/19); and for a single GRB we were unlucky to observe the wrong field (1/19). Regarding this latter point, during scheduling we use the positions from the BAT triggers to determine which field to observe. The BAT error boxes are $3'$ in radius, which usually sits easily within the field of view of MeerLICHT. The BAT error box for GRB 210919A was unfortunate to sit right on the edge of one of MeerLICHT's fields. Once an X-ray counterpart was identified we discovered that the coordinates were located just off the edge of our image, and therefore in a neighbouring field which we had not observed.

Table 2.3: *Swift* GRB triggers

Trigger[a]	GRB[b]	Observable[c] (Y/N)	< 5 hours[d] (Y/N)	Observed[e] (Y/N)
GRB210603.407				
GRB210610.628	210610A	Y	Y	Y (technical/manual)
GRB210610.827	210610B	Y	Y	Y (technical/manual)
GRB210612.543				
GRB210618.072	210618A	N (north)		
GRB210620.000	210619B	N (north)		
GRB210621.712				
GRB210702.797	210702A	Y	Y (0.0)	Y
GRB210708.101	210708A	Y	N (14.28)	
GRB210708.558				
GRB210712.405	210712A	N (Sun)		
GRB210722.871	210722A	Y	Y (3.58)	N (weather)
GRB210723.615	210723A	N (Sun)		
GRB210724.843	210724A	Y	Y (0.00)	Y
GRB210725.158	210725A	Y	N (13.05)	
GRB210725.501	210725B	Y	Y (4.83)	Y
GRB210726.805	210726A	Y	N (21.55)	
GRB210730.207	210730A	N (north)		
GRB210731.606				
GRB210731.931	210731A	Y	Y (0.00)	Y
GRB210807.419	210807A	N (north)		
GRB210807.956	210807C	N (Sun)		
GRB210818.043	210818A	Y	Y (0.00)	N (weather)
GRB210818.678				
GRB210820.735	210820A	Y	N (5.15)	
GRB210822.388	210822A	Y	N (8.24)	
GRB210824.174	210824A	Y	N (12.96)	
GRB210825.287				
GRB210901.628	210901A	Y	Y (2.11)	N (weather)
GRB210905.009	210905A	Y	Y (0.00)	N (technical)
GRB210910.425				
GRB210912.459	210912A	N (north)		
GRB210918.332				
GRB210919.020	210919A	Y	Y (0.06)	N (wrong field)
GRB210930.116	210930A	N (north)		
GRB211001.030				
GRB211010.446				

Table 2.3: Continued.

Trigger	GRB	Observable (Y/N)	< 5 hours (Y/N)	Observed (Y/N)
GRB211023.879	211023B	N (north)		
GRB211024.931	211024B	N (Sun)		
GRB211025.216	211025A	N (north)		
GRB211105.436				
GRB211129.410	211129A	N (north)		
GRB211203.377				
GRB211207.870	211207A	Y	Y (1.91)	N (weather)
GRB211211.549	211211A	N (Sun)		
GRB211221.867	211221A	Y	Y (0.00)	Y
GRB211223.604	211223C	N (Sun)		
GRB211225.550	211225B	N (Sun)		
GRB211227.981	211227A	Y	Y (0.00)	N (weather)
GRB220101.215	220101A	N (north)		
GRB220117.680	220117A	Y	Y (2.39)	N (weather)
GRB220117.837	220117B	Y	Y (2.74)	N (weather)
GRB220118.764	220118A	Y	N (7.47)	
GRB220218.937	220218A	N (north)		
GRB220302.320	220302A	N (north)		
GRB220305.676	220305A	Y	Y (1.73)	N (technical)
GRB220306.761	220306B	N (north)		
GRB220319.736	220319A	N (north)		
GRB220325.720	220325A	Y	N (7.09)	
GRB220402.163				
GRB220427.875	220427A	Y	Y (0.17)	Y (manual)
GRB220430.579	220430A	Y	Y (3.00)	Y
GRB220501.828	220501A	N (Sun)		
GRB220518.263	220528A	N (Sun)		
GRB220521.972	220521A	Y	Y (0.05)	N (weather)
GRB220527.934				
GRB220530.856				
GRB220611.751	220611A	N (Sun)		
GRB220618.382	220618A	N (north)		
GRB220618.851				
GRB220621.639				
GRB220623.295	220623A	N (north)		
GRB220629.602				
GRB220701.203	220701A	N (north)		
GRB220701.518				
GRB220702.079				
GRB220706.673	220706A	Y	N (8.51)	
GRB220708.194	220708A	N (north)		
GRB220711.761	220711B	Y	Y (1.10)	N (weather)
GRB220714.582	220714B	Y	N (13.27)	
GRB220715.934	220715B	Y	Y (0.05)	Y
GRB220730.659	220730A	Y	Y (1.08)	N (weather)
GRB220806.756	220806A	Y	Y (0.01)	N (weather)
GRB220813.808	220813A	Y	N (8.19)	

Table 2.3: Continued.

Trigger	GRB	Observable (Y/N)	< 5 hours (Y/N)	Observed (Y/N)
GRB220826.497	220826A	Y	N (5.22)	
GRB220907.587	220907A	N (A_V)		
GRB220930.467	220930A	Y	N (12.33)	
GRB221009.590	221009A	Y	Y (3.47)	Y
GRB221009.595	221009A	Y	Y (3.35)	Y
GRB221016.986	221016A	Y	Y (0.00)	N (weather)
GRB221024.542	221024A	N (north)		
GRB221027.801	221027B	N (north)		
GRB221028.553	221028A	N (north)		
GRB221029.504				
GRB221110.103	221110A	Y	N (15.69)	
GRB221201.517	221201A	N (Sun)		
GRB221202.838	221202A	Y	Y (0.00)	Y (technical/manual)
GRB221215.150				
GRB221216.473	221216A	Y	N (7.36)	
GRB221226.945	221226B	Y	N (20.12)	
GRB230113.019				
GRB230116.648	230116C	N (Sun)		
GRB230116.878	230116D	N (north)		
GRB230121.239				
GRB230123.430	230123A	Y	N (8.41)	
GRB230126.495				
GRB230204.123	230204A	N (A_V)		
GRB230205.437	230205A	N (north)		
GRB230210.245				
GRB230216.617	230216A	Y	Y (3.56)	N (weather/technical)
GRB230217.912	230217A	N (Sun)		
GRB230223.997				
GRB230228.244	230228A	N (north)		
GRB230309.261				
GRB230310.875				
GRB230320.329				
GRB230322.882	230322B	N (Sun)		
GRB230325.136	230325A	Y	N (23.92)	
GRB230328.621	230328B	N (north)		
GRB230405.832	230405B	Y	Y (4.87)	Y
GRB230409.206	230409B	N (north)		
GRB230414.677	230414B	N (north)		
GRB230420.430	230420A	N (north)		
GRB230423.797	230423A	Y	Y (0.02)	N (weather)
GRB230427.439	230427A	N (north)		
GRB230506.715	230506C	N (north)		
GRB230510.504	230510A	N (north)		
GRB230622.420	230622A	Y	N (10.99)	
GRB230628.935	230628E	Y	N (18.21)	
GRB230723.488	230723B	Y	N (5.12)	
GRB230728.118	230728A	N (north)		

Table 2.3: Continued.

Trigger	GRB	Observable (Y/N)	$<$ 5 hours (Y/N)	Observed (Y/N)
GRB230802.285	230802A	N (Sun)		
GRB230805.475	230805B	N (north)		
GRB230816.673	230816A	N (north)		
GRB230818.977	230818A	N (north)		
GRB230820.798				
GRB230824.583				
GRB230824.788				
GRB230825.378				
GRB230825.848				
GRB230825.852				
GRB230825.980				
GRB230826.814	230826A	N (north)		
GRB230903.724	230903A	Y	Y (4.07)	N (technical)
GRB230911.366	230911C	Y	N (8.52)	
GRB230914.342				
GRB231028.173	231028A	N (Sun)		
GRB231104.075	231104A	N (north)		
GRB231110.889	231110A	N (north)		
GRB231111.595	231111A	N (north)		
GRB231117.127	231117A	Y	N (15.22)	
GRB231118.720	231118A	Y	Y (1.00)	Y
GRB231129.212	231129A	N (north)		
GRB231205.697	231205B	Y	Y (4.11)	N (weather)
GRB231210.895	231210B	Y	Y (0.02)	Y
GRB231214.850	231214A	N (Sun)		
GRB231215.408	231215A	N (north)		
GRB231216.775	231216A	N (north)		
GRB231230.062	231230A	N (north)		

[a] Internal trigger name.

[b] GRB name if trigger is related to a genuine GRB. If blank, the trigger is spurious.

[c] If not observable with MeerLICHT (N) we indicate in parentheses the reason, which may be due to the GRB position being too far north (north), Sun-constrained (Sun), or not satisfying our $A_V < 5$ mag limit (A_V).

[d] We indicate whether the trigger satisfied our $<$ 5 hour time constraint. In parentheses we show the time till first observable in hours.

[e] We indicate whether the trigger was observed. If not (N) we indicate the reason in parentheses, which is either due to weather (weather), a technical or software error (technical), or observing the wrong field (wrong field). For four bursts we had to submit the scheduling scripts manually. These are indicated by Y (manual).

2.4.3 GRBs with MeerLICHT follow-up observations

Table 2.4 provides a summary of all the GRBs observed with MeerLICHT throughout our observing campaign. A burst-by-burst account of each GRB followed-up by MeerLICHT is presented in Section 2.A, along with our light curves and photometry for selected bursts. We followed-up a total of 29 GRBs, of which 15 were in response to *Swift* GRBs, 10 in response to *Fermi* GRBs, and 4 were due to localisations from missions such as *INTEGRAL*, *AGILE*, and GUANO (Figure 2.5). For the *Swift*-triggered bursts, 11 out of 15 were fully automatically triggered, while for the

Fermi bursts, 7 out of 10 were automatically triggered.

Only two of the bursts in our sample are short GRBs under the 2 s dividing line, neither of which had an optical counterpart. The remaining GRBs are therefore all long GRBs. Our response time is summarised in Figure 2.6. We started observations within 1 hour of the trigger time for a total of 10/29 bursts (34%). Our three fastest response times were 129, 202 and 286 seconds for GRB 220715B, GRB 231210B and GRB 210731A, respectively. The 8 bursts which were observed after our self-imposed 5 hour time limit were all manually scheduled except for GRB 220114A and GRB 230405B. For 220114A there was a 10.5 hour delay between the burst being detected and us receiving the GCN Notice that prompted MeerLICHT to begin automatic observations, while for GRB 230405B automatic *Fermi*-triggered observations began before they were overridden by *Swift*-triggered observations.

We detected optical afterglows to 12 of the GRBs within our sample. Three GRBs have a ‘possible’ designation in Table 2.4: GRB 211130A, GRB 220810A and GRB 231104B. For GRB 211130A we identified a promising afterglow candidate but only reported our results to the GCN 10 days post-trigger, so no other groups were able to confirm our detection. For GRB 220810A, we reported two transient candidates but these were also not confirmed. For GRB 231104B, our analysis was conducted several months after the trigger time and so our promising afterglow candidate could not be confirmed. We were very active in reporting our results to the GCN, with 22 GCN Circulars submitted for 21 individual GRBs.

In our initial investigation into the rates with which we could expect to observe *Fermi* GRBs (Section 2.1), we found that 42 GRBs would have been observable with 80 or fewer tiles over a 19 month period. This translates to 26.5 bursts per year. To increase the sample size, we required that 80 fields or fewer encompass a probability of at least 70% (instead of 90%). Over the 25.5 months of our *Fermi*/GBM follow-up we observed 10 out of 15 triggers which satisfied our triggering criteria. A total of 15 triggers over 25.5 months equates to 7 GRBs per year, which is significantly lower than the 26.5 per year which would have been observable with 80 or fewer tiles. Going forward, one simple way to increase the number of *Fermi* triggers would be to do away with the 5 hour time constraint. This would have almost doubled the sample of triggers from 15 to 31. Considering that it usually takes at least 3 hours to tile an entire error box twice, we believe this is an acceptable trade-off to increase the number of triggers. For *Swift* bursts we predicted that we would be able to observe 10 GRBs per year within 1 hour of the trigger time. During our programme we responded to 5 *Swift* triggers within 1 hour over the course of 31 months, which equates to 1.9 per year, or 1 in 5 of what we might have expected. Poor weather prevented us from following-up 6 bursts which were observable within 1 hour of the trigger. These would have increased our rate to 4.4 per year, just below half of what we would have expected. The declining sensitivity of *Swift* played a strong role in reducing the number of bursts we could trigger on - the average number of GRBs detected between 2005 and March 2021 was 82 per year whereas only 46 and 45 GRBs were detected in each of 2022 and 2023, respectively.

In terms of scientific returns, the *Swift* bursts were the most fruitful. Two of these led to publications in combination with observational data from across the electromagnetic spectrum. Our *Fermi*/GBM follow-up was less fruitful. We did not discover any confirmed afterglows via our follow-up, though our GRB 211130A and GRB 231104B candidates were highly promising. For GRB 220627A we were unlucky not to observe the field containing the eventual afterglow candidate on our first night (Figure 2.15). A *Fermi*/LAT detection greatly reduced the size of the error box, which led to the detection of the afterglow after manually-scheduled observations. The follow-up of *Fermi* bursts was still useful in that it gave us an opportunity to test our systems for GW follow-up: for GRB 211130A it took us 10 days to report an afterglow candidate whereas for GRB 220810A this time had reduced to ~ 1.6 days. We are now at the stage where we can identify promising candidates within 24 hours of observing a GW or GRB error box.

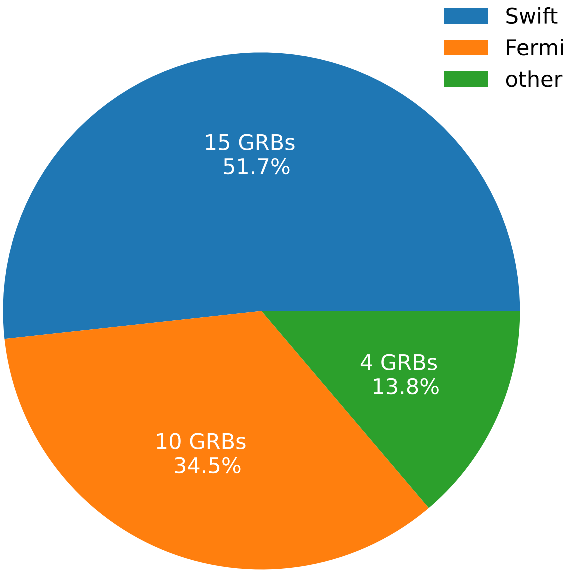

Figure 2.5: Triggering missions for GRBs observed by MeerLICHT.

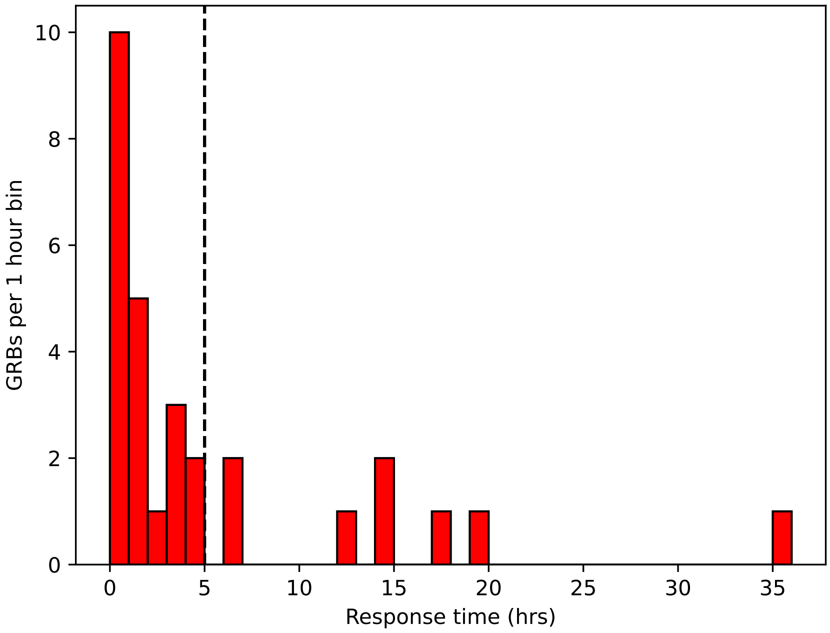

Figure 2.6: Response times for GRBs observed in our programme. The vertical dashed line denotes our 5 hour triggering limit. A total of 8 bursts were observed after this time.

Table 2.4: GRBs with MeerLICHT (ML) follow-up observations

GRB	UT time	Triggering mission[a]	T_{90} (s)[b]	Response time (hrs)	ML afterglow detection (Y/N)[c]	Field ID[d]	ML GCN
210610A	15:03:43	*Swift*/manual	13.62	1.75	Y	10601	(de Wet et al. 2021f)
210610B	19:51:27	*Swift*/manual	69.38	1.15	Y	10626	(de Wet et al. 2021d)
210702A	19:07:13	*Swift*	138.2	0.25	Y	3388	(Groot et al. 2021b)
210724A	20:14:09	*Swift*	50.57	0.18	N	7658	(de Wet et al. 2021b)
210725B	12:00:48	*Swift*	48.00	4.83	N	11036	-
210731A	22:21:08	*Swift*	22.51	0.07	Y	3433	(de Wet et al. 2021e)
211106A	04:37:31	*INTEGRAL*/GUANO/manual	1.75	14.02	N	1822	(de Wet et al. 2021g)
211130A	15:16:27	*Fermi*	218.63	3.25	Possible	Multiple/4772	(de Wet et al. 2021c)
211221A	20:48:40	*Swift*	671.67	3.59	N	8479	(Groot et al. 2021a)
220114A	14:01:47	*Fermi*	0.73	12.62	N	Multiple	-
220418B	17:16:21	GUANO/manual	2.43	1.17	N	6080	-
220427A	21:00:34	*Swift*/manual	57.2	2.69	Y	1521	(de Wet et al. 2022i)
220430A	13:53:15	*Swift*	43.10	3.28	N	9861	(Groot et al. 2022a)
220514A	12:24:32	*Fermi*/*INTEGRAL*/manual	66.31	6.79	Y	10343	(de Wet et al. 2022j)
220527A	09:17:15	*AGILE*/manual	10.50	17.60	Y	6363	(de Wet et al. 2022h)
220627A	21:21:00	*Fermi*	136.71, 126.98	0.35	Y	Multiple/3975	(Groot et al. 2022b) (de Wet et al. 2022c)
220715B	22:24:42	*Swift*	40.40	0.04	N	3810	-
220810A	23:15:42	*Fermi*	8.96	0.24	Possible	Multiple/8856/9314	(de Wet et al. 2022g)
220921A	11:05:59	*Fermi*/manual	44.29	14.64	Y	2977	(de Wet et al. 2022a,b)
221009A	13:16:59	*Swift*	> 1068.40	4.55	Y	11312	(de Wet et al. 2022d)
221115B	09:46:15	GUANO/manual	~ 5	35.52	N	5976	(de Wet et al. 2022e)
221202A	20:06:10	*Swift*/manual	10.34	1.14	N	1202	(de Wet et al. 2022f)
230209B	22:32:36	*Fermi*/manual	67.33	19.98	N	Multiple	-
230405B	19:58:03	*Swift*	14.14	6.38	N	2400	(de Wet et al. 2023b)
230808B	16:46:11	*Fermi*	20.99	0.71	N	Multiple	-
230827A	18:17:52	*Fermi*	83.20	0.36	N	Multiple	-
231104B	23:10:39	*Fermi*	13.57	0.40	Possible	Multiple/3130	-
231118A	17:16:29	*Swift*	37.63	1.70	Y	02126	(de Wet et al. 2023a)
231210B	21:29:04	*Swift*	7.47	0.06	Y	02165	(de Wet et al. 2023c)

[a] Triggering mission for GRB. If observations were automatically triggered as part of our follow-up programme, the word *manual* is not used. *Manual* indicates that observations were manually scheduled, either due to a technical error when a burst should have been automatically triggered within our programme, or due to availability of a better localisation from a mission outside of our programme.

[b] For bursts discovered by *Swift* we report the T_{90} from refined *Swift*/BAT analysis GCN Circulars. For bursts discovered with *Fermi*, we obtain the duration from the online *Fermi* GBM Burst Catalog.

[c] In some cases, an optical afterglow may have been detected by other groups but not by MeerLICHT.

[d] MeerLICHT fixed sky-grid field ID number. For *Swift*-triggered bursts, a single MeerLICHT field usually contained the entire BAT error box. For *Fermi*-triggered bursts, multiple fields may have been observed. If an afterglow was identified we list the field ID containing the afterglow. For some GRBs, observations were manually scheduled due to a more accurate localisation, for which we also show the field ID.

Bibliography

Abbott, B. P., Abbott, R., Abbott, T. D., et al. 2017a, Phys. Rev. Lett., 119, 161101

Abbott, B. P., Abbott, R., Abbott, T. D., et al. 2017b, ApJ, 848, L13

Alexander, K. D., Laskar, T., Kilpatrick, C., et al. 2021, GRB Coordinates Network, 30218, 1

Ambrosi, E., D'Ai, A., D'Elia, V., et al. 2022, GRB Coordinates Network, 31972, 1

Anandagoda, S., Pellegrin, K., & Hartmann, D. 2021, GRB Coordinates Network, 30221, 1

Atwood, W. B., Abdo, A. A., Ackermann, M., et al. 2009, ApJ, 697, 1071

Barthelmy, S. D., Ambrosi, E., Krimm, H. A., et al. 2022, GRB Coordinates Network, 31981, 1

Barthelmy, S. D., Barbier, L. M., Cummings, J. R., et al. 2005, Space Sci. Rev., 120, 143

Barthelmy, S. D., Cummings, J. R., Krimm, H. A., et al. 2021a, GRB Coordinates Network, 30186, 1

Barthelmy, S. D., Krimm, H. A., Laha, S., et al. 2021b, GRB Coordinates Network, 31289, 1

Beardmore, A. P., Evans, P. A., Goad, M. R., Osborne, J. P., & Swift-XRT Team. 2023, GRB Coordinates Network, 33574, 1

Becerra, R. L., Watson, A. M., Butler, N., et al. 2021, GRB Coordinates Network, 30190, 1

Belkin, S., Pozanenko, A., Burhonov, O., et al. 2021a, GRB Coordinates Network, 30775, 1

Belkin, S., Pozanenko, A., Pankov, N., Krugov, M., & GRB IKI FuN Collaboration. 2021b, GRB Coordinates Network, 30365, 1

Berger, E., Fong, W., & Chornock, R. 2013, ApJ, 774, L23

Berger, E., Rouco Escorial, A., & Fong, W. 2021, GRB Coordinates Network, 31145, 1

Bernardini, M. G., D'Avanzo, P., Kennea, J. A., et al. 2021, GRB Coordinates Network, 30508, 1

Biltzinger, B., Preis, T., Greiner, J., & Burgess, J. 2023, GRB Coordinates Network, 34581, 1

Bissaldi, E. 2022, GRB Coordinates Network, 32574, 1

Bissaldi, E., Scotton, L., Axelsson, M., & Fermi-LAT Team. 2022, GRB Coordinates Network, 32131, 1

Buckley, D., Lipunov, V., Kornilov, V., et al. 2023, GRB Coordinates Network, 35313, 1

Burrows, D. N., Hill, J. E., Nousek, J. A., et al. 2005, Space Sci. Rev., 120, 165

Caputo, R., Bernardini, M. G., Brivio, R., et al. 2022, GRB Coordinates Network, 33005, 1

Connaughton, V., Briggs, M. S., Goldstein, A., et al. 2015, ApJS, 216, 32

Coughlin, M. W., Ahumada, T., Cenko, S. B., et al. 2019, PASP, 131, 048001

Cucchiara, A., Levan, A. J., Fox, D. B., et al. 2011, ApJ, 736, 7

Dafcikova, M., Ripa, J., Pal, A., et al. 2023a, GRB Coordinates Network, 34588, 1

Dafcikova, M., Ripa, J., Pal, A., et al. 2023b, GRB Coordinates Network, 34583, 1

D'Ai, A., Ambrosi, E., D'Elia, V., et al. 2022, GRB Coordinates Network, 31960, 1

D'Ai, A., Evans, P. A., Goad, M. R., & Swift-XRT Team. 2021, GRB Coordinates Network, 30569, 1

Dalessi, S., Meegan, C., & Fermi GBM Team. 2023, GRB Coordinates Network, 33324, 1

D'Avanzo, P., Bernardini, M. G., Kennea, J. A., et al. 2021a, GRB Coordinates Network, 30497, 1

D'Avanzo, P., Fugazza, D., Melandri, A., Covino, S., & REM Team. 2022, GRB Coordinates Network, 32145, 1

D'Avanzo, P., Melandri, A., Covino, S., Fugazza, D., & REM Team. 2021b, GRB Coordinates Network, 30238, 1

de Ugarte Postigo, A., Izzo, L., Pugliese, G., et al. 2022, GRB Coordinates Network, 32648, 1

de Ugarte Postigo, A., Thoene, C., Agui Fernandez, J. F., et al. 2021a, GRB Coordinates Network, 30194, 1

de Ugarte Postigo, A., Thoene, C. C., Kann, D. A., et al. 2021b, GRB Coordinates Network, 30511, 1

de Wet, S., Groot, P. J., Bloemen, S., et al. 2021a, A&A, 649, A72

de Wet, S., Groot, P. J., & Buckley, D. A. H. 2022a, GRB Coordinates Network, 32572, 1

de Wet, S., Groot, P. J., Buckley, D. A. H., & Meerlicht Consortium. 2022b, GRB Coordinates Network, 32582, 1

de Wet, S., Groot, P. J., Levan, A. J., & Vreeswijk, P. M. 2021b, GRB Coordinates Network, 30498, 1

de Wet, S., Groot, P. J., Levan, A. J., Vreeswijk, P. M., & Meerlicht Consortium. 2021c, GRB Coordinates Network, 31196, 1

de Wet, S., Groot, P. J., Levan, A. J., Vreeswijk, P. M., & Meerlicht Consortium. 2021d, GRB Coordinates Network, 30180, 1

de Wet, S., Groot, P. J., Malesani, D. B., et al. 2022c, GRB Coordinates Network, 32289, 1

de Wet, S., Groot, P. J., & Meerlicht Consortium. 2022d, GRB Coordinates Network, 32646, 1

de Wet, S., Groot, P. J., & Meerlicht Consortium. 2022e, GRB Coordinates Network, 32943, 1

de Wet, S., Groot, P. J., & Meerlicht Consortium. 2022f, GRB Coordinates Network, 33007, 1

de Wet, S., Groot, P. J., Pieterse, D., et al. 2022g, GRB Coordinates Network, 32460, 1

de Wet, S., Groot, P. J., Vreeswijk, P. M., & Meerlicht Consortium. 2022h, GRB Coordinates Network, 32143, 1

de Wet, S., Groot, P. J., Vreeswijk, P. M., & Meerlicht Consortium. 2023a, GRB Coordinates Network, 35126, 1

de Wet, S., Groot, P. J., Vreeswijk, P. M., et al. 2023b, GRB Coordinates Network, 33582, 1

de Wet, S., Levan, A. J., Groot, P. J., Vreeswijk, P. M., & Meerlicht Consortium. 2021e, GRB Coordinates Network, 30570, 1 de Wet, S., Malesani, D. B., Vreeswijk, P. M., Groot, P. J., & Meerlicht Consortium. 2022i, GRB Coordinates Network, 32032, 1

de Wet, S., Vreeswijk, P. M., Groot, P. J., Levan, A., & Meerlicht Consortium. 2021f, GRB Coordinates Network, 30168, 1

de Wet, S., Vreeswijk, P. M., Groot, P. J., & Meerlicht Consortium. 2023c, GRB Coordinates Network, 35323, 1

de Wet, S., Vreeswijk, P. M., Levan, A. J., et al. 2021g, GRB Coordinates Network, 31063, 1

de Wet, S., Vreeswijk, P. M., Malesani, D. B., & Meerlicht Consortium. 2022j, GRB Coordinates Network, 32044, 1

DeLaunay, J., Tohuvavohu, A., Raman, G., & Kennea, J. A. 2022a, GRB Coordinates Network, 31921, 1

DeLaunay, J., Tohuvavohu, A., Raman, G., Kennea, J. A., & Parsotan, T. 2022b, GRB Coordinates Network, 32941, 1

D'Elia, V., D'Ai, A., Sbarufatti, B., et al. 2021a, GRB Coordinates Network, 31068, 1

D'Elia, V., D'Ai, A., Sbarufatti, B., et al. 2021b, GRB Coordinates Network, 31051, 1

di Lalla, N., Axelsson, M., Arimoto, M., Omodei, N., & Crnogoreeviae, M. 2022, GRB Coordinates Network, 32283, 1

Dornic, D., Klotz, A., Sabahaddin, A., et al. 2022, GRB Coordinates Network, 31977, 1

Dutta, A., Kumar, H., Sahu, D. K., et al. 2021a, GRB Coordinates Network, 30200, 1

Dutta, A., Kumar, H., Sahu, D. K., et al. 2021b, GRB Coordinates Network, 30201, 1

Dutton, D., Dubay, M., Schlekat, D., et al. 2023, GRB Coordinates Network, 35103, 1

Evans, P. A. 2022, GRB Coordinates Network, 32567, 1

Evans, P. A., Osborne, J. P., Capalbi, M., et al. 2022, GRB Coordinates Network, 31979, 1

Evans, P. A. & Swift Team. 2022a, GRB Coordinates Network, 32132, 1

Evans, P. A. & Swift Team. 2022b, GRB Coordinates Network, 32284, 1

Fermi GBM Team. 2019, GRB Coordinates Network, 25726, 1

Fermi GBM Team. 2021, GRB Coordinates Network, 31151, 1

Fermi GBM Team. 2022a, GRB Coordinates Network, 31449, 1

Fermi GBM Team. 2022b, GRB Coordinates Network, 31915, 1

Fermi GBM Team. 2022c, GRB Coordinates Network, 32038, 1

Fermi GBM Team. 2022d, GRB Coordinates Network, 32130, 1

Fermi GBM Team. 2022e, GRB Coordinates Network, 32278, 1

Fermi GBM Team. 2022f, GRB Coordinates Network, 32404, 1

Fermi GBM Team. 2022g, GRB Coordinates Network, 32455, 1

Fermi GBM Team. 2023a, GRB Coordinates Network, 33570, 1

Fermi GBM Team. 2023b, GRB Coordinates Network, 34373, 1

Fermi GBM Team. 2023c, GRB Coordinates Network, 34575, 1

Fermi GBM Team. 2023d, GRB Coordinates Network, 34949, 1

Fermi GBM Team. 2023e, GRB Coordinates Network, 35100, 1

Fletcher, C., Dalessi, S., Meegan, C., & Fermi GBM Team. 2022, GRB Coordinates Network, 31928, 1

Fletcher, C. & Fermi-GBM Team. 2021a, GRB Coordinates Network, 31055, 1

Fletcher, C. & Fermi-GBM Team. 2021b, GRB Coordinates Network, 31291, 1

Fouad, A. M., Takey, A., & Azzam, Y. 2022, GRB Coordinates Network, 31503, 1

Frederiks, D., Golenetskii, S., Lysenko, A., et al. 2021a, GRB Coordinates Network, 30196, 1

Frederiks, D., Golenetskii, S., Lysenko, A., et al. 2021b, GRB Coordinates Network, 30366, 1

Frederiks, D., Golenetskii, S., Lysenko, A., et al. 2021c, GRB Coordinates Network, 30197, 1

Frederiks, D., Lysenko, A., Ridnaia, A., et al. 2022a, GRB Coordinates Network, 31964, 1

Frederiks, D., Lysenko, A., Ridnaia, A., et al. 2022b, GRB Coordinates Network, 32668, 1

Frederiks, D., Lysenko, A., Ridnaya, A., et al. 2022c, GRB Coordinates Network, 32295, 1

Fynbo, J. P. U., Izzo, L., de Ugarte Postigo, A., Malesani, D. B., & Pursimo, T. 2021, GRB Coordinates Network, 30182, 1

Gehrels, N., Chincarini, G., Giommi, P., et al. 2004, ApJ, 611, 1005

Ghosh, S., Bloemen, S., Nelemans, G., Groot, P. J., & Price, L. R. 2016, A&A, 592, A82

Giarratana, S., Leung, J., Wang, Z., et al. 2022, GRB Coordinates Network, 32454, 1

Goad, M. R., Osborne, J. P., Beardmore, A. P., Evans, P. A., & Swift-XRT Team. 2021, GRB Coordinates Network, 30510, 1

Goldstein, A., Fletcher, C., Veres, P., et al. 2020, ApJ, 895, 40

Gopalakrishnan, R., Prasad, V., Waratkar, G., et al. 2022a, GRB Coordinates Network, 31987, 1

Gopalakrishnan, R., Prasad, V., Waratkar, G., et al. 2022b, GRB Coordinates Network, 32070, 1

Gopalakrishnan, R., Prasad, V., Waratkar, G., et al. 2022c, GRB Coordinates Network, 32140, 1

Górski, K. M., Hivon, E., Banday, A. J., et al. 2005, ApJ, 622, 759

Gotz, D., Mereghetti, S., Savchenko, V., et al. 2022, GRB Coordinates Network, 32660, 1

Groot, P. J., de Wet, S., Malesani, D. B., et al. 2022a, GRB Coordinates Network, 31974, 1

Groot, P. J., de Wet, S., Malesani, D. B., Vreeswijk, P. M., & Meerlicht Consortium. 2021a, GRB Coordinates Network, 31277, 1

Groot, P. J., de Wet, S., Vreeswijk, P. M., Levan, A. J., & Meerlicht Consortium. 2021b, GRB Coordinates Network, 30354, 1

Groot, P. J., de Wet, S., Vreeswijk, P. M., & Meerlicht Consortium. 2022b, GRB Coordinates Network, 32281, 1

Groot, P. J., Vreeswijk, P. M., Ter Horst, R., et al. 2022c, GRB Coordinates Network, 32678, 1

Gropp, J. D., Kennea, J. A., Tohuvavohu, A., et al. 2022a, GRB Coordinates Network, 32469, 1

Gropp, J. D., Kennea, J. A., Tohuvavohu, A., et al. 2022b, GRB Coordinates Network, 32464, 1

Hjorth, J., Sollerman, J., Møller, P., et al. 2003, Nature, 423, 847

Horiuchi, T., Hanayama, H., Murata, K. L., et al. 2021, GRB Coordinates Network, 30169, 1

Hosenie, Z., Bloemen, S., Groot, P., et al. 2021, Experimental Astronomy, 51, 319

Hosokawa, R., Murata, K. L., Niwano, M., et al. 2021, GRB Coordinates Network, 30161, 1

Hu, Y. D., Fernandez-Garcia, E., Castro-Tirado, A. J., et al. 2022a, GRB Coordinates Network, 32408, 1

Hu, Y. D., Fernandez-Garcia, E., Sun, T. R., et al. 2021a, GRB Coordinates Network, 30367, 1

Hu, Y. D., Sun, T. R., Caballero-Garcia, M. D., et al. 2022b, GRB Coordinates Network, 31980, 1

Hu, Y. D., Sun, T. R., Castro-Tirado, A. J., et al. 2021b, GRB Coordinates Network, 31279, 1

Hu, Y. D., Sun, T. R., Fernandez-Garcia, E., et al. 2021c, GRB Coordinates Network, 30177, 1

Huang, Y., Hu, S., Chen, S., et al. 2022, GRB Coordinates Network, 32677, 1

Ibrahimov, M., Nalivkin, M., Nikolenko, I., Pons, O., & a larger Team. 2021, GRB Coordinates Network, 30226, 1

Imai, Y., Sato, S., Hosokawa, R., et al. 2022, GRB Coordinates Network, 32138, 1

Izzo, L., D'Elia, V., de Ugarte Postigo, A., et al. 2022, GRB Coordinates Network, 32291, 1

Jiang, S. Q., Zhu, Z. P., Fu, S. Y., et al. 2022, GRB Coordinates Network, 31999, 1

Kann, D. A., de Ugarte Postigo, A., Agui Fernandez, J. F., et al. 2021a, GRB Coordinates Network, 30211, 1

Kann, D. A., de Ugarte Postigo, A., Thoene, C., et al. 2021b, GRB Coordinates Network, 30551, 1

Kann, D. A., Izzo, L., Levan, A. J., et al. 2021c, GRB Coordinates Network, 30583, 1

Kennea, J. A., Williams, M., & Swift Team. 2022, GRB Coordinates Network, 32635, 1

Kerr, M., Cheung, C. C., Grove, J. E., et al. 2023, GRB Coordinates Network, 34603, 1

Kilpatrick, C. D., Berger, E., & Fong, W. 2021a, GRB Coordinates Network, 31146, 1

Kilpatrick, C. D., Berger, E., & Fong, W. 2021b, GRB Coordinates Network, 31157, 1

Kilpatrick, C. D., Berger, E., & Fong, W. 2021c, GRB Coordinates Network, 31300, 1

Klotz, A., Blazek, M., Christensen, N., et al. 2022, GRB Coordinates Network, 31991, 1

Komesh, T., Grossan, B., Maksut, Z., et al. 2021, GRB Coordinates Network, 31285, 1

Kozyrev, A. S., Golovin, D. V., Litvak, M. L., et al. 2021, GRB Coordinates Network, 31161, 1

Kozyrev, A. S., Golovin, D. V., Litvak, M. L., et al. 2023, GRB Coordinates Network, 33323, 1

Kuin, N. P., Tohuvavohu, A., & Swift/UVOT Team. 2021a, GRB Coordinates Network, 31079, 1

Kuin, N. P. M., Lien, A. Y., & Swift/UVOT Team. 2021b, GRB Coordinates Network, 30356, 1

Kuin, N. P. M. & Swift/UVOT Team. 2021, GRB Coordinates Network, 30355, 1

Kuin, N. P. M., Troja, E., & Swift/UVOT Team. 2021c, GRB Coordinates Network, 30572, 1

Kuin, N. P. M., Troja, E., & Swift/UVOT Team. 2022, GRB Coordinates Network, 32410, 1

Kumar, H., Bhalerao, V., Stanzin, U., et al. 2021a, GRB Coordinates Network, 30163, 1

Kumar, H., Stanzin, J., Bhalerao, V., et al. 2021b, GRB Coordinates Network, 30174, 1

Laha, S., Barthelmy, S. D., D'Avanzo, P., et al. 2021, GRB Coordinates Network, 30513, 1

Laha, S., Ferro, M., Gronwall, C., et al. 2023, GRB Coordinates Network, 35101, 1

Laskar, T. 2021, GRB Coordinates Network, 30479, 1

Laskar, T., Alexander, K. D., Berger, E., et al. 2022, GRB Coordinates Network, 32577, 1

Laskar, T., Alexander, K. D., Kilpatrick, C., et al. 2021a, GRB Coordinates Network, 30217, 1

Laskar, T., Berger, E., Zauderer, B. A., et al. 2013, ApJ, 776, 119

Laskar, T. & Bhandari, S. 2021, GRB Coordinates Network, 30477, 1

Laskar, T., Bhandari, S., Alexander, K. D., et al. 2021b, GRB Coordinates Network, 30424, 1

Laskar, T., Buchner, S., Legodi, S., et al. 2021c, GRB Coordinates Network, 30538, 1

Laskar, T. & Perley, D. 2021, GRB Coordinates Network, 30423, 1

Lesage, S., Veres, P., Roberts, O. J., et al. 2022, GRB Coordinates Network, 32642, 1

Leung, J., Wang, Z., An, T., et al. 2022, GRB Coordinates Network, 32341, 1

Levan, A. J., Barclay, T., Bhirombhakdi, K., et al. 2022a, GRB Coordinates Network, 32921, 1

Levan, A. J., Barclay, T., Burns, E., et al. 2022b, GRB Coordinates Network, 32821, 1

Lien, A. Y., Barthelmy, S. D., Kennea, J. A., et al. 2021, GRB Coordinates Network, 30351, 1

Lipunov, V., Buckley, D., Kuznetsov, A., et al. 2023, GRB Coordinates Network, 35109, 1

Lipunov, V., Buckley, D. A. H., Tiurina, N., et al. 2022, GRB Coordinates Network, 32570, 1

Lipunov, V., Gorbovskoy, E., Tyurina, N., et al. 2021a, GRB Coordinates Network, 30578, 1

Lipunov, V., Zhirkov, K., Kornilov, V., et al. 2021b, GRB Coordinates Network, 30166, 1

Lipunov, V. M., Gorosabel, J., Pruzhinskaya, M. V., et al. 2016, MNRAS, 455, 712

Lysenko, A., Frederiks, D., Ridnaia, A., et al. 2022, GRB Coordinates Network, 32152, 1

Malacaria, C., Hristov, B., & Fermi GBM Team. 2021, GRB Coordinates Network, 30199, 1

Malesani, D. B., D'Avanzo, P., Levan, A. J., Nicuesa Guelbenzu, A., & Stargate Consortium. 2021a, GRB Coordinates Network, 31070, 1

Malesani, D. B., Zhu, Z., Viitanen, A., & Biancalani, E. 2021b, GRB Coordinates Network, 31276, 1

Marchini, A., Lorini, A., Leonini, S., Italy), & Bonnoli, G. 2021, GRB Coordinates Network, 30198, 1

Markwardt, C. B., Barthelmy, S. D., Bernardini, M. G., et al. 2021, GRB Coordinates Network, 30516, 1

Meegan, C., Lichti, G., Bhat, P. N., et al. 2009, ApJ, 702, 791

Mereghetti, S., Gotz, D., Ferrigno, C., et al. 2022, GRB Coordinates Network, 32041, 1

Mong, Y. L., Ackley, K., Galloway, D. K., et al. 2021a, MNRAS, 507, 5463

Mong, Y. L., Wiersema, K., Starling, R., et al. 2021b, GRB Coordinates Network, 30193, 1

Moskvitin, A. S. & GRB follow-up Team. 2021, GRB Coordinates Network, 30187, 1

Moskvitin, A. S., Maslennikova, O. A., & GRB follow-up Team. 2021, GRB Coordinates Network, 30229, 1

Murata, K. L., Hosokawa, R., Imai, Y., et al. 2022, GRB Coordinates Network, 32059, 1

Navaneeth, P. K., Waratkar, G., Vibhute, A., et al. 2023a, GRB Coordinates Network, 33575, 1

Navaneeth, P. K., Waratkar, G., Vibhute, A., et al. 2023b, GRB Coordinates Network, 35116, 1

Nicuesa Guelbenzu, A., Klose, S., & Rau, A. 2021a, GRB Coordinates Network, 31069, 1

Nicuesa Guelbenzu, A., Klose, S., & Rau, A. 2022, GRB Coordinates Network, 32304, 1

Nicuesa Guelbenzu, A., Klose, S., Schmidl, S., & Rau, A. 2021b, GRB Coordinates Network, 30574, 1

Nissinen, M. & Oksanen, A. 2021, GRB Coordinates Network, 30231, 1

Niwano, M., Sato, S., Tateda, M., et al. 2022, GRB Coordinates Network, 32159, 1

Noonan, K., Gokuldass, P., Orange, N., et al. 2022, GRB Coordinates Network, 32422, 1

Noto, R., Hosokawa, R., Murata, K. L., et al. 2021, GRB Coordinates Network, 30220, 1

Page, K. L., Baer, M. A., Gropp, J. D., et al. 2021a, GRB Coordinates Network, 30160, 1

Page, K. L., Barthelmy, S. D., Cenko, S. B., et al. 2021b, GRB Coordinates Network, 31273, 1

Page, K. L., Gronwall, C., Gropp, J. D., et al. 2023a, GRB Coordinates Network, 33571, 1

Page, K. L., Gropp, J. D., Kennea, J. A., et al. 2021c, GRB Coordinates Network, 30170, 1

Page, K. L., Gropp, J. D., Kennea, J. A., et al. 2023b, GRB Coordinates Network, 35314, 1

Pankov, N., Belkin, S., Pozanenko, A., et al. 2022, GRB Coordinates Network, 31976, 1

Pankov, N., Pozanenko, A., Rumyantsev, V., Belkin, S., & GRB FuN, I. 2021, GRB Coordinates Network, 30212, 1

Pendleton, G. N., Briggs, M. S., Kippen, R. M., et al. 1999, ApJ, 512, 362

Pérez-Fournon, I., Poidevin, F., Akoudad-Ekajouan, H., et al. 2023, GRB Coordinates Network, 35316, 1

Perley, D. A. 2021, GRB Coordinates Network, 30216, 1

Perley, D. A., Cenko, S. B., Corsi, A., et al. 2014, ApJ, 781, 37

Perley, D. A., Yao, Y., Ho, A. Y. Q., et al. 2021, GRB Coordinates Network, 30206, 1

Piano, G., Verrecchia, F., Bulgarelli, A., et al. 2022, GRB Coordinates Network, 32657, 1

Pillera, R., Bissaldi, E., & di Lalla, N. 2022a, GRB Coordinates Network, 32568, 1

Pillera, R., Bissaldi, E., Omodei, N., et al. 2022b, GRB Coordinates Network, 32658, 1

Rhodes, L., Anderson, G. E., van der Horst, A. J., et al. 2023, GRB Coordinates Network, 35358, 1

Ridnaia, A., Frederiks, D., Golenetskii, S., et al. 2021a, GRB Coordinates Network, 31054, 1

Ridnaia, A., Frederiks, D., Lysenko, A., et al. 2021b, GRB Coordinates Network, 31162, 1

Ripa, J., Pal, A., Werner, N., et al. 2022, GRB Coordinates Network, 32685, 1

Roberts, O. J., Hristov, B., Meegan, C., & Fermi Gamma-ray Burst Monitor Team. 2022, GRB Coordinates Network, 32288, 1

Romanov, F. D. 2021a, GRB Coordinates Network, 30181, 1

Romanov, F. D. 2021b, GRB Coordinates Network, 30364, 1

Roming, P. W. A., Kennedy, T. E., Mason, K. O., et al. 2005, Space Sci. Rev., 120, 95

Rossi, A., Pugliese, G., Kann, D. A., et al. 2022, GRB Coordinates Network, 33014, 1

Rouco Escorial, A., Fong, W., Kilpatrick, C. D., et al. 2021, GRB Coordinates Network, 31259, 1

Rumyantsev, V., Pozanenko, A., Belkin, S., Pankov, N., & GRB IKI FuN. 2021a, GRB Coordinates Network, 30178, 1

Rumyantsev, V., Pozanenko, A., Belkin, S., Pankov, N., & GRB IKI FuN. 2021b, GRB Coordinates Network, 30175, 1

Saccardi, A., Schneider, B., Izzo, L., et al. 2023, GRB Coordinates Network, 35317, 1

Sbarufatti, B., Beardmore, A. P., Osborne, J. P., et al. 2022a, GRB Coordinates Network, 32135, 1

Sbarufatti, B., Burrows, D. N., Osborne, J. P., et al. 2022b, GRB Coordinates Network, 31930, 1

Schnoor, P. W., Nicholson, P., & Welch, D. L. 2022, GRB Coordinates Network, 32744, 1

Shrestha, M., Sand, D., Alexander, K. D., et al. 2023, GRB Coordinates Network, 35113, 1

Siegel, M. H., Bernardini, M. G., & Swift/UVOT Team. 2021a, GRB Coordinates Network, 30526, 1

Siegel, M. H., Page, K. L., & Swift/UVOT Team. 2021b, GRB Coordinates Network, 31317, 1

Singer, L. P., Cenko, S. B., Kasliwal, M. M., et al. 2013, ApJ, 776, L34

Singer, L. P., Kasliwal, M. M., Cenko, S. B., et al. 2015, ApJ, 806, 52

Smith, I. A., Perley, D. A., & Tanvir, N. R. 2021, GRB Coordinates Network, 30359, 1

Stamatikos, M., Barthelmy, S. D., D'Ai, A., et al. 2022, GRB Coordinates Network, 31968, 1

Stanek, K. Z., Matheson, T., Garnavich, P. M., et al. 2003, ApJ, 591, L17

Strausbaugh, R. & Cucchiara, A. 2022a, GRB Coordinates Network, 31995, 1

Strausbaugh, R. & Cucchiara, A. 2022b, GRB Coordinates Network, 33009, 1

Strausbaugh, R. & Cucchiara, A. 2023, GRB Coordinates Network, 35110, 1

Sun, T., Hu, L., Hu, M., et al. 2022, GRB Coordinates Network, 32146, 1

Sun, T. R., Hu, Y. D., Sota, A., et al. 2021, GRB Coordinates Network, 30185, 1

Svinkin, D., Frederiks, D., Ulanov, M., et al. 2022, GRB Coordinates Network, 32575, 1

Svinkin, D., Golenetskii, S., Frederiks, D., et al. 2021, GRB Coordinates Network, 31078, 1

Swain, V., Kumar, H., Angail, K., et al. 2022, GRB Coordinates Network, 31997, 1

Tanvir, N. R., Levan, A. J., Fruchter, A. S., et al. 2013, Nature, 500, 547

Tohuvavohu, A. 2022, GRB Coordinates Network, 32136, 1

Tohuvavohu, A., DeLaunay, J., Raman, G., & Kennea, J. A. 2022, GRB Coordinates Network, 31919, 1

Tohuvavohu, A., Kennea, J. A., DeLaunay, J., et al. 2020, ApJ, 900, 35

Tohuvavohu, A., Raman, G., DeLaunay, J., & Kennea, J. A. 2021, GRB Coordinates Network, 31049, 1

Troja, E., Ambrosi, E., D'Elia, V., et al. 2021, GRB Coordinates Network, 30568, 1

Troja, E., D'Avanzo, P., Dichiara, S., et al. 2022, GRB Coordinates Network, 32405, 1

Ursi, A., Longo, F., Verrecchia, F., et al. 2022a, GRB Coordinates Network, 31975, 1

Ursi, A., Panebianco, G., Pittori, C., et al. 2022b, GRB Coordinates Network, 32650, 1

Ursi, A., Piano, G., Pittori, C., et al. 2022c, GRB Coordinates Network, 32129, 1

Ursi, A., Pittori, C., Verrecchia, F., et al. 2021a, GRB Coordinates Network, 30363, 1

Ursi, A., Verrecchia, F., Longo, F., et al. 2021b, GRB Coordinates Network, 30195, 1

Veres, P., Burns, E., Bissaldi, E., et al. 2022, GRB Coordinates Network, 32636, 1

Veres, P., Hristov, B., Fletcher, C., Meegan, C., & Fermi GBM Team. 2021, GRB Coordinates Network, 30233, 1

von Kienlin, A., Meegan, C. A., Paciesas, W. S., et al. 2020, ApJ, 893, 46

Vreeswijk, P. M. & Broens, E. 2021, GRB Coordinates Network, 30205, 1

Watson, A. M., Butler, N., Becerra, R. L., et al. 2022, GRB Coordinates Network, 32576, 1

Watson, A. M., Butler, N., Kutyrev, A., et al. 2021, GRB Coordinates Network, 30191, 1

Xiao, H., Krucker, S., & Daniel, R. 2022, GRB Coordinates Network, 32661, 1

Xu, D., Izzo, L., de Ugarte Postigo, A., et al. 2021a, GRB Coordinates Network, 30357, 1

Xu, D., Zhu, Z. P., Fu, S. Y., & Liu, X. 2021b, GRB Coordinates Network, 30162, 1

Xu, D., Zhu, Z. P., Izzo, L., et al. 2022, GRB Coordinates Network, 32141, 1

Yamaoka, K., Yoshida, A., Sakamoto, T., et al. 2021, GRB Coordinates Network, 30362, 1

Yamaoka, K., Yoshida, A., Sakamoto, T., et al. 2013, in International Cosmic Ray Conference, Vol. 33, International Cosmic Ray Conference, 2948

Yan, S., Andrade, C., Beradze, S., et al. 2022, GRB Coordinates Network, 32058, 1

Yoshida, A., Sakamoto, T., Sugita, S., et al. 2022, GRB Coordinates Network, 32948, 1

Zheng, W., Brink, T. G., Filippenko, A. V., & KAIT GRB Team. 2022a, GRB Coordinates Network, 32158, 1

Zheng, W., Filippenko, A. V., & KAIT GRB Team. 2021a, GRB Coordinates Network, 30203, 1

Zheng, W., Filippenko, A. V., & KAIT GRB Team. 2021b, GRB Coordinates Network, 30204, 1

Zheng, W., Filippenko, A. V., & KAIT GRB Team. 2021c, GRB Coordinates Network, 30582, 1

Zheng, W., Filippenko, A. V., & KAIT GRB Team. 2022b, GRB Coordinates Network, 32051, 1

Zhu, Z. P., Fu, S. Y., Jiang, S. Q., et al. 2022, GRB Coordinates Network, 32532, 1

Zhu, Z. P., Xu, D., Fu, S. Y., & Liu, X. 2021, GRB Coordinates Network, 30164, 1

2.A GRBs followed-up by MeerLICHT

2.A.1 GRB 210610A

Swift/BAT was triggered at 15:03:43 UT on 2021 June 6 by a burst with a duration of ∼15 s. The XRT started observing 90 s after the trigger and identified an uncatalogued X-ray source within the BAT error region, at coordinates (RA,Dec) = (204.2828,14.4652) with a 2.2″ positional uncertainty. UVOT began observing 93 s post-trigger and found a candidate afterglow 2.2″ from the XRT position in its first 150 s *white* filter exposure, with an estimated magnitude of 17.12 (Page et al. 2021a). The refined BAT analysis found a duration of 13.62 s (Barthelmy et al. 2021a), making this a long GRB. GRB 210610A was also observed by *Fermi*/GBM (Veres et al. 2021), and Konus-Wind (Frederiks et al. 2021c). The optical afterglow to GRB 210610A was observed by numerous telescopes (Hosokawa et al. 2021; Xu et al. 2021b; Kumar et al. 2021a; Lipunov et al. 2021b; Horiuchi et al. 2021; Sun et al. 2021; Watson et al. 2021; Zheng et al. 2021a; Kann et al. 2021a; Pankov et al. 2021; Moskvitin et al. 2021; Belkin et al. 2021a), while a spectroscopic redshift of $z = 3.54$ from the Xinglong-2.16 m telescope was reported within 2.5 hours of the GRB trigger (Zhu et al. 2021) and later verified by the Himalayan Chandra Telescope (HCT) (Dutta et al. 2021a). Sub-mm observations at 1.73 days revealed no counterpart at 850 and 450 μm (Smith et al. 2021).

This was the very first GRB afterglow observed by MeerLICHT. We received the *Swift* alert promptly and should have started observing immediately. A bug, however, prevented the scheduling file from being submitted. We therefore began observations almost 2 hours after the GRB trigger at 16:48:15 UT after submitting the scheduling file manually. Our observations consisted of 60 s exposures following the filter sequence for *Swift* GRBs (Table 2.1). Monitoring

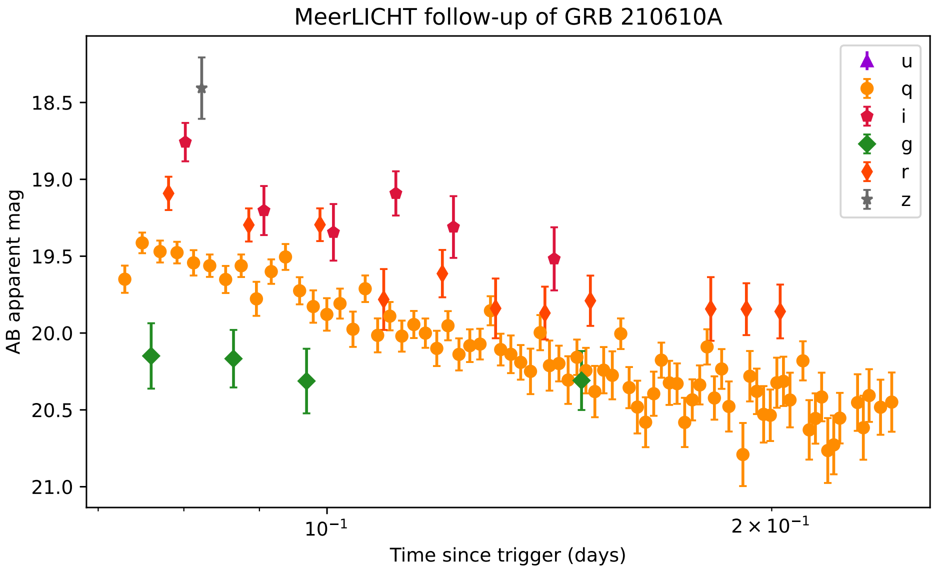

Figure 2.7: Optical detections of the GRB 210610A afterglow taken with MeerLICHT, spanning 1.75 to 5.92 hours post-trigger. We only show 5σ detections. These are listed in Table 2.6.

continued until 20:58:58 UT after which MeerLICHT began observing GRB 210610B. We reported our preliminary results to the GCN at 18:56:04 UT - our first GRB Circular (de Wet et al. 2021f). MeerLICHT detections are shown in Figure 2.7.

2.A.2 GRB 210610B

A mere 4.8 hours after the GRB 210610A trigger, *Swift*/BAT was triggered again at 19:51:27 UT by a burst with a duration of around 100 s, and at a very similar declination to the A burst. Starting observations 83.9 s after the BAT trigger, XRT found a new X-ray source at coordinates (RA,Dec) = (243.9180,14.3977) with a positional uncertainty of 6.7″. A 150 s exposure in the UVOT *white* filter beginning 91 s post-trigger refined the position of the afterglow to an uncertainty of 0.61″ and found the afterglow with a brightness of 13.70 mag (Page et al. 2021c). *AGILE*, Konus-WIND, and *Fermi*/GBM also detected GRB 210610B (Ursi et al. 2021b; Frederiks et al. 2021a; Malacaria et al. 2021), with the *Fermi* team reporting clear spectral evolution across the burst duration. The refined *Swift*/BAT duration was 69.38 s. A large number of optical telescopes reported detections of the optical afterglow (Kumar et al. 2021b; Rumyantsev et al. 2021b; Hu et al. 2021c; Rumyantsev et al. 2021a; Romanov 2021a; Fynbo et al. 2021; Moskvitin & GRB follow-up Team 2021; Becerra et al. 2021; Mong et al. 2021b; Marchini et al. 2021; Zheng et al. 2021b; Vreeswijk & Broens 2021; Perley et al. 2021; Perley 2021; Noto et al. 2021; Anandagoda et al. 2021; Ibrahimov et al. 2021; Moskvitin et al. 2021; Nissinen & Oksanen 2021; D'Avanzo et al. 2021b), while a first tentative redshift of $z = 1.13$ was reported by the Nordic Optical Telescope at 3.75 hours post-trigger (Fynbo et al. 2021). This redshift was confirmed through observations with the 10.4 m Gran Telescopio Canarias (de Ugarte Postigo et al. 2021a) and also verified by the HCT (Dutta et al. 2021b). A millimeter detection at 90.5 GHz with ALMA at 10.5 hours was reported (Laskar et al. 2021a), while a radio detection at 14.7 GHz with the VLA at 9.4 hours was also reported (Alexander et al. 2021).

Similarly as for GRB 210610A, MeerLICHT observations should have started automatically very soon after the GRB trigger, but due to the fact that MeerLICHT was already observing GRB 210610A, observations did not begin immediately. This was because our scheduling scripts were not yet setup to handle additional observations with the same priority being scheduled. Following this GRB trigger, we amended our software so that any new trigger would take immediate

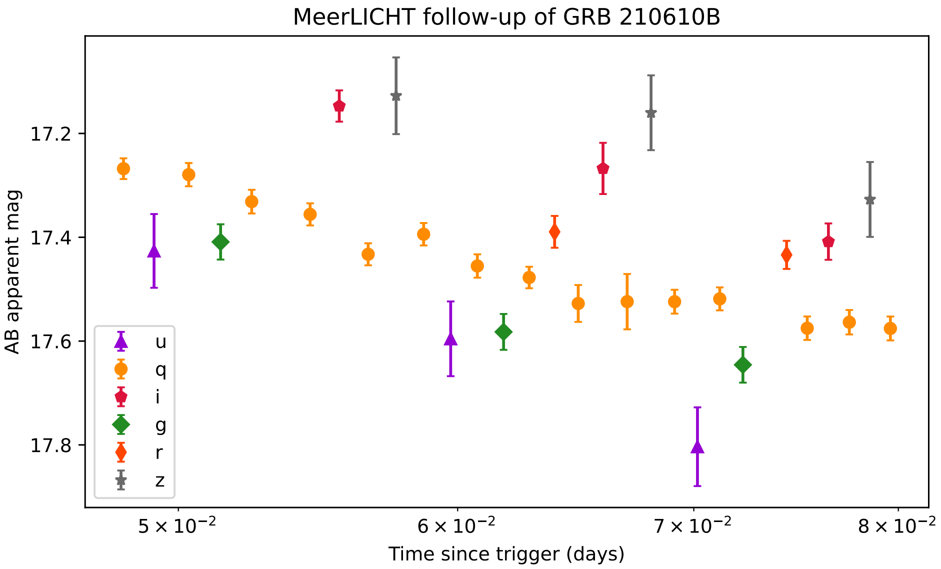

Figure 2.8: Optical detections of the GRB 210610B afterglow taken with MeerLICHT, spanning 1.15 to 1.9 hours post-trigger. We only show 5σ detections. These are listed in Table 2.6 .

priority over ongoing observations. Nevertheless, after manually submitting the scheduling scripts observations began 1.15 hours after the trigger at 21:00:23 UT, following the usual filter sequence for *Swift* bursts. Our observations continued for 45 minutes before humidity constraints halted observing. Our preliminary results were reported to the GCN (de Wet et al. 2021d), and we show our MeerLICHT detections in Figure 2.8.

2.A.3 GRB 210702A

GRB 210702A was detected by *Swift*/BAT at 19:07:13 UT on 2021 July 2 with a duration of ∼100 s. X-ray and optical afterglows were promptly discovered by XRT and UVOT at an optically-determined position of (RA,Dec) = (168.57846,-36.74690) with a 0.61″ uncertainty (Lien et al. 2021). The first UVOT u-band detection at ∼5.5 minutes post-trigger was bright with a magnitude of 11.37 (Kuin et al. 2021b). MeerLICHT was automatically triggered and started observing the BAT error box ∼15 minutes after the GRB trigger following the usual filter sequence, and continued for a further 25 minutes before strong wind forced the dome to close. The afterglow was well detected in all of our images with a magnitude of 12.82 in our first q-band exposure (Figure 2.9). Our results were reported to the GCN within 2.5 hours of the GRB (Groot et al. 2021b). *Swift*/UVOT obtained a grism spectrum starting 4.7 minutes post-trigger which was used to determine a redshift estimate of $z = 1.176$ (Kuin & Swift/UVOT Team 2021), and which was later refined to a value of $z = 1.160$ through X-shooter observations with the VLT (Xu et al. 2021a). The CALET, *AGILE* and Konus-Wind γ-ray observatories also detected GRB 210702A (Yamaoka et al. 2021; Ursi et al. 2021a; Frederiks et al. 2021b). Optical observations were reported by three other telescopes (Romanov 2021b; Belkin et al. 2021b; Hu et al. 2021a), while there was also extensive follow-up at longer wavelengths from ALMA and ATCA, reported six days after the burst (Laskar & Perley 2021; Laskar et al. 2021b). Intriguingly, significant millimeter and radio rebrightenings were later reported by the same groups (Laskar & Bhandari 2021; Laskar 2021). MeerKAT detections were also reported (Laskar et al. 2021c). GRB 210702A was the first GRB for which MeerLICHT responded fully-autonomously, ably demonstrating our rapid follow-up capabilities. Through collaboration with Dr Tanmoy Laskar, this burst was turned into a publication (Chapter 5).

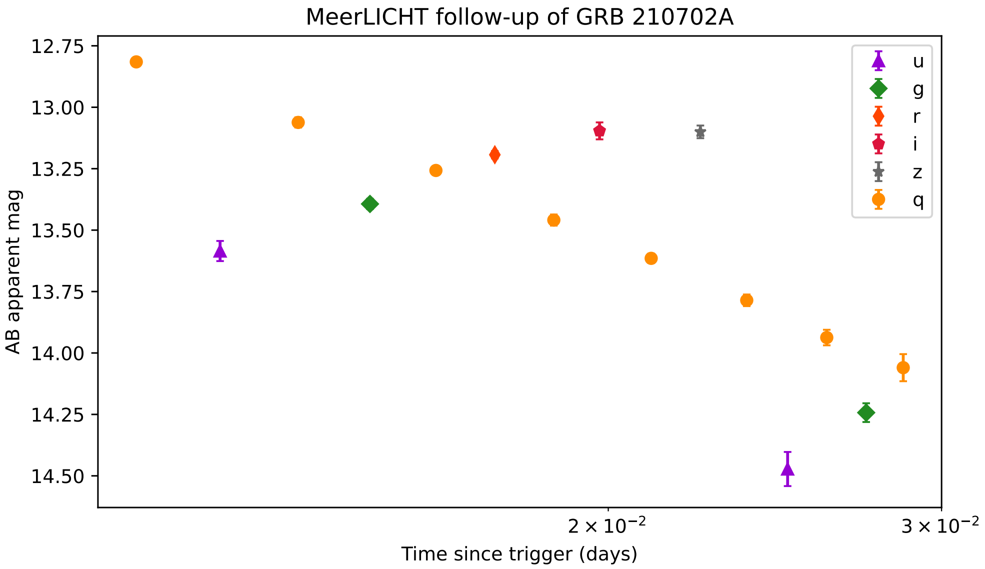

Figure 2.9: Optical detections of GRB 210702A with MeerLICHT. We only show 5σ detections. These are listed in Table 2.6 .

2.A.4 GRB 210724A

Swift/BAT detected a burst at 20:14:09 UT on 2021 July 24 with a duration of 50.57 s (D'Avanzo et al. 2021a; Laha et al. 2021). An X-ray afterglow was promptly discovered by the XRT at coordinates (RA,Dec) = (227.4118,-6.2911) with a 1.9″ positional uncertainty. No optical afterglow was found by UVOT in its first 150 s *white* filter exposure starting 2 minutes post-trigger, resulting in an upper limit of > 20.8 mag. MeerLICHT was automatically triggered by the BAT trigger and started observations 11 minutes post-trigger. No afterglow was visible in any of our images across all filters (de Wet et al. 2021b), consistent with the UVOT upper limits. Our observations continued for approximately 1 hour. The depth of our images was limited by the full moon, such that our average 60 s q-band limit was ∼19.62 mag across all exposures. An optical afterglow candidate with $r' = 22.00$ mag was reported from observations taken 1.88 hours post-trigger with the 10.4 m GTC (de Ugarte Postigo et al. 2021b), at a position outside the refined XRT error circle but within the initial one.

Interestingly, earlier observations with the 2.2 m Calar Alto Telescope (CAHA) at 1.16 hours found no afterglow candidate down to $r' > 22.0$ mag, suggestive of a slowly rising afterglow (Kann et al. 2021b). We post facto decided to co-add our 60 s exposures in each filter in order to obtain deeper limits. No source was detected at the XRT afterglow position or the GTC optical afterglow candidate position in any of our co-added images. Our full-frame 5σ upper limits in each filter were $u > 18.98$, $g > 19.77$, $q > 20.95$, $r > 19.67$, $i > 19.66$ and $z > 18.48$ magnitudes.

2.A.5 GRB 210725B

GRB 210725B was detected by *Swift*/BAT at 12:00:48 UT on 2021 July 25, with a duration of 48.00 s (Bernardini et al. 2021; Markwardt et al. 2021). XRT identified an X-ray afterglow within the BAT error circle at coordinates (RA,Dec) = (192.9219,17.1080), but no optical counterpart was found by UVOT in the initial data products and in later analysis down to limiting magnitudes of $u > 20.5$, $b > 20.0$, and $uvw2 > 19.4$ (Siegel et al. 2021a). MeerLICHT was automatically triggered as the BAT error box was observable within 4.83 hours of the trigger, just within our self-imposed observing constraint of < 5 hours. Two exposures were obtained just after evening twilight and just before the field dropped below an airmass of 2. We detected no source at the enhanced XRT position (Goad et al. 2021) down to limiting magnitudes of $u > 18.46$ and $q > 19.91$. No other optical upper limits or observations were reported.

2.A.6 GRB 210731A

On 2021 July 21 at 22:21:08 UT, *Swift*/BAT detected a burst with a duration of ~40 s. XRT and UVOT started observing the BAT error circle 200.9 and 210 s post-trigger, respectively. A bright X-ray source was found within the BAT error circle at coordinates (RA,Dec) = (300.3036,-28.0595) with a positional uncertainty of 5.8″ (Troja et al. 2021). UVOT did not detect an optical counterpart in the first 63 s *white* filter exposure down to a 3σ upper limit of ~19.6 mag (Troja et al. 2021). MeerLICHT was automatically triggered by the *Swift* detection and started observations following the usual procedure at 22:25:54 UT, 286 s after the BAT trigger. We detected a new transient candidate in our first q-band exposure at coordinates (RA,Dec) = (300.30494,-28.06114). This position was 0.3″ away from the enhanced XRT position (D'Ai et al. 2021), and we therefore regarded it as the optical afterglow to GRB 210731A (de Wet et al. 2021e). Observations continued until 4.29 hours post-trigger before reaching the telescope's observing limits for the night. Our early-time MeerLICHT light curve showed a complex evolution with an initial smooth hump followed by a steady rise with two further peaks, as shown in Figure 2.10. Optical detections were reported by UVOT, GROND, MASTER and KAIT (Kuin et al. 2021c; Nicuesa Guelbenzu et al. 2021b; Lipunov et al. 2021a; Zheng et al. 2021c), and a redshift of $z = 1.25$ was determined from observations with X-shooter mounted on the VLT (Kann et al. 2021c).

Our unusual light curve prompted us to obtain further observations with MeerLICHT over the following 3 nights. We also obtained four epochs of VLA and three epochs of MeerKAT radio observations through two director's discretionary time (DDT) proposals (PIs de Wet). A radio afterglow was detected in all four VLA epochs at 6 and 10 GHz, but no radio source was detected at the afterglow position in the MeerKAT data. All groups which reported observations of GRB 210731A were contacted to gain permission for using their data, barring publicly available data (from *Swift* for instance). The multi-wavelength analysis and interpretation of the GRB 210731A data set was turned into a publication (see Chapter 3).

2.A.7 GRB 211106A

GRB 211106A was first detected by *INTEGRAL* at 04:37:31.2 UT on 2021 November 6. *Swift*/BAT was not triggered by GRB 211106A, but following the *INTEGRAL* notice the Gamma-ray Urgent Archiver for Novel Opportunities (GUANO; Tohuvavohu et al. 2020) was triggered. This led to *Swift*/BAT saving 90 s of its event-mode data around the time of the burst. The BAT data showed that the burst was confidently detected with a duration of $T_{90} = 1.75 \pm 0.05$ s, making GRB 211106A a short GRB under the 2 s dividing line (Tohuvavohu et al. 2021). The BAT data allowed the burst to be localised to coordinates (RA,Dec) = (343.643,-53.236) with a 7′ positional uncertainty, following which XRT and UVOT follow-up was requested. GRB 211106A was also detected by Konus-Wind (Ridnaia et al. 2021a) and *Fermi*/GBM (Fletcher & Fermi-GBM Team 2021a), and later triangulated by the InterPlanetary Network (IPN) (Svinkin et al. 2021), though the IPN triangulation error box did not improve on the BAT-GUANO error box.

We scheduled 10×60 s observations in the q-band of the MeerLICHT field containing the BAT-GUANO error box for the following night. Our observations began approximately 14 hours after the GRB trigger at 18:36:45 UT. We co-added the 10 exposures to create a deeper image with a full-frame 5σ limiting magnitude of $q = 21.90$, and performed difference imaging with an archival reference image which had a limiting magnitude of $q = 20.54$. The XRT follow-up campaign identified a number of new X-ray sources within the GUANO error box. None of their initial candidates could be definitively identified as the X-ray afterglow (D'Elia et al. 2021b). Our transient pipeline found a single transient candidate within the BAT-GUANO error box,

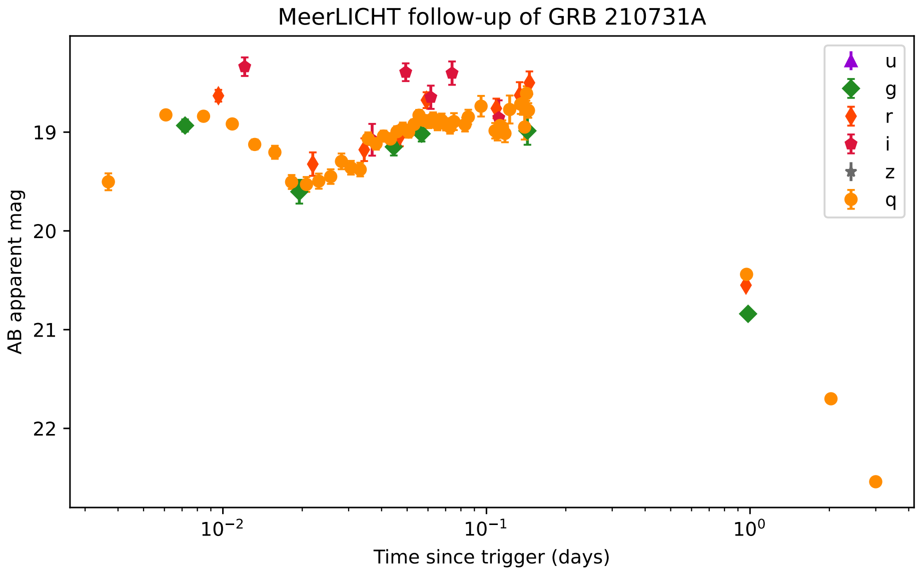

Figure 2.10: Optical detections of GRB 210731A taken with MeerLICHT. The early-time data until 0.2 days was obtained through automatically-triggered observations. The remaining three epochs of data were obtained through manually-scheduled observations and deep co-additions. See Chapter 3 for further details.

spatially coincident with XRT source 1[4]. The XRT source at this position was very near to the galaxy LEDA 432583, which was itself spatially very close to a nearby 17th magnitude star. Our detected optical variability was due to the star showing variable behaviour rather than a transient in the galaxy, ruling out the association of this transient with GRB 211106A. No other promising candidates were found in our data at the positions of the XRT candidates nor in the entire GUANO error box, and our results were reported to the GCN ~3.25 days after the trigger (de Wet et al. 2021g).

Approximately 9 hours after our results were reported, a GCN Circular from the *Swift*/XRT team indicated that one of the sources had been identified as a strong X-ray afterglow candidate based on fading behaviour (D'Elia et al. 2021a). Deeper upper limits at the position of this candidate were subsequently reported by GROND (Nicuesa Guelbenzu et al. 2021a), the VLT equipped with FORS2 (Malesani et al. 2021a), and *Swift*/UVOT (Kuin et al. 2021a). The VLT observations excluded an optical source within the XRT error box down to $R > 26.2$ (Vega magnitudes) at 2.92 days post-trigger. VLT/MUSE observations of the field surrounding the X-ray afterglow identified three galaxies at 4.8″, 7.9″, and 8.3″ from the centre of the XRT error circle with measured redshifts of 0.097, 0.294 and 1.012, respectively, though the association of the GRB with any of these galaxies was not confirmed. Further X-ray observations with Chandra and XMM-Newton at 10.4, 15, and 22 days pinpointed the afterglow position to an accuracy of 0.8″ and showed that the X-ray afterglow was declining with a power law index of −1.02 (Berger et al. 2021; Rouco Escorial et al. 2021). Hubble Space Telescope (HST) observations at 19.17, 25.26, and 48.15 days post-trigger found a source coincident with the X-ray sources with a constant brightness across the 3 epochs, indicative of the host galaxy of GRB 211106A (Kilpatrick et al. 2021a,b,c).

---

[4] See the list of sources at the UK Swift Science Data centre website.

2.A.8 GRB 211130A

Fermi/GBM was triggered by GRB 211130A at 15:16:27 UT on 2021 November 30, localising the burst to coordinates (RA,Dec) = (18.3,-24.3) with a statistical uncertainty of 1.4 degrees (Fermi GBM Team 2021). This was the first *Fermi* GRB to automatically trigger tiled observations with MeerLICHT, as the GBM HealPIX fits file associated with the burst satisfied our observing constraints that a cumulative probability of at least 70% be observable with 80 tiles or fewer starting within 5 hours of the GRB trigger. Within 18 minutes of the GRB trigger we had automatically scheduled observations comprising 72 tiles encompassing a probability of 90% (see Figure 2.11), with observations beginning 3.25 hours post-trigger at 18:31:26 UT. Each observation consisted of a 60 s q-band exposure, with a total of 206 exposures obtained across $\sim$5 hours with an average full-frame 5σ limiting magnitude of 20.79. A total of 67 of the 72 fields were observed 3 times, and 5 of the fields only once, though after data processing 7 of the fields had no non-red flagged files. We searched for afterglow candidates in our data by examining the data products from our difference-imaging pipeline, `ZOGY`. A total of 62 fields had at least 1 non-red flagged transient file. The 10 fields without any transient files included 4 fields that had no existing reference images (4886, 5305, 5306, 5307) and 6 of the 7 fields that had no usable files (4877, 4881, 5087, 5300, 5514, 5733). Many transients ($\sim$1000) were found during a preliminary analysis which used the method outlined in de Wet et al. (2021a), though none of these were identified as promising afterglow candidates. We obtained further observations the following night, but around a quarter of the fields were not observed due to a scheduling error.

Approximately 3 days after the GRB trigger, an IPN GCN Circular was made public with a triangulated error box made from data obtained with BepiColombo, Konus-Wind (Ridnaia et al. 2021b), *INTEGRAL*, and *Fermi*/GBM (Kozyrev et al. 2021). The error box was centred on (RA,Dec) = (21.148,-27.829) with a sky area of 734 square arcminutes and elongated in the southeast-northwest direction (see the inset in Figure 2.11). Most of the IPN error box was encompassed by the field with ID 4472. This field was observed 3 times on the first night but not on the second night due to the scheduling error. A search for transients within this field revealed 2 promising candidates very near the IPN region: one candidate within the error box, and one located just north. We ruled out the candidate inside the IPN region based on its apparent motion of $\sim 1.5''$ across the 3 epochs spanning $\sim$3 hours, making it a likely asteroid. The remaining candidate was detected at coordinates (RA,Dec) = (21.2186,-27.6993) with a brightness that declined across the 3 epochs, making it a probable afterglow candidate (Figure 2.12). We reported our results to the GCN approximately 10 days post-trigger (de Wet et al. 2021c). At this time, if our candidate was indeed the optical afterglow it would have been too faint to detect for all but the largest optical telescopes. No other optical telescopes reported observing campaigns or afterglow candidates related to GRB 211130A.

2.A.9 GRB 211221A

GRB 211221A was detected by *Swift*/BAT at 20:48:40 UT on 2021 December 21. An X-ray counterpart was promptly discovered by XRT at coordinates (RA,Dec) = (78.89820,0.91421) with a positional uncertainty of $3.7''$. UVOT did not find any optical afterglow in the first 150 s *white*-filter exposure starting 63 s after the BAT trigger (Page et al. 2021b). The refined BAT analysis indicated that the light curve showed hints of precursor activity and low-level post-peak emission. The main peak had a duration of $\sim$20 s, while T_{90} was measured as 671.67 ± 105.96 s in the 15-350 keV energy range (Barthelmy et al. 2021b). There was also a sub-threshold detection reported by *Fermi*/GBM 2 days post-burst (Fletcher & Fermi-GBM Team 2021b).

MeerLICHT was immediately triggered by the *Swift* burst and would have started observations 3 minutes after the GRB trigger had it not been for cloudy conditions in Sutherland. Our scheduling scripts were, however, submitted to the telescope queue. The weather cleared enough to allow observations to start at 00:24:11 UT on December 22, 3.59 hours post-trigger, following the usual

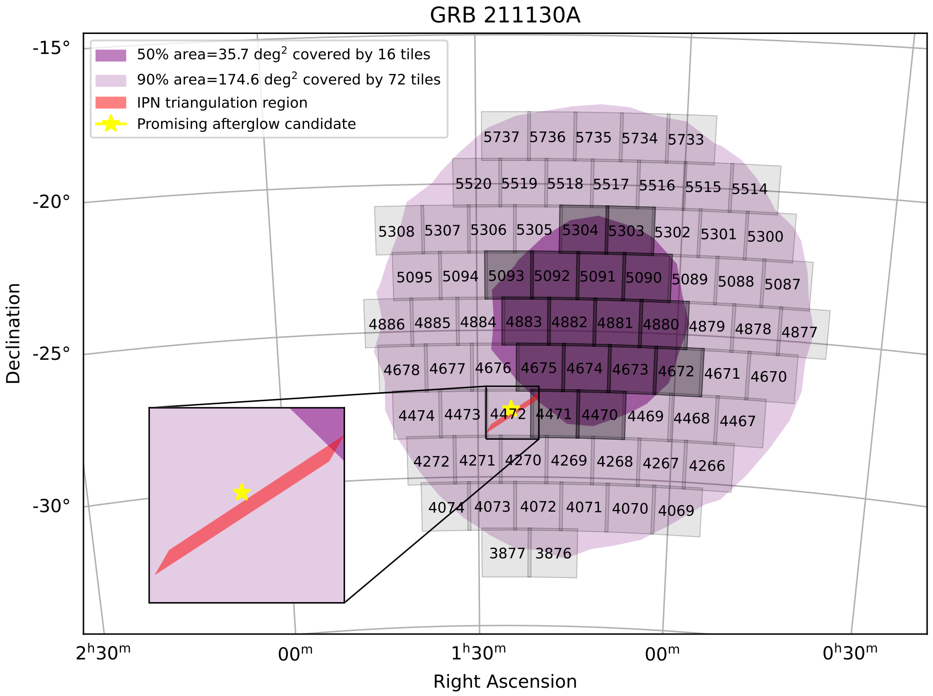

Figure 2.11: The 72 fields required to cover a cumulative probability of 90% of the *Fermi*/GBM error box are shown along with their field IDs, all of which were observed at least once on the first night of observations. We show the IPN triangulation region made public 3 days after the GRB trigger along with the position of our most promising afterglow candidate, located just to the north of the IPN region.

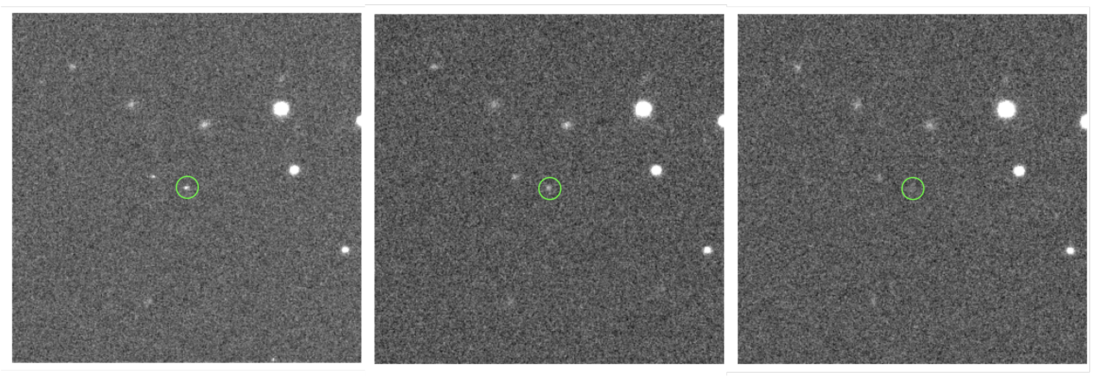

Figure 2.12: Thumbnail images of the promising afterglow candidate from our follow-up of *Fermi*/GBM GRB 211130A at three epochs. Each thumbnail is in the q-band and is $3' \times 3'$ in dimension, with north up, east to the left. The candidate decreased in brightness from $q = 19.83 \pm 0.07$ to $q = 20.05 \pm 0.10$ to $q = 20.66 \pm 0.20$ at times of 3.74, 5.57 and 7.05 hours post-trigger, respectively.

observing sequence of 60 s exposures in the *quqgqrqiqz* filters. A total of 37 exposures were obtained. We co-added all images in each filter in order to obtain deeper images, and reported 3σ AB magnitude limits at the XRT position of $u > 19.97$, $g > 20.55$, $q > 21.85$, $r > 20.67$, $i > 20.32$ and $z > 19.70$ mag to the GCN (Groot et al. 2021a). Our limits were consistent with deep upper limits reported by the Nordic Optical Telescope (NOT) at 3.5 hours post-trigger (Malesani et al. 2021b), and upper limits reported by the MASTER, BOOTES-4/MET, NUTTelA-TAO, UVOT, and KAO optical telescopes (Hu et al. 2021b; Komesh et al. 2021; Siegel et al. 2021b; Fouad et al. 2022).

2.A.10 GRB 220114A

GRB 220114A triggered *Fermi*/GBM at 14:01:47 UT on 2022 January 14 (Fermi GBM Team 2022a). The GRB was identified as a likely short GRB with $T_{90} = 0.70 \pm 0.37$ as taken from the GBM Burst Catalog. We only received the GCN Notice for this burst 10.5 hours after the GRB trigger. At the time of receiving this Notice, MeerLICHT would have been able to observe the error box within 5 hours of the GRB trigger time, hence automatic observations of 66 MeerLICHT fields were triggered encompassing a cumulative probability of 85% of the GBM skymap. This region of the sky was observable for 1.7 hours towards the end of the night, between 01:01:00 and 02:43:00 UT on January 15. Due to high humidity, only 4 exposures in the q-band of 4 individual fields were taken, with the first beginning at 02:39:01 UT, 12.62 hours after the GBM trigger. The reason for this delay was that Observations stopped shortly afterwards due to morning twilight. None of these 4 images were usable as a result of condensation in the optical system, on the crysotat window. As a result, we could not undertake a search for an optical afterglow to GRB 220114A.

2.A.11 GRB 220418B

Fermi/GBM was triggered by a likely short-GRB candidate at 17:16:21 UT on 2022 April 18. The *Fermi* localisation was centred at coordinates (RA, Dec)=(216.5, -26.6) with a statistical uncertainty of 29.8 degrees (Fermi GBM Team 2022b). Although this sky location would have been immediately visible with MeerLICHT, observations were not automatically triggered due to the very large error box requiring 391 fields to cover at least 90% of the *Fermi* skymap localisation probability, far more than our limit of 80 fields. The GBM 50-300 keV light curve showed a single peak with a duration of ∼1.7 s (Fletcher et al. 2022). Approximately 12 hours later, a GCN Circular was sent out with a *Swift*/BAT-GUANO candidate arcminute localisation, at coordinates (RA, Dec)= $(224.329, -17.514)$ degrees, with a $5'$ uncertainty (Tohuvavohu et al. 2022). A further refined location was sent out 7.5 hours later with an uncertainty of only $3'$, but fully consistent with the previous location (DeLaunay et al. 2022a). Given the short nature of the burst and small error box, follow-up from other facilities was strongly encouraged.

We therefore decided to schedule 3×300 s exposures in each of the q and i filters with MeerLICHT for the following night. Our observations began ∼1.17 days after the trigger. The average limiting magnitude across the 3 images in each filter was 21.08 and 20.50 in q and i, respectively. Based on our difference-imaging products we found no promising optical counterpart within the *Swift*/BAT-GUANO error box. We also co-added the images in each filter to obtain deeper images with full-frame 5σ limiting magnitudes of $q = 21.66$ and $i = 21.09$, and detected no new transients within the GUANO error box within these images. Follow-up X-ray observations with *Swift* between 1.31 and 1.72 days post-trigger also found no promising X-ray afterglow candidate (Sbarufatti et al. 2022b). We did not report our observations to the GCN.

2.A.12 GRB 220427A

GRB 220427A was detected by *Swift*/BAT at 21:00:34 on 2022 April 27, with the BAT light curve showing a complex structure with an ∼80 s duration. X-ray and optical counterparts were

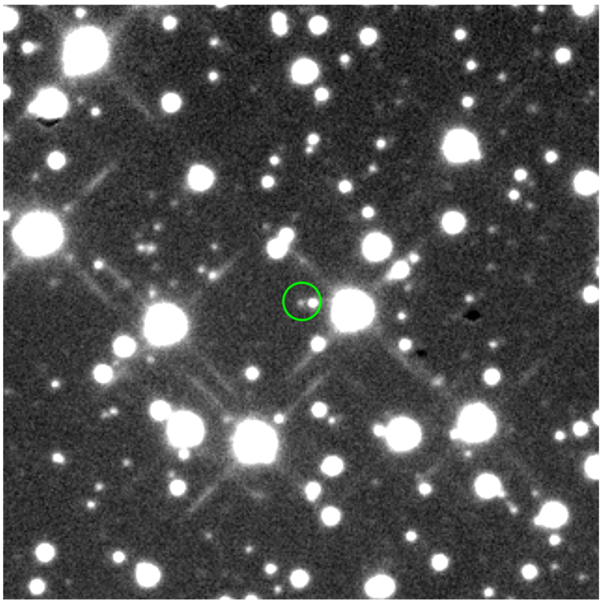

Figure 2.13: $3' \times 3'$ thumbnail cutout of our very deep q-band coadd made from 87×60 s exposures showing the optical afterglow to GRB 220427A as the faint source at the centre of the green circle. The image is orientated with north up and east to the left. The afterglow had a measured AB magnitude of $q = 20.58 \pm 0.04$, while the full-frame 5σ limiting magnitude was 23.09.

promptly identified by the XRT and UVOT aboard *Swift*, localised by UVOT to (RA,Dec) = (275.88882,-56.25507) with an error radius of $0.61''$ and a *white* filter brightness of 17.23 mag at ~4 minutes post-trigger (D'Ai et al. 2022). The burst was also detected by Konus-Wind (Frederiks et al. 2022a), while a refined BAT analysis found $T_{90} = 57.2 \pm 12.2$ (Stamatikos et al. 2022).

MeerLICHT observations were automatically scheduled following the GRB trigger and according to our scheduling scripts, observing should have begun at 21:10 UT, 10 minutes post-trigger. Observations did not start automatically at 21:10, however, due to the fact that our scheduling scripts at the time did not take into account the local hour angle limits of -3 and 4.5 hours for MeerLICHT. Taking these into account, the earliest we could have started observing was 22:20 UT. Our observations had to be manually scheduled, and as a result, our first exposure started 2.69 hours post-trigger at 23:41:47 UT, following the usual observing sequence for *Swift* GRBs. Observations continued for a further 4.52 hours until morning twilight at 04:13:12 UT. The optical afterglow was very faintly detected in some of our 60 s q-band exposures. We therefore decided to co-add all of the exposures in each filter in order to obtain deeper images and detected the afterglow in all filters except for the u band at an average time of 3.83 hours post-trigger, as reported to the GCN (de Wet et al. 2022i). The very deep q-band coadded image (with a 5σ limiting magnitude of $q = 23.09$) is shown in Figure 2.13. We also grouped the q-band images into 9 sets of images evenly spaced in time logarithmically, from which 9 co-added images were made. These were used to examine the temporal evolution of the afterglow. Our light curve was consistent with the temporal decay reported from measurements with the VLT, GRANDMA, and Las Cumbres Observatory (Klotz et al. 2022; Strausbaugh & Cucchiara 2022a).

2.A.13 GRB 220430A

Swift/BAT was triggered by GRB 220430A at 13:53:15 UT on 2022 April 30. The initial *Swift* GCN Circular noted that an X-class solar flare occurred near the time of the GRB and may have contributed to the light curve activity. They further noted that the low Galactic latitude ($b = -0.26°$) raised the possibility of the trigger being caused by a Galactic plane transient. A bright X-ray counterpart was promptly discovered by the XRT at (RA,Dec) = (97.61267,9.54730), but no optical counterpart was reported by UVOT (Ambrosi et al. 2022). The burst was also detected by the *AGILE* and AstroSat CZTI γ-ray detectors (Ursi et al. 2022a; Gopalakrishnan et al. 2022a). Refined BAT analysis indicated that $T_{90} = 43.10 \pm 0.57$ s (Barthelmy et al. 2022), while refined XRT analysis indicated that the X-ray light curve was showing typical X-ray afterglow behaviour and therefore provided support for a GRB origin to the burst (Evans et al. 2022).

Automatic observations with MeerLICHT were triggered with the first exposures beginning 3.28 hours post-trigger at 17:09:48 UT, following the usual observing sequence. The GRB position was setting very soon after evening twilight, hence only 14 exposures were obtained. No afterglow was detected at the XRT position in our images down to AB limiting magnitudes of $u > 19.0$, $q > 20.4$ and $i > 18.6$. Our results were promptly reported to the GCN (Groot et al. 2022a), and were consistent with optical upper limits reported by Mondy and AbAO, GRANDMA, CAHA, GIT and Nanshan/HMT (Pankov et al. 2022; Dornic et al. 2022; Hu et al. 2022b; Swain et al. 2022; Jiang et al. 2022). We also made deep co-adds retrospectively for the bands in which more than 1 exposure was obtained (ugq), which led to deeper limits of $u > 19.41$, $g > 20.64$, and $q > 21.56$. No optical afterglow to GRB 220430A was reported by any other groups.

2.A.14 GRB 220514A

Fermi/GBM was triggered by GRB 220514A at 12:24:32 UT on 2022 May 14. The GBM team reported that the burst had been localised to (RA,Dec) = (145.6,13.6) with a statistical uncertainty of 1.8 degrees, and was a likely long duration burst (Fermi GBM Team 2022c). The *Fermi* Burst Catalog later listed the duration as $T_{90} = 66.31 \pm 1.56$ s. At 14:11:38 UT, 1.79 hours post-trigger, the *INTEGRAL* team reported that GRB 220514A had been detected by *INTEGRAL* and localised to (RA,Dec) = (147.6670,13.1472) with an uncertainty of only $1.5'$ (Mereghetti et al. 2022). The burst was also detected by AstroSAT CZTI (Gopalakrishnan et al. 2022b).

The *Fermi* detection triggered automatic observations with MeerLICHT consisting of 69 fields encompassing 90% of the error box. Observations were scheduled to begin at 16:43 UT, 4.32 hours post-trigger and therefore within our 5 hour time constraint. The small *INTEGRAL* error box, however, motivated us to halt the automatically-scheduled GBM observations and instead manually schedule 2 × 300 s observations in all of MeerLICHT's filters of the single field containing the *INTEGRAL* error box. Examination of the data revealed that all of our images were significantly trailed, rendering them unusable for science. The autoguiding system was being tested at this time, and this may have led to a problem with the telescope's tracking. We were able to rectify the autoguiding and fit in 2 × 300 s q-band observations just before the sky position moved above an airmass of 2, beginning at 19:09:15 UT. Comparison of our data with an existing reference image of the field revealed a new transient well within the *INTEGRAL* error box at coordinates (RA,Dec) = (147.66556,13.15628), $33''$ from the centre of the error box (see Figure 2.14) and with a magnitude $q = 19.89 \pm 0.13$. No underlying source could be found in our archival reference image nor in PanSTARRS images of the field, and we also excluded an asteroid origin through querying the Minor Planet Centre database. We reported our promising afterglow candidate to the GCN 9.38 hours post-trigger (de Wet et al. 2022j), and its authenticity was confirmed following reported detections by KAIT, GRANDMA and MITSuME Akeno which showed fading behaviour (Zheng et al. 2022b; Yan et al. 2022; Murata et al. 2022).

2.A.15 GRB 220527A

The *AGILE* satellite detected GRB 220527A at 09:17:15 UT on 2022 May 27 with a measured duration of about 15 s (Ursi et al. 2022c). The burst was also detected by *Fermi*/GBM, *Fermi*/LAT, AstroSat CZTI, and Konus-Wind (Fermi GBM Team 2022d; Bissaldi et al. 2022;

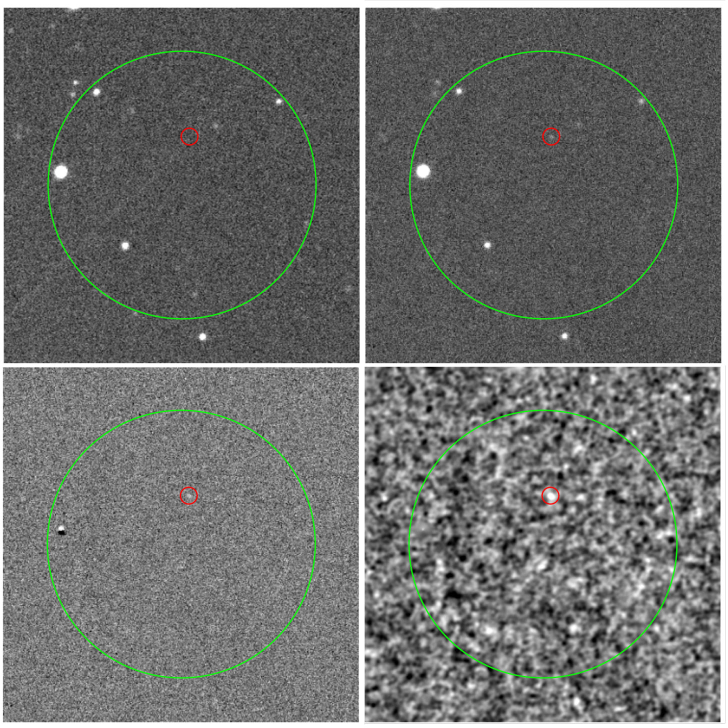

Figure 2.14: Clockwise from top left: Reference image, science image, difference image, and corrected significance (S_{corr}) image showing the 1.5′ *INTEGRAL* error box in green and our GRB 220514A afterglow candidate position in red. Our science image was the first good q-band exposure taken at a midtime of 6.79 hours post-trigger. All images are $4' \times 4'$ in dimension, orientated with north up and east to the left. The difference and S_{corr} images show the new transient candidate, detected with a significance of 6.90.

Gopalakrishnan et al. 2022c; Lysenko et al. 2022), with the LAT team reporting a well-localised sky position of (RA,Dec) = (323.57,-14.9) with an error radius of 0.08 degrees. The small LAT error box prompted ToO observations with the *Swift* XRT and UVOT (Evans & Swift Team 2022a). The *Swift* team reported a strong X-ray afterglow candidate 15.88 hours post-trigger at position (RA,Dec) = (323.52805,-14.97183) with a 2.6$''$ positional uncertainty (Sbarufatti et al. 2022a). Approximately 1 hour later an optical source consistent with the X-ray position was identified by UVOT with a u-band magnitude of 17.8 (Tohuvavohu 2022), confirming the source as the likely afterglow to GRB 220527A.

We therefore manually scheduled 2 × 300 s observations in the q band and 300 s observations in the g and r bands with MeerLICHT, with the first exposure starting at 02:43:04 UT on May 28. We detected the optical afterglow to GRB 220527A in all 4 images and reported our detections to the GCN (de Wet et al. 2022h). Spectroscopic observations with NOT were used to determine a redshift of $z = 0.857$ based on absorption features in the spectrum (Xu et al. 2022), while further optical photometric observations were reported by a number of groups (Imai et al. 2022; D'Avanzo et al. 2022; Sun et al. 2022; Zheng et al. 2022a; Niwano et al. 2022).

2.A.16 GRB 220627A

The detection of GRB 220627A by *Fermi*/GBM at 21:21:00.09 UT on 2022 June 27 triggered automatic observations with MeerLICHT. The initial *Fermi* GCN Circular reported the detection of a likely long GRB localised to coordinates (RA,Dec) = (211.5,-35.1) with a statistical uncertainty of 4.2 degrees (Fermi GBM Team 2022e). The GBM HEALPix fits file associated with the *Fermi* trigger was automatically downloaded and used to create an observing schedule. Figure 2.15 shows that a total of 90 telescope pointings would have been required to cover a probability of at least 90%, encompassing a sky area of 216.5 deg^2. Based on the GBM skymap and the telescope observing constraints, 52 fields were scheduled for observations encompassing a cumulative probability of 71%. The unique field IDs for these 52 fields are shown in Figure 2.15, where it is evident that a large number of western fields could not be observed since they would be the first to set. Our observations began 21 minutes after the GRB trigger at 21:42:23 UT and continued for a further 1.6 hours. All 52 fields were observed at least once, while 10 (2) of the 52 fields on the eastern edge of the error box were observed twice (thrice), encompassing a probability of 7.5%. Seven transient candidates with at least two detections were identified through our difference imaging pipeline and transients database, of which 5 were confirmed as known asteroids. The remaining 2 candidates (see their position in Figure 2.15) were reported as possible afterglow candidates (Groot et al. 2022b).

At 07:00:40 UT the following morning a GCN Circular was sent out indicating that *Fermi*/LAT had detected high-energy γ-ray emission from GRB 220627A and had localised the burst to (RA,Dec) = (201.2,-32.5) with a 0.2 degree error radius - a much smaller error box than the GBM error box (di Lalla et al. 2022). The LAT Circular indicated that the highest energy photon was detected at 15.7 GeV, and that *Swift* Target of Opportunity (ToO) observations had been requested. The LAT error box straddled two MeerLICHT fields, neither of which had been observed on the previous night (see Figure 2.15). We scheduled 2 × 300 s observations in the q-band for these fields (IDs 3975,3974) in order to search for an optical afterglow within the LAT error box. Our observations began just after evening twilight under new moon conditions at 17:12:15 UT, approximately 0.83 days post-trigger. The *Swift* ToO observations identified a number of X-ray sources within the LAT error box that may have been associated with GRB 220627A (Evans & Swift Team 2022b), most having error regions with radii smaller than 8$''$. Among the three most promising candidates, only one source was uncatalogued: source number[5] 3. Our MeerLICHT images showed that there was a faint new optical source within the error box of this source at coordinates (RA,Dec) = (201.36872,-32.42592) with a positional uncertainty of

---

[5] See the list of sources at the UK Swift Science Data Centre website.

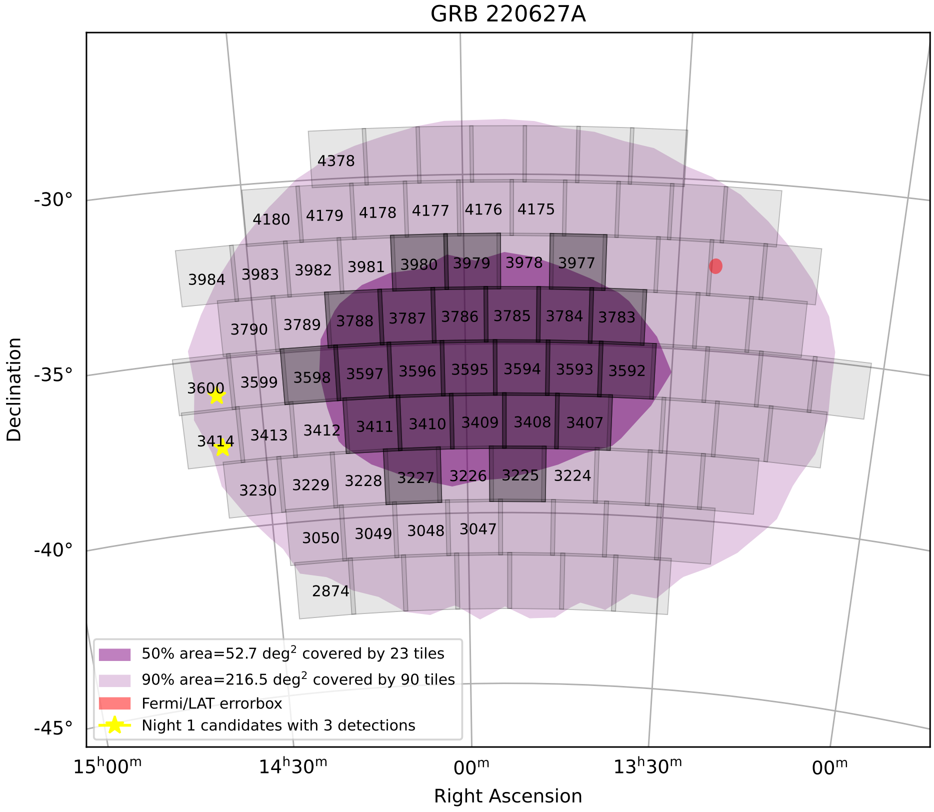

Figure 2.15: MeerLicht pointings required to cover a cumulative probability of 90% of the *Fermi*/GBM error box. The 52 fields that were observed automatically following the trigger are indicated by their field IDs. We show the position of the 2 transient candidates that were later ruled out following the announcement of the LAT error region (red).

0.1″ in each coordinate. With a brightness of $q = 21.25 \pm 0.09$ mag in our first exposure, the lack of any source at the same position down to $q > 21.71$ in an archival image from 2 months earlier made it likely that this source was the optical afterglow to GRB 220627A. We reported our results to the GCN (de Wet et al. 2022c).

Initial interest in GRB 220627A was high after the *Fermi*/GBM team proposed that GRB 220627A could be a lensed or ultra-long GRB based on the fact that the GBM was triggered 1000 s after the initial burst by a burst localised to a similar sky location and with a similar temporal shape and duration (Roberts et al. 2022). Konus-Wind also detected two bursts separated temporally by ∼1000 s with a similar structure to the GBM bursts (Frederiks et al. 2022c). Based on the possibility of a lensed or ultra-long GRB, the Stargate consortium triggered observations of the MeerLICHT afterglow candidate with the integral-field unit spectrograph MUSE on the VLT. Their observations at 1.17 days post-trigger revealed a trough in the spectrum at 4960 Å which was interpreted as damped Lyman Alpha neutral hydrogen absorption at a redshift of $z = 3.084$ (Izzo et al. 2022). A number of other metal lines confirmed the redshift, while an additional intervening system at $z = 2.665$ was also identified through the presence of absorption lines. GROND also reported detections in the *griz* bands at 2.18 days which confirmed the decaying behaviour (Nicuesa Guelbenzu et al. 2022). A radio counterpart was detected with ATCA at 7.3 days (Leung et al. 2022), while non-detections at 1.28 GHz with MeerKAT were also reported (Giarratana et al. 2022). The data on this burst was turned into a publication, presented in Chapter 4.

2.A.17 GRB 220715B

Swift/BAT and *Fermi*/GBM were triggered by GRB 220715B at 22:24:42 UT on 2022 July 15 (Troja et al. 2022; Fermi GBM Team 2022f). An X-ray counterpart was promptly identified by *Swift*/XRT at (RA,Dec) = (254.87520,-33.59766) with an uncertainty of 5.7″ (Troja et al. 2022). No optical afterglow was identified by UVOT in its initial observations. MeerLICHT was triggered by *Swift*/BAT and began automatic follow-up observations at 22:26:51 UT, 129 seconds after the GRB trigger time. A total of 31 × 60 s exposures were obtained, following our usual sequence for *Swift* triggers. All images from this night, however, were red-flagged and unusable due to the presence of high cirrus clouds. We did not report our results to the GCN. No optical afterglow was identified by *Swift*/UVOT (Kuin et al. 2022), the BOOTES-network (Hu et al. 2022a), nor the Virgin Island Robotic Telescope (Noonan et al. 2022).

2.A.18 GRB 220810A

GRB 220810A was detected by *Fermi*/GBM at 23:15:42 UT on 2022 August 10 with a duration of approximately 9 s (Fermi GBM Team 2022g). Following the GBM detection, observations with MeerLICHT were automatically triggered. A total of 69 fields encompassing a cumulative probability of 90% of the GBM error box were scheduled, with observing beginning approximately 14 minutes post-trigger at 23:30:01 UT. A total of 23 of the highest probability fields were each observed once before cirrus clouds forced MeerLICHT to halt observing. All exposures lasted 60 s and were taken in the q band. Three of the 23 fields did not have reference images, so no difference-imaging products could be created. The remaining 20 fields encompassed a cumulative probability of 58% of the GBM error box (see Figure 2.16).

We conducted a search for promising transients within our data by identifying all transients that were detected for the first time on that night having a real-bogus machine learning score > 0.8 (Hosenie et al. 2021). We then excluded all transient candidates with Gaia EDR3 matches within 1″ of the transient position. Thumbnail images displaying the new, reference, difference, and S_{corr} images were used to vet all remaining 252 candidates in order to identify promising transients. Thirteen transient candidates without underlying sources in their reference images were identified. Of these 13, the positions of 11 sources were consistent with known Minor Planet

Table 2.5: GRB 220810A afterglow candidates

RA	Dec	Mag (AB)	5σ limiting mag	UT time
311.31569	5.11110	11.51 ± 0.06	$q > 15.79$	23:59:19
312.35241	1.93601	17.52 ± 0.07	$q > 18.77$	23:44:42

Centre objects, excluding them from being associated with GRB 220810A. The remaining two candidates both had no underlying counterparts in PanSTARRS images, making them likely astrophysical transients. Table 2.5 shows their positions, brightnesses, observing times, and full-frame limiting magnitudes. The first, bright candidate was identified in an image in which the sources were trailed. However, human inspection confirmed that the source was not an artefact. We reported both candidates to the GCN (de Wet et al. 2022g). *Swift*/XRT ToO observations were conducted for both sources at approximately 1.9 and 2.4 days post-trigger, respectively, but no X-ray counterpart was reported (Gropp et al. 2022b,a).

2.A.19 GRB 220921A

Fermi/GBM triggered on GRB 220921A at 11:05:59 UT on 2022 September 21. The burst was also detected by *Fermi*/LAT with the highest energy photon having an energy of 855 MeV. The LAT Circular released at ~8 hours post-trigger indicated that the burst had been localised to (RA,Dec) = (66.79,-40.25) with an 90% containment error radius of 0.42 degrees (Pillera et al. 2022a). The GBM Circular indicated that the burst duration was approximately 210 s (Bissaldi 2022), which was similar to the duration of ~231 s reported by Konus-Wind (Svinkin et al. 2022).

Based on the relatively small LAT error box, *Swift*/XRT initiated tiled observations in order to search for an X-ray afterglow (Evans 2022). Approximately 11 hours after the burst, the MASTER team indicated that they had found a new optical source within the LAT error box with an unfiltered magnitude of 17.8 and located at a position of (RA,Dec) = (66.4725833,-40.4057500) (Lipunov et al. 2022). Automatic observations were not scheduled with MeerLICHT due to the burst location only becoming observable more than 12 hours after the trigger. We decided to manually trigger observations of a single field containing the entire LAT error box (ID 2977), and obtained a repeated series of 60 s exposures following the usual filter sequence for *Swift* bursts, beginning at 01:29:34 UT on 2022 September 22 and continuing for a further two hours. The images obtained after the first 30 minutes were all red-flagged, however, due to deteriorating observing conditions. A total of 14 images were obtained in the q-band and two to three images in each of the remaining bands. We co-added images in each filter in order to obtain more significant detections, and detected the afterglow with a SNR> 7 in all six filters. The afterglow had a brightness of $q = 18.47 \pm 0.02$ mag at a mid-time of 0.61 days after the LAT trigger. We reported our results to the GCN (de Wet et al. 2022a). Further optical detections were reported by DDOTI (Watson et al. 2022), while a millimeter detection with ALMA at 97.5 GHz was also reported (Laskar et al. 2022). We also obtained 300 s observations at two further epochs in each MeerLICHT band and detected the afterglow in each filter (de Wet et al. 2022b).

2.A.20 GRB 221009A

The *Swift* Burst Alert Telescope was triggered by a new transient at 14:10:17 UT on 2022 October 9. X-ray and optical counterparts were promptly discovered by the XRT and UVOT aboard *Swift*, with the *white* filter exposure measuring an estimated magnitude of 16.63 at a position (RA,Dec) = (288.26452,19.77350) with an uncertainty of $\sim 0.61''$. The new transient was given the name Swift J1913.1+1946 and was reported to the GCN at 14:39:22 UT (Zhu et al. 2022). Eight hours later, the *Swift* team indicated that the transient may in fact have been a GRB due to strong fading in the X-ray data and a possible association with a *Fermi*/GBM trigger that occurred almost an hour earlier at 13:16:59 UT, adding that it was likely a highly energetic event

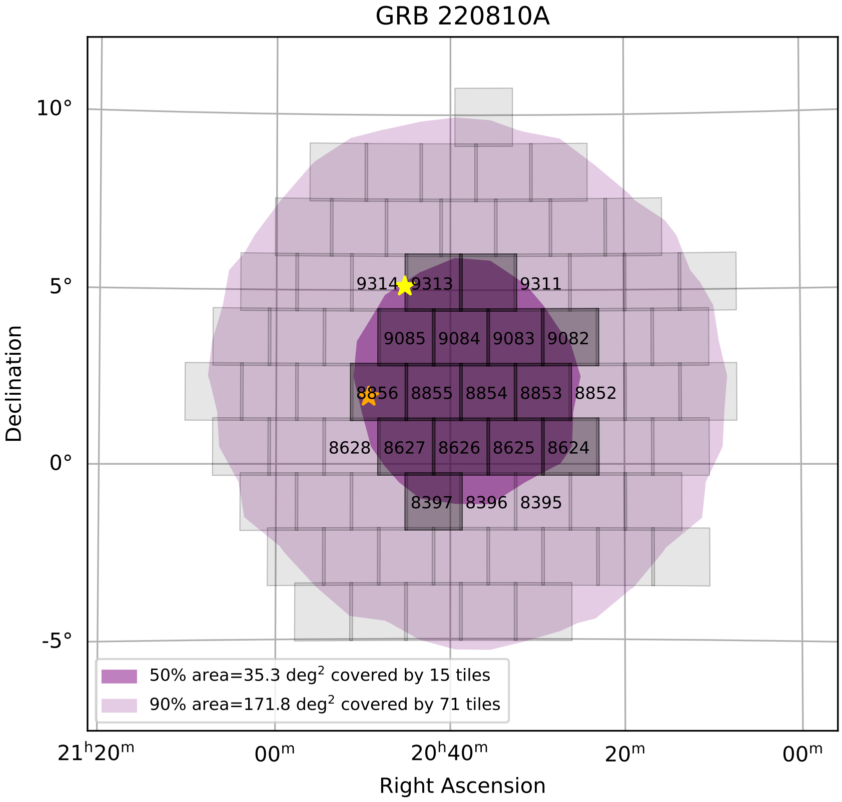

Figure 2.16: GRB 220810A skymap showing the 90% and 50% GBM probability regions in purple, and the MeerLICHT fields required to cover the 90% probability region. The fields containing field ID numbers are the 20 fields observed by MeerLICHT possessing difference-imaging products, encompassing a probability of 58%. We show the positions of the two transient candidates in yellow (first row in Table 2.5) and orange (second row in Table 2.5).

(Kennea et al. 2022). At 20:54:36 UT, the *Fermi* team released a GCN Circular indicating that the previously-mentioned trigger was from an event that was the brightest GRB ever detected by the GBM should it be confirmed as a GRB (Veres et al. 2022). The burst duration was estimated as 327 s by *Fermi*/GBM (Lesage et al. 2022), and *Fermi*/LAT reported the detection of a photon with an energy of 99.3 GeV - the highest-energy photon ever detected by *Fermi*/LAT (Pillera et al. 2022b). A large number of missions detected γ-ray emission from GRB 221009A, including *INTEGRAL*, Konus-Wind, AGILE, Solar Orbiter STIX, GRBALpha (Gotz et al. 2022; Frederiks et al. 2022b; Ursi et al. 2022b; Piano et al. 2022; Xiao et al. 2022; Ripa et al. 2022). The LHAASO observatory reported the detection of very-high energy photons up to a maximum energy of 18 TeV, making this the first detection of photons with energies above 10 TeV for a GRB (Huang et al. 2022). Amazingly, the prompt γ-ray and X-ray emission from GRB 221009A ionised parts of the upper atmosphere. These sudden ionospheric disturbances modified the radio propagation properties of the waveguide between the Earth's surface and the ionosphere, and were seen as rapid variations in the the signal strengths from radio transmitters below 100 KHz (Schnoor et al. 2022).

The *Swift* trigger on GRB 221009A led to automatic observations with MeerLICHT starting 4.55 hours after the *Fermi* trigger at 17:49:44 UT. Our observations followed the usual filter sequence of 60 s exposures for *Swift* triggers and continued for ~1 hour. The afterglow was detected in all bands except for the u-band, with the brightness ranging by almost 4 magnitudes between the blue and red observing bands from $g = 18.22$ to $z = 14.89$ (de Wet et al. 2022d). This highly reddened spectrum was consistent with the low Galactic latitude of the GRB position ($b = 4.32°$) and a high degree of dust extinction along the line-of-sight. Some of our observations were affected by cirrus cloud. We were one of the earliest ground-based telescopes to report our observations to the GCN, at 09:14:47 UT the following day. The redshift of GRB 221009A was confirmed through spectroscopic observations with X-Shooter mounted on the VLT beginning approximately 11.5 hours after the GBM trigger. The redshift was determined to be $z = 0.151$ due to the presence of Ca I,II and NaID absorption lines (de Ugarte Postigo et al. 2022). A vast number of optical and near-infrared observatories conducted follow-up observing campaigns of GRB 221009A, including the Hubble Space Telescope (Levan et al. 2022a) and James Webb Space Telescope (Levan et al. 2022b). There was also much excitement within the BlackGEM consortium after the BG3 telescope observed GRB 221009A during commissioning and reported its first scientific results (Groot et al. 2022c). GRB 221009A was also followed-up extensively at millimeter and radio frequencies, and will end up being one of the most intensely studied GRBs ever due to its incredible γ-ray brightness.

2.A.21 GRB 221115B

GRB 221115B was detected by *Swift*/BAT on 2022 November 15 but was not localised onboard the spacecraft (DeLaunay et al. 2022b). The CALET Gamma-ray Burst Monitor (Yamaoka et al. 2013) detected the burst at T_0 = 09:46:15 and sent a Notice which triggered GUANO to save 200 s of BAT event-mode data around the time of the burst. The burst duration as detected by CALET was $T_{90} = 2.1 \pm 0.2$ seconds (Yoshida et al. 2022). The burst was well-detected in the BAT data with a duration of ~ 5 s, and was localised to (RA,Dec) = (54.788,-16.701) with a $3'$ uncertainty (DeLaunay et al. 2022b). The GUANO localisation was reported to the GCN at 23:40:37 UT, or around ~ 14 hours post-trigger. The next day, we decided to schedule observations with MeerLICHT for the following night. We obtained 2 × 300 s observations in the q-band of the field containing the GUANO error box, starting at 21:21:30 UT on November 16, 1.48 days post-trigger. Our images reached full-frame 5σ limiting magnitudes of $q = 22.10$ and $q = 22.18$, respectively, while our archival reference image had a limiting magnitude of $q = 21.10$. Our difference-imaging products showed no new significant transients down to a 5σ limiting magnitude of $q > 20.80$, and we reported our results to the GCN approximately 2 days after the GRB (de Wet et al. 2022e).

2.A.22 GRB 221202A

Swift/BAT detected GRB 221202A at 20:06:10 UT on 2022 December 2, with a light curve showing a duration of about 20 s. An X-ray counterpart was promptly discovered at (RA,Dec) = (77.08221,-59.83213) with an uncertainty of $1.9''$. No UV/optical counterpart was found by UVOT in its first 150 s exposure in the *white* filter starting 101 s after the BAT trigger (Caputo et al. 2022). MeerLICHT should have begun observations immediately following the BAT trigger, but due to an update to the scheduling system to accommodate the BlackGEM telescopes, the GRB scheduling scripts did not produce the necessary observing scripts. We therefore had to schedule the observations manually. Our first 60 s exposures following the usual filter sequence for *Swift* bursts began at 20:44:15 UT, 38 minutes after the BAT trigger. Due to the non-detection of any optical source at the XRT position, we decided to schedule deeper, 300 s exposures in all bands excepting the u-band. Our observations yielded upper limits of $q > 21.80$, $z > 20.01$, $i > 21.02$, $r > 21.53$, and $g > 21.58$ at approximately 1.14 hours post-trigger (de Wet et al. 2022f), in agreement with the upper limits reported by the SAAO Las Cumbres telescopes (Strausbaugh & Cucchiara 2022b). The optical afterglow to GRB 221202A was detected by FORS2 on the VLT with a brightness of $R = 23.10$ measured at ∼10.73 hours after the burst (Rossi et al. 2022).

2.A.23 GRB 230209B

GRB 230209B triggered *Fermi*/GBM at 22:32:36 UT on 2023 February 9 with a measured duration of ∼ 20 s (Dalessi et al. 2023). The *Fermi* detection did not trigger automatic observations with MeerLICHT since the field of GRB 230209B would only be observable approximately 20 hours after the GBM trigger – well outside of the 5-hour limit for automatic triggering. The burst was well-localised (by *Fermi* standards) as a total of 60 MeerLICHT pointings would have been needed to encompass a probability of 86%. We decided to conduct follow-up observations as practice for the forthcoming O4 gravitational wave observing run, since it would allow us to test the updated real-bogus machine learning classifier (Hosenie et al. 2021) and give us an opportunity to attempt to identify transient candidates quickly. Our observations began at 18:31:31 UT on February 10, taking 60 s exposures in the q-band as usual for *Fermi* bursts. We observed 55 distinct fields at least once each, encompassing a cumulative probability of 80%. Of these 55 fields, 25 were observed twice and 18 were observed three times (see Figure 2.17). We conducted a search for transients within our observations by only considering the 43 fields which had more than one observation. These fields encompassed a probability of 70%. We required that a transient candidate be detected at least twice with a real-bogus score of $RB > 0.8$ in each image and have no previous detections. In total, we identified 11 candidates with no counterparts in their reference images. After further inspection and consultation, we deduced that 8 of the candidates were likely image artefacts from reflections. This reduced the number of candidates to three. One of these candidates had a much fainter counterpart in deeper PanSTARRS images, and another had been detected by ZTF previously. We deduced that all three candidates were likely Galactic in origin. An IPN triangulation region was announced ∼4.5 days post-trigger that localised the burst to a small region in the northern part of the GBM error box (Kozyrev et al. 2023). We did not observe the fields covering this location as the position was too far north for MeerLICHT (Figure 2.17). We did not report the results of our follow-up campaign. No afterglow was reported by any other groups.

2.A.24 GRB 230405B

Swift/BAT triggered on GRB 230405B at 19:58:03 UT on 2023 April 5, detecting a single-peaked burst with a duration of ∼10 s. An X-ray counterpart was promptly discovered by XRT which began observing the BAT error region 65.7 s after the BAT trigger. No optical counterpart was found by UVOT in its initial 150 s exposure in the *white* filter (Page et al. 2023a). GRB 230405B

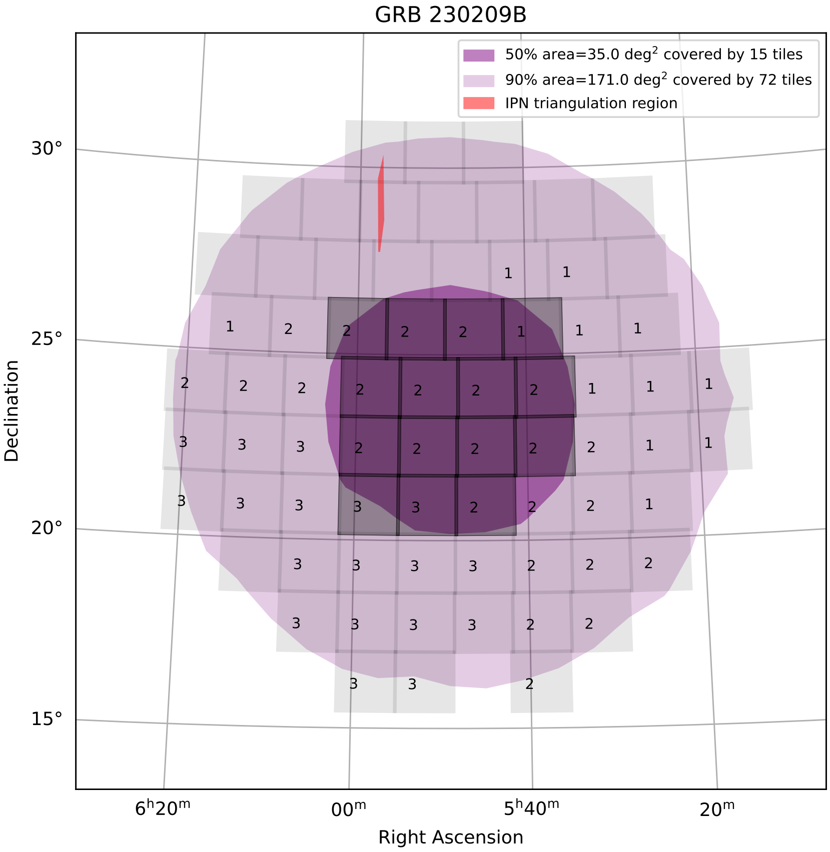

Figure 2.17: GRB 230209B skymap. The numbers within each tile indicate the number of observations obtained of each field. The IPN triangulation (red) was not observed during our follow-up campaign.

was also detected by *Fermi*/GBM (Fermi GBM Team 2023a) and AstroSat (Navaneeth et al. 2023a).

Both the *Swift* and the *Fermi* triggers led to the creation of scheduling scripts for MeerLICHT, with the GBM trigger requiring 69 fields to encompass a probability of 90%. Observations of the GBM fields would have started 4.38 hours post-trigger at 00:21 UT, while observations of the single *Swift* field (Field ID 2400) would have begun 4.87 hours post-trigger at 00:50 UT. Since both the *Swift* and *Fermi* triggers satisfied the < 5 hour observing constraint (see Table 2.1), both scheduling scripts were submitted automatically. A number of observations of the *Fermi*/GBM error box occurred before observations of the single *Swift* field began at 02:20:05, 6.38 hours post-trigger. A total of 71 exposures were obtained with 33, 7, 7, 7, 7, 6 in each of the q, u, g, r, i and z bands, respectively. No obvious optical counterpart was apparent in these images at the enhanced XRT position (Beardmore et al. 2023), so we decided to co-add the images in each filter. No new optical source was present in any of our co-added images when compared to a deep DECam r-band image of this field. Our deepest upper limit was in the q-band with $q > 22.6$ mag. We reported our 3σ upper limits to the GCN as usual (de Wet et al. 2023b).

2.A.25 GRB 230808B

Fermi/GBM detected GRB 230808B at 16:46:11 UT on 2023 August 8 (Fermi GBM Team 2023b). Tee *Fermi* trigger led to automatic observations with MeerLICHT. According to our alert emails, 7 fields would be required to cover a probability of 92%. The reason for the very low number fields was that the *Fermi*/GBM skymap was not immediately available upon receiving the trigger. In these cases, we use the *Fermi*-estimated position and error radius to determine which fields to observe. The given error radius does not include a systematic uncertainty in the GBM localisations, which results in a much smaller error box than is typically the case. MeerLICHT obtained a single observation of each of these 7 fields with the first exposure beginning at 17:28:38 UT - 42.5 minutes after the GRB trigger time. Thereafter, the telescope was forced to close due to bad weather. We found no promising afterglow candidates in our analysis of the data, and did not report our results to the GCN. No follow-up or detections were reported by any other groups.

2.A.26 GRB 230827A

Fermi/GBM was triggered by a burst of γ-ray activity at 18:17:52 UT on 2023 August 27 (Fermi GBM Team 2023c). The *Fermi* trigger prompted automatic observations of the error box with MeerLICHT beginning 0.36 hours post-trigger at 18:39:28 UT. In total we obtained 155×60 s exposures of 52 unique fields which encompassed 82% of the GBM error box. All fields were observed at least 3 times except for field 05701 which was observed twice. No promising transient candidates were found within our data. The burst was also detected by GRBAlpha (Dafcikova et al. 2023b), Glowbug (Kerr et al. 2023) and VZLUSAT-2 (Dafcikova et al. 2023a). A BALROG localisation was also reported (Biltzinger et al. 2023). We did not report the results of our observations.

2.A.27 GRB 231104B

Fermi/GBM detected GRB 231104B at 23:10:39 UT on 2023 November 4 (Fermi GBM Team 2023d). MeerLICHT responded automatically to the *Fermi* trigger and began tiled observations of the error box 23.75 minutes post-trigger at 23:34:24 UT. A total of 62 fields covering a cumulative probability of 0.83 were scheduled for observations. MeerLICHT obtained a total of 81×60 s exposures in the q-band of 59 unique fields. Three of the fields were observed three times, 16 were observed twice, and the remaining 40 fields were each observed once. Figure 2.18 shows the fields which were observed along with the number of observations obtained. We additionally obtained further observations on the night of November 5. The analysis of the data for GRB

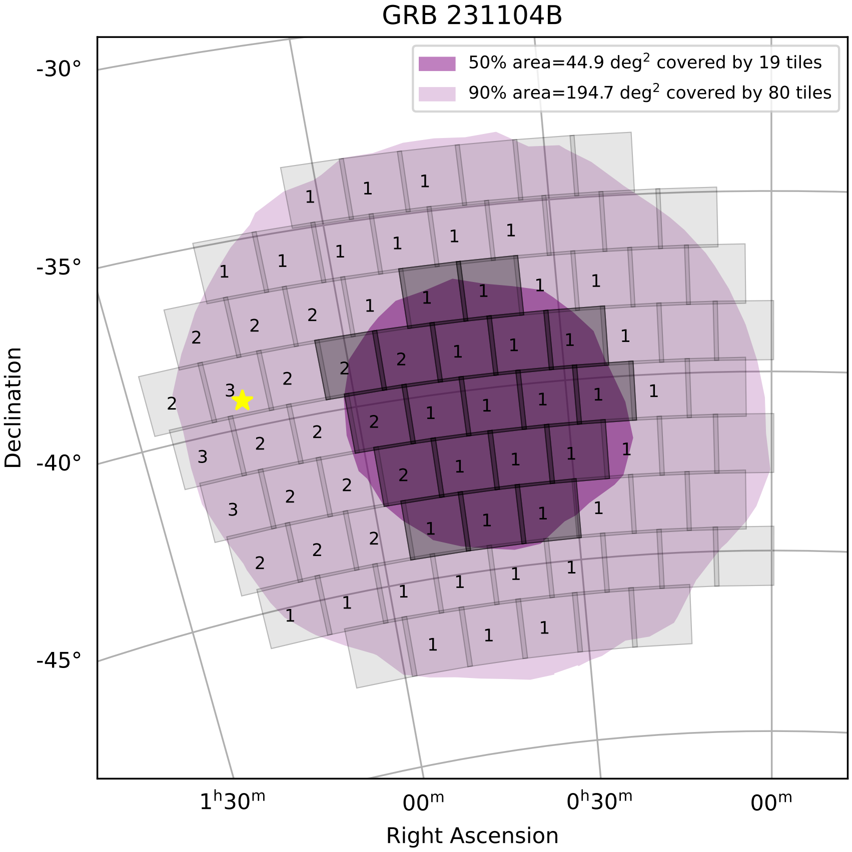

Figure 2.18: GRB 231104B skymap. The numbers within each tile indicate the number of observations obtained of each field. We show the position of the promising afterglow candidate.

231104B was delayed until after our programme had ended. As a result, no GCN Circular was submitted for this burst. In the delayed analysis of our data, we identified a single promising afterglow candidate at (RA,Dec) = (18.80407, -39.26300). The candidate was detected 6 times - 3 times on the first night and 3 times on the second night - and showed evidence of fading from $q = 18.75$ to $q = 19.10$ between the two nights. Additionally, no underlying counterpart was found in deep Legacy Survey imaging at the candidate's position. Due to the unfortunate delay in analysing the data, the veracity of this candidate could not be confirmed.

2.A.28 GRB 231118A

Fermi/GBM and *Swift*/BAT were triggered by GRB 231118A on 2023 November 18 at 17:16:29 and 17:16:33 UT, respectively (Fermi GBM Team 2023e; Laha et al. 2023). MeerLICHT began observing the BAT error box 1.7 hours post-trigger at 18:58:24 UT following the usual filter sequence for *Swift* triggers. We obtained a total of 95 × 60 s exposures before observations ended. An optical afterglow was reported soon after the GRB trigger by the 0.4 m Skynet optical telescope, which began observing 3 minutes after the trigger and detected a source with a brightness of $R = 14.8$ mag in their first exposure (Dutton et al. 2023). We detected the optical afterglow at a position consistent with the Skynet detection with a brightness of $q = 17.65 \pm 0.05$ mag in our first exposure (see Figure 2.19). Our high cadence q-band observations showed a power-law decline with temporal decay rate of -1.63 ± 0.03. We reported our results to the GCN (de Wet et al. 2023a). Other optical detections were also reported by MASTER (Lipunov et al. 2023) and

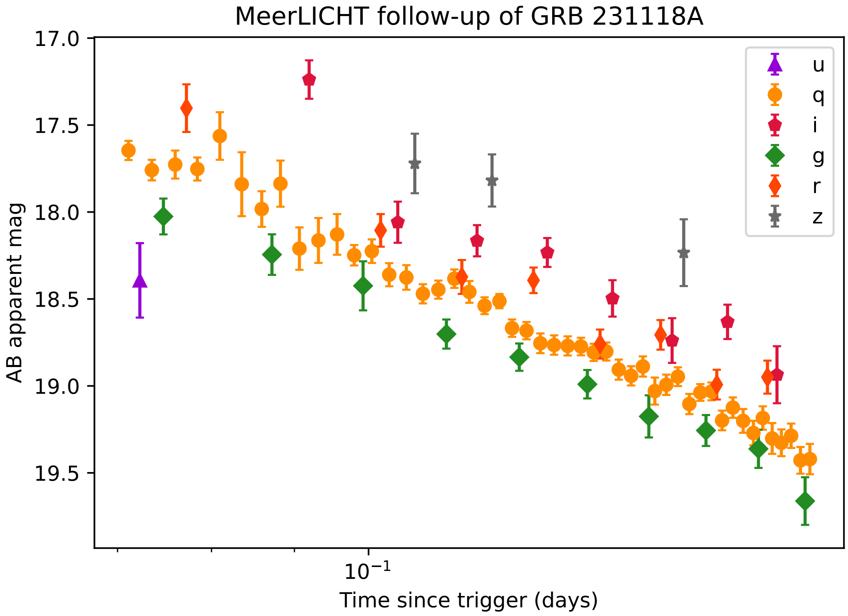

Figure 2.19: Optical detections of GRB 231118A with MeerLICHT. We only show 5σ detections. These are listed in Table 2.6 .

LCOGT (Strausbaugh & Cucchiara 2023; Shrestha et al. 2023). The burst was also detected by AstroSat (Navaneeth et al. 2023b).

2.A.29 GRB 231210B

Swift/BAT triggered on GRB 231210B at 21:29:04 UT on 2023 December 10, with the initial *Swift* GCN Circular indicating that the burst had a duration of about 15 s (Page et al. 2023b). MeerLICHT was automatically triggered and began observations at 21:32:26, only 202 s after the *Swift* trigger. Our first q-band image showed a new optical transient with a brightness of $q = 17.15 \pm 0.02$ mag within the XRT error circle (de Wet et al. 2023c). We obtained a total of 74 × 60 s exposures over following the usual filter sequence for *Swift* triggers. The q-band light curve showed a power-law decline with a temporal index of -1.20 ± 0.01. The optical afterglow was also observed by MASTER and LCOGT (Buckley et al. 2023; Pérez-Fournon et al. 2023), while spectroscopic observations with X-Shooter on the VLT secured the burst redshift to $z = 3.13$ (Saccardi et al. 2023). A radio non-detection with ATCA at 1.5 days was reported from observations at 5.5 and 9 GHz (Rhodes et al. 2023).

2.B Light curve photometry

Table 2.6: Light curve photometry

Time (days)	Filter	Magnitude	Uncertainty
		GRB 210610A	
0.0730	q	19.65	0.09
0.0750	q	19.41	0.07
0.0760	g	20.15	0.21
0.0771	q	19.47	0.07
0.0781	r	19.09	0.11

Table 2.6: Continued.

Time (days)	Filter	Magnitude	Uncertainty
0.0792	q	19.48	0.07
0.0802	i	18.76	0.12
0.0812	q	19.54	0.08
0.0823	z	18.41	0.20
0.0833	q	19.56	0.07
0.0854	q	19.65	0.09
0.0864	g	20.17	0.19
0.0875	q	19.56	0.07
0.0885	r	19.30	0.11
0.0896	q	19.78	0.11
0.0906	i	19.20	0.16
0.0917	q	19.60	0.08
0.0937	q	19.51	0.08
0.0958	q	19.73	0.09
0.0969	g	20.31	0.21
0.0979	q	19.83	0.11
0.0989	r	19.30	0.11
0.1000	q	19.88	0.11
0.1010	i	19.34	0.18
0.1020	q	19.81	0.10
0.1041	q	19.98	0.11
0.1061	q	19.71	0.09
0.1082	q	20.02	0.11
0.1092	r	19.78	0.20
0.1103	q	19.89	0.09
0.1113	i	19.09	0.14
0.1124	q	20.02	0.10
0.1145	q	19.94	0.09
0.1166	q	20.00	0.10
0.1187	q	20.10	0.11
0.1197	r	19.61	0.15
0.1207	q	19.95	0.09
0.1218	i	19.31	0.20
0.1228	q	20.14	0.10
0.1249	q	20.08	0.11
0.1269	q	20.07	0.10
0.1290	q	19.85	0.09
0.1301	r	19.84	0.19
0.1311	q	20.11	0.10
0.1332	q	20.14	0.12
0.1352	q	20.19	0.11
0.1373	q	20.25	0.15
0.1394	q	20.00	0.11
0.1404	r	19.87	0.17
0.1414	q	20.21	0.16
0.1425	i	19.52	0.21
0.1435	q	20.20	0.12
0.1456	q	20.31	0.16

Table 2.6: Continued.

Time (days)	Filter	Magnitude	Uncertainty
0.1476	q	20.16	0.12
0.1487	g	20.31	0.19
0.1497	q	20.24	0.15
0.1508	r	19.79	0.16
0.1518	q	20.38	0.17
0.1539	q	20.24	0.15
0.1560	q	20.28	0.16
0.1581	q	20.00	0.10
0.1602	q	20.36	0.13
0.1622	q	20.48	0.17
0.1643	q	20.58	0.16
0.1664	q	20.39	0.14
0.1684	q	20.18	0.11
0.1705	q	20.32	0.14
0.1726	q	20.33	0.13
0.1746	q	20.58	0.16
0.1767	q	20.43	0.13
0.1788	q	20.34	0.13
0.1808	q	20.09	0.11
0.1819	r	19.84	0.21
0.1829	q	20.42	0.14
0.1850	q	20.23	0.13
0.1871	q	20.48	0.16
0.1912	q	20.79	0.21
0.1923	r	19.84	0.17
0.1933	q	20.28	0.16
0.1954	q	20.38	0.15
0.1975	q	20.53	0.18
0.1995	q	20.54	0.17
0.2016	q	20.32	0.16
0.2027	r	19.86	0.17
0.2037	q	20.31	0.16
0.2058	q	20.44	0.18
0.2100	q	20.18	0.13
0.2120	q	20.63	0.19
0.2141	q	20.56	0.16
0.2162	q	20.42	0.16
0.2183	q	20.76	0.21
0.2203	q	20.73	0.19
0.2224	q	20.55	0.16
0.2286	q	20.45	0.18
0.2307	q	20.62	0.21
0.2328	q	20.41	0.17
0.2370	q	20.48	0.18
0.2411	q	20.45	0.19
GRB 210610B			
0.0482	q	17.27	0.02
0.0492	u	17.43	0.07

Table 2.6: Continued.

Time (days)	Filter	Magnitude	Uncertainty
0.0503	q	17.28	0.02
0.0514	g	17.41	0.03
0.0525	q	17.33	0.02
0.0545	q	17.36	0.02
0.0555	i	17.15	0.03
0.0566	q	17.43	0.02
0.0576	z	17.13	0.07
0.0587	q	17.39	0.02
0.0597	u	17.60	0.07
0.0608	q	17.46	0.02
0.0618	g	17.58	0.03
0.0629	q	17.48	0.02
0.0639	r	17.39	0.03
0.0649	q	17.53	0.04
0.0660	i	17.27	0.05
0.0670	q	17.52	0.05
0.0681	z	17.16	0.07
0.0691	q	17.52	0.02
0.0702	u	17.80	0.08
0.0712	q	17.52	0.02
0.0723	g	17.65	0.03
0.0744	r	17.43	0.03
0.0754	q	17.58	0.02
0.0764	i	17.41	0.04
0.0775	q	17.56	0.02
0.0785	z	17.33	0.07
0.0796	q	17.58	0.02
GRB 210702A			
0.0113	q	12.82	0.02
0.0125	u	13.59	0.04
0.0137	q	13.06	0.02
0.0150	g	13.39	0.02
0.0162	q	13.26	0.02
0.0174	r	13.20	0.01
0.0187	q	13.46	0.02
0.0198	i	13.10	0.03
0.0211	q	13.62	0.02
0.0224	z	13.11	0.03
0.0237	q	13.79	0.02
0.0249	u	14.48	0.07
0.0261	q	13.94	0.03
0.0274	g	14.25	0.04
0.0286	q	14.06	0.06
GRB 231118A			
0.0711	q	17.65	0.06
0.0723	u	18.39	0.21
0.0735	q	17.76	0.06
0.0747	g	18.03	0.10

Table 2.6: Continued.

Time (days)	Filter	Magnitude	Uncertainty
0.0760	q	17.73	0.08
0.0772	r	17.40	0.14
0.0784	q	17.75	0.07
0.0810	q	17.56	0.14
0.0835	q	17.84	0.18
0.0859	q	17.98	0.10
0.0872	g	18.24	0.12
0.0882	q	17.84	0.13
0.0906	q	18.21	0.12
0.0919	i	17.24	0.11
0.0931	q	18.16	0.13
0.0956	q	18.13	0.12
0.0980	q	18.25	0.06
0.0992	g	18.42	0.14
0.1005	q	18.23	0.07
0.1017	r	18.11	0.09
0.1030	q	18.36	0.07
0.1042	i	18.06	0.12
0.1055	q	18.38	0.07
0.1068	z	17.72	0.17
0.1080	q	18.47	0.06
0.1104	q	18.45	0.05
0.1117	g	18.70	0.08
0.1130	q	18.38	0.05
0.1142	r	18.37	0.10
0.1154	q	18.46	0.06
0.1167	i	18.17	0.09
0.1179	q	18.54	0.05
0.1192	z	17.82	0.15
0.1204	q	18.51	0.04
0.1226	q	18.67	0.05
0.1239	g	18.83	0.08
0.1252	q	18.68	0.05
0.1264	r	18.39	0.07
0.1277	q	18.75	0.06
0.1289	i	18.23	0.08
0.1302	q	18.77	0.06
0.1327	q	18.77	0.06
0.1352	q	18.77	0.05
0.1365	g	18.99	0.08
0.1377	q	18.81	0.05
0.1390	r	18.76	0.08
0.1402	q	18.80	0.05
0.1414	i	18.50	0.10
0.1427	q	18.91	0.06
0.1452	q	18.94	0.06
0.1477	q	18.89	0.06
0.1489	g	19.18	0.12

Table 2.6: Continued.

Time (days)	Filter	Magnitude	Uncertainty
0.1502	q	19.03	0.08
0.1514	r	18.71	0.09
0.1527	q	18.99	0.06
0.1539	i	18.74	0.13
0.1552	q	18.95	0.05
0.1565	z	18.23	0.19
0.1577	q	19.10	0.06
0.1602	q	19.04	0.05
0.1615	g	19.26	0.09
0.1628	q	19.03	0.05
0.1640	r	18.99	0.09
0.1652	q	19.20	0.06
0.1665	i	18.63	0.10
0.1678	q	19.12	0.06
0.1703	q	19.20	0.07
0.1728	q	19.27	0.07
0.1740	g	19.36	0.11
0.1751	q	19.18	0.07
0.1763	r	18.95	0.09
0.1774	q	19.30	0.09
0.1787	i	18.94	0.16
0.1798	q	19.33	0.08
0.1823	q	19.29	0.07
0.1847	q	19.43	0.08
0.1859	g	19.66	0.14
0.1872	q	19.42	0.09
GRB 231210B			
0.0027	q	17.15	0.02
0.0037	u	19.67	0.20
0.0047	q	17.84	0.02
0.0057	g	18.69	0.04
0.0067	q	18.27	0.02
0.0077	r	18.11	0.03
0.0087	q	18.54	0.03
0.0098	i	18.15	0.05
0.0108	q	18.80	0.03
0.0118	z	18.30	0.11
0.0129	q	19.17	0.04
0.0148	q	19.35	0.05
0.0158	g	20.19	0.12
0.0169	q	19.41	0.05
0.0179	r	19.18	0.07
0.0189	q	19.69	0.06
0.0199	i	19.42	0.12
0.0210	q	19.99	0.07
0.0230	q	20.01	0.07
0.0250	q	20.04	0.07
0.0271	q	20.20	0.08

Table 2.6: Continued.

Time (days)	Filter	Magnitude	Uncertainty
0.0281	r	19.93	0.12
0.0291	q	20.25	0.09
0.0302	i	19.65	0.14
0.0312	q	20.32	0.09
0.0332	q	20.68	0.12
0.0353	q	20.52	0.10
0.0373	q	20.42	0.10
0.0384	r	20.29	0.16
0.0394	q	20.72	0.12
0.0404	i	19.73	0.14
0.0414	q	20.75	0.13
0.0435	q	20.83	0.14
0.0455	q	20.94	0.15
0.0476	q	20.83	0.14
0.0486	r	20.54	0.20
0.0496	q	20.95	0.15
0.0517	q	20.77	0.13
0.0537	q	20.73	0.13
0.0558	q	20.96	0.16
0.0578	q	21.01	0.16
0.0598	q	21.00	0.17
0.0618	q	20.98	0.16

Notes. All times are relative to the *Swift*/BAT trigger time for the relevant GRB. Magnitudes are in the AB system, at the 5σ level.

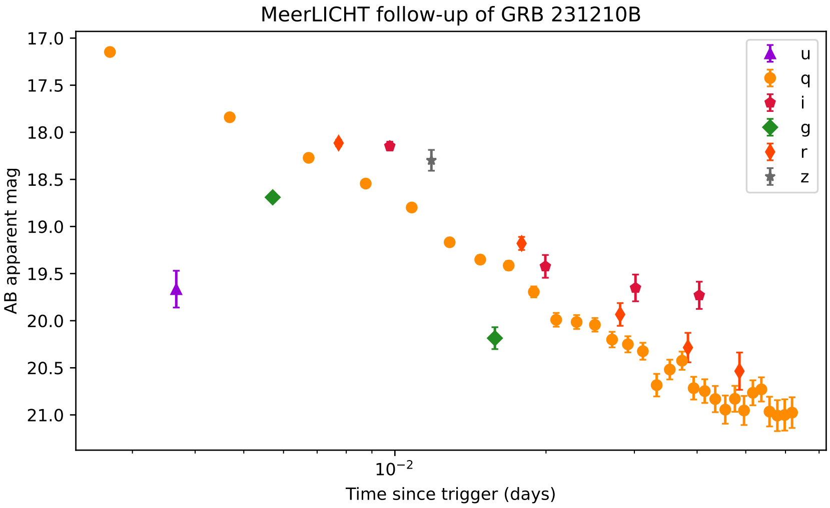

Figure 2.20: Optical detections of GRB 231210B with MeerLICHT. We only show 5σ detections. These are listed in Table 2.6 .

Chapter 3

The triple-peaked afterglow of GRB 210731A from X-ray to radio frequencies

S. de Wet[1], T. Laskar[2,3], P.J. Groot[1,3,4], F. Cavallaro[1,5], A. Nicuesa Guelbenzu[6], S. Chastain[7], L. Izzo[8], A. Levan[3], D.B. Malesani[3,9,10], I.M. Monageng[1,4], A.J. van der Horst[7], W. Zheng[11], S. Bloemen[3], A.V. Filippenko[11], D.A. Kann[12], S. Klose[6], D.L.A. Pieterse[3], A. Rau[13], P.M. Vreeswijk[3], P. Woudt[1], Z.-P. Zhu[14]

Based on the paper published in Astronomy & Astrophysics, Volume 671, A116, March 2023

---

[1] Inter-University Institute for Data Intensive Astronomy & Department of Astronomy, University of Cape Town, Private Bag X3, Rondebosch, 7701, South Africa
[2] Department of Physics & Astronomy, University of Utah, Salt Lake City, UT 84112, USA
[3] Department of Astrophysics/IMAPP, Radboud University, P.O. Box 9010, 6500 GL, Nijmegen, The Netherlands
[4] South African Astronomical Observatory, P.O. Box 9, 7935, Observatory, South Africa
[5] INAF-Osservatorio Astrofisico di Catania, Via S. Sofia 78, I-95123 Catania, Italy
[6] Thüringer Landessternwarte Tautenburg, Sternwarte 5, 07778 Tautenburg, Germany
[7] Department of Physics, The George Washington University, 725 21st Street NW, Washington, DC 20052, USA
[8] DARK, Niels Bohr Institute, University of Copenhagen, Jagtvej 128, 2200 Copenhagen, Denmark
[9] Cosmic Dawn Center (DAWN), Denmark
[10] Niels Bohr Institute, University of Copenhagen, Rådmandsgade 62-64, 2200, Copenhagen N, Denmark
[11] Department of Astronomy, University of California, Berkeley, CA 94720-3411, USA
[12] Hessian Research Cluster ELEMENTS, Giersch Science Center, Max-von-Laue-Strasse 12, Goethe University Frankfurt, Campus Riedberg, 60438 Frankfurt am Main, Germany
[13] Max-Planck-Institut für Extraterrestrische Physik, Giessenbachstraße, 85748 Garching, Germany
[14] Department of Astronomy, School of Physics, Huazhong University of Science and Technology, Wuhan, 430074, China

Abstract

GRB 210731A was a long-duration ($T_{90} = 22.5$ s) gamma-ray burst discovered by the Burst Alert Telescope (BAT) aboard the *Neil Gehrels Swift* observatory. *Swift* triggered the wide-field, robotic MeerLICHT optical telescope in Sutherland; it began observing the BAT error circle 286 seconds after the *Swift* trigger and discovered the optical afterglow of GRB 210731A in its first 60-second q-band exposure. Multi-colour observations of the afterglow with MeerLICHT revealed a light curve that showed three peaks of similar brightness within the first four hours. The unusual optical evolution prompted multi-wavelength follow-up observations that spanned from X-ray to radio frequencies. We present the results of our follow-up campaign and interpret our observations in the framework of the synchrotron forward shock model. We performed temporal and spectral fits to determine the spectral regime and external medium density profile, and performed detailed multi-wavelength theoretical modelling of the afterglow following the last optical peak at ~0.2 days to determine the intrinsic blast wave parameters. We find a preference for a stellar wind

density profile consistent with a massive star origin, while our theoretical modelling results in fairly typical shock microphysics parameters. Based on the energy released in γ rays and the kinetic energy in the blast wave, we determine a low radiative efficiency of $\eta \approx 0.02$. The first peak in the optical light curve is likely the onset of the afterglow. We find that energy injection into the forward shock offers the simplest explanation for the subsequent light curve evolution, and that the blast wave kinetic energy increasing by a factor of ∼1000 from the first peak to the last peak is indicative of substantial energy injection. Our highest-likelihood theoretical model over-predicts the 1.4 GHz flux by a factor of approximately three with respect to our upper limits, possibly implying a population of thermal electrons within the shocked region.

3.1 Introduction

Gamma-ray bursts (GRBs) are the most energetic explosions in the Universe, with isotropic γ-ray energies of up to $\sim 10^{55}$ erg (Kumar & Zhang 2015). Long-duration bursts are typically associated with the core collapse of massive stars (Colgate 1968; Woosley 1993; van Paradijs et al. 1997; Galama et al. 1998a; Woosley & Bloom 2006), where the compact object remnant acts as a central engine powering a collimated relativistic jet. In the fireball shock model (Rees & Meszaros 1992; Meszaros & Rees 1993; Mészáros & Rees 1997; Sari et al. 1998), internal shocks within the expanding ejecta are the source of the prompt γ-ray emission and the interaction of the relativistic outflow with the circumburst medium (the external forward shock) is the source of the afterglow emission.

Prior to the launch of the *Neil Gehrels Swift* Observatory (Gehrels et al. 2004) in 2004, observations of afterglows showed broad agreement with the basic external shock model (Galama et al. 1998b; Panaitescu & Kumar 2001, 2002; Yost et al. 2003). Rapid X-ray and UV/optical follow-up of GRB triggers with *Swift* have revealed rich features in early-time X-ray and optical light curves that challenge the standard theory. Similar to the 'canonical' X-ray light curve (Zhang et al. 2006; Nousek et al. 2006), optical light curves have been decomposed into a number of distinct components that arise from different emission sites and physical mechanisms (see the synthetic light curve in Li et al. 2012). In addition to the normal and jet break decay segments explained by the standard forward shock model, onset bumps, steep decay segments, flares, and late-time re-brightenings have been observed in optical afterglows. Early onset bumps with a smooth transition to the normal decay segment are regarded as the onset of afterglow and were predicted within the standard theory (Sari & Piran 1999; Kobayashi & Zhang 2007); steep decay segments early on (some with an additional steep rise) have been attributed to reverse shock emission (Mészáros & Rees 1997; Sari & Piran 1999; Zhang et al. 2003; Yi et al. 2020); similar to X-ray light curves, shallow decay and plateau segments and flares have been observed in a number of bursts (Mangano et al. 2007; Greiner et al. 2009; Swenson et al. 2013); late-time re-brightenings have also been observed in some optical afterglows (Nardini et al. 2011; Liang et al. 2013), with a few having rarer simultaneous X-ray re-brightenings (e.g. GRB 120326A; Melandri et al. 2014; Urata et al. 2014; Hou et al. 2014; Laskar et al. 2015). Furthermore, small-scale bumps and wiggles have been seen superposed over the larger-scale light curve features (e.g. GRBs 021004 and 030329; Holland et al. 2003; Lipkin et al. 2004). Proposed explanations for these additional features include inhomogeneities in the circumburst medium, multiple-component jets, structured jets, varying microphysical parameters, and energy injection into the forward shock (Lazzati et al. 2002; Dai & Wu 2003; Mundell et al. 2007; Racusin et al. 2008; Filgas et al. 2011; Mészáros et al. 1998; Zhang & Mészáros 2002a; Rossi et al. 2002; Ioka et al. 2006; Fan & Piran 2006; Granot et al. 2006; Sari & Mészáros 2000; Zhang & Mészáros 2002b; Björnsson et al. 2004; Laskar et al. 2015; Lin et al. 2018).

Here we report on multi-wavelength observations of the long-duration gamma-ray burst GRB 210731A discovered by *Swift* (Gehrels et al. 2004). Our early-time MeerLICHT optical observations show a complex light curve evolution with an initial smooth bump followed by two further re-brightenings. We combine our observations with X-ray and radio data that span 200 seconds to 118 days post-trigger and interpret our observations in the traditional synchrotron forward shock framework. We investigate the nature of the early optical light curve evolution.

We adopt a Λ cold dark matter cosmology with $\Omega_m = 0.31$, $\Omega_\Lambda = 0.69$, and $H_0 = 68$ km s^{-1} Mpc^{-1} (Planck Collaboration et al. 2016). All reported magnitudes are in the AB magnitude system unless stated otherwise, and errors are reported at the 1σ level.

3.2 Observations

3.2.1 Prompt gamma-ray emission

The *Swift* Burst Alert Telescope (BAT; Barthelmy et al. 2005) was triggered by GRB 210731A at 22:21:08 UT on 2021 July 31, with the mask-weighted 15–350 keV light curve showing a single-pulse structure of duration $T_{90} = 22.5 \pm 2.8$ s (Stamatikos et al. 2021), making GRB 210731A a long-duration GRB under the traditional > 2 s duration limit. GRB 210731A triggered the *Fermi* Gamma-ray Burst Monitor (GBM; Meegan et al. 2009; Lesage et al. 2021) one second earlier than *Swift*/BAT, with the 10-1000 keV light curve showing a single pulse with duration[1] $T_{90} = 25.9 \pm 5.3$ s, in agreement with the BAT duration. The time-averaged spectra for both BAT and GBM were best-fitted with a power law function and exponential high-energy cutoff with photon indices of -0.25 ± 0.59 and -0.1 ± 0.1, and cutoff energies of (107 ± 27) keV and (175 ± 11) keV, respectively (Stamatikos et al. 2021; Lesage et al. 2021). The 10-1000 keV GBM fluence[2] integrated over the burst duration was $(3.05 \pm 0.06) \times 10^{-6}$ erg cm^{-2}. Using a measured afterglow redshift of $z = 1.2525$ obtained by X-Shooter on the Very Large Telescope at 1.19 days post-trigger (Kann et al. 2021), this corresponds to an isotropic-equivalent γ-ray energy of $E_{\gamma,\mathrm{iso}} = (1.29 \pm 0.03) \times 10^{52}$ erg.

We take the *Swift*/BAT trigger time as T_0 for this burst and reference all future times with respect to this T_0.

3.2.2 X-ray observations

The *Swift* X-Ray Telescope (XRT; Burrows et al. 2005) started observing the field of GRB 210731A 201 seconds post-trigger, finding a bright new X-ray source consistent with the BAT position (Troja et al. 2021). The initial 62 seconds of data were obtained in windowed timing (WT) mode after which *Swift* had to slew away. Data capture recommenced in photon counting (PC) mode at 3.3 hours post-trigger. We obtained the X-ray light curve and spectra from the online Swift-XRT GRB Catalogue[3] (Evans et al. 2007, 2009). The Burst Analyser (Evans et al. 2010) count-rate light curve showed that the X-ray flux was decreasing rapidly during the WT-mode observations with a spectrum that hardened from a photon index of $\Gamma_\mathrm{X} = 3.2$ to 2.2 over 60 seconds. Once data capture resumed in PC mode at 10 ks, the X-ray light curve was in a shallow decay phase before declining more steeply at $\sim$20 ks post-trigger.

We fitted the PC-mode spectrum with a photoelectrically absorbed power-law model (`tbabs*ztbabs*pow`) in Xspec version 12.12.0, fixing the source redshift at 1.2525 and Galactic hydrogen column density at $N_\mathrm{H}^\mathrm{Gal} = 1.15 \times 10^{21}$ cm^{-2} for consistency with the online fit. The fitted spectrum was characterised by a photon index of $\Gamma = 2.00^{+0.11}_{-0.11}$ with a host galaxy column density of $N_\mathrm{H}^\mathrm{host} = 2.46^{+1.99}_{-1.56} \times 10^{21}$ cm^{-2} and C-stat 182.1 for 213 degrees of freedom. There were insufficient photons in the PC-mode light curve for time-resolved analysis and to test for spectral evolution. We converted the PC-mode count-rate light curve to a 1 keV flux density light curve using the spectral index from our PC-mode spectral fit of $\beta_\mathrm{X} \equiv 1 - \Gamma_\mathrm{X} \approx -1.00$ and the online unabsorbed count-to-flux conversion factor of 4.36×10^{-11} erg cm^{-2} ct^{-1}. We performed a similar

---

[1] Obtained from the online Fermi GBM Burst Catalog (von Kienlin et al. 2020).

[2] See footnote 1.

[3] The Burst Analyser for GRB 210731A is available on the UK Swift Data Science Centre website.

procedure for the WT-mode data using the spectral parameters in the automated fit on the *Swift* website, with a photon index of 3.07 and unabsorbed count-to-flux conversion factor of 4.69×10^{-11} erg cm^{-2} ct^{-1}.

3.2.3 Optical/near-infrared observations

The fully robotic, 60 cm MeerLICHT optical telescope (Bloemen et al. 2016) was automatically triggered by *Swift*/BAT and began observing the field of GRB 210731A 286 seconds after the BAT trigger, taking 60 second exposures in the u, g, r, i, z, and q optical bands (where the q band is roughly equivalent to $g+r$), following the sequence $quqgqrqiqz$ in order to obtain high cadence coverage in the wider and more sensitive q band with quasi-simultaneous multi-colour coverage of the evolving afterglow. Comparison of the first q-band image with an existing MeerLICHT reference image revealed a new transient candidate at $\alpha = 20^{\rm h}01^{\rm m}13.19^{\rm s}$, $\delta = -28^{\rm d}03^{\rm m}40.10^{\rm s}$ (J2000). This position was $0.3''$ away from the refined XRT position (D'Ai et al. 2021), confirming the new source as the optical afterglow of GRB 210731A (de Wet et al. 2021). These observations continued until the target set, approximately 4.29 hours post-trigger. Four cycles of the same filter sequence were obtained the following night in two time intervals separated by ∼2 hours. Since the afterglow was by this point in a declining phase and below the 60 second single-exposure detection limit, repeated q-band exposures were taken on the nights of 2021 August 2 and 3 in order to track the optical light curve. The MeerLICHT pipeline (Vreeswijk et al., in prep) was used to perform standard charge-coupled device (CCD) reduction tasks as well as astrometry and point-spread function (PSF) photometry, producing a catalogue file containing all 5σ source detections for each image. For images where the afterglow was fainter than 5σ above the background we used forced photometry to obtain magnitudes that were at least at the 3σ level. Images from the night of 2021 August 1 onwards were co-added to produce more significant detections or deeper upper limits.

The *Swift* UltraViolet and Optical Telescope (UVOT; Roming et al. 2005) took a single 61.7 second exposure in the *white* filter beginning 210.4 seconds after the BAT trigger but did not continue observing the field of the GRB until 3.27 hours after the trigger, whereafter it was observed with multiple filters intermittently over the next five days (Troja et al. 2021; Kuin et al. 2021). We performed aperture photometry on the *Swift*/UVOT data using standard analysis tools from the HEASoft (Nasa High Energy Astrophysics Science Archive Research Center (Heasarc) 2014) *Swift* FTOOLS software package (version 6.29c[4]). We extracted magnitudes using the tool `uvotsource` with a $3.5''$ radius aperture centred on the afterglow position, and a nearby background aperture with a $10''$ radius. A total of 64 individual exposures in all seven UVOT filters were taken over the course of the follow-up campaign. We co-added exposures in the same filter with clear detections but taken close to each other temporally using `uvotimsum` in order to produce more significant detections, and once the afterglow became too faint to detect in individual exposures we co-added images within wider time baselines in order to provide the deepest limiting magnitudes.

The afterglow of GRB 210731A was observed simultaneously in the $g'r'i'z'JHK$ bands with the Gamma-Ray Burst Optical Near-Infrared Detector (GROND; Greiner et al. 2008) mounted at the 2.2 m MPG telescope at the European Southern Observatory (ESO) La Silla Observatory in Chile. The afterglow was clearly detected in all bands in the first epoch of observations taken 4.2 hours after the GRB trigger (Nicuesa Guelbenzu et al. 2021a). A further three epochs were obtained at 1.225, 2.214, and 5.253 days post-trigger (Nicuesa Guelbenzu et al. 2021b). We also obtained deep host-galaxy observations at 285 days that yielded detections in the g' and r' bands, and which we regard as the host-galaxy flux. The multi-colour GROND data were analysed through standard PSF photometry using DAOPHOT (Stetson 1987) and ALLSTAR tasks of IRAF (Tody 1993), in a similar way to the procedure described in Krühler et al. (2008). The

---

[4] Available at https://heasarc.gsfc.nasa.gov/docs/software/lheasoft/

optical data were calibrated against the Pan-STARRS catalogue[5] (Chambers et al. 2016), while for the near-infrared (NIR) bands, photometric calibration was performed against the 2MASS catalogue (Skrutskie et al. 2006), resulting in a typical absolute accuracy of 0.04 mag in $g'r'i'z'$, 0.06 mag in JH and 0.08 mag in K.

The 76 cm Katzman Automatic Imaging Telescope located at the Lick Observatory (KAIT; Filippenko et al. 2001) obtained 20×60 second exposures in the *clear* band (similar to R; see Li et al. 2003), starting ∼9.04 hours after the BAT trigger (Zheng et al. 2021). All images were reduced and co-added using a custom pipeline (Ganeshalingam et al. 2010; Stahl et al. 2019), whereafter PSF photometry was performed on the co-added image using DAOPHOT. Several nearby stars were chosen from the Pan-STARRS1 catalogue for flux calibration, with their magnitudes transformed into Landolt magnitudes following Eq. 6 of Tonry et al. (2012). The optical afterglow of GRB 210731A was clearly detected in the co-added image.

Images in the SDSS g, r, and z filters were obtained at a single epoch 1.18 days post-trigger with the acquisition camera of the X-shooter spectrograph, mounted on the ESO Very Large Telescope (VLT) UT3 (Melipal). Reduction was carried out using standard procedures. For the z-band image, a fringe correction was applied, using a template fringe pattern provided by the observatory. We also observed the afterglow at two epochs in the r and z bands with the Nordic Optical Telescope (NOT) equipped with the ALFOSC imager. The images were reduced following standard procedures including subtraction of a master bias and correction with sky flats. Magnitudes were measured using aperture photometry, and photometric calibration was carried out against the Pan-STARRS catalogue.

We show all UV/optical/NIR photometry separated by instrument and filter in Fig. 3.1.

3.2.4 Radio observations

We obtained three epochs of radio continuum observations with the MeerKAT radio telescope (Jonas & MeerKAT Team 2016) in the L band (1.4 GHz) through director's discretionary time (DDT) proposal DDT-20120810-SD-01 (PI de Wet). Each observation had a total integration time on source of 0.78 hours, using J1939–6342 as the flux and bandpass calibrator and J1924–2914 as the gain calibrator. All data were reduced using the oxkat pipeline[6] (Heywood 2020). No radio afterglow was detected at 1.4 GHz across the three epochs at 10.8, 34.1 and 59.7 days post-trigger. The RMS noise was $\approx 14\ \mu$Jy at the 1σ-level in each image. We take upper limits on the afterglow flux as three times the RMS noise.

Radio continuum observations were also obtained with the *Karl G. Jansky* Very Large Array (JVLA; Perley et al. 2011) in the C and X bands (centred on 6 and 10 GHz) through DDT proposals 21B-333 and 21B-342 (PI de Wet) at four epochs spanning 18.2 to 118 days post-trigger. The total integration time per observation was 0.44 hours in each band, with 3C286 used as the flux and bandpass calibrator and J1924–2914 as the complex gain calibrator. We performed preliminary imaging on the pipeline-calibrated measurements sets using standard Common Astronomy Software Applications (CASA; McMullin et al. 2007) procedures and detected the radio afterglow to GRB 210731A in all four epochs at 10 GHz and in all but the first epoch at 6 GHz.

The first epoch National Radio Astronomy Observatory (NRAO) -calibrated measurement set failed to pass internal quality thresholds for science usability so we chose to calibrate manually from the raw data to obtain more accurate flux measurements. We used CASA version 5.8.0 and performed imaging with the task `tclean` and flux measurements with the task `imfit`. We obtained satisfactory results with our X-band calibration, but the C-band calibration contained persistent phase errors as a result of de-correlation problems during observing, and the measured flux of all sources in the field was substantially lower than in subsequent epochs. Despite these

---

[5] See http://archive.stsci.edu/panstarrs/search.php.

[6] See https://github.com/IanHeywood/oxkat/blob/master/README.md and references therein.

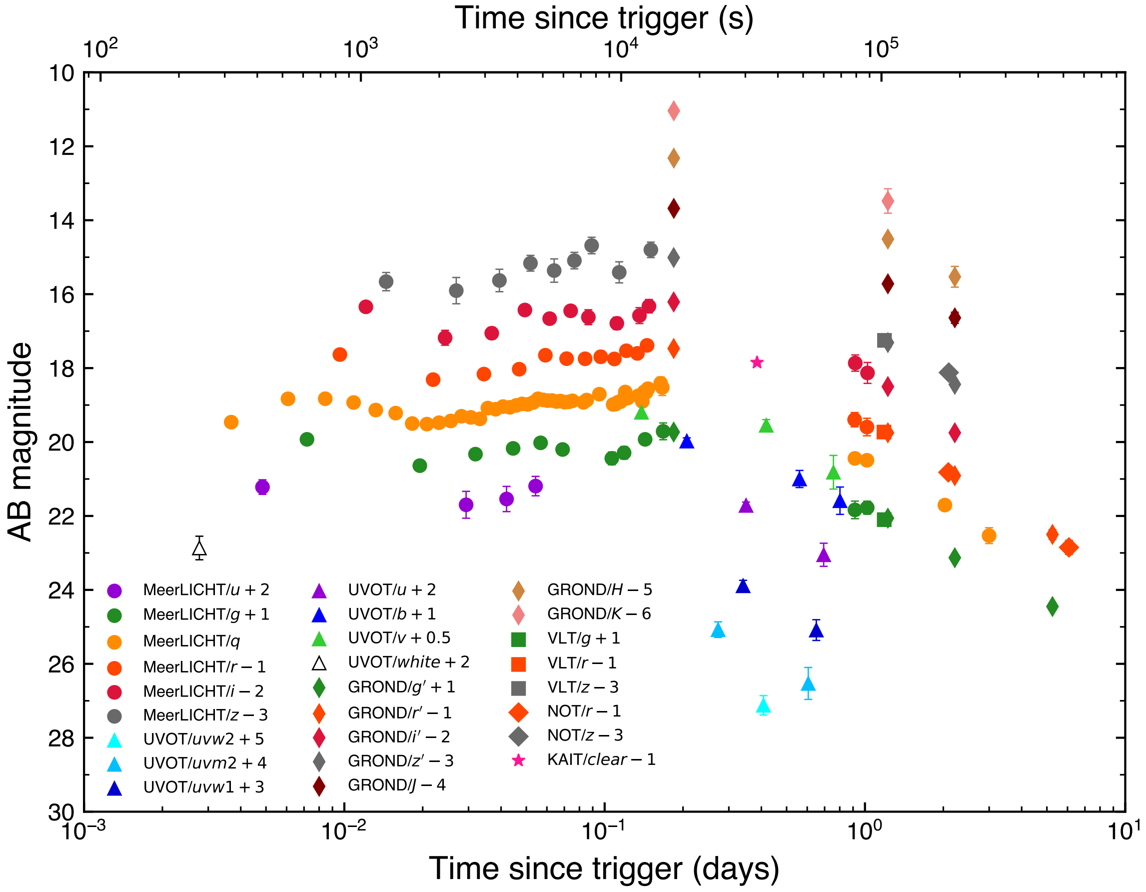

Figure 3.1: Combined UV/optical/NIR photometry of GRB 210731A. We only show detections where all magnitudes are in the AB system and have not been corrected for Galactic extinction. Times are relative to the *Swift*/BAT trigger time.

problems, imaging on the re-calibrated data showed a radio source at the afterglow position, in contrast with preliminary imaging. We therefore adopted the following approach to calculate the flux of the afterglow. We identified six point-like sources present at all four epochs in the C band and measured their fluxes. For each source a flux correction factor could then be calculated between the first epoch flux and the flux in each subsequent epoch. The correcting factors ranged from 1.2 to 2.2, with a mean value of 1.77 and standard deviation of 0.26. No obvious trends in the correcting factor were found as a function of source brightness or offset from the image centre across all epochs, so we took the mean correcting factor as the flux correcting factor to apply to the measured afterglow flux in the first epoch image. We incorporate the standard deviation of the correction factor as an additional source of systematic uncertainty in the flux measurement from the first epoch in the C band.

The third epoch X-band measurement set also had major phase issues, so we performed the same procedure as for the C-band first epoch data, calibrating the raw data and determining a mean flux correcting factor to apply to our afterglow measurement. Only two sources were used in determining the mean correcting factor as the X-band images had far fewer sources than the C-band images. The correcting factors ranged from 1.3 to 1.6, with a mean value of 1.47 and standard deviation of 0.1.

All X-ray, optical, and radio flux measurements associated with GRB 210731A are presented in Table 4.1.

3.3 Afterglow temporal and spectral analysis

We interpret our combined multi-wavelength data in the framework of synchrotron radiation emitted by electrons accelerated to a power-law distribution in energy behind the forward shock, with $N(\gamma) \propto \gamma^{-p}$ for $\gamma > \gamma_{\rm min}$, with $\gamma_{\rm min}$ being the minimum Lorentz factor of electrons in the distribution and p being the electron energy index, which we assume to be bounded between 2 and 3, though values of less than 2 have been suggested in the literature (Dai & Cheng 2001; Panaitescu & Kumar 2002). The synchrotron spectra are characterised by power-law segments that join at a number of break frequencies, namely the synchrotron self-absorption frequency ν_{sa}, the characteristic synchrotron frequency ν_m corresponding to emission from $\gamma_{\rm min}$ electrons, and the cooling frequency ν_c. The orderings of the spectral breaks depend on the hydrodynamic evolution of the forward shock, which is described by the Blandford & McKee (1976) spherical self-similar solution of an adiabatic relativistic blast wave expanding into a cold medium with a circumburst density profile varying as a power-law with radius: $n(r) = n_0 r^{-k}$. We consider two density profiles: the constant $k = 0$ case corresponding to an interstellar-medium-like density profile; and the $k = 2$ case corresponding to a stellar wind from a massive star progenitor. The synchrotron forward shock model is described in Sari et al. (1998), Chevalier & Li (2000), and Granot & Sari (2002), and we follow the convention $F_\nu(t) \propto t^\alpha \nu^\beta$ throughout.

3.3.1 Optical/X-ray temporal evolution

The most striking feature of our GRB 210731A dataset is the three peaks in our early-time optical data (see Fig. 3.1). To characterise this light curve further, we created a composite R-band light curve by combining our q-, r-, and R-band data since they are the most well-sampled optical bands and also have similar central wavelengths. We also included the KAIT *clear* flux measurement since it is calibrated to the R band. We used an optical spectral index of $\beta_{\rm opt} = -0.81 \pm 0.05$ derived from the first GROND epoch (see Sect. 3.3.2) to transform the data to an R-band central wavelength of 700 nm[7]. The composite R-band light curve (see Fig. 3.2) exhibits three distinct peaks occurring within the first 0.3 days of the GRB trigger, each with rising and decaying segments of varying steepness and smoothness. We investigate the nature of the optical peaks in

---

[7] For direct comparison with the sample in Li et al. (2012) and Liang et al. (2013).

Table 3.1: Parameters derived from fits to the composite R-band light curve and X-ray 1 keV light curve, as shown in Fig. 3.2. The R-band light curve was fitted with the sum of three BPLs, while the X-ray light curve was fitted with a single BPL.

	α_1	α_2	t_p (days)	χ^2/dof
Optical BPL 1	1.39 ± 0.36	-2.58 ± 0.75	0.0088 ± 0.0013	1.32
Optical BPL 2	1.19 ± 0.62	-5.16 ± 2.58	0.066 ± 0.007	-
Optical BPL 3	0.99 ± 0.16	-1.84 ± 0.04	0.27 ± 0.01	-
X-ray 1 keV BPL	0.44 ± 0.62	-1.69 ± 0.19	0.26 ± 0.09	0.39

Sect. 5.6. After the last peak at ∼0.2 days, the light curve entered a final declining phase until the last optical observation at 6.2 days post-trigger.

We follow two approaches to fit the data: first we fitted a single power-law to each rising and decaying segment[8] directly in order to get an indication of the steepness of each segment (we use these in Sect. 3.5.1); then we performed an empirical fit as in Li et al. (2012) by decomposing the light curve into separate components, each of which may arise from different emission sites or physical mechanisms. Since we have three clear peaks in our light curve, we employed a model that comprises the sum of three broken power-law (BPL) components (Beuermann et al. 1999; Price et al. 2001; Zeh et al. 2004), each characterised by a normalising flux level, F_0, rise and decay indices, α_1 and α_2, break time, t_b , and break smoothness, ω, according to

$$F(t) = F_0 \left[\left(\frac{t}{t_\mathrm{b}} \right)^{-\alpha_1 \omega} + \left(\frac{t}{t_\mathrm{b}} \right)^{-\alpha_2 \omega} \right]^{-1/\omega} . \tag{3.1}$$

If α_1 is positive and α_2 is negative, the light curve peaks at a time, t_p, between rising and decaying segments; $t_\mathrm{b} = t_\mathrm{p}$ in Eq. 5.1. We also include a constant term to account for the host-galaxy r'-band brightness of 24.7 ± 0.2 mag measured at 285 days by GROND. Considering values of 1, 3, 5 and 9 for ω, we find that a smoother break with a value of 1 produces a fit with a χ^2_r value closer to 1. To confirm whether the second, intermediate peak is statistically significant and not merely due to short time-scale variability, we perform the same fit but with two BPL components instead of three. This yields a χ^2_r value of 2.68, which is worse than the case with three BPL components which had $\chi^2_\mathrm{r} = 1.32$ (see Table 3.1). Performing an F-test to compare the two model fits, we find that the three BPL model results in a significantly better fit at a confidence level of greater than 99%. Our fit allows us to compare the temporal evolution in each optical band, which we do in Sect. 3.3.2.

Examining the X-ray light curve, the WT-mode data within the first 300 seconds shows a steep decline with $\alpha_\mathrm{X} = -3.52 \pm 0.36$ and a photon index that hardened from 3.2 to 2.2, as taken from the online Burst Analyser. The most likely explanation is high latitude prompt emission, as the temporal and spectral indices agree broadly with the $\alpha = -2 + \beta$ curvature effect relation (Kumar & Panaitescu 2000; Willingale et al. 2010). It is unfortunate that we have no X-ray data during the time of the first two optical peaks, rendering a direct comparison between the two bands unfeasible. There is, however, X-ray data from ∼0.13 days onwards starting when the optical light curve was rising to its final peak. The X-ray light curve started in a shallow decay or plateau phase before steepening, which coincided with the final decaying phase in the optical. We fit a BPL according to Eq. 5.1 to determine the break time and temporal slopes, fixing the break smoothness at 1, 3, 5, or 9. Each fit had a similar reduced χ^2_r value (∼0.4); therefore, we employed a break smoothness of $\omega = 1$ to match the value used in the optical fit, though this results in a pre-break index that is poorly constrained. The R-band and 1 keV light curves are presented in Fig. 3.2 along with their fits, and we present the results of the fits in Table 3.1.

---

[8] We determine the boundary between each segment by eye. These are shown as vertical dotted lines in Fig. 3.2.

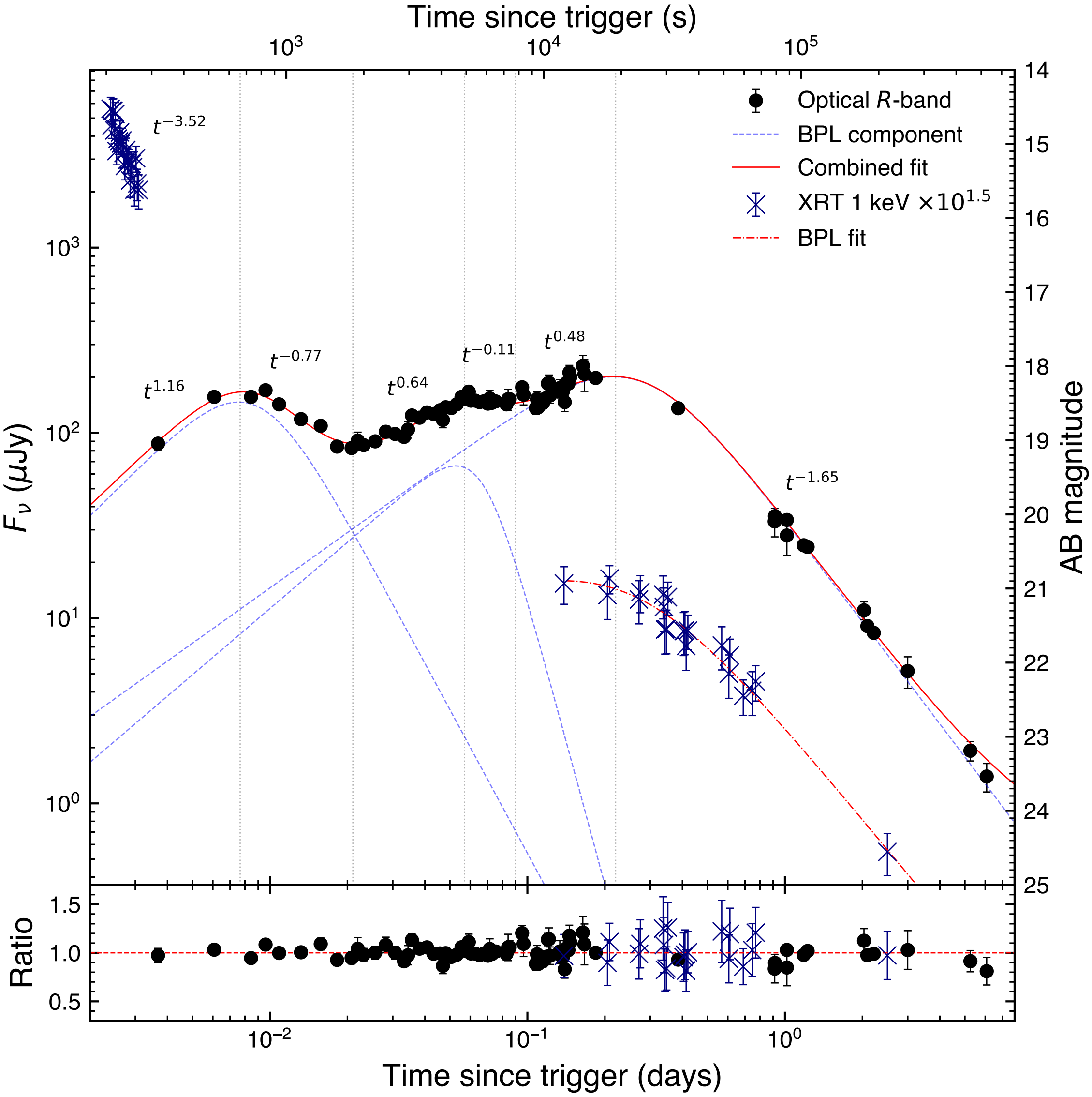

Figure 3.2: Composite R-band light curve and X-ray 1 keV light curve for GRB 210731A. For each rising and decaying segment of the optical light curve, we show the power-law slope (t^α) as an indicator of the steepness of the light curve between each pair of adjacent vertical dotted lines. We also show the fit comprising the sum of three BPL components and a constant term equal to the r'-band host galaxy flux measured by GROND at 285 days (solid red line), along with each individual BPL component (dashed blue lines). For the X-ray light curve, we indicate the steepness of the WT-mode segment and we show the BPL fit to the PC-mode data as a dashed-dotted red line. The results of the X-ray and optical fits are presented in Table 3.1. The ratio of observed flux to fitted flux is shown in the lower panel.

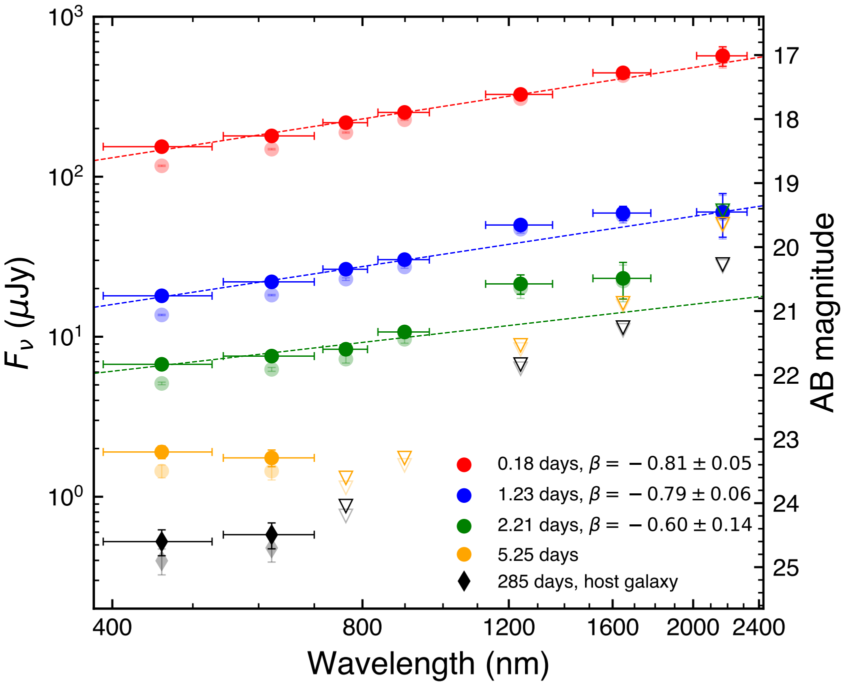

Figure 3.3: Power-law fits to the GROND optical/NIR data at three epochs, corrected for a Galactic extinction of $A_V = 0.24$ mag. The uncorrected magnitudes are shown in a lighter shade below each corrected data point. We also show the fourth epoch, which only had detections in the g' and r' bands, as well as the detections (shown as diamonds) and limits from deep observations of the host galaxy at 285 days. Upper limits are shown as upside-down triangles.

3.3.2 Achromatic optical/X-ray spectral evolution

We now investigate if there is evidence for spectral evolution in the optical data. In Fig. 3.3 we show the optical spectral energy distributions (SEDs) formed using data from the first three of five GROND epochs corrected for a Galactic extinction of $A_\mathrm{V} = 0.24$ mag in the direction of the GRB (Schlafly & Finkbeiner 2011). We fitted the data with power-laws in frequency, with the first epoch yielding a spectral index of $\beta_\mathrm{opt} = -0.81 \pm 0.05$. There does not appear to be substantial spectral evolution between the first two epochs at 0.184 and 1.225 days, particularly in the optical g', r', i', and z' bands. It is unclear why there is excess emission in the near infrared J, H, and K bands during the second and third epochs. A possible explanation is that there is contaminating emission from the host galaxy, in which case we would expect the light curves to flatten towards a constant value. The observed decline to below detection levels at 5.25 and 285 days appears to rule out this possibility. It could also be the case that there is an additional unaccounted-for source of systematic photometric error.

For our early-time data, we took our composite R-band light curve fit (Fig. 3.2) and fitted the flux in each of the optical bands with this model, which amounts to shifting the R-band fit light curve vertically until it fits the data in a given band. The spectral slope in the blue and UV bands (u through $uvw2$) was steeper than in the optical owing to Galactic extinction and damping by Lyα absorption at the redshift of the burst. We therefore shifted the MeerLICHT u-band data to the UVOT u band using an approximate spectral index of $\beta_\mathrm{UV} \approx -4$ measured from the UVOT/u, $uvw1$, $uvm1$, and $uvw2$ data. Figure 3.4 shows that the data in each of the UV and optical bands is reasonably well fitted by the R-band light curve. Deviations from the fit at earlier times (< 0.2 days) are visible in the u, g, i, and z bands but they do not appear

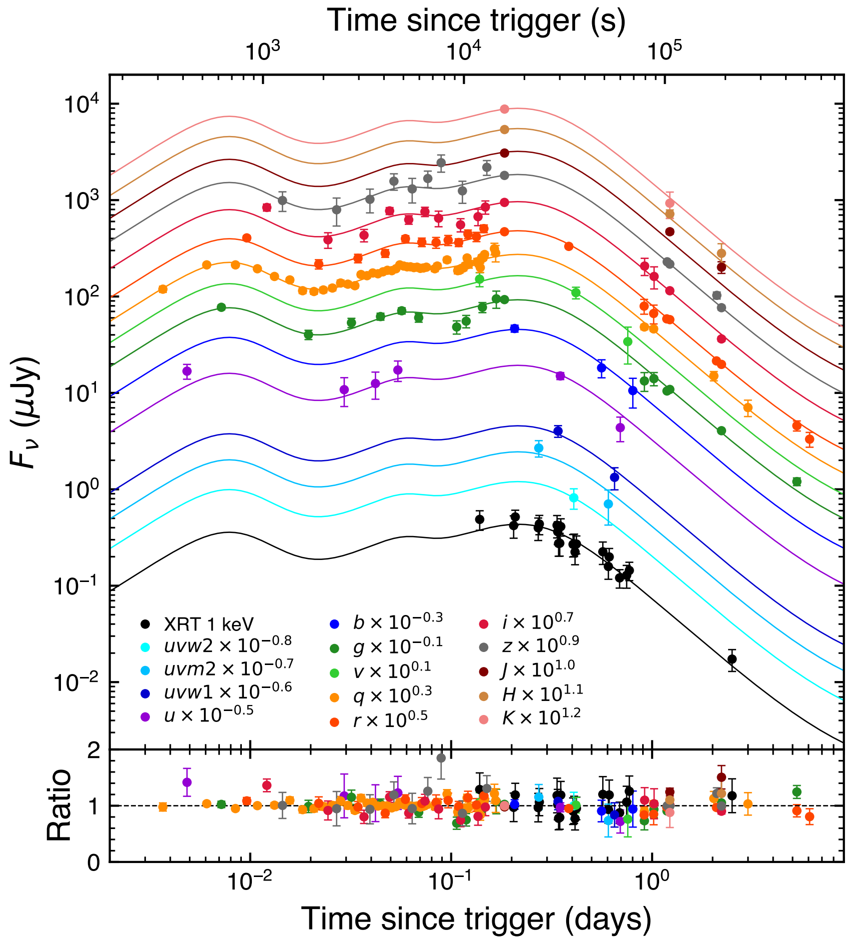

Figure 3.4: Fits to the data in each optical band using the best-fit model to the composite R-band light curve in Fig. 3.2. We also fitted this model to the X-ray PC-mode data. The lower panel presents the ratio of measured flux to model flux.

statistically significant - only 7.5% of the UV/optical/NIR data points deviate by 2σ or more from each model fit. Overall the optical evolution appears achromatic and consistent with a constant optical spectrum, which points towards a hydrodynamical rather than spectral origin to the complex early-time optical light curve.

As mentioned in Sect. 5.2.2, insufficient X-ray photons were collected during the PC-mode observations to create time-sliced spectra. The photon index from the online Burst Analyser was fairly constant during PC mode, however, with a mean value of $\Gamma_{\mathrm{X}} = 1.84 \pm 0.27$. This is indicative of insubstantial spectral evolution in the X-ray band during PC mode. The X-ray spectral index of $\beta_{\mathrm{X}} = -1.00 \pm 0.11$ from our spectral fit in Sect. 5.2.2 (with a mean photon arrival time of 0.42 days) is steeper than the first GROND epoch (at 0.18 days) spectral index of $\beta_{\mathrm{opt}} = -0.81 \pm 0.05$, by $\Delta\beta = 0.19 \pm 0.12$. This difference is suggestive of a spectral break lying between the X-ray and optical bands. If the break was the cooling break, we would expect $\Delta\beta = 0.5$, however. This discrepancy could be explained by the fact that the cooling break is always smooth (Uhm & Zhang 2014) or that ν_c may lie near to either the optical or X-ray bands. We investigate this further in Sect. 3.3.3.

3.3.3 Closure relation analysis

Within the synchrotron forward shock model the ‘closure relations’ relate the spectral index β with the temporal index α in the convention $F_\nu \propto t^\alpha \nu^\beta$ and depend on the physical regime, spectral regime, and external medium density profile (Zhang & Mészáros 2004; Zhang et al. 2006). The closure relations can be adapted to describe a variety of alternative scenarios to the standard self-similar deceleration phase, including the post-jet break scenario, whether there is energy injection involved, the reverse shock crossing phase, or the Newtonian/non-relativistic phase (see the comprehensive review in Gao et al. 2013). It is important to note that the spectral breaks are inherently smooth, so that a transitioning spectral break or spectral break near to an observing band may define a 'grey zone' where the $\alpha - \beta$ relations are not strictly satisfied (Zhang et al. 2006; Uhm & Zhang 2014).

If we assume that the final declining phase of our optical and X-ray light curves arises from standard forward shock emission in the slow cooling regime ($\nu_m < \nu_c$), which is usually the case at later times, we can determine which spectral regime and density profile best fits our data by performing a closure relation analysis. Our X-ray and optical data both have negative spectral slopes, with fluxes that decline with increasing frequency. There are two spectral regimes that give rise to negative spectral slopes: $\nu_c < \nu$ (Regime I) with $\beta = -p/2$, or $\nu_m < \nu < \nu_c$ (Regime II) with $\beta = (1-p)/2$. For the optical spectral index of $\beta_{\rm opt} = -0.81 \pm 0.05$ derived from the first GROND epoch we would have $p = 1.62 \pm 0.10$ or $p = 2.62 \pm 0.10$ in Regime I and II, respectively. The decay index for both a wind or interstellar medium (ISM) environment in Regime I is $\alpha = (2 - 3p)/4$ resulting in $\alpha = -0.72 \pm 0.08$ with $p = 1.62 \pm 0.10$, too shallow for the observed decay rate of $\alpha_{\rm opt} = -1.84 \pm 0.04$ from our three BPL-component fit. In Regime II, we have $\alpha = 3(1-p)/4$ or $\alpha = (1-3p)/4$ for an ISM or wind density profile, respectively. With $p = 2.62 \pm 0.10$ we get $\alpha = -1.22 \pm 0.08$ or $\alpha = -1.72 \pm 0.08$ for the ISM or wind profiles. Clearly, the observed optical temporal index of $\alpha_{\rm opt} = -1.84 \pm 0.04$ is most consistent with the optical spectral index in Regime II for a wind profile.

In a wind medium the cooling break moves to higher frequencies as $t^{1/2}$, with light curves that are shallower by $\Delta\alpha = 0.25$ above ν_c. With the cooling break between the optical and X-rays one could therefore expect the X-ray light curve to decline more slowly than the optical light curve. Our fits to the X-ray and optical light curves in Sect. 3.3.1 result in $\Delta\alpha = 0.15 \pm 0.19$, which agrees within uncertainties with the predicted difference of $\Delta\alpha = 0.25$. We also see, however, that this $\Delta\alpha$ value is consistent with a zero difference within 1σ and is supported by the fact that the composite R-band light curve provides a good fit to the X-ray light curve, as shown in Fig. 3.4. It is therefore not possible to conclusively say whether ν_c lies between the optical and X-ray bands from our data, though we note that the slightly different temporal and spectral (see Sect. 3.3.2) indices between the two bands does hint at this possibility. In summary, our optical and X-ray data can be accommodated within the standard closure relations in a wind medium.

3.3.4 Broadband SED evolution

The optical and X-ray data alone can only place weak constraints on the location of ν_m and the peak flux of the evolving synchrotron spectrum. Our late-time radio observations, which probe the low-frequency end of the synchrotron spectrum, can provide valuable constraints on the location of ν_m and the peak flux, and can therefore lead to an estimation of the intrinsic blast wave parameters (see Sect. 4.4).

Our three epochs of L-band (at 1.4 GHz) observations all yielded non-detections, whereas our four epochs of C-band and X-band data yielded detections spanning 18 to 118 days post-trigger. The flux across the first two epochs at 18.2 and 34.2 days was fairly constant in both the C and X bands, which is consistent with the predicted evolution of t^0 for the spectral ordering $\nu_{sa} < \nu < \nu_m$ in a wind medium undergoing slow cooling. The spectral slope between the first epoch C- and X-band detections of $\beta_{6-10\ {\rm GHz}} = 0.57 \pm 0.27$ is also close to the predicted value of $\nu^{1/3}$ for the same spectral segment. The subsequent decline in flux across the last two epochs can be interpreted as the passage of ν_m through 6 and 10 GHz, whereafter both bands lie in Regime II of the synchrotron spectrum in which the flux declines with time and the spectrum declines with increasing frequency. This is seen in our last two epochs where the C-band flux is in fact brighter than the X-band flux. At 34.2 days we have quasi-simultaneous flux measurements at 1.4, 6 and 10 GHz (see Fig. 3.6). The spectral index between the C and X bands is $\beta_{6-10\text{ GHz}} = 0.69 \pm 0.23$, which is closer to the optically thin spectral slope of $\nu^{1/3}$ than the synchrotron self-absorbed slope of ν^2. Based on the C-band detection and L-band upper limit, we place a lower limit on the spectral slope of $\beta_{1.4-6\text{ GHz}} > 0.84$. It therefore may be the case that synchrotron self-absorption is responsible for the non-detections at 1.4 GHz, since our L-band limit is consistent with a ν^2 spectrum. In that case, the self-absorption frequency could lie between 1.4 and 10 GHz at 34.2 days.

In a wind medium, ν_m moves to lower frequencies as $t^{-3/2}$ with the corresponding peak flux of the synchrotron spectrum declining as $t^{-1/2}$ for the spectral break ordering $\nu_{sa} < \nu_m < \nu_c$. From our GROND SED at $t = 0.184$ days (Fig. 3.3), we know that ν_m lies below the K band with a peak flux greater than the measured K-band flux of 555 μJy. If we assume that ν_m passes through the radio X band (10 GHz) at 34.2 days with a peak flux of ~250 μJy, we would have expected ν_m to be at 1.48×10^{12} Hz with a peak flux of 1320 μJy at 1.22 days, the time of our second GROND epoch. This frequency lies below the K-band frequency of 1.38×10^{14} Hz, as expected. The spectral index between this expected peak flux value and the measured K-band flux value at 1.22 days results in $\beta \approx -0.7$, which is in agreement with the measured optical spectral index of $\beta_{\text{opt}} = -0.79 \pm 0.06$ at this time. We also note that the X-ray to optical R-band spectral index at ~0.38 days ($\beta_{\text{opt,X}} \approx -0.95$) is between the X-ray-only ($\beta_{\text{X}} = -1.00 \pm 0.11$) and optical-only index ($\beta_{\text{opt}} = -0.81 \pm 0.05$), demonstrating that both observing bands can be accommodated via a forward shock model.

With these basic considerations, we attempted to find a first-guess set of blast wave parameters that can explain our data. We have the following assumed constraints: (i) ν_m passes through 10 GHz at 34.2 days; (ii) the corresponding peak flux at this frequency and time is ~250 μJy; (iii) ν_c lies between the optical and X-ray bands at early times (i.e. $\nu_c \approx 10^{17}$ Hz at 0.3 days); and (iv) ν_{sa} lies between 1.4 and 10 GHz at 34.2 days.

With these four constraints we can attempt to solve the system of four equations describing the locations of the spectral breaks and their corresponding flux densities in a wind medium, given in Table 2 of Granot & Sari (2002). Our solution given the above constraints results in an unphysical value of $\epsilon_e > 1$, which is driven primarily by the requirement that the self-absorption frequency lies between 1.4 and 10 GHz at 34.2 days. Lowering ν_{sa} to a frequency of $\sim 10^7$ Hz results in a physical solution for all of the blast wave parameters. Our L-band limits therefore pose a challenge to the interpretation of our multi-wavelength afterglow data. We return to this point in Sect. 3.5.2.

3.3.5 Early jet-break scenario

Our optical light curve during the final declining phase had a temporal index of $\alpha_{\text{opt}} = -1.84 \pm 0.04$ from the combined fit or $\alpha_{\text{opt}} = -1.65 \pm 0.04$ from the direct fit to the late-time data only, which is somewhat steep for normal pre-jet break evolution (see Fig. 4 in Wang et al. 2018), but still consistent with pre-jet break evolution. An alternative scenario to explain the steep final declining phase in the optical and X-ray light curves is post-jet break decay. If the jet break is due to a purely geometric edge effect (Panaitescu et al. 1998), the light curves within all spectral regimes should steepen by $t^{-3/4}$ for the ISM case and $t^{-1/2}$ for the wind case once the ejecta has slowed down such that the relativistic beaming angle $1/\Gamma$ is greater than the jet half-opening angle θ_j, assuming a top-hat jet. Sideways expansion of a conical jet would result in a steeper jet break decay of approximately t^{-p} in Regimes I and II for an ISM (Rhoads 1999; Sari et al. 1999).

Considering the edge effect only, a jet break will not change the temporal evolution of the synchrotron spectral break frequencies. If an early jet break occurred we would expect our radio data to show declining light curves that decay as $t^{-1/2}$ in a wind medium under the assumption that $\nu_{sa} < \nu_{6,10\text{ GHz}} < \nu_m$. Taking into account sideways expansion, the evolution of the break frequencies is altered, though we would still expect declining light curves at radio frequencies

(Sari et al. 1999). The rising radio light curves in the C and X bands until ∼34 days are therefore inconsistent with an early jet break. This implies that the steep optical and X-ray decline is normal pre-jet break decay in a wind medium, supporting our analysis in Sect. 3.3.3.

3.4 Theoretical modelling

We have shown in the previous sections that our X-ray, optical, and radio data after the last optical peak can be reconciled within the synchrotron forward shock model in a wind medium with $p \approx 2.6$ if we exclude our L-band limits. We now proceed to find a set of blast wave parameters that can describe our data by employing the smoothly connected power-law spectra outlined in Granot & Sari (2002) and fitting for the forward shock parameters p, ϵ_e, ϵ_B, $A_\star$, and $E_{\rm K,iso}$, where $E_{\rm K,iso}$ is the total isotropic-equivalent kinetic energy in the blast wave; ϵ_e and ϵ_B are the fractions of shock internal energy given to the electrons and the magnetic fields, respectively; and $A_\star = A/(5 \times 10^{11}\ \mathrm{g\ cm^{-1}})$ is the wind density parameter as defined in Chevalier & Li (2000). We correct the data for Galactic extinction with $A_V = 0.24$ mag.

We perform a Markov chain Monte Carlo (MCMC) analysis with `emcee` (Foreman-Mackey et al. 2013) using 512 walkers and 2000 steps, discarding the initial 250 steps as burn-in. The details of our implementation are described in Laskar et al. (2013, 2014). The host galaxy extinction, $A_{\rm V,host}$, is a free parameter in our model. We include the effects of Klein-Nishina (KN) corrections (G. McCarthy & T. Laskar in prep) using prescriptions from Nakar et al. (2009) and Jacovich et al. (2021). We used uniform, uninformative priors flat in log space, and restricted $\epsilon_e + \epsilon_B < 1$, although this limit is not reached. We did not include data before the inferred time of the last optical peak at ∼0.3 days in the modelling, and discuss these data further in Sect. 5.6. We also did not include the MeerKAT 1.4 GHz observations, as we do not expect these to be fit with this model (Sect. 3.3.4). We present theoretical modelling including the L-band limits in Appendix 3.A. For completeness, we also include the possibility of a jet break following Rhoads (1999). We set a lower limit on the jet break time of $t_{\rm jet} \gtrsim 34$ days since there is no evidence for an earlier jet break in the data, as discussed in Sect. 3.3.5.

The physical parameters for the highest-likelihood model and those derived from the MCMC analysis are presented in Table 3.2, while the corresponding light curves are presented in Fig. 3.7. For these parameters, both inverse Compton and KN effects are important at early times ($\lesssim 1$ day), with Compton $Y \approx 4$ at ∼0.3 days. At this time, the relevant spectral break frequencies are located at $\nu_m \approx 4 \times 10^{13}$ Hz, $\nu_c \approx \hat{\nu}_c \approx 10^{16}$ Hz, and $\hat{\nu}_m \approx 10^{21}$ Hz, resulting in the spectral ordering $\nu_{\rm opt} < \nu_c \approx \hat{\nu}_c \lesssim \nu_{\rm X}$, where $\hat{\nu}_c$ and $\hat{\nu}_m$ are KN spectral breaks as outlined in Nakar et al. (2009). The cooling frequency passes through the X-ray band between ≈ 0.6 to 12 days, consistent with the discussion in Sects. 3.3.2 and 3.3.3. In this regime, the spectral index in the X-rays is expected to be intermediate between $(1-p)/2 \approx -0.88$ and $-p/2 \approx -1.34$, which is consistent with the observed X-ray spectral index of $\beta_{\rm X} = -1.00 \pm 0.11$. Taking into account the 1σ confidence intervals from the MCMC analysis, the derived value of $p = 2.75 \pm 0.03$ is consistent with the value of $p = 2.62 \pm 0.10$ inferred from our closure relation analysis in Sect. 3.3.3. This model also requires an intrinsic extinction of $A_{\rm V,host} \approx 0.2$ mag, consistent with the observed UV suppression (Fig. 3.5). The corner plot in Fig. 4.10 shows that there are strong correlations between some pairs of parameters, especially those involving ϵ_e, ϵ_B, $A_\star$, and $t_{\rm jet}$. The model over-predicts the 1.4 GHz flux by a factor of ≈ 3 with respect to our MeerKAT upper limits (Fig. 3.6); even when taking scintillation into account, the upper limits are all more than 4σ below the model flux. We return to this point in Sect. 3.5.2.

Our shock microphysics parameters are fairly typical. Our value of $p = 2.75 \pm 0.03$ is within the 1σ range of the sample in Wang et al. (2015), for which they find $p = 2.33 \pm 0.48$. Santana et al. (2014) collect ϵ_e and ϵ_B values in the literature and find that ϵ_e is narrowly distributed across one order of magnitude between ∼0.02 to 0.6 with a median of value 0.22. Our value of ≈ 0.1 is a normal value within their sample. For the magnetic field equipartition factor, they find

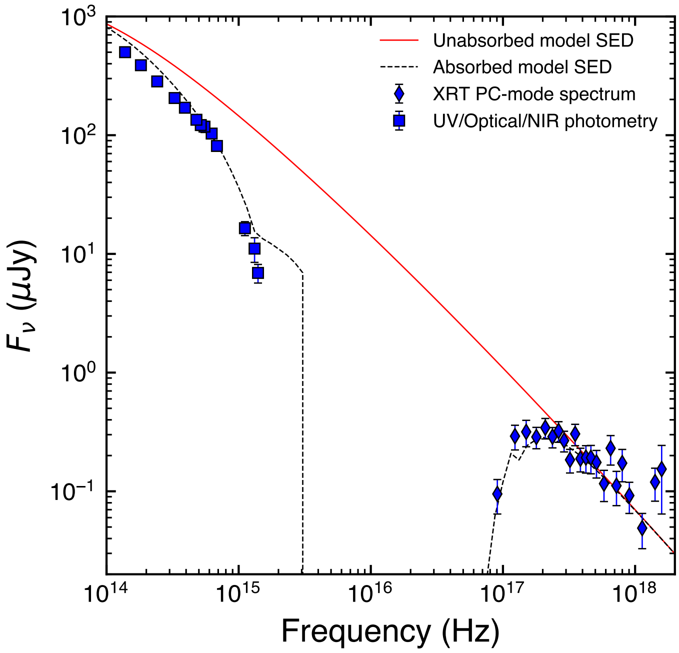

Figure 3.5: Optical to X-ray SED at 0.3 days along with the highest-likelihood theoretical model SED, both absorbed (dashed line) and unabsorbed (solid line). The optical photometric data points were derived from the light curve fits to each observing band (see Fig. 3.4) through interpolating each fit to 0.3 days. The X-ray PC-mode spectrum had a mean photon arrival time of 0.43 days, so we used the X-ray BPL light curve fit in Fig. 3.2 to determine a correcting factor to shift the spectrum to the expected flux level at 0.3 days.

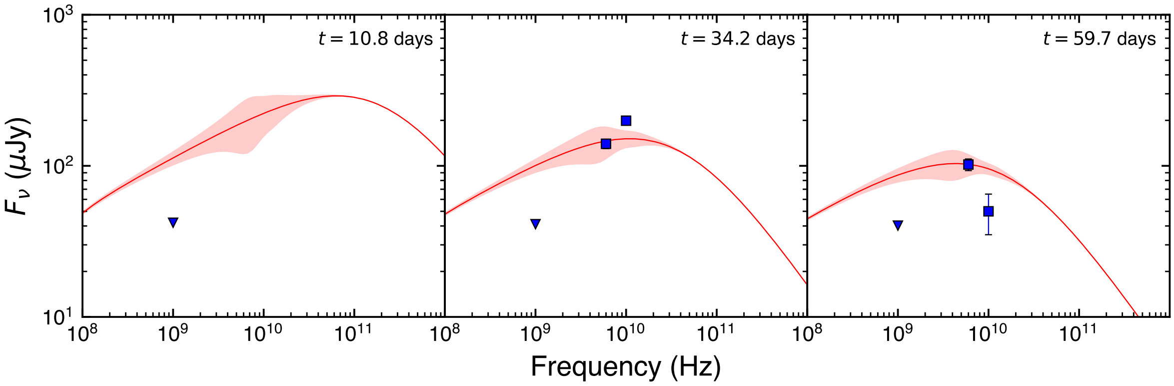

Figure 3.6: Radio SEDs at the times of the three MeerKAT epochs. We show the highest-likelihood unabsorbed model SED along with the effects of Galactic scintillation at the 1σ level as derived from the NE2001 model (Cordes & Lazio 2002) for the GRB line of sight through the Milky Way. For the second epoch we show the C- and X-band detections obtained quasi-simultaneously at 34.2 days, while for the third epoch we show the C- and X-band detections obtained 7.4 days after the third MeerKAT epoch.

Table 3.2: Parameters derived from our multi-wavelength theoretical modelling of the afterglow data after 0.3 days. We show both the highest-likelihood model parameters from a maximum-likelihood (ML) estimation and the median values along with their corresponding 1σ confidence intervals from the MCMC marginalised posterior distributions presented in Fig. 4.10. The beaming-corrected prompt γ-ray and kinetic energies are given in the lower panel of the table, where we have placed a lower limit on the opening angle of the jet based on a limit of $t_{\rm jet} \gtrsim 118$ days.

Parameter	ML estimate	MCMC results
p	2.75	2.75 ± 0.03
ϵ_e	9.7×10^{-2}	$9.6^{+1.3}_{-1.0} \times 10^{-2}$
ϵ_B	1.7×10^{-3}	$2.2^{+1.9}_{-0.9} \times 10^{-3}$
$A_\star$	7.1×10^{-2}	$6.4^{+1.6}_{-1.5} \times 10^{-2}$
$E_{\rm K,iso}$ (10^{52} erg)	63	69^{+32}_{-19}
$A_{\rm V,host}$ (mag)	0.22	0.23 ± 0.01
$t_{\rm jet}$ (days)	64	55^{+23}_{-14}
$\theta_{\rm jet}$ (deg)	$\gtrsim 6$	-
E_γ (erg)	$\gtrsim 7.07 \times 10^{49}$	-
$E_{\rm K}$ (erg)	$\gtrsim 3.45 \times 10^{51}$	-

a much wider distribution varying across almost 5 orders of magnitude from $\sim 3.5 \times 10^{-5}$ to 0.33. Our value of $\epsilon_B \approx 0.2 \times 10^{-2}$ is close to their median value of 1.0×10^{-2}. Additionally, Beniamini & van der Horst (2017) use radio light curve peaks to determine the distribution of ϵ_e and find a value of $\log_{10}\epsilon_e = -0.88 \pm 0.26$ for a wind medium. Again, our derived valued is consistent with their sample value. Laskar et al. (2015) found that the values of the circumburst density (n_0 or $A_\star$) span 8 orders of magnitude from 10^{-5} to 10^3. Our derived $A_\star$ value of 7.1×10^{-2} is fully consistent with their sample.

The model requires a jet break at $t_{\rm jet} \approx 64$ days, which is driven by the declining radio light curves after this time. For the highest-likelihood parameters, this corresponds to a jet opening angle of $\theta_{\rm jet} \approx 5°$. In the absence of a jet break, the model over-predicts the final X-band detection by $\approx 3.5\sigma$. However, we note that the evidence in support of a jet break is fairly weak and this inferred opening angle should be interpreted with caution. For a limit of $t_{\rm jet} \gtrsim 118$ days (the last radio detection), the highest-likelihood model yields a lower limit on the opening angle of $\theta_{\rm jet} \gtrsim 6°$. The corresponding beaming correction of $f_b = (1 - \cos\theta_{\rm jet}) \gtrsim 5.48 \times 10^{-3}$ implies constraints on the true γ-ray and kinetic energy of $E_\gamma \gtrsim 7.07 \times 10^{49}$ erg and $E_{\rm K} \gtrsim 3.45 \times 10^{51}$ erg, respectively, where we have used the maximum-likelihood (ML) estimate from Table 3.2 for $E_{\rm K,iso}$.

3.5 Discussion

The optical light curve of GRB 210731A is unusual for showing three distinct peaks of similar brightness within the first five hours of the GRB trigger. Multiple peaks in optical light curves have been observed before (e.g. GRBs 060904B, 080928, 100621A, 100814A, 100901A; Klotz et al. 2008; Rossi et al. 2011; Greiner et al. 2013; Nardini et al. 2014; Laskar et al. 2015). We investigate a number of explanations proposed in the literature for peaks and re-brightenings in afterglow light curves, including the passage of a spectral break, flaring behaviour, secondary jets, an off-axis viewing angle, energy injection into the forward shock, and the onset of afterglow. We also consider the implications of our L-band upper limits.

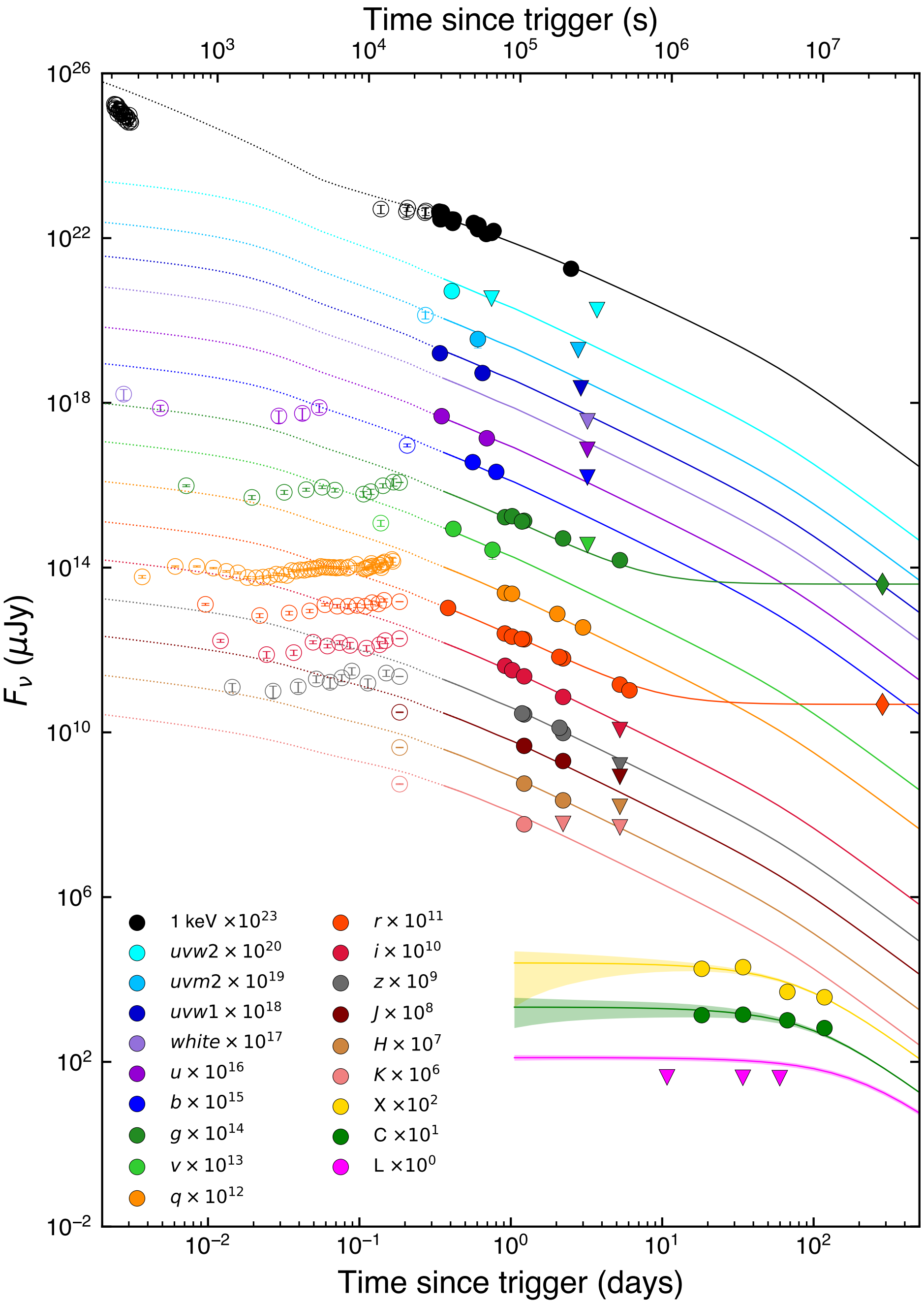

Figure 3.7: Light curves from our highest-likelihood theoretical model shown for each observing band, spanning X-ray, optical, and radio frequencies. Only data points after 0.3 days were used in the modelling, and we show these as filled-in data points, in contrast to the earlier time data points shown as empty circles. Upper limits are shown as upside-down triangles. The shaded regions surrounding the three radio bands (X, C, and L) represent the effects of Galactic scintillation at the 1σ level. The optical g- and r-band model fits plateau towards the measured host-galaxy flux levels at 285 days, shown as diamonds.

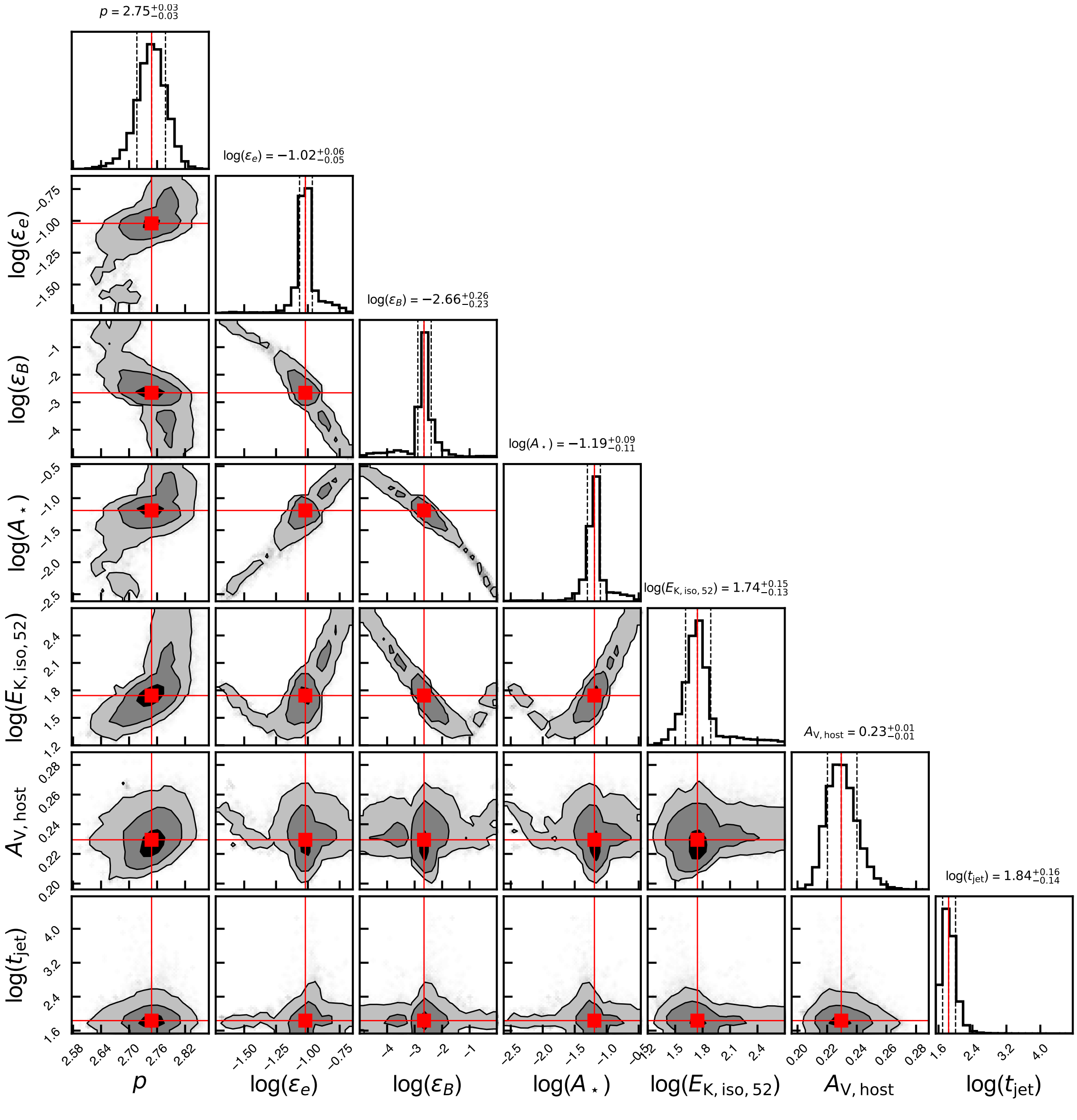

Figure 3.8: Corner plot showing the marginalised posterior distributions for each model parameter along with the 2D marginalised posterior distributions for each pair of model parameters, from our MCMC analysis. Contours are at the 1σ, 2σ, and 3σ levels, and the red lines denote the median values derived from the marginalised posterior distributions for each model parameter.

3.5.1 The nature of the optical re-brightenings

Passage of a spectral break

The passage of the spectral break associated with the peak of the synchrotron spectrum (ν_m) through the optical bands could in principle give rise to a peak in the optical light curves. Since ν_m moves to lower frequencies with increasing time, we would expect the spectral index to transition from a positive to negative value over the rise and fall of the light curve. We have shown in Sect. 3.3.2 and in Fig. 3.4, however, that our optical evolution is achromatic, ruling out a spectral break origin to any of the peaks.

Flaring behaviour

The peaks in the early light curve are too smooth and long-lived to be due to flares. Hence, the observed structure in the optical light curve cannot be due to any of the mechanisms that are typically invoked to explain flares, such as late-time central engine activity, density fluctuations, or reverse shock emission.

Off-axis viewing angle

It is possible to obtain a rising light curve if the GRB jet is viewed from an angle outside the cone of the jet (i.e. $\theta_{\mathrm{obs}} \gtrsim \theta_{\mathrm{jet}}$; Granot et al. 2002). The peak of the light curve corresponds to the time when the Lorentz factor of the jet is $\sim 1/\theta_{\mathrm{obs}}$, whereafter the light curve evolves in a post-jet break manner. Our radio data and theoretical modelling does not support an early jet break however, as discussed in Sects. 3.3.5 and 4.4. Although it would be possible to explain a single peak in the light curve through viewing angle effects, it is difficult to interpret all three light curve peaks within such a scenario. Due to the relativistic beaming effect, one would also expect to observe negligible prompt γ-ray emission when the viewing angle is outside the jet cone, resulting in an orphan afterglow (Rhoads 1999; Granot et al. 2002; Zou et al. 2007). The prompt γ-ray observations of GRB 210731A therefore do not support an off-axis viewing angle interpretation.

Two-component jet model

The two-component jet model (Peng et al. 2005) has been invoked to explain chromatic behaviour and late-time re-brightenings observed in a number of GRB afterglows (Berger et al. 2003; Racusin et al. 2008; Filgas et al. 2011; Nicuesa Guelbenzu et al. 2011; Kann et al. 2018). In this model a fast, narrow inner jet powers the prompt emission and early afterglow emission, while a slower, wider jet powers the late-time afterglow evolution, with both jets viewed on-axis. This model was preferred by Liang et al. (2013) to explain the re-brightenings observed in their sample of optical afterglows, in which the deceleration of the slow jet explains the re-brightening peaks, analogous to the onset peaks. They claim that the similar rising and decaying indices of the onset and re-brightening peaks supports this interpretation. Furthermore, they find that the properties of the re-brightenings are not correlated with the prompt emission properties (contrary to the onset peaks), and so they are likely independent emission components. The fact that the GRB 210731A optical light curve shows three distinct peaks appears to rule out the two-component jet model. A three-component jet might be able to explain the three light curve peaks, but we consider it beyond the scope of this work.

Energy injection

The most straightforward explanation for the optical light curve evolution is energy injection into the forward shock. Energy injection, or a refreshed shock, has been invoked to explain the plateaus and shallow decay segments seen in X-ray (Campana et al. 2005; Vaughan et al. 2006;

Nousek et al. 2006; Zhang et al. 2006; Liang et al. 2007; Evans et al. 2009) and optical light curves (Mangano et al. 2007; Greiner et al. 2009; Swenson et al. 2013). In this framework, the blast wave energy increases with time during the energy injection period, rather than remaining constant. Two physical mechanisms have been proposed: the first is a long-lasting central engine that continuously injects a Poynting flux into the blast wave as in the case of a spin-down millisecond magnetar (Dai & Lu 1998; Zhang & Mészáros 2001), where the central engine luminosity is described as a power law in time with $L(t) = L_0(t/t_0)^{-q}$. The injected energy $E_{\rm inj}$ is essentially constant when $q \geq 1$, while the total energy in the blast wave can only increase significantly with time when $q < 1$. Once the injected energy begins to exceed the original energy in the blast wave, the total energy will scale as $E_{\rm tot} \propto t^{1-q}$. The second case could arise from an impulsive central engine injection episode, producing a stratified ejecta distribution where the ejecta mass above a certain Lorentz factor Γ is described as a power law, for example $M(>\Gamma) \propto \Gamma^{-s}$. The energy in a shell with Lorentz factor Γ is added to the blast wave when the blast wave bulk Lorentz factor has slowed down to Γ, so that the energy in the blast wave scales as $E(>\Gamma) \propto \Gamma^{1-s}$ (Rees & Mészáros 1998; Sari & Mészáros 2000). For both cases the blast wave scaling laws can be derived and applied to the synchrotron spectra to obtain closure relations that depend on either q or s. Both forms of energy injection can be cast in an equivalent form, and simple relations between q and s can be derived (Zhang et al. 2006). From a closure relation analysis with energy injection alone, it is therefore impossible to distinguish energy injection from a long-lasting central engine or from injection of a stratified ejecta.

The R-band light curve segments between the first and final peaks have temporal indices of $\alpha = [-0.77, 0.64, -0.11, 0.48]$ (from the direct fit to each segment in Fig. 3.2). Adopting the q-formalism, we can determine the energy injection index q for each segment by making use of the closure relations for a wind medium in the slow cooling regime (Zhang et al. 2006). We make the assumption that the R band remained in the spectral regime satisfying $\nu_m < \nu_R < \nu_c$ during all four segments of energy injection, which is valid since our data supports achromatic optical evolution. In this regime, $\alpha = \frac{(2-2p)-(p+1)q}{4}$, so employing $p = 2.75$ from our theoretical modelling we derive values of $q = [-0.11, -1.62, -0.82, -1.45]$ for each light curve segment after the first peak. The energy increase during a time period from t_0 to t_1 is calculated as

$$E_{\rm K,iso,1} = E_{\rm K,iso,0} \left(\frac{t_1}{t_0}\right)^{1-q}. \tag{3.2}$$

Assuming that the blast wave kinetic energy evolves according to Eq. 3.2 during each of the four power law segments, we can determine the energy at the time of the first peak, $E_{\rm K,iso,0}$, using

$$E_{\rm K,iso,f} = E_{\rm K,iso,0} \left(\frac{t_1}{t_0}\right)^{1-q_1} \left(\frac{t_2}{t_1}\right)^{1-q_2} \left(\frac{t_3}{t_2}\right)^{1-q_3} \left(\frac{t_4}{t_3}\right)^{1-q_4} \tag{3.3}$$

along with the start and end times of each segment[9], our values calculated for q above, and a final blast wave energy of $E_{\rm K,iso,f} = 6.3 \times 10^{53}$ erg from our theoretical modelling. We find that the blast wave energy at the time of the first optical peak is equal to 7.3×10^{50} erg, smaller by a factor of $\sim$1000 compared to the final kinetic energy, indicative of substantial energy injection.

Laskar et al. (2015) argue that the significant X-ray and optical re-brightenings seen in a sample of GRB afterglows are best explained by the stratified ejecta model, since energy injection from a spinning-down millisecond magnetar should not lead to a significant increase in the blast wave energy (i.e. $q \geq 1$). They also exclude fall-back accretion onto a black hole as the theoretically-predicted accretion rate is insufficient to power plateaus or re-brightenings. In the stratified ejecta formalism, there is a gap between the initial blast wave shell and the fast outer shell of the stratified ejecta that is moving with some maximum Lorentz factor, $\Gamma_{\rm max}$. As

---

[9] We use the vertical dashed lines in Fig. 3.2 as the start and end times of each segment. These have values of $t_0 = 0.0077$, $t_1 = 0.021$, $t_2 = 0.057$, $t_3 = 0.09$, and $t_4 = 0.22$ days.

Table 3.3: Parameters derived from each BPL component of our R-band light curve fit.

F_p (10^{-12} erg cm^{-2} s^{-1})	t_p (s)	w (s)	$L_\mathrm{R,p}$ (10^{45} erg s^{-1})	$E_\mathrm{R,iso}$ (10^{48} erg)
1.92 ± 0.27	760 ± 111	956	15.69 ± 2.22	8.28
0.75 ± 0.27	5704 ± 645	5385	6.11 ± 2.21	16.96
2.62 ± 0.10	23161 ± 1179	39824	21.41 ± 0.78	464.53

the initial shell slows down, the stratified ejecta deposits energy into the blast wave until the slowest shell moving with Lorentz factor Γ_min has deposited its energy, whereafter the afterglow evolves following the standard framework. From their study of a sample of afterglows exhibiting later-time re-brightenings, Laskar et al. (2015) showed that a large amount of the kinetic energy deposited into the blast wave comes from the slowest-moving ejecta. They also find that the GRBs with significant energy injection have low radiative efficiencies, consistent with the prompt γ-ray emission being produced by the fastest-moving ejecta and a large amount of kinetic energy being carried by the slower ejecta. With our value of $E_{\gamma,\mathrm{iso}} = 1.29 \times 10^{52}$ erg and $E_\mathrm{K,iso} = 63 \times 10^{52}$ erg, we calculate a radiative efficiency using $\eta \equiv E_{\gamma,\mathrm{iso}}/(E_{\gamma,\mathrm{iso}} + E_\mathrm{K,iso})$ of $\eta \approx 0.02$, a low radiative efficiency consistent with significant energy injection. We also note that the energy released in γ rays is ≈ 18 times greater than the kinetic energy in the blast wave derived at the time of the first optical peak. This is unphysical if the kinetic energy at that time is the true energy reservoir from which the prompt emission is drawn, and adds support to the final kinetic energy being the true energy reservoir.

Afterglow onset and initial Lorentz factor, Γ_0

The synchrotron forward shock model predicts a smooth onset peak in optical light curves as the expanding blast wave is slowed down by the circumburst medium (Sari & Piran 1999; Kobayashi & Zhang 2007). Such onset peaks are not uncommon in early optical afterglows and have been studied by a number of authors (Zhang et al. 2003; Molinari et al. 2007; Xue et al. 2009; Liang et al. 2010, 2013). For an ISM density profile, the deceleration time (or onset peak time) is most sensitive to the bulk Lorentz factor of the ejecta and depends weakly on other parameters. Onset peaks can therefore provide a valuable way of constraining the initial Lorentz factor Γ_0 of the GRB blast wave. For a non-ISM density profile, however, the dependence of the deceleration time on other parameters becomes stronger.

The first optical detection associated with GRB 210731A was made in the UVOT *white* filter starting 210 seconds post-trigger, with subsequent detections showing a steady rise to a smooth peak around 700 seconds. Thereafter, the light curve entered a declining phase before starting to rise steadily again at ∼1700 seconds. Li et al. (2012) and Liang et al. (2013) define an onset peak as a smooth hump peaking within one hour post-trigger that is followed by a normal power-law decay component. By comparing our onset peak with the sample of 38 onset peaks in Liang et al. (2013), we can assess how likely it is that our first peak is indeed the onset of afterglow. From our combined R-band fit (Fig. 3.2 and Table 3.1) we derive a number of additional properties from each BPL component. These include the peak flux (F_p), peak time (t_p), full width at half maximum (w), peak R-band luminosity ($L_\mathrm{R,p}$), and the isotropic energy release in the interval $[t_\mathrm{p}/5, 5t_\mathrm{p}]$, as shown in Table 3.3.

Liang et al. (2013) find that the onset peak times of their sample span a range of 30-3000 seconds, with typical rising and decaying indices of 1.5 and -1.15 in ranges of [0.3,4] and [-1.8,-0.6], respectively. Our peak time of 760 ± 111 seconds and rising index of 1.39 ± 0.36 are typical values within this sample, but our decaying index of -2.58 ± 0.75 from BPL 1 in Table 3.1 is steeper than average, though it does fall within the sample range within uncertainty. It should be noted that the decaying slope of our first peak is not well determined owing to the uncertain contribution of the second BPL component at this time. Furthermore, the authors derive a number of empirical relations between pairs of properties of onset peaks (see their Figs. 7 and 9): the width of a peak is strongly correlated with the peak time; the R-band peak luminosity is anti-correlated with the rest-frame time; and the peak luminosity and energy are correlated with the isotropic γ-ray energy. We find that our measured values in Table 3.3 agree closely with their empirical relations, lending support to the onset peak claim.

Under the assumption that GRB 210731A occurred in a stellar wind medium ($k = 2$), we calculate the initial Lorentz factor following Zhang (2018) as

$$\Gamma_0 \simeq 1.3^{1/4} \left(\frac{3E_{\mathrm{K,iso}}(1+z)}{8\pi A c^3 t_{\mathrm{dec}}} \right)^{1/4} \simeq 120 t_{\mathrm{dec}}^{-1/4} \left(\frac{1+z}{2} \right)^{1/4} E_{52}^{1/4} A_{\star}^{-1/4}, \tag{3.4}$$

where after the last equality, t_{dec}, is measured in seconds, E_{52} in units of 10^{52} erg, and $A_\star$ is the wind density parameter as described previously. Equation 3.4 depends on the assumption of an impulsive fireball, that is, the thin shell regime. The isotropic-equivalent kinetic energy of the blast wave $E_{\mathrm{K,iso}}$ can be inferred from theoretical modelling of the afterglow, which we do in Sect. 4.4. However, the value calculated in Sect. 4.4 was only applicable to the late-time light curve, so we employ the value for $E_{\mathrm{K,iso}}$ of 7.3×10^{50} erg at the time of the first optical peak calculated in Sect. 3.5.1. Using the $A_\star$ value from our theoretical modelling and the peak time of our first peak, we calculate an initial Lorentz factor of $\Gamma_0 \approx 24$. As mentioned previously, the dependence of the deceleration time on other parameters is stronger for a non-ISM density profile. This is also the case if there is energy injection during deceleration, which may be the case during our early optical observations (Sect. 3.5.1). We therefore caution that our calculation of Γ_0 is an estimate.

3.5.2 Suppressed L-band flux

Our highest-likelihood theoretical model can provide an adequate fit to all of our late-time data except for the L band, where the model over-predicts the flux by a factor of ≈ 3 compared to our MeerKAT upper limits. We did not expect our model to fit the L-band data since we found that requiring the synchrotron self-absorption frequency to lie above the L band at 34.2 days resulted in an unphysical value of $\epsilon_e > 1$. We therefore need to consider an additional source of opacity at these observing frequencies to explain our L-band limits.

One possible source of additional opacity is a thermal electron population within the GRB shock front. Ressler & Laskar (2017) modelled afterglow spectra and light curves while considering the effect of such a population and find that it has two effects on the spectra: an excess of flux near the peak synchrotron frequency of the thermal electrons that fades with time as the electrons cool; and additional opacity in the optically thick portion of the spectrum compared to the case with only non-thermal electrons. The latter effect is consistent with a higher self-absorption frequency by a factor of 10-100. It could therefore be the case that our suppressed L-band flux points towards a population of thermal electrons. We leave the detailed modelling including a thermal population of electrons to a future work.

3.6 Conclusion

GRB 210731A was a long-duration burst discovered by *Swift*/BAT. Observations with the optical telescope MeerLICHT starting 286 seconds post-trigger found an unusual optical light curve evolution with three peaks of similar brightness within the first 4.3 hours; afterwards, the burst entered a declining phase. We find that the early optical evolution is consistent with a constant optical spectrum, pointing towards a hydrodynamical origin. A closure relation analysis based on the optical SED and temporal decay after the last peak showed a preference for a stellar wind environment, consistent with the long GRB duration and therefore a massive star origin. We find that the first optical peak can be explained as the onset of afterglow, while energy injection into the forward shock from a stratified ejecta is a natural explanation for the two subsequent re-brightenings. We estimate that the blast wave kinetic energy increased by a factor of ∼1000 from the first optical peak to the last peak. Detailed theoretical modelling of the optical, X-ray, and radio data after the last optical peak at ∼0.3 days resulted in typical blast wave and shock microphysics parameters. Our MeerKAT L-band upper limits could not be reconciled with our model, however, possibly implying a thermal electron population within the shocked region that provided an additional source of opacity. Future multi-wavelength modelling of GRB afterglows, especially at millimetre and radio frequencies, will shed light on the electron distribution in GRB shocks.

Acknowledgements

The MeerLICHT consortium is a partnership between Radboud University, the University of Cape Town, the Netherlands Organisation for Scientific Research (NWO), the South African Astronomical Observatory (SAAO), the University of Oxford, the University of Manchester and the University of Amsterdam, in association with and, partly supported by, the South African Radio Astronomy Observatory (SARAO), the European Research Council and the Netherlands Research School for Astronomy (NOVA). We acknowledge the use of the Inter-University Institute for Data Intensive Astronomy (IDIA) data intensive research cloud for data processing. IDIA is a South African university partnership involving the University of Cape Town, the University of Pretoria and the University of the Western Cape. SdW and PJG are supported by NRF SARChI Grant 111692. Part of the funding for GROND (both hardware and personnel) was generously granted from the Leibniz-Prize to G. Hasinger (DFG grant HA 1850/28-1) and by the Thüringer Landessternwarte Tautenburg. AVF is grateful for financial assistance from the Christopher R. Redlich Fund and numerous individual donors. KAIT and its ongoing operation were made possible by donations from Sun Microsystems, Inc., the Hewlett-Packard Company, AutoScope Corporation, Lick Observatory, the U.S. NSF, the University of California, the Sylvia & Jim Katzman Foundation, and the TABASGO Foundation. Research at Lick Observatory is partially supported by a generous gift from Google. This work made use of data supplied by the UK *Swift* Science Data Centre at the University of Leicester. This publication made use of the python package `corner.py` (Foreman-Mackey 2016).

Bibliography

Barthelmy, S. D., Barbier, L. M., Cummings, J. R., et al. 2005, Space Sci. Rev., 120, 143

Beniamini, P. & van der Horst, A. J. 2017, MNRAS, 472, 3161

Berger, E., Kulkarni, S. R., Pooley, G., et al. 2003, Nature, 426, 154

Beuermann, K., Hessman, F. V., Reinsch, K., et al. 1999, A&A, 352, L26

Björnsson, G., Gudmundsson, E. H., & Jóhannesson, G. 2004, ApJ, 615, L77

Blandford, R. D. & McKee, C. F. 1976, Physics of Fluids, 19, 1130

Bloemen, S., Groot, P., Woudt, P., et al. 2016, in Society of Photo-Optical Instrumentation Engineers (SPIE) Conference Series, Vol. 9906, Ground-based and Airborne Telescopes VI, ed. H. J. Hall, R. Gilmozzi, & H. K. Marshall, 990664

Burrows, D. N., Hill, J. E., Nousek, J. A., et al. 2005, Space Sci. Rev., 120, 165

Campana, S., Antonelli, L. A., Chincarini, G., et al. 2005, ApJ, 625, L23

Chambers, K. C., Magnier, E. A., Metcalfe, N., et al. 2016, arXiv e-prints, arXiv:1612.05560

Chevalier, R. A. & Li, Z.-Y. 2000, ApJ, 536, 195

Colgate, S. A. 1968, Canadian Journal of Physics Supplement, 46, 476

Cordes, J. M. & Lazio, T. J. W. 2002, arXiv e-prints, astro

D'Ai, A., Evans, P. A., Goad, M. R., & Swift-XRT Team. 2021, GRB Coordinates Network, 30569, 1

Dai, Z. G. & Cheng, K. S. 2001, ApJ, 558, L109

Dai, Z. G. & Lu, T. 1998, Phys. Rev. Lett., 81, 4301

Dai, Z. G. & Wu, X. F. 2003, ApJ, 591, L21

de Wet, S., Levan, A. J., Groot, P. J., Vreeswijk, P. M., & Meerlicht Consortium. 2021, GRB Coordinates Network, 30570, 1

Evans, P. A., Beardmore, A. P., Page, K. L., et al. 2009, MNRAS, 397, 1177

Evans, P. A., Beardmore, A. P., Page, K. L., et al. 2007, A&A, 469, 379

Evans, P. A., Willingale, R., Osborne, J. P., et al. 2010, A&A, 519, A102

Fan, Y. & Piran, T. 2006, MNRAS, 369, 197

Filgas, R., Krühler, T., Greiner, J., et al. 2011, A&A, 526, A113

Filippenko, A. V., Li, W. D., Treffers, R. R., & Modjaz, M. 2001, in Astronomical Society of the Pacific Conference Series, Vol. 246, IAU Colloq. 183: Small Telescope Astronomy on Global Scales, ed. B. Paczynski, W.-P. Chen, & C. Lemme, 121

Foreman-Mackey, D. 2016, The Journal of Open Source Software, 1, 24

Foreman-Mackey, D., Hogg, D. W., Lang, D., & Goodman, J. 2013, PASP, 125, 306

Galama, T. J., Vreeswijk, P. M., van Paradijs, J., et al. 1998a, Nature, 395, 670

Galama, T. J., Wijers, R. A. M. J., Bremer, M., et al. 1998b, ApJ, 500, L97

Ganeshalingam, M., Li, W., Filippenko, A. V., et al. 2010, ApJS, 190, 418

Gao, H., Lei, W.-H., Zou, Y.-C., Wu, X.-F., & Zhang, B. 2013, New A Rev., 57, 141

Gehrels, N., Chincarini, G., Giommi, P., et al. 2004, ApJ, 611, 1005

Granot, J., Königl, A., & Piran, T. 2006, MNRAS, 370, 1946

Granot, J., Panaitescu, A., Kumar, P., & Woosley, S. E. 2002, ApJ, 570, L61

Granot, J. & Sari, R. 2002, ApJ, 568, 820

Greiner, J., Bornemann, W., Clemens, C., et al. 2008, PASP, 120, 405

Greiner, J., Krühler, T., McBreen, S., et al. 2009, ApJ, 693, 1912

Greiner, J., Krühler, T., Nardini, M., et al. 2013, A&A, 560, A70

Heywood, I. 2020, oxkat: Semi-automated imaging of MeerKAT observations

Holland, S. T., Weidinger, M., Fynbo, J. P. U., et al. 2003, AJ, 125, 2291

Hou, S. J., Geng, J. J., Wang, K., et al. 2014, ApJ, 785, 113

Ioka, K., Toma, K., Yamazaki, R., & Nakamura, T. 2006, A&A, 458, 7

Jacovich, T. E., Beniamini, P., & van der Horst, A. J. 2021, MNRAS, 504, 528

Jonas, J. & MeerKAT Team. 2016, in MeerKAT Science: On the Pathway to the SKA, 1

Kann, D. A., Izzo, L., Levan, A. J., et al. 2021, GRB Coordinates Network, 30583, 1

Kann, D. A., Schady, P., Olivares, E. F., et al. 2018, A&A, 617, A122

Klotz, A., Gendre, B., Stratta, G., et al. 2008, A&A, 483, 847

Kobayashi, S. & Zhang, B. 2007, ApJ, 655, 973

Krühler, T., Küpcü Yoldaş, A., Greiner, J., et al. 2008, ApJ, 685, 376

Kuin, N. P. M., Troja, E., & Swift/UVOT Team. 2021, GRB Coordinates Network, 30572, 1

Kumar, P. & Panaitescu, A. 2000, ApJ, 541, L51

Kumar, P. & Zhang, B. 2015, Phys. Rep., 561, 1

Laskar, T., Berger, E., Margutti, R., et al. 2015, ApJ, 814, 1

Laskar, T., Berger, E., Tanvir, N., et al. 2014, ApJ, 781, 1

Laskar, T., Berger, E., Zauderer, B. A., et al. 2013, ApJ, 776, 119

Lazzati, D., Rossi, E., Covino, S., Ghisellini, G., & Malesani, D. 2002, A&A, 396, L5

Lesage, S., Meegan, C., & Fermi Gamma-ray Burst Monitor Team. 2021, GRB Coordinates Network, 30573, 1

Li, L., Liang, E.-W., Tang, Q.-W., et al. 2012, ApJ, 758, 27

Li, W., Filippenko, A. V., Chornock, R., & Jha, S. 2003, PASP, 115, 844

Liang, E.-W., Li, L., Gao, H., et al. 2013, ApJ, 774, 13

Liang, E.-W., Yi, S.-X., Zhang, J., et al. 2010, ApJ, 725, 2209

Liang, E.-W., Zhang, B.-B., & Zhang, B. 2007, ApJ, 670, 565

Lin, D.-B., Huang, B.-Q., Liu, T., et al. 2018, ApJ, 852, 136

Lipkin, Y. M., Ofek, E. O., Gal-Yam, A., et al. 2004, ApJ, 606, 381

Mangano, V., Holland, S. T., Malesani, D., et al. 2007, A&A, 470, 105

McMullin, J. P., Waters, B., Schiebel, D., Young, W., & Golap, K. 2007, in Astronomical Society of the Pacific Conference Series, Vol. 376, Astronomical Data Analysis Software and Systems XVI, ed. R. A. Shaw, F. Hill, & D. J. Bell, 127

Meegan, C., Lichti, G., Bhat, P. N., et al. 2009, ApJ, 702, 791

Melandri, A., Virgili, F. J., Guidorzi, C., et al. 2014, A&A, 572, A55

Meszaros, P. & Rees, M. J. 1993, ApJ, 405, 278

Mészáros, P. & Rees, M. J. 1997, ApJ, 476, 232

Mészáros, P., Rees, M. J., & Wijers, R. A. M. J. 1998, ApJ, 499, 301

Molinari, E., Vergani, S. D., Malesani, D., et al. 2007, A&A, 469, L13

Mundell, C. G., Melandri, A., Guidorzi, C., et al. 2007, ApJ, 660, 489

Nakar, E., Ando, S., & Sari, R. 2009, ApJ, 703, 675

Nardini, M., Elliott, J., Filgas, R., et al. 2014, A&A, 562, A29

Nardini, M., Greiner, J., Krühler, T., et al. 2011, A&A, 531, A39

Nasa High Energy Astrophysics Science Archive Research Center (Heasarc). 2014, HEAsoft: Unified Release of FTOOLS and XANADU

Nicuesa Guelbenzu, A., Klose, S., Rossi, A., et al. 2011, A&A, 531, L6

Nicuesa Guelbenzu, A., Klose, S., Schmidl, S., & Rau, A. 2021a, GRB Coordinates Network, 30574, 1

Nicuesa Guelbenzu, A., Klose, S., Schmidl, S., Rau, A., & Kann, D. A. 2021b, GRB Coordinates Network, 30584, 1

Nousek, J. A., Kouveliotou, C., Grupe, D., et al. 2006, ApJ, 642, 389

Panaitescu, A. & Kumar, P. 2001, ApJ, 560, L49

Panaitescu, A. & Kumar, P. 2002, ApJ, 571, 779

Panaitescu, A., Mészáros, P., & Rees, M. J. 1998, ApJ, 503, 314

Peng, F., Königl, A., & Granot, J. 2005, ApJ, 626, 966

Perley, R. A., Chandler, C. J., Butler, B. J., & Wrobel, J. M. 2011, ApJ, 739, L1

Planck Collaboration, Ade, P. A. R., Aghanim, N., et al. 2016, A&A, 594, A13

Price, P. A., Harrison, F. A., Galama, T. J., et al. 2001, ApJ, 549, L7

Racusin, J. L., Karpov, S. V., Sokolowski, M., et al. 2008, Nature, 455, 183

Rees, M. J. & Meszaros, P. 1992, MNRAS, 258, 41

Rees, M. J. & Mészáros, P. 1998, ApJ, 496, L1

Ressler, S. M. & Laskar, T. 2017, ApJ, 845, 150

Rhoads, J. E. 1999, ApJ, 525, 737

Roming, P. W. A., Kennedy, T. E., Mason, K. O., et al. 2005, Space Sci. Rev., 120, 95

Rossi, A., Schulze, S., Klose, S., et al. 2011, A&A, 529, A142

Rossi, E., Lazzati, D., & Rees, M. J. 2002, MNRAS, 332, 945

Santana, R., Barniol Duran, R., & Kumar, P. 2014, ApJ, 785, 29

Sari, R. & Mészáros, P. 2000, ApJ, 535, L33

Sari, R. & Piran, T. 1999, ApJ, 520, 641

Sari, R., Piran, T., & Halpern, J. P. 1999, ApJ, 519, L17

Sari, R., Piran, T., & Narayan, R. 1998, ApJ, 497, L17

Schlafly, E. F. & Finkbeiner, D. P. 2011, ApJ, 737, 103

Skrutskie, M. F., Cutri, R. M., Stiening, R., et al. 2006, AJ, 131, 1163

Stahl, B. E., Zheng, W., de Jaeger, T., et al. 2019, MNRAS, 490, 3882

Stamatikos, M., Barthelmy, S. D., Krimm, H. A., et al. 2021, GRB Coordinates Network, 30580, 1

Stetson, P. B. 1987, PASP, 99, 191

Swenson, C. A., Roming, P. W. A., De Pasquale, M., & Oates, S. R. 2013, ApJ, 774, 2

Tody, D. 1993, in Astronomical Society of the Pacific Conference Series, Vol. 52, Astronomical Data Analysis Software and Systems II, ed. R. J. Hanisch, R. J. V. Brissenden, & J. Barnes, 173

Tonry, J. L., Stubbs, C. W., Lykke, K. R., et al. 2012, ApJ, 750, 99

Troja, E., Ambrosi, E., D'Elia, V., et al. 2021, GRB Coordinates Network, 30568, 1

Uhm, Z. L. & Zhang, B. 2014, ApJ, 780, 82

Urata, Y., Huang, K., Takahashi, S., et al. 2014, ApJ, 789, 146

van Paradijs, J., Groot, P. J., Galama, T., et al. 1997, Nature, 386, 686

Vaughan, S., Goad, M. R., Beardmore, A. P., et al. 2006, ApJ, 638, 920

von Kienlin, A., Meegan, C. A., Paciesas, W. S., et al. 2020, The Astrophysical Journal, 893, 46

Wang, X.-G., Zhang, B., Liang, E.-W., et al. 2015, ApJS, 219, 9

Wang, X.-G., Zhang, B., Liang, E.-W., et al. 2018, ApJ, 859, 160

Willingale, R., Genet, F., Granot, J., & O'Brien, P. T. 2010, MNRAS, 403, 1296

Woosley, S. E. 1993, ApJ, 405, 273

Woosley, S. E. & Bloom, J. S. 2006, ARA&A, 44, 507

Xue, R. R., Fan, Y. Z., & Wei, D. M. 2009, A&A, 498, 671

Yi, S.-X., Wu, X.-F., Zou, Y.-C., & Dai, Z.-G. 2020, ApJ, 895, 94

Yost, S. A., Harrison, F. A., Sari, R., & Frail, D. A. 2003, ApJ, 597, 459

Zeh, A., Klose, S., & Hartmann, D. H. 2004, ApJ, 609, 952

Zhang, B. 2018, The Physics of Gamma-Ray Bursts

Zhang, B., Fan, Y. Z., Dyks, J., et al. 2006, ApJ, 642, 354

Zhang, B., Kobayashi, S., & Mészáros, P. 2003, ApJ, 595, 950

Zhang, B. & Mészáros, P. 2001, ApJ, 552, L35

Zhang, B. & Mészáros, P. 2002a, ApJ, 571, 876

Zhang, B. & Mészáros, P. 2002b, ApJ, 566, 712

Zhang, B. & Mészáros, P. 2004, International Journal of Modern Physics A, 19, 2385

Zheng, W., Filippenko, A. V., & KAIT GRB Team. 2021, GRB Coordinates Network, 30582, 1

Zou, Y. C., Wu, X. F., & Dai, Z. G. 2007, A&A, 461, 115

Table 3.4: Same as Table 3.2, but for the fit including the L-band upper limits.

Parameter	ML estimate	MCMC results
p	2.76	$2.76^{+0.03}_{-0.04}$
ϵ_e	1.2×10^{-2}	$1.2^{+0.1}_{-0.2} \times 10^{-1}$
ϵ_B	3.1×10^{-3}	$5.7^{+17.7}_{-2.5} \times 10^{-3}$
$A_\star$	4.1×10^{-2}	$3.1^{+0.8}_{-1.3} \times 10^{-2}$
$E_{\mathrm{K,iso}}$ (10^{52} erg)	39	30^{+11}_{-10}
$A_{\mathrm{V,host}}$ (mag)	0.22	0.23 ± 0.01
t_{jet} (days)	125	186^{+37}_{-87}

3.A Theoretical modelling with MeerKAT L-band limits

We repeated the theoretical modelling following the procedure outlined in Sect. 4.4, but including the MeerKAT L-band limits. The radio light curves from the highest-likelihood model are shown in Fig. 3.9, and the MCMC parameter distributions are presented in Fig. 3.10 and Table 3.4.

Including the MeerKAT L-band limits leads to a poorer fit. This is demonstrated by the highest-likelihood light curve under-predicting the C- and X-band fluxes while still over-predicting the L-band flux, and the actual likelihood value of this fit being lower than for the fit excluding the MeerKAT limits. We measured a maximum log likelihood of 236.9 for the fit without the limits vs 225.1 for the fit including the MeerKAT limits. As we expected, including the MeerKAT data does not lead to a model with a steep enough spectral index to accommodate the non-detections.

3.B Flux measurements

Table 4.1 contains all the X-ray, optical, and radio observations used in this work.

Table 3.5: X-ray/optical/radio flux measurements of GRB 210731A.

Δt (days)	Telescope	Band/Filter	Frequency (Hz)	Flux (μJy)	Uncertainty (μJy)	Detection? (1 = yes)
0.00241	*Swift*/XRT	1 keV	2.42e+17	177.589	27.077	1
0.00243	*Swift*/XRT	1 keV	2.42e+17	144.408	21.527	1
0.00245	*Swift*/XRT	1 keV	2.42e+17	173.501	26.453	1
0.00247	*Swift*/XRT	1 keV	2.42e+17	173.423	27.678	1
0.00249	*Swift*/XRT	1 keV	2.42e+17	135.870	20.254	1
0.00251	*Swift*/XRT	1 keV	2.42e+17	166.523	25.390	1
0.00254	*Swift*/XRT	1 keV	2.42e+17	104.861	16.356	1
0.00257	*Swift*/XRT	1 keV	2.42e+17	122.493	18.260	1
0.00259	*Swift*/XRT	1 keV	2.42e+17	118.424	17.654	1
0.00262	*Swift*/XRT	1 keV	2.42e+17	132.423	20.190	1
0.00264	*Swift*/XRT	1 keV	2.42e+17	115.389	17.201	1
0.00267	*Swift*/XRT	1 keV	2.42e+17	119.856	19.577	1
0.00270	*Swift*/XRT	1 keV	2.42e+17	102.343	17.113	1
0.00273	*Swift*/XRT	1 keV	2.42e+17	87.334	13.938	1
0.00276	*Swift*/XRT	1 keV	2.42e+17	106.299	16.965	1
0.00279	*Swift*/XRT	1 keV	2.42e+17	94.213	15.036	1
0.00283	*Swift*/XRT	1 keV	2.42e+17	93.477	13.935	1
0.00287	*Swift*/XRT	1 keV	2.42e+17	72.925	13.765	1
0.00290	*Swift*/XRT	1 keV	2.42e+17	89.665	14.310	1
0.00294	*Swift*/XRT	1 keV	2.42e+17	85.993	14.046	1

Table 3.5: Continued.

Δt (days)	Telescope	Band/Filter	Frequency (Hz)	Flux (μJy)	Uncertainty (μJy)	Detection? (1 = yes)
0.00298	*Swift*/XRT	1 keV	2.42e+17	64.979	11.965	1
0.00302	*Swift*/XRT	1 keV	2.42e+17	96.119	15.340	1
0.00305	*Swift*/XRT	1 keV	2.42e+17	70.237	13.596	1
0.00309	*Swift*/XRT	1 keV	2.42e+17	64.675	13.529	1
0.13866	*Swift*/XRT	1 keV	2.42e+17	0.507	0.116	1
0.20459	*Swift*/XRT	1 keV	2.42e+17	0.438	0.114	1
0.20839	*Swift*/XRT	1 keV	2.42e+17	0.538	0.093	1
0.27115	*Swift*/XRT	1 keV	2.42e+17	0.415	0.109	1
0.27459	*Swift*/XRT	1 keV	2.42e+17	0.455	0.103	1
0.33652	*Swift*/XRT	1 keV	2.42e+17	0.441	0.115	1
0.33905	*Swift*/XRT	1 keV	2.42e+17	0.378	0.100	1
0.34243	*Swift*/XRT	1 keV	2.42e+17	0.285	0.075	1
0.34705	*Swift*/XRT	1 keV	2.42e+17	0.287	0.076	1
0.35107	*Swift*/XRT	1 keV	2.42e+17	0.427	0.087	1
0.40418	*Swift*/XRT	1 keV	2.42e+17	0.280	0.073	1
0.40918	*Swift*/XRT	1 keV	2.42e+17	0.283	0.074	1
0.41349	*Swift*/XRT	1 keV	2.42e+17	0.233	0.061	1
0.42004	*Swift*/XRT	1 keV	2.42e+17	0.282	0.060	1
0.56853	*Swift*/XRT	1 keV	2.42e+17	0.234	0.061	1
0.60579	*Swift*/XRT	1 keV	2.42e+17	0.165	0.043	1
0.61160	*Swift*/XRT	1 keV	2.42e+17	0.207	0.046	1
0.68902	*Swift*/XRT	1 keV	2.42e+17	0.125	0.027	1
0.74695	*Swift*/XRT	1 keV	2.42e+17	0.133	0.035	1
0.77010	*Swift*/XRT	1 keV	2.42e+17	0.150	0.032	1
2.50026	*Swift*/XRT	1 keV	2.42e+17	0.018	0.005	1
0.00368	MeerLICHT	q	5.169e+14	59.71	4.40	1
0.00485	MeerLICHT	u	7.889e+14	74.48	13.03	1
0.00607	MeerLICHT	q	5.169e+14	106.67	3.93	1
0.00719	MeerLICHT	g	6.246e+14	97.28	5.38	1
0.00844	MeerLICHT	q	5.169e+14	106.67	3.93	1
0.00962	MeerLICHT	r	4.789e+14	128.24	7.09	1
0.01086	MeerLICHT	q	5.169e+14	97.28	3.58	1
0.01210	MeerLICHT	i	3.919e+14	167.50	13.88	1
0.01320	MeerLICHT	q	5.169e+14	80.91	3.73	1
0.01447	MeerLICHT	z	3.276e+14	124.75	28.72	1
0.01575	MeerLICHT	q	5.169e+14	74.48	4.12	1
0.01823	MeerLICHT	q	5.169e+14	57.55	3.71	1
0.01950	MeerLICHT	g	6.246e+14	50.59	5.59	1
0.02076	MeerLICHT	q	5.169e+14	56.50	3.64	1
0.02193	MeerLICHT	r	4.789e+14	68.55	7.58	1
0.02311	MeerLICHT	q	5.169e+14	58.62	3.78	1
0.02438	MeerLICHT	i	3.919e+14	77.27	14.23	1
0.02564	MeerLICHT	q	5.169e+14	61.38	3.96	1
0.02691	MeerLICHT	z	3.276e+14	100.01	32.24	1
0.02818	MeerLICHT	q	5.169e+14	69.19	5.10	1
0.02936	MeerLICHT	u	7.889e+14	47.87	15.87	1
0.03061	MeerLICHT	q	5.169e+14	67.30	4.34	1

Table 3.5: Continued.

Δt (days)	Telescope	Band/Filter	Frequency (Hz)	Flux (μJy)	Uncertainty (μJy)	Detection? (1 = yes)
0.03189	MeerLICHT	g	6.246e+14	67.30	7.44	1
0.03318	MeerLICHT	q	5.169e+14	64.87	3.58	1
0.03438	MeerLICHT	r	4.789e+14	78.71	7.97	1
0.03559	MeerLICHT	q	5.169e+14	84.73	4.68	1
0.03684	MeerLICHT	i	3.919e+14	86.30	12.72	1
0.03811	MeerLICHT	q	5.169e+14	82.42	4.55	1
0.03942	MeerLICHT	z	3.276e+14	128.24	35.43	1
0.04071	MeerLICHT	q	5.169e+14	87.91	4.05	1
0.04199	MeerLICHT	u	7.889e+14	55.47	17.37	1
0.04321	MeerLICHT	q	5.169e+14	86.30	3.97	1
0.04450	MeerLICHT	g	6.246e+14	77.99	6.46	1
0.04577	MeerLICHT	q	5.169e+14	90.37	4.16	1
0.04696	MeerLICHT	r	4.789e+14	88.72	8.17	1
0.04815	MeerLICHT	q	5.169e+14	93.76	5.18	1
0.04939	MeerLICHT	i	3.919e+14	154.18	12.78	1
0.05064	MeerLICHT	q	5.169e+14	92.90	4.28	1
0.05189	MeerLICHT	z	3.276e+14	197.71	38.24	1
0.05312	MeerLICHT	q	5.169e+14	97.28	3.58	1
0.05430	MeerLICHT	u	7.889e+14	76.56	18.33	1
0.05548	MeerLICHT	q	5.169e+14	106.67	4.91	1
0.05675	MeerLICHT	g	6.246e+14	89.54	6.60	1
0.05801	MeerLICHT	q	5.169e+14	103.76	4.78	1
0.05919	MeerLICHT	r	4.789e+14	125.90	9.28	1
0.06037	MeerLICHT	q	5.169e+14	101.87	4.69	1
0.06149	MeerLICHT	i	3.919e+14	124.75	12.64	1
0.06275	MeerLICHT	q	5.169e+14	101.87	5.63	1
0.06398	MeerLICHT	z	3.276e+14	164.45	46.95	1
0.06522	MeerLICHT	q	5.169e+14	100.01	5.53	1
0.06766	MeerLICHT	q	5.169e+14	100.93	6.51	1
0.06893	MeerLICHT	g	6.246e+14	75.86	7.69	1
0.07020	MeerLICHT	q	5.169e+14	98.18	5.43	1
0.07143	MeerLICHT	r	4.789e+14	115.88	11.74	1
0.07275	MeerLICHT	q	5.169e+14	99.09	5.48	1
0.07403	MeerLICHT	i	3.919e+14	151.37	16.73	1
0.07527	MeerLICHT	q	5.169e+14	100.93	5.58	1
0.07651	MeerLICHT	z	3.276e+14	210.88	40.79	1
0.08293	MeerLICHT	q	5.169e+14	97.28	6.27	1
0.08413	MeerLICHT	r	4.789e+14	114.82	14.81	1
0.08532	MeerLICHT	q	5.169e+14	103.76	6.69	1
0.08659	MeerLICHT	i	3.919e+14	129.43	23.84	1
0.08914	MeerLICHT	z	3.276e+14	307.63	62.33	1
0.09540	MeerLICHT	q	5.169e+14	120.23	7.75	1
0.09662	MeerLICHT	r	4.789e+14	121.35	14.53	1
0.10654	MeerLICHT	g	6.246e+14	60.82	9.52	1
0.10781	MeerLICHT	q	5.169e+14	92.90	6.85	1
0.10899	MeerLICHT	r	4.789e+14	114.82	10.58	1
0.11016	MeerLICHT	q	5.169e+14	93.76	6.05	1

Table 3.5: Continued.

Δt (days)	Telescope	Band/Filter	Frequency (Hz)	Flux (μJy)	Uncertainty (μJy)	Detection? (1 = yes)
0.11138	MeerLICHT	*i*	3.919e+14	110.67	17.33	1
0.11252	MeerLICHT	*q*	5.169e+14	98.18	6.33	1
0.11377	MeerLICHT	*z*	3.276e+14	157.05	40.50	1
0.11503	MeerLICHT	*q*	5.169e+14	99.09	6.39	1
0.11754	MeerLICHT	*q*	5.169e+14	104.72	6.75	1
0.11877	MeerLICHT	*g*	6.246e+14	69.83	10.29	1
0.12003	MeerLICHT	*q*	5.169e+14	125.90	6.96	1
0.12121	MeerLICHT	*r*	4.789e+14	140.61	14.25	1
0.12248	MeerLICHT	*q*	5.169e+14	108.65	10.01	1
0.13362	MeerLICHT	*r*	4.789e+14	131.83	14.57	1
0.13482	MeerLICHT	*q*	5.169e+14	114.82	9.52	1
0.13604	MeerLICHT	*i*	3.919e+14	134.28	25.97	1
0.13725	MeerLICHT	*q*	5.169e+14	113.77	11.53	1
0.13958	MeerLICHT	*q*	5.169e+14	100.01	11.05	1
0.14195	MeerLICHT	*q*	5.169e+14	127.07	8.19	1
0.14305	MeerLICHT	*g*	6.246e+14	97.28	11.65	1
0.14430	MeerLICHT	*q*	5.169e+14	125.90	6.96	1
0.14550	MeerLICHT	*r*	4.789e+14	159.97	14.73	1
0.14670	MeerLICHT	*q*	5.169e+14	136.78	7.56	1
0.14797	MeerLICHT	*i*	3.919e+14	169.05	26.47	1
0.15050	MeerLICHT	*z*	3.276e+14	275.44	48.20	1
0.16412	MeerLICHT	*q*	5.169e+14	157.05	21.70	1
0.16650	MeerLICHT	*q*	5.169e+14	141.91	27.45	1
0.16775	MeerLICHT	*g*	6.246e+14	119.13	24.14	1
0.913	MeerLICHT	*r*	4.789e+14	25.12	4.40	1
0.915	MeerLICHT	*q*	5.169e+14	24.21	1.56	1
0.915	MeerLICHT	*g*	6.246e+14	16.75	3.70	1
0.918	MeerLICHT	*i*	3.919e+14	41.31	8.37	1
1.018	MeerLICHT	*r*	4.789e+14	21.09	4.66	1
1.018	MeerLICHT	*q*	5.169e+14	23.12	1.28	1
1.020	MeerLICHT	*g*	6.246e+14	17.70	2.77	1
1.023	MeerLICHT	*i*	3.919e+14	32.21	8.31	1
2.03	MeerLICHT	*q*	5.169e+14	7.52	0.83	1
3.00	MeerLICHT	*q*	5.169e+14	3.53	0.68	1
0.00277	*Swift*/UVOT	*white*	7.488e+14	16.29	4.80	1
0.13848	*Swift*/UVOT	*v*	5.511e+14	120.23	19.93	1
0.20686	*Swift*/UVOT	*b*	6.848e+14	92.90	7.70	1
0.27287	*Swift*/UVOT	*uvm*2	1.319e+15	13.43	2.60	1
0.340	*Swift*/UVOT	*uvw*1	1.115e+15	16.00	2.21	1
0.349	*Swift*/UVOT	*u*	8.583e+14	47.43	3.93	1
0.408	*Swift*/UVOT	*uvw*2	1.401e+15	5.15	1.23	1
0.418	*Swift*/UVOT	*v*	5.511e+14	87.10	12.03	1
0.560	*Swift*/UVOT	*b*	6.848e+14	36.31	7.69	1
0.606	*Swift*/UVOT	*uvm*2	1.319e+15	3.53	1.40	1
0.650	*Swift*/UVOT	*uvw*1	1.115e+15	5.30	1.37	1
0.694	*Swift*/UVOT	*u*	8.583e+14	13.80	3.94	1
0.747	*Swift*/UVOT	*uvw*2	1.401e+15	3.40	1.13	0

Table 3.5: Continued.

Δt (days)	Telescope	Band/Filter	Frequency (Hz)	Flux (μJy)	Uncertainty (μJy)	Detection? (1 = yes)
0.757	*Swift*/UVOT	v	5.511e+14	27.04	11.21	1
0.802	*Swift*/UVOT	b	6.848e+14	21.09	7.19	1
2.79	*Swift*/UVOT	$uvm2$	1.319e+15	1.91	0.64	0
2.90	*Swift*/UVOT	$uvw1$	1.115e+15	2.25	0.75	0
3.20	*Swift*/UVOT	u	8.583e+14	7.24	2.41	0
3.21	*Swift*/UVOT	b	6.848e+14	15.42	5.14	0
3.21	*Swift*/UVOT	*white*	7.488e+14	3.56	1.19	0
3.21	*Swift*/UVOT	v	5.511e+14	35.32	11.77	0
3.71	*Swift*/UVOT	$uvw2$	1.401e+15	1.79	0.60	0
0.18419	GROND	g'	6.536e+14	116.96	1.08	1
0.18419	GROND	r'	4.820e+14	148.60	1.37	1
0.18419	GROND	i'	3.924e+14	188.81	1.74	1
0.18419	GROND	z'	3.335e+14	227.00	2.09	1
0.18437	GROND	J	2.418e+14	307.63	5.67	1
0.18437	GROND	H	1.820e+14	428.57	7.89	1
0.18437	GROND	K	1.381e+14	554.66	15.33	1
1.225	GROND	g'	6.536e+14	13.68	0.13	1
1.225	GROND	r'	4.820e+14	18.20	0.17	1
1.225	GROND	i'	3.924e+14	22.91	0.42	1
1.225	GROND	z'	3.335e+14	27.29	0.50	1
1.225	GROND	J	2.418e+14	46.99	2.60	1
1.225	GROND	H	1.820e+14	57.02	5.78	1
1.225	GROND	K	1.381e+14	58.62	17.82	1
2.21	GROND	g'	6.536e+14	5.11	0.09	1
2.21	GROND	r'	4.820e+14	6.25	0.17	1
2.21	GROND	i'	3.924e+14	7.24	0.40	1
2.21	GROND	z'	3.335e+14	9.64	0.53	1
2.21	GROND	J	2.418e+14	20.14	2.78	1
2.21	GROND	H	1.820e+14	22.29	5.75	1
2.21	GROND	K	1.381e+14	59.71	19.90	0
5.25	GROND	g'	6.536e+14	1.51	0.14	1
5.25	GROND	r'	4.820e+14	1.45	0.17	1
5.25	GROND	i'	3.924e+14	1.14	0.38	0
5.25	GROND	z'	3.335e+14	1.57	0.52	0
5.25	GROND	J	2.418e+14	8.32	2.77	0
5.25	GROND	H	1.820e+14	15.56	5.19	0
5.25	GROND	K	1.381e+14	49.21	16.40	0
285.0	GROND	g'	6.536e+14	0.40	0.07	1
285.0	GROND	r'	4.820e+14	0.48	0.09	1
285.0	GROND	i'	3.924e+14	0.76	0.25	0
285.0	GROND	J	2.418e+14	6.31	2.10	0
285.0	GROND	H	1.820e+14	10.97	3.66	0
285.0	GROND	K	1.381e+14	27.54	9.18	0
0.385	KAIT	*clear*	4.722e+14	104.72	4.82	1
1.183	VLT	r	4.830e+14	18.54	0.34	1
1.186	VLT	g	6.394e+14	13.18	0.24	1
1.189	VLT	z	3.124e+14	28.84	0.80	1

Table 3.5: Continued.

Δt (days)	Telescope	Band/Filter	Frequency (Hz)	Flux (μJy)	Uncertainty (μJy)	Detection? (1 = yes)
2.09	NOT	r	4.830e+14	6.79	0.25	1
2.10	NOT	z	3.124e+14	12.94	1.07	1
6.08	NOT	r	4.830e+14	1.05	0.18	1
10.8	MeerKAT	L	1.4e+09	42.0	14.0	0
18.2	VLA	C	6.0e+09	136.0	32.0	1
18.2	VLA	X	1.0e+10	182.0	8.0	1
34.1	MeerKAT	L	1.4e+09	41.1	13.7	0
34.2	VLA	C	6.0e+09	140.0	10.0	1
34.2	VLA	X	1.0e+10	199.0	9.0	1
59.7	MeerKAT	L	1.4e+09	40.2	13.4	0
67.1	VLA	C	6.0e+09	102.0	9.0	1
67.1	VLA	X	1.0e+10	50.0	15.0	1
118.0	VLA	C	6.0e+09	66.0	11.0	1
118.0	VLA	X	1.0e+10	37.0	7.0	1

Notes. All times are relative to the *Swift*/BAT trigger time. X-ray, optical and radio data are separated by horizontal lines. Detections are all at least at the 3σ level except for the first UVOT/*white* detection, which was at the 2.3σ level. Optical and radio upper limits are at the 3σ level.

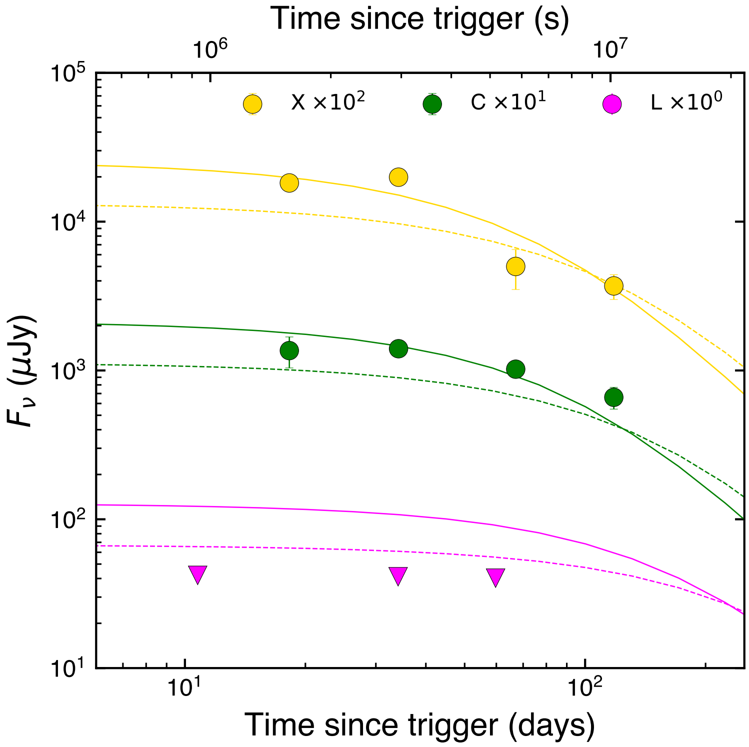

Figure 3.9: Highest-likelihood model for the fit that includes the L-band data (dashed lines) and the fit that excludes the L-band data (solid lines). The fit to the optical and X-ray light curves is similar in both models.

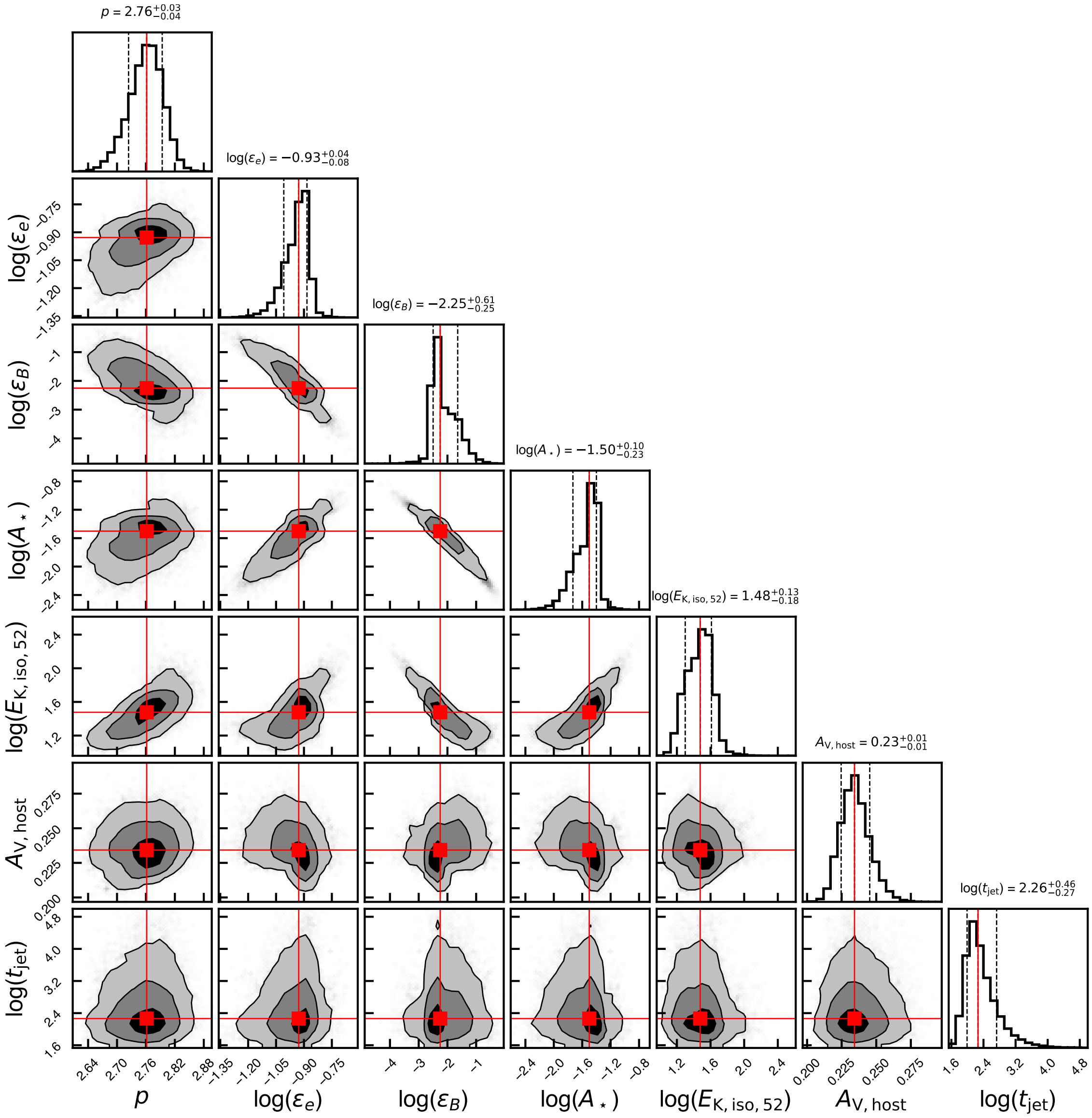

Figure 3.10: Same as Fig. 4.10, but for the fit including the L-band upper limits.

Chapter 4

The ultra-long GRB 220627A at $z = 3.08$

S. de Wet[1], L. Izzo[2], P.J. Groot[1,3,4], S. Bisero[5], V. D'Elia[6,7], M. De Pasquale[8], D.H. Hartmann[9], K.E. Heintz[10,11], P. Jakobsson[12], T. Laskar[13], A. Levan[3], A. Martin-Carrillo[14], A. Melandri[7], A. Nicuesa Guelbenzu[15], G. Pugliese[16], A. Rossi[17], A. Saccardi[5], S. Savaglio[17,18,19], P. Schady[20], N.R. Tanvir[21], H. van Eerten[20], S. Vergani[5]

Based on the paper published in Astronomy & Astrophysics, Volume 677, A32, September 2023

---

[1] Inter-University Institute for Data Intensive Astronomy & Department of Astronomy, University of Cape Town, Private Bag X3, Rondebosch, 7701, South Africa

[2] DARK, Niels Bohr Institute, University of Copenhagen, Jagtvej 128, 2200 Copenhagen, Denmark

[3] Department of Astrophysics/IMAPP, Radboud University, P.O. Box 9010, 6500 GL, Nijmegen, The Netherlands

[4] South African Astronomical Observatory, P.O. Box 9, 7935, Observatory, South Africa

[5] GEPI, Observatoire de Paris, Université PSL, CNRS, 5 Place Jules Janssen, 92190 Meudon, France

[6] Space Science Data Center (SSDC) - Agenzia Spaziale Italiana (ASI), 00133 Roma, Italy

[7] INAF - Osservatorio Astronomico di Roma, Via Frascati 33, 00040 Monte Porzio Catone, Italy

[8] Mathematics, Informatics, Physics, and Earth Science Department, University of Messina, Polo Papardo, Via F. S. D'Alcontres 31, 98166 Messina, Italy

[9] Department of Physics and Astronomy, Clemson University, Clemson, SC 29634, USA

[10] Cosmic Dawn Center (DAWN), Denmark

[11] Niels Bohr Institute, University of Copenhagen, Jagtvej 128, 2200 Copenhagen, Denmark

[12] Centre for Astrophysics and Cosmology, Science Institute, University of Iceland, Dunhagi 5, 107 Reykjavík, Iceland

[13] Department of Physics & Astronomy, University of Utah, Salt Lake City, UT 84112, USA

[14] School of Physics and Centre for Space Research, University College Dublin, Belfield, D04 V1W8 Dublin, Ireland

[15] Thüringer Landessternwarte Tautenburg, Sternwarte 5, 07778 Tautenburg, Germany

[16] Astronomical Institute Anton Pannekoek, University of Amsterdam, 1090 GE Amsterdam, The Netherlands

[17] INAF – Osservatorio di Astrofisica e Scienza dello Spazio, Via Piero Gobetti 93/3, 40129 Bologna, Italy

[18] Department of physics, University of Calabria, Via P. Bucci, Arcavacata di Rende (CS), Italy

[19] INFN - Laboratori Nazionali di Frascati, Frascati, Italy

[20] Physics Department, University of Bath, Claverton Down, Bath, BA2 7AY, UK

[21] School of Physics and Astronomy, University of Leicester, University Road, Leicester, LE1 7RH, United Kingdom

Abstract

GRB 220627A is a rare burst with two distinct γ-ray emission episodes separated by almost 1000 s that triggered the *Fermi* Gamma-ray Burst Monitor twice. High-energy GeV emission was detected by the *Fermi* Large Area Telescope coincident with the first emission episode but not the second.The discovery of the optical afterglow with MeerLICHT led to MUSE observations which secured the burst redshift to $z = 3.08$, making this the most distant ultra-long gamma-ray burst (GRB) detected to date. The progenitors of some ultra-long GRBs have been suggested in the literature to be different to those of normal long GRBs. Our aim is to determine whether the afterglow and host properties of GRB 220627A agree with this interpretation. We performed empirical and theoretical modelling of the afterglow data within the external forward shock framework, and determined the metallicity of the GRB environment through modelling the absorption lines in the MUSE spectrum. Our optical data show evidence for a jet break in the light curve at ∼1.2 days, while our theoretical modelling shows a preference for a homogeneous circumburst medium. Our forward shock parameters are typical for the wider GRB population, and we find that the environment of the burst is characterised by a sub-solar metallicity. Our observations and modelling of GRB 220627A do not suggest that a different progenitor compared to the progenitor of normal long GRBs is required. We find that more observations of ultra-long GRBs are needed to determine if they form a separate population with distinct prompt and afterglow features, and possibly distinct progenitors.

4.1 Introduction

Gamma-ray bursts (GRBs) are flashes of γ-rays lasting from milliseconds to hours typically with isotropic γ-ray luminosities of $\sim 10^{51} - 10^{53}$ erg s^{-1}, making them the most luminous explosions observed in the Universe (Zhang 2018). GRBs have traditionally been separated into long and short bursts based on an observed bimodality in their duration distribution, with 2 s taken as the dividing line (Kouveliotou et al. 1993). Short bursts are thought to be caused by the coalescence of two compact objects involving a neutron star, while long bursts are thought to result from the collapse of a massive Wolf-Rayet star, though recent observations have shown there is an overlap between these two classes (e.g. GRB 211211A; Rastinejad et al. 2022; Yang et al. 2022).

A very small number of bursts have been detected with extremely long durations greater than 1000 s (e.g. GRBs 091024A, 101225A, 111209A, 130925A; Gruber et al. 2011; Virgili et al. 2013; Thöne et al. 2011; Levan et al. 2014; Gendre et al. 2013; Stratta et al. 2013; Evans et al. 2014; Piro et al. 2014). Some authors have suggested that these GRBs form a distinct class of so-called ultra-long GRBs whose progenitors may be different with respect to the collapsar model (Gendre et al. 2013; Levan et al. 2014). Levan et al. (2014) studied three ultra-long GRBs – GRB 101225A, GRB 111209A, and GRB 121027A – and found that they had very similar long-lasting X-ray emission with flares and were situated close to the cores of highly star-forming dwarf galaxies. The extremely long duration of these bursts led them to conclude that their central engines were active for much longer than normal long GRBs, and therefore their progenitors may be blue supergiant stars (Mészáros & Rees 2001; Nakauchi et al. 2013) which have much larger radii than the compact Wolf-Rayet stars that are commonly regarded as the progenitors of long GRBs (Woosley & Bloom 2006). This was the preferred explanation by Gendre et al. (2013) for the extremely long duration of ∼25000 s for GRB 111209A, where the additional mass from the outer layers of such a star can power the central engine for much longer, leading to longer-duration γ-ray emission.

Zhang et al. (2014), however, pointed out that not all bursts that had been claimed as ultra-long were actually ultra-long in γ-rays (e.g. GRB 121027A). Instead, the long duration of highly variable X-ray light curves had been used to infer the ultra-long duration (Levan et al. 2014). *Swift* observations of X-ray flares and internal plateaus have shown that the central engine duration is much longer than T_{90} values suggest. Zhang et al. (2014) therefore used X-ray data in addition to γ-ray data to derive central engine durations for 343 GRBs, and found that 21.9% of GRBs have durations $t_{\mathrm{burst}} \gtrsim 10^3$ s, and 11.5% have $t_{\mathrm{burst}} \gtrsim 10^4$ s. The inference is that ultra-long GRBs may be the tail of a single long GRB population and do not require a separate, blue supergiant progenitor even though the data do not exclude it. Additionally, observations suggest that the afterglow properties of ultra-long GRBs are not different to those of other, classical, long GRBs (Virgili et al. 2013). In order to assess the claim that ultra-long GRBs form a distinct population compared to other long GRBs, further multi-wavelength observational evidence encompassing afterglow and host galaxy properties is needed.

On 2022 June 27, the *Fermi* Gamma-ray Burst Monitor (GBM; Meegan et al. 2009) was triggered by two events separated by 956 s, leading to the speculation that GRB 220627A was a gravitationally lensed or ultra-long GRB with a duration of ∼1000 s (Roberts et al. 2022). The Large Area Telescope (LAT; Atwood et al. 2009) aboard *Fermi* detected high-energy photons coincident with the first GBM trigger and localised the first burst to a 0.2 degree-radius error circle (di Lalla et al. 2022), which led to the eventual identification of the optical and X-ray afterglows at ∼0.8 days post-trigger. Here we report the results of our observational follow-up campaign and place GRB 220627A in the context of the ultra-long GRB population.

We note that there is no universally agreed-upon definition for ultra-long GRBs, so we defer to adopting the convention that ultra-long bursts satisfy $T_{90} \gtrsim 1000$ s, as used by Lien et al. (2016). We report all uncertainties at the 1σ level unless stated otherwise, and all magnitudes in the AB system. We follow the conventions with $F_\nu \propto \nu^\beta t^\alpha$ and $N_E(E) \propto E^{-\Gamma}$, and adopt a Lambda cold dark matter (ΛCDM) cosmology with $\Omega_m = 0.31$, $\Omega_\Lambda = 0.69$, and $H_0 = 68$ km s^{-1} Mpc^{-1} (Planck Collaboration et al. 2016). The first *Fermi*/GBM trigger occurred at 21:21:00.09 UT. We take this time as T_0 for GRB 220627A, and reference all other observations with respect to this time.

4.2 Observations

4.2.1 MeerLICHT optical afterglow discovery

MeerLICHT is a 65-cm aperture fully-robotic optical telescope located at the South African Astronomical Observatory (SAAO) site in Sutherland, South Africa (Bloemen et al. 2016). The primary science goal behind MeerLICHT is to provide simultaneous optical coverage of the radio sky as observed by the 64-antennae MeerKAT radio array, which is also located within the arid Karoo region of the South African interior. MeerLICHT's wide field-of-view of 2.7 deg^2 ($98.6' \times 98.6'$) and robotic operation make it suitable for the discovery of new transients and follow-up of events with large error boxes on the plane of the sky, such as gravitational wave (GW) events and poorly-localised GRBs, while its six filters (SDSS *ugriz* plus a wide *q* filter spanning 440–720 nm, roughly equivalent to $g + r$) make it suitable for multi-colour monitoring of transients.

MeerLICHT began an observing programme in June 2021 to follow-up GRBs detected by the *Swift* and *Fermi* missions. For *Swift* bursts the aim is to start observing Burst Alert Telescope (BAT) error boxes as soon as possible after a trigger, regardless of whether an X-ray or optical counterpart is discovered by *Swift*. For *Fermi* bursts the aim is to observe a cumulative probability of at least 70% of the GBM HEALPix skymaps with 80 or fewer telescope pointings, an observing criterion which naturally targets brighter bursts since they are better-localised. Observations are automatically triggered for bursts if they can begin within five hours of a trigger, with manual scheduling available for specific cases such as LAT-detected bursts or bursts with a high scientific interest.

GRB 220627A triggered automatic observations with MeerLICHT starting 21 minutes after the trigger at 21:42:23 UT, when the fields became visible given the telescope's observing constraints. The first GBM trigger had a 90% (50%) error area of 216.5 (52.7) deg^2, while the second trigger had a 90% (50%) error area of 213.8 (32.5) deg^2. A total of 52 fields encompassing a cumulative probability of 71% of the first trigger GBM skymap (see Fig. 4.1) were observed during the 1.6 hours that MeerLICHT was observing. All observations consisted of 60 s *q*-band exposures, since the *q*-band is our most sensitive band and also has the most complete set of archival reference images. Our automatic scheduling aims to target the highest probability fields first, but due to the western fields setting first only the most eastern fields were scheduled. All 52 fields were observed at least once in the q band, while ten of the most eastern fields were observed twice encompassing a cumulative probability of 7.5%. Two of these ten fields were observed three times. The MeerLICHT transient detection pipeline was used to identify two afterglow candidates which were reported via the GCN within six hours of the first trigger (Groot et al. 2022).

The next morning at 07:00:40 UT, a *Fermi*/LAT GCN circular indicated that high-energy γ-rays had been detected along with a 0.2 degree radius localisation - a much smaller error box than the GBM error box (di Lalla et al. 2022). The LAT error box straddled two MeerLICHT fields which had not been observed on the previous night, ruling out our two initial afterglow candidates. We scheduled 2×300 s observations in the q-band for these fields in order to search for an optical afterglow within the LAT error box. Observations began just after the evening twilight under new moon conditions at 17:12:15 UT, at approximately 0.83 days post-trigger. *Swift*/XRT target of opportunity (ToO) observations identified 15 X-ray sources[1] within the LAT error box that may have been associated with GRB 220627A (Evans & Swift Team 2022), most having error regions with radii smaller than $8''$. Among the three most promising[2] candidates (green in Fig. 4.1), only one source was uncatalogued. Our two MeerLICHT images at 0.84 and 0.87 days showed a new optical transient within the error box of this source at coordinates $\alpha = 13^{\mathrm{h}}25^{\mathrm{m}}28.49^{\mathrm{s}}$, $\delta = -32^{\mathrm{d}}25^{\mathrm{m}}33.31^{\mathrm{s}}$ (ICRS). The brightness of $q = 21.25 \pm 0.09$ mag in our first exposure, and the lack of any source at the same position down to $q > 21.71$ in an archival image from two months earlier made it likely that this source was indeed the optical afterglow to GRB 220627A (de Wet et al. 2022). The source was confirmed as the afterglow through spectroscopic observations with MUSE mounted on the VLT (see Sect. 4.2.5 below, and Izzo et al. 2022).

4.2.2 Prompt emission

The duration of the burst associated with the first GBM trigger was $T_{90} = 136.71 \pm 1.28$ s, while that of the burst associated with the second trigger was $T_{90} = 126.98 \pm 8.84$ s, as taken from the online Fermi GBM Burst Catalog (von Kienlin et al. 2020). The $10 - 1000$ keV fluence for the first and second triggers (from the Burst Catalog) are $(4.54 \pm 0.01) \times 10^{-5}$ erg cm^{-2} and $(1.08 \pm 0.02) \times 10^{-5}$ erg cm^{-2}, resulting in a total fluence of $(5.62 \pm 0.02) \times 10^{-5}$ erg cm^{-2} across both episodes. At the burst redshift of $z = 3.08$ (Sect. 4.2.5) this results in a high isotropic γ-ray energy of $E_{\gamma,\mathrm{iso}} = (4.81 \pm 0.02) \times 10^{54}$ erg. Among the $\sim$130 GRBs with known redshift listed in the 10-year Fermi-GBM Gamma-Ray Burst Spectral Catalog (Poolakkil et al. 2021), only two bursts have a larger isotropic γ-ray energy: GRBs 090323 and 160625B. Both emission episodes were also detected by *Konus-Wind* (Aptekar et al. 1995). The *Konus-Wind* light curve had a similar structure to the GBM light curve, though it was reported that a weak emission tail may have been present in the soft energy bands ($20 - 100$ keV) lasting up until $T_0 + 3700$ s (Frederiks et al. 2022).

GeV photons were detected by *Fermi*/LAT coincident with the first GBM trigger but not with the second one (di Lalla et al. 2022). The detection of GeV photons makes GRB 220627A the first ultra-long (with duration > 1000 s) GRB detected at these energies. The prompt emission from GBM and LAT was studied in detail by Huang et al. (2022). They found that the time-integrated spectrum for the first emission episode is best described by a cutoff power law plus a power law component, where the power law component (with $\Gamma = 1.92 \pm 0.05$) is necessary to account for the detected LAT photons. The second emission episode is best described by a cutoff power law alone. The cutoff energy for the first and second episodes are $E_c = 286.96 \pm 38.00$ keV and $E_c = 248.64 \pm 66.58$ keV, while their low-energy photon indices are $\Gamma = 0.73 \pm 0.10$ and $\Gamma = 1.06 \pm 0.11$, respectively. Huang et al. (2022) argue that the gravitational-lensing scenario to explain the two triggers can be ruled out at the 5.1σ level based on the non-detection of any LAT

---

[1] See the list of sources at the UK Swift Science Data Centre website.

[2] After source detection, *Swift* sources are given a quality flag (Good, Reasonable or Poor) which indicates how likely a source is to be real.

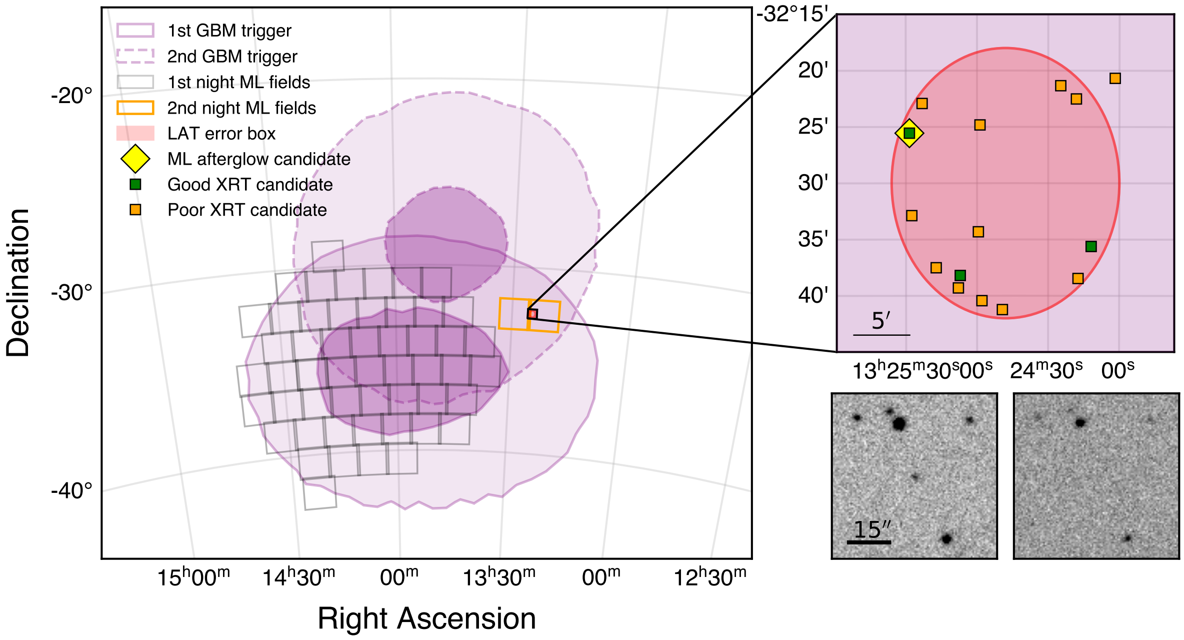

Figure 4.1: Localisation of GRB 220627A. *Left:* 50% and 90% uncertainty regions for both GBM triggers associated with GRB 220627A are outlined in purple. A total of 52 MeerLICHT fields (grey boxes) were automatically scheduled for observations immediately following the first trigger. Following the announcement of the *Fermi*/LAT localisation region (red circle), two MeerLICHT fields (orange boxes) were scheduled for observations the following night. *Top right:* *Swift*/XRT ToO observations identified 15 X-ray sources within the LAT error box. MeerLICHT identified a new optical transient within the error box of the third 'good' XRT source (yellow diamond). *Bottom right:* First MeerLICHT detection of the new transient (left), and an archival image taken two months previously on 2022 April 26 (right). Both thumbnails are $1' \times 1'$ in dimension.

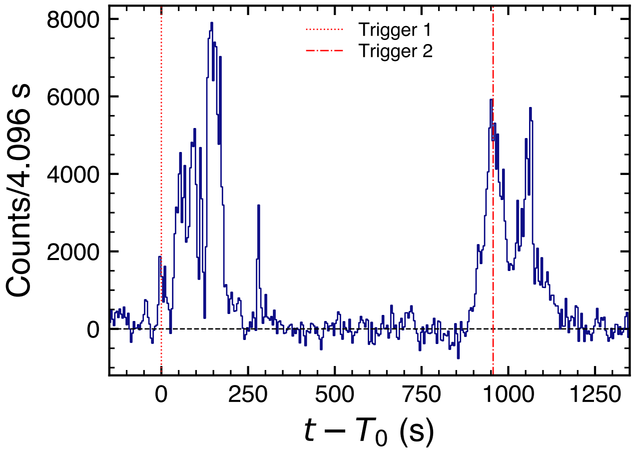

Figure 4.2: Prompt emission light curve created through summing the background-subtracted light curves from seven GBM NaI detectors. We measure $T_{90} \approx 1092$ s. Vertical lines mark the *Fermi*/GBM trigger times.

photons coincident with the second trigger. Furthermore, they place a lower limit on the bulk Lorentz factor of $\Gamma \geq 300$ by using the optical depth to pair production method along with the highest energy LAT photon with an energy of 15.3 GeV.

In order to quantify the duration of GRB 220627A across both emission episodes, we obtained the CSPEC data from the NASA HEASARC data archive for the NaI detectors where the burst position was within 50° of the detector normal – these were naturally the detectors with the strongest detected signal. For trigger 1 these were detectors $n0$, $n1$, $n3$ and $n6$, while for trigger 2 these were $n3$, $n4$, $n6$, $n7$, and $n8$. We considered photons with energies between 8 keV and 1 MeV and rebinned the count-rate light curve for each detector in 4.096 s time bins, fitting the background with polynomials of varying order in three time intervals for each detector: before the first trigger, between both triggers, and after the second trigger. These time intervals correspond to $[-250.0, -60.0]$, $[300.0, 900.0]$ and $[1200.0, 1500.0]$ s with respect to T_0. The summed count rate light curve for all seven detectors is shown in Fig. 4.2. We determine a burst duration of $T_{90} \approx 1092$ s as the time difference between the times when the cumulative background-subtracted count rate was between 5% and 95% of its total value. We note that this duration depends on the time binning used and the detectors included in the summed light curve, and hence should be regarded as approximate.

The spectral hardness versus duration diagram has long been used as a means of categorising bursts into long and soft or short and hard classes (Kouveliotou et al. 1993), notwithstanding the fact that the burst duration is energy and detector-dependent (Qin et al. 2013; Bromberg et al. 2013). For both emission episodes we calculated the hardness ratio as the ratio of the integrated flux in the 50–300 keV to 10–50 keV energy ranges, making use of the best-fit parameters from the cutoff power law fits performed by Huang et al. (2022). Figure 4.3 compares the position of both emission episodes in the hardness-duration diagram with the sample of triggers from the Fourth *Fermi*/GBM Gamma-Ray Burst Catalog (von Kienlin et al. 2020). We see that both emission episodes sit in the long and soft portion of the diagram, providing support for a collapsar origin.

4.2.3 X-rays

The *Swift* X-Ray Telescope (XRT; Burrows et al. 2005) conducted ToO observations of the LAT error box in order to search for X-ray afterglow candidates (Evans & Swift Team 2022). The MeerLICHT identification of an optical source coincident with one of the potential X-ray afterglow candidates (see Sect. 4.2.1) confirmed this source as the X-ray afterglow, along with evidence of

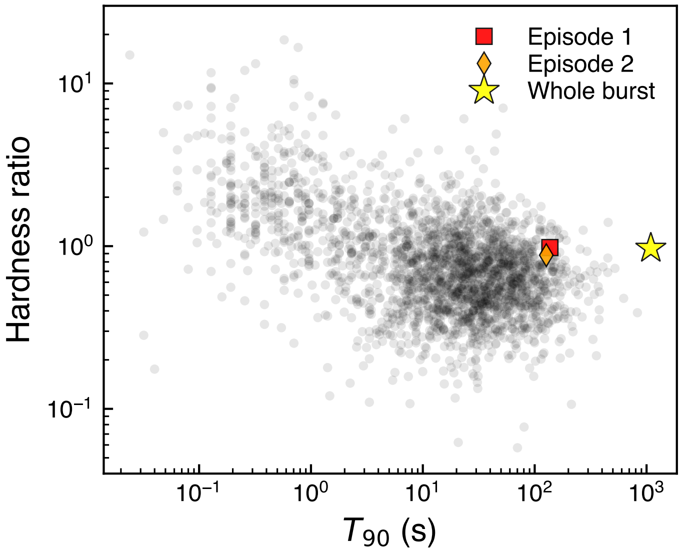

Figure 4.3: Hardness-duration diagram for both GRB 220627A emission episodes in comparison with the sample from the Fourth *Fermi*/GBM Gamma-Ray Burst Catalog (von Kienlin et al. 2020).

X-ray fading. A total of three orbits of Photon Counting mode (PC) observations of the afterglow were acquired at mid-times of 0.52, 1.59 and 4.62 days post-trigger. We obtained the X-ray count-rate light curve and spectrum from the online *Swift*/XRT GRB Catalogue hosted on the UK Swift Science Data Centre (UKSSDC) website (Evans et al. 2007, 2009). We fitted the photon spectrum with a photoelectrically absorbed power law model (`tbabs*ztbabs*pow`) in Xspec version 12.12.1, fixing the Galactic hydrogen column density at $N_{\rm H}^{\rm Gal} = 4.90 \times 10^{20}$ cm^{-2} (Willingale et al. 2013) and fixing the source redshift to $z = 3.08$. From our fit we derive a host column density of $N_{\rm H}^{\rm host} = 3.75^{+7.83}_{-3.74} \times 10^{22}$ cm^{-2} and a photon index of $\Gamma = 1.73^{+0.78}_{-0.51}$ with a C-statistic of 14.7 for 19 degrees of freedom. The unabsorbed $0.3-10$ keV flux was $1.05^{+0.28}_{-0.24} \times 10^{-12}$ erg cm^{-2} s^{-1}, from which we derive an unabsorbed counts-to-flux conversion factor of 3.60×10^{-11} erg cm^{-2} count^{-1}. Using this value along with a spectral index of $\beta_{\rm X} \equiv 1 - \Gamma_{\rm X} \approx -0.73$ we created a 1 keV X-ray light curve. The light curve consisted of two detections at 0.52 and 1.59 days, and a 3σ upper limit at 4.62 days (see Fig. 4.4).

4.2.4 Optical/near-infrared photometry

Following confirmation of the afterglow detection, we obtained 600 s exposures in each of the q, g, r, and i bands with MeerLICHT at $\sim$1.84 days post-trigger. We used the MeerLICHT pipeline (Vreeswijk et al., in prep) to perform standard CCD reduction tasks including calibration, astrometry and point-spread function (PSF) photometry. Due to the faintness of the afterglow in some of our images, we employed a forced photometry routine (developed as part of the MeerLICHT pipeline) to accurately measure the flux and significance of the detections. The afterglow was detected with a high significance ($> 15\sigma$) in the first two q-band images at 0.84 and 0.87 days. The afterglow was detected at more than 5σ significance in the q and r bands at 1.84 days, and at 4.7σ significance in the g band. The i-band observation yielded a low-significance measurement of 2.7σ which we do not include as a detection.

We obtained 6×600 s exposures at approximately 0.93 days post-trigger in the g, r, and i bands with the 1-m SAAO Lesedi optical telescope (Worters et al. 2016) located in Sutherland and equipped with the Mookodi spectrograph and imager (Erasmus et al., in prep). We employed an adapted version of the MeerLICHT pipeline to perform astrometry and photometry on each image since both telescopes make use of the SDSS *ugriz* filter set. The pipeline produced a catalogue file containing all 5σ source detections. We detected the afterglow in each image.

We acquired three epochs of imaging in the Bessel R filter at 1.13, 5.09, and 360.2 days post-trigger with the European Southern Observatory Very Large Telescope (ESO VLT) UT1 (Antu) equipped with FORS2. We obtained the last epoch approximately one year after the GRB in order to constrain any host galaxy emission long after the afterglow had faded. Each epoch consisted of 6×200 s, 3×200 s and 3×300 s exposures, respectively. We performed photometric calibration in the R band using ri DELVE DR2 photometry (Drlica-Wagner et al. 2022) of a large number of stars in the field along with the Lupton (2005)[3] transformation equation $R = r - 0.2936 * (r - i) - 0.1439$. We employed the Aperture Photometry Tool (APT; Laher et al. 2012) with a three-pixel radius aperture in an automated mode to extract instrumental magnitudes of all 3σ point sources within the FORS2 images, and derived image zero-points of 33.18 ± 0.02, 33.37 ± 0.01, and 33.42 ± 0.03 mag in the images from 1.13, 5.09, and 360.2 days, respectively. We detected the afterglow with a brightness of $R = 21.25 \pm 0.02$ and $R = 24.61 \pm 0.10$ mag during the first two epochs, and derived a 3σ upper limit of $R > 25.92$ mag during the third epoch.

We further obtained two epochs of follow-up observations of GRB 220627A in the $g'r'i'z'JHK$ bands with the Gamma-ray Burst Optical Near-Infrared Detector (GROND; Greiner et al. 2008) mounted at the 2.2-m MPG telescope at the ESO La Silla observatory in Chile. The afterglow was detected in all the optical bands ($g'r'i'z'$) but not in the near-infrared bands (JHK) during the first epoch of observations at 2.18 days post-trigger (Nicuesa Guelbenzu et al. 2022). The afterglow was detected in only the g' and r' bands during the second epoch at 3.21 days. The GROND data were reduced using standard PSF photometry through DAOPHOT (Stetson 1987) and IRAF (Tody 1993). The optical data were calibrated to the Pan-STARRS catalogue (Chambers et al. 2016) while the NIR data were calibrated to the 2MASS catalogue (Skrutskie et al. 2006). We present all optical detections of GRB 220627A in Fig. 4.4.

4.2.5 Optical spectroscopy

Following the detection of the optical afterglow by MeerLICHT, we observed the GRB afterglow region with the Multi-Unit Spectroscopic Explorer (MUSE; Bacon et al. 2010) mounted on UT4 at the ESO VLT. A set of four exposures of 600 s were obtained at 1.17 days post-trigger covering the wavelength range 4800–9300 Å with the corresponding spectral resolution ranging from $R{\sim}1800$–3500. Data from each exposure was reduced and stacked using standard *esorex* recipes. Finally, we subtracted the sky background in the reduced data cube using *zap* (Soto et al. 2016). We extracted a spectrum from the MUSE data cube using a circular aperture of $0.6''$. The spectrum is characterised by the presence of a broad damped Lyα absorption feature and the presence of several narrow metal absorption lines, including O I, Si II, Si II*, C II, C II*, Si IV, C IV, Al II, Fe II, at the common redshift of $z = 3.084$ (Izzo et al. 2022). An intervening absorber at $z = 2.665$ was also identified by the presence of S IV, Si II, C IV, Fe II, Al II lines (Izzo et al. 2022). The white light image, obtained by integrating over the entire wavelength region covered by MUSE, is shown in Fig. 4.5 along with the resulting spectrum.

4.2.6 Radio

Radio observations with the ATCA and MeerKAT arrays were obtained at 8 and 44 days post-trigger, respectively (Leung et al. 2022; Giarratana et al. 2022). The radio afterglow of GRB 220627A was detected by ATCA with a flux of ~0.4 mJy at a frequency of 17 GHz at 7.3 days, while no source was detected by MeerKAT in the L-band at 8.9 and 35.7 days where the image RMS noise was 9 and 14 μJy for each epoch, respectively. We assume a conservative 33% error on the ATCA flux measurement, and the upper limits as three times the RMS noise (3σ).

All flux measurements and upper limits used in this work are presented in Table 4.1, where

---

[3] See http://classic.sdss.org/dr4/algorithms/sdssUBVRITransform.html.

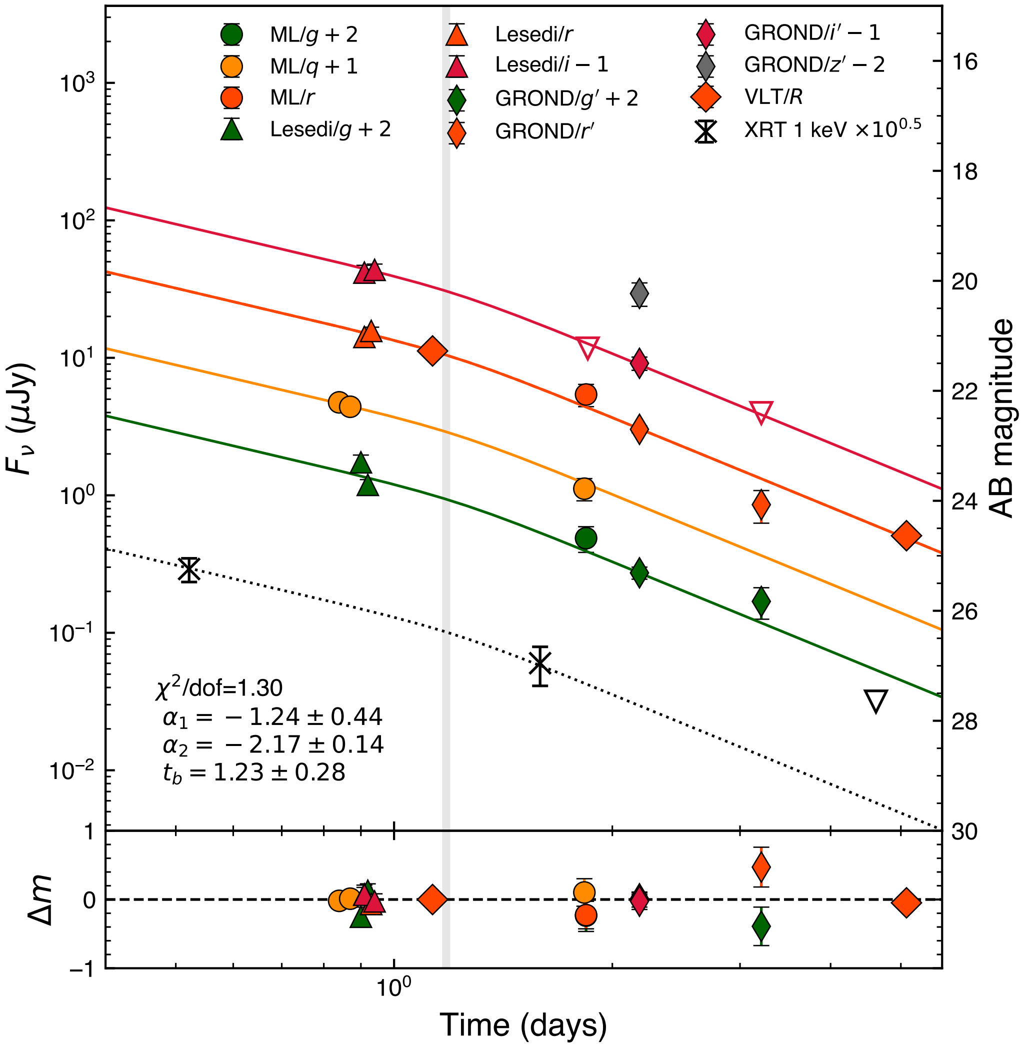

Figure 4.4: X-ray and optical light curves associated with GRB 220627A, organised by observing band and instrument. MeerLICHT is abbreviated to ML in the legend. The vertical grey region denotes the time of the MUSE spectroscopic observations. We show the broken power law fits to each of the g, q, r and i bands, where the break time and temporal indices were constrained to be the same across each fit. Residuals are shown in magnitudes in the lower panel. We show the two X-ray detections as crosses and the single upper limit as an upside-down triangle. The dotted line is the optical light curve fit shifted vertically to the X-ray band.

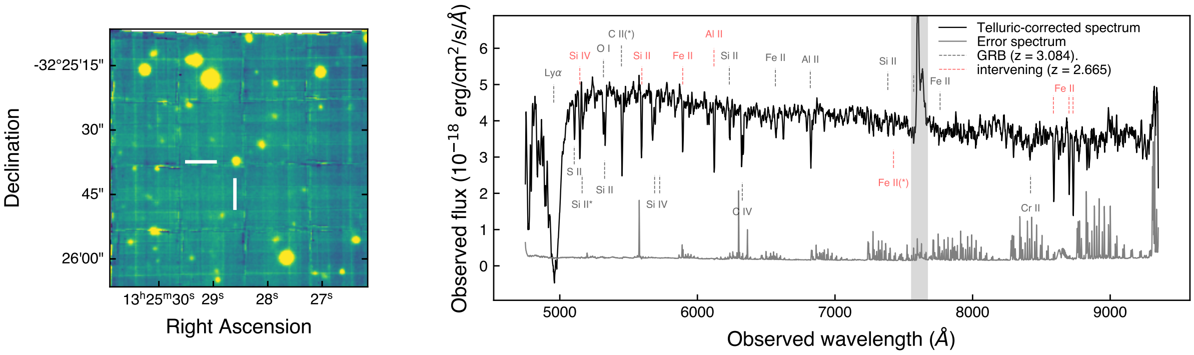

Figure 4.5: MUSE spectroscopy of GRB 220627A. *Left:* White light image resulting from the final MUSE data cube. The GRB afterglow is clearly visible at the centre of the image. *Right:* Telluric-corrected spectrum (black) and error spectrum (grey) of GRB 220627A extracted from the MUSE data cube using an aperture with a radius of $0.6''$. We show identified absorption lines at the GRB redshift ($z = 3.084$) and the intervening system ($z = 2.665$) in grey and red, respectively. The vertical shaded region is heavily affected by telluric lines.

we have converted AB magnitudes to flux densities in μJy. The frequency of each optical filter corresponds to the effective wavelength of that filter, which we obtained from the SVO Filter Profile Service for the VLT and GROND filters, while for MeerLICHT and Lesedi we obtained them internally.

4.3 Results

4.3.1 External forward shock framework

We interpret our afterglow observations in the framework of the synchrotron external forward shock model (Mészáros & Rees 1997; Sari et al. 1998; Chevalier & Li 2000). In this model, the GRB central engine – usually assumed to be a black hole or neutron star – powers an extremely relativistic, collimated outflow that sweeps up mass in the surrounding circumburst medium, forming a shock front behind which electrons are accelerated to a power law distribution in energies with $N(\gamma_e) \propto \gamma_e^{-p}$ for $\gamma_e > \gamma_m$, where γ_m is the minimum Lorentz factor of the electrons in the distribution and p is the electron spectral index. The electrons produce synchrotron radiation whose emission spectrum is a multi-segment broken power law characterised by three break frequencies: the frequency associated with the peak of the spectrum, ν_m, corresponding to electrons with the Lorentz factor γ_m in the instantaneous electron distribution; the cooling frequency ν_c corresponding to the Lorentz factor beyond which electrons are cooling efficiently by synchrotron radiation over the lifetime of the system; and the self-absorption frequency ν_{sa} corresponding to the frequency below which the synchrotron emission is self-absorbed. The ordering and evolution of the spectral breaks with time is dictated by the dynamics of the blast wave. After reverse shock crossing, the decelerating blast wave enters a self-similar regime described by the Blandford-McKee (BM; Blandford & McKee 1976) solution for a spherical, relativistic blast wave expanding into a medium with a density profile $n(r) \propto r^{-k}$. From this solution, the spectral flux density is given as a power law of both time and frequency, from which so-called closure relations can be derived relating the temporal and spectral indices within a given spectral regime (Zhang & Mészáros 2004; Zhang et al. 2006; Gao et al. 2013). We consider both a constant density ISM-like medium ($k = 0$) or a stellar wind medium ($k = 2$) in the relativistic (BM) regime, as in Granot & Sari (2002).

Table 4.1: X-ray, optical and radio observations of GRB 220627A used in this work.

Δt (days)	Telescope	Band	Wavelength (nm)	Frequency (Hz)	Flux (μJy)	Uncertainty (μJy)
0.52	*Swift*/XRT	1 keV	-	2.42e+17	0.092	0.018
1.59	*Swift*/XRT	1 keV	-	2.42e+17	0.019	0.006
4.62	*Swift*/XRT	1 keV	-	2.42e+17	< 0.010	-
0.84	MeerLICHT	q	580	5.169e+14	11.91	0.66
0.87	MeerLICHT	q	580	5.169e+14	11.07	0.71
1.83	MeerLICHT	q	580	5.169e+14	2.81	0.52
1.84	MeerLICHT	g	480	6.246e+14	3.08	0.65
1.84	MeerLICHT	r	626	4.789e+14	5.45	1.00
1.85	MeerLICHT	i	765	3.919e+14	< 4.66	-
0.90	Lesedi	g	466	6.439e+14	10.97	1.41
0.91	Lesedi	r	611	4.907e+14	13.93	1.28
0.91	Lesedi	i	758	3.954e+14	16.60	2.14
0.92	Lesedi	g	466	6.439e+14	7.52	0.69
0.93	Lesedi	r	611	4.907e+14	15.42	0.99
0.94	Lesedi	i	758	3.954e+14	17.38	1.76
1.13	VLT	R	642	4.666e+14	11.59	0.21
5.09	VLT	R	642	4.666e+14	0.53	0.05
360.2	VLT	R	642	4.666e+14	< 0.156	-
2.18	GROND	g'	459	6.536e+14	1.72	0.17
2.18	GROND	r'	622	4.820e+14	3.02	0.17
2.18	GROND	i'	764	3.924e+14	3.63	0.40
2.18	GROND	z'	899	3.335e+14	4.66	0.90
2.18	GROND	J	1240	2.418e+14	< 10.00	-
2.18	GROND	H	1647	1.820e+14	< 20.89	-
2.18	GROND	K	2170	1.381e+14	< 47.87	-
3.21	GROND	g'	459	6.536e+14	1.07	0.28
3.21	GROND	r'	622	4.820e+14	0.85	0.23
3.21	GROND	i'	764	3.924e+14	< 1.58	-
3.21	GROND	J	1240	2.418e+14	< 12.02	-
3.21	GROND	H	1647	1.820e+14	< 22.91	-
3.21	GROND	K	2170	1.381e+14	< 47.86	-
7.3	ATCA	Ku	-	1.7e+10	400	132
8.9	MeerKAT	L	-	1.4e+09	< 27	-
35.7	MeerKAT	L	-	1.4e+09	< 42	-

Notes. The optical data have not been corrected for Galactic or host galaxy extinction. Radio measurements were obtained from GCN circulars (Leung et al. 2022; Giarratana et al. 2022). We provide the central wavelength of the optical/NIR observing bands, and list all upper limits at the 3σ level.

4.3.2 Evidence for a jet break

Optical detections of GRB 220627A are presented in Fig. 4.4, separated by observing band. To account for the slight differences in observing filters, we shifted the r- and R-band data to a common frequency of 4.820×10^{14} Hz (the GROND r'-band effective frequency) using a spectral index of $\beta \approx -1$. This is the approximate spectral index derived from the GROND r', i' and z' bands at 2.18 days, uncorrected for Galactic extinction. We excluded the g' band detection from the spectral fit as there is a clear dip in the spectral energy distribution (SED) in this band compared to the redder bands, due to rest-frame Lyα absorption (see Fig. 4.5).

We fitted the light curves in each of the g, q, r, and i bands with two analytic functions: a simple power law (PL), and a smoothly broken power law[4] (BPL), constraining the temporal indices and break times (for the BPL) to be the same across each fit. We employed a break smoothness parameter of $\omega = 9$ since smoother breaks result in fits with higher reduced χ^2 values. The BPL fit had a reduced χ^2 value substantially closer to one compared to the simple PL fit (1.30 versus 1.87). Furthermore, the Bayesian information criterion (BIC) for the two fits gives preference to the BPL model (16.09 versus 19.86). Figure 4.4 shows the best-fit BPL model in each optical band. The pre- and post-break temporal indices are $\alpha_1 = -1.24 \pm 0.44$ and $\alpha_2 = -2.17 \pm 0.14$, with a break time of $t_b = 1.23 \pm 0.28$ days. Our late-time constraint on any host galaxy emission of $R > 25.92$ mag allows us to place an upper limit to any possible host galaxy contribution to the final R-band detection at 5.09 days of <30%, providing additional support to the steepening observed in the light curve. The BPL model is also compatible with the X-rays, as the data can accommodate the optical light curve fit shifted to the X-ray band (Fig. 4.4).

At X-ray and optical frequencies, an achromatic steepening of the afterglow light curves from a 'normal' temporal index of $\alpha \approx -1$ to a post-break index of $\alpha \approx -2$ has often been attributed to the jet break effect. Observationally, jet breaks have been studied extensively (see the sample in Wang et al. 2018). As the blast wave decelerates, a deficit in flux will be observed once $1/\Gamma > \theta_j$, resulting in a steepening of the light curves. If the jet break is purely due to sharp edges of the jet (e.g. a top-hat jet) coming into view rather than due to lateral spreading or a combination of both, the light curves at all frequencies will steepen by $t^{-3/4}$ or $t^{-1/2}$ in an ISM or stellar wind environment, respectively. Rhoads (1999) and Sari et al. (1999) considered sideways expansion of a conical jet and found that the bulk Lorentz factor of the jet decreases exponentially after $1/\Gamma > \theta_j$, producing a steeper post-jet break decay. For the spectral break ordering with $\nu_a < \nu_m < \nu_c$ (usually relevant when a jet break occurs), Sari et al. (1999) found that the light curves decay as t^{-p} for $\nu > \nu_m$, $t^{-1/3}$ for $\nu_a < \nu < \nu_m$, and t^0 for $\nu < \nu_a$. Numerical simulations, however, have shown that sideways expansion should not contribute before Γ has decreased considerably, though post-jet break decay is predicted to be steeper than with the edge effect only so that t^{-p} may be a reasonable approximation (van Eerten & MacFadyen 2012b; Granot & Piran 2012; Zhang & MacFadyen 2009).

The passage of the cooling frequency through the optical bands can in principle lead to a temporal break in optical light curves. For both an ISM and wind medium undergoing slow cooling the difference in spectral index between the spectral segments either side of the cooling break is $\Delta\beta = 0.5$. Interpolating and extrapolating the R-band light curve fit to the same time as the two X-ray detections, we find that the optical to X-ray spectral index either side of the break in the light curve is $\beta_{\mathrm{O,X}} \approx -0.9$, indicative of negligible spectral evolution between the optical and X-ray bands during this time. This spectral slope is also consistent with the optical in-band spectral index of $\beta_{\mathrm{O}} = -0.91$ at 2.18 days, indicating that both bands may lie on the same spectral segment. The difference in decay rate between the regimes either side of the cooling break is $|\Delta\alpha| = 0.25$, so that the passage of ν_c should not lead to a steepening of more than

---

[4] We employ the functional form $F(t) = F_0 \left[\left(\frac{t}{t_b}\right)^{-\alpha_1 \omega} + \left(\frac{t}{t_b}\right)^{-\alpha_2 \omega} \right]^{-1/\omega}$ in which F_0 is the normalising flux level, α_1 and α_2 are the pre- and post-break temporal indices, t_b is the break time, and ω is a smoothness parameter.

$\Delta\alpha = -0.25$. We also expect the temporal break to be chromatic, that is it occurs at different times in different observing bands. Our light curves steepen by $\Delta\alpha = -0.93 \pm 0.46$, which is too large for the passage of the cooling break but is consistent with a jet break due to the edge effect ($\Delta\alpha = -0.75$ in an ISM medium) or lateral spreading (t^{-p}). Furthermore, the post-break decay index of $\alpha \approx -2.2$ is difficult to reconcile within the standard closure relations. The steepest decay rate is expected in the regime with $\nu_m < \nu < \nu_c$ within a stellar wind scenario, where $\alpha = (1 - 3p)/4$. An extreme electron power law index of $p = 3$ would result in $\alpha = -2$, which is still shallower than our measured value of $\alpha \approx -2.2$. It is therefore likely that the break in our light curve is a jet break. We investigate the jet-break scenario further via theoretical modelling in Sect. 4.4.

4.3.3 Broadband temporal and spectral considerations

The GROND optical spectral energy distribution (SED) at 2.18 days has a spectral slope of $\beta_{\mathrm{O}} = -0.91 \pm 0.16$ as derived from the r', i' and z' bands (The JHK near-infrared bands did not constrain the spectral slope) corrected for Galactic extinction using the Milky Way extinction curve from Fitzpatrick (1999) with $R_V = 3.1$ and $A_{\mathrm{V}} = 0.13$ mag for the GRB line of sight (Schlafly & Finkbeiner 2011). We note that these observing bands correspond to rest-frame ultraviolet (UV) wavelengths at the redshift of GRB 220627A ($z = 3.08$), so that the intrinsic spectral slope may be shallower than this value if there is significant host-galaxy extinction. The X-ray spectral index from our fit in Sect. 4.2 was $\beta_{\mathrm{X}} = -0.73^{+0.57}_{-0.77}$. We calculate an optical to X-ray spectral index at the time of the second X-ray detection at 1.59 days by interpolating our r-band fit to this time. We take the mean relative error in our r-band flux measurements as the error on the interpolated r-band flux, approximately 10%. We measure a spectral index of $\beta_{\mathrm{O,X}} = -0.93 \pm 0.08$, which is consistent with the GROND spectral index of $\beta_{\mathrm{O}} = -0.91 \pm 0.16$. With even moderate host-galaxy extinction, we would expect this to set an upper limit on the optical to X-ray spectral index, such that a value $\beta \approx -1$ is likely from optical to X-ray frequencies.

Due to a paucity of data, we are not able to estimate the location or evolution of the cooling break, ν_c. It is therefore difficult to perform an accurate closure relation analysis to determine the circumburst medium density profile and electron energy spectral index p. Nevertheless, if we start with the assumption that $p \approx 2.2$ based on a post-jet break decay of $\alpha_2 = -2.17 \pm 0.14$, we can draw some broad conclusions. In the slow cooling regime ($\nu_m < \nu_c$) we have spectral slopes of $\beta = (1 - p)/2$ and $\beta = -p/2$ below and above ν_c, respectively. Assuming $p \approx 2.2$, we would have $\beta \approx -0.6$ and $\beta \approx -1.1$ below and above ν_c. Our optical to X-ray spectral index of $\beta \approx -1$ therefore appears more consistent with being in the spectral regime above ν_c. With $p = 2.2$, the expected light curve decay rate in this spectral regime is $\alpha = (2 - 3p)/4 = -1.15$, which is fully consistent with the pre-break temporal index of $\alpha = -1.24 \pm 0.44$ from our optical light curve fit. In an ISM environment, ν_c moves to lower frequencies as $t^{-1/2}$, while in a stellar wind environment ν_c is expected to rise as $t^{1/2}$ (Granot & Sari 2002). The most plausible[5] scenario is that we are in an ISM environment where ν_c has already moved below the optical observing bands at the time of our measurement of $\beta_{\mathrm{O,X}}$ at 1.59 days.

The radio data consists of a single detection at 7.3 days at 17 GHz, and two non-detections in the L-band (1.4 GHz) at 8.9 and 35.7 days. If we assume that the MeerKAT upper limit at 8.9 days also holds at 7.3 days, we can constrain the spectral slope between the L-band and 17 GHz (Ku band) to $\beta_{\mathrm{L-Ku}} \gtrsim 1.07$ at 7.3 days. This implies that the spectrum is likely synchrotron self-absorbed at GHz frequencies.

Since we cannot precisely constrain the location of ν_m, ν_c, or ν_a, there are likely to be extensive model degeneracies when performing theoretical modelling, as shown in Sect. 4.4.

---

[5] We cannot conclusively rule out a wind environment with ν_c below the optical since the optical light curve spans less than a single decade in time which corresponds to a change in ν_c by a factor of ~ 3 given a $t^{1/2}$ evolution.

4.3.4 MUSE spectroscopy

The huge photon flux emitted by early GRB afterglows allows us to investigate the composition of the immediate environment surrounding the GRB progenitor star (Savaglio et al. 2003; Jakobsson et al. 2004; Fynbo et al. 2006; Prochaska et al. 2007; Heintz et al. 2018; Bolmer et al. 2019; Saccardi et al. 2023). This is one of the main motivations to get an optical/near-IR GRB spectrum as soon as an optical counterpart has been identified. Early GRB afterglow spectra have shown the presence of neutral and singly-ionised low-excitation metal absorption lines, such as O I, C II, Si II, S II, Fe II, Ni II, Zn II, Al II, and Al III (Vreeswijk et al. 2007). In several cases, fine structure and meta-stable levels of Si II and Fe II have also been detected (D'Elia et al. 2007). The study of these absorption features can provide us with information on the metallicity of the immediate GRB region, while from the estimate of the column densities N_X, with X being the element under consideration, one can also obtain a rough estimate of the extinction $A_{\rm V}$ along our line of sight (De Cia et al. 2016). Due to their large redshifts, GRB afterglows are therefore one of the most important tools for investigating the evolution of the properties of the ISM in long GRB host galaxies, and consequently, in star-forming galaxies over a large redshift range.

The HI column density in GRB 220627A is derived by modelling the broad Lyα absorption trough with a Voigt profile using VoigtFit (Krogager 2018). This code convolves the intrinsic model with the spectral resolution and determines the redshift z, broadening parameter b, and column density N, of the input lines. Due to the substantial column density of HI, the Lorentzian wings dominate the line profile allowing for accurate estimates of the column density. We derive a best-fit $\log(N_{\rm HI}/{\rm cm}^{-2}) = 21.15 \pm 0.05$ (see Fig. 4.6).

We also attempt to measure the column densities of the main elements identified in the MUSE spectrum (Fig. 4.7). To this aim, and given the spectral resolution of MUSE, we have used the curve of growth (CoG) methodology, which provides a relation between the equivalent width (EW) of ISM lines and the corresponding column densities (Spitzer 1998). For low EW values (<0.1 Å), the EW is directly proportional to the column density, while for larger values the situation is complicated by saturation effects. The dependence of the EW from the column density is also related to the Doppler parameter b, which could not be very well constrained with the spectral resolution provided by MUSE. However, if we identify at least two absorption lines originating from the same electronic transition of the same ion (such as Si II 1260, 1808 Å), we can roughly estimate the b value from their EWs, given that these lines have the same column density. Then, under the assumption that the curve of growth of ions with similar excitation potential is described by the same Doppler parameter, we can estimate their column density from their rest-frame EW. Figure 4.8 shows the results of our methodology. The majority of the lines used for the analysis are consistent with the CoG determined using Si II lines, with the interesting exception of S II. We also note that we have not applied any correction for dust depletion, which can considerably affect ions such as Fe II.

Following prescriptions in Savaglio et al. (2012), we estimate metal abundances assuming that ions with ionisation potentials just above the ionisation energy of hydrogen constitute the dominant ionisation level, and finally give an estimate for the element abundance. We also do not include any ionisation correction given that this is negligible in Damped Lyman α (DLA) systems (Jenkins 2009), and especially when $\log(N_{\rm HI}/{\rm cm}^{-2}) > 10^{20.5}$ (Péroux et al. 2007), as with GRB 220627A. To determine the metallicity, we derive the relative metal to hydrogen abundances in the GRB afterglow spectrum assuming Solar values provided by Asplund et al. (2009). The metallicity is then determined as $[{\rm X/H}] = \log(N_{\rm X}/N_{\rm H})_{\rm GRB} - \log(N_{\rm X}/N_{\rm H})_{\odot}$ for each element identified in the GRB spectrum. In Table 4.2 we report our final estimates of [X/H] for each ion identified in the GRB spectrum. In Fig. 4.9 we compare our results with the distribution of absorption-derived GRB and QSO-DLA metallicities (Rafelski et al. 2012; Thöne et al. 2013; Bolmer et al. 2019; Saccardi et al. 2023), where [X/H] is mainly derived from the S II and Si II ions, which are also the faintest detected lines in the GRB 220627A spectrum, see also Fig.4.7. We further notice that for the estimate of the metallicity from S II lines, we have used the S II 1253 Å

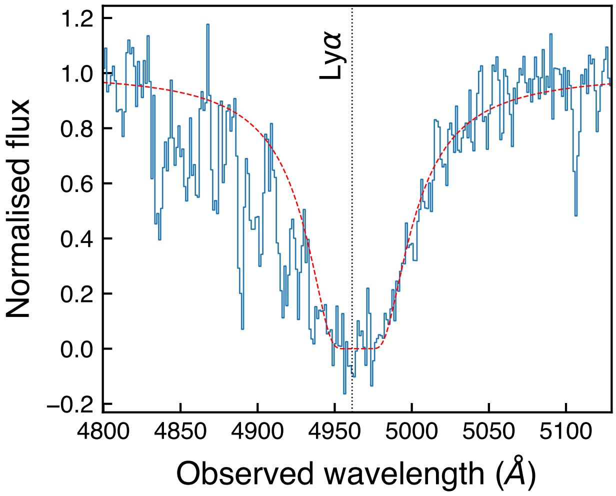

Figure 4.6: Lyα absorption feature in the MUSE spectrum. The best-fit Voigt profile is shown in red, with $\log(N_{\rm HI}/{\rm cm}^{-2}) = 21.15 \pm 0.05$.

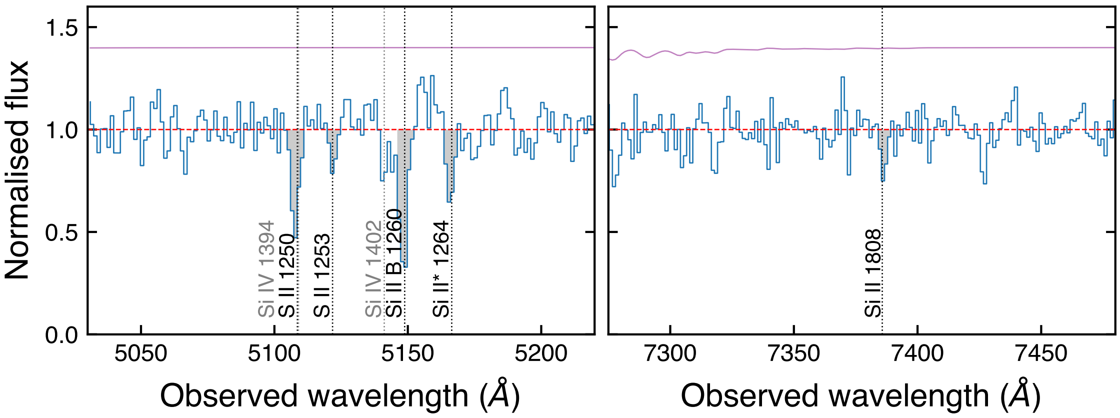

Figure 4.7: Absorption lines of S II and Si II used in the CoG analysis. We show in grey the Si IV lines from the intervening absorber at $z = 2.665$. The Si IV 1394 line from the absorber is blended with the Si II 1250 line. The purple horizontal line denotes the telluric correction applied to the spectrum, shifted vertically up by 1.4 flux units.

transition, given that the other line visible in the spectrum, S II 1250 Å, is strongly blended with Si IV 1394 Å from the intervening absorber. The environment of GRB 220627A is characterised by a typical sub-solar GRB afterglow metallicity.

Prochaska (2006) discussed this methodology comprehensively and concluded that column densities obtained using low-resolution spectra are likely to be underestimated due to instrumental line broadening and consequent blending of more intrinsically narrow absorption components. This is particularly true when metal absorption lines display heavily saturated profiles. In the case of GRB 220627A, we are also limited by the low spectral resolution provided by MUSE, which is not suitable to study ISM lines with smaller Doppler parameters. With these prescriptions, the metallicity values determined above must be considered as lower limits, especially for oxygen and carbon that can be heavily saturated. However, we also note that in the very few cases where GRB afterglows have been studied with both high- and low- resolution data, the results obtained using analysis based with Voigt-line profile fits and with the CoG method were fully in agreement (D'Elia et al. 2011).

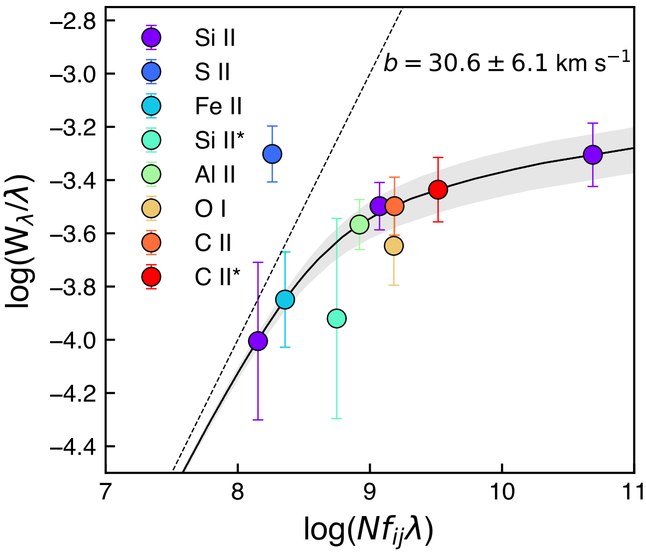

Figure 4.8: The results obtained with the CoG analysis on the ISM ($z = 3.084$) absorption lines identified in the spectrum of GRB 220627A. The dashed line represents the linear approximation regime ($W_\lambda \propto N$) of the CoG.

Table 4.2: Metallicity computed from the MUSE spectrum and using the CoG method for metal lines.

Ion	$\lambda_{\rm obs}$ (Å)	EW$_\lambda$ (Å)	log $N_{\rm X}$ (cm^{-2})	[X/H]
S II 1253	5119.7	0.62±0.11	15.08±0.09	-1.19±0.06
Si II 1260	5146.4	2.55±0.24	14.99±0.10	-1.67±0.08
Si II* 1264	5164.1	1.20±0.09	13.61±0.10	-
O I 1302	5316.4	1.69±0.08	15.35±0.11	-2.49±0.13
Si II 1304	5326.3	1.60±0.06	14.99±0.10	-1.67±0.08
C II 1334	5448.6	1.73±0.10	14.95±0.10	-2.63±0.13
C II* 1335	5454.4	2.00±0.13	15.33±0.10	-
Fe II 1608	6568.0	0.93±0.08	14.38±0.09	-2.37±0.12
Al II 1670	6822.1	1.85±0.09	13.45±0.09	-2.15±0.11
Si II 1808	7384.4	0.73±0.15	14.99±0.10	-1.67±0.08

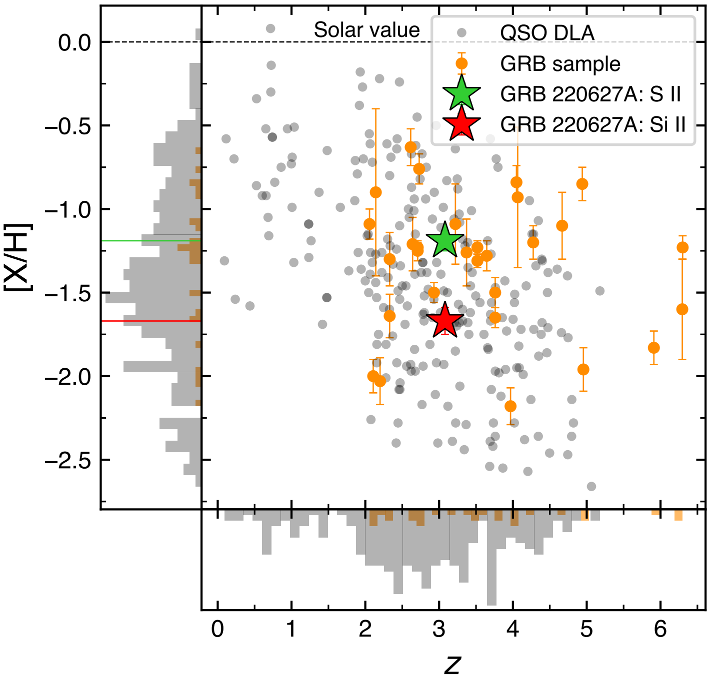

Figure 4.9: Metallicities obtained from the analysis of S II and Si II absorption lines in GRB afterglows (orange points; Thöne et al. 2013; Bolmer et al. 2019; Saccardi et al. 2023) compared with the corresponding [X/H] values obtained from the same elements in GRB 220627A (green and red data), as a function of redshift. We also show the absorption-derived metallicity values for a large sample of QSO-DLA systems (grey points; Rafelski et al. 2012; De Cia et al. 2016; Saccardi et al. 2023).

4.4 Theoretical afterglow modelling

We perform theoretical afterglow modelling to determine the physical blast wave parameters of the forward shock, with the aim of establishing whether the afterglow properties of this ultra-long GRB are unusual compared to the wider GRB population.

4.4.1 Model

We make use of the `ScaleFit` software package to perform theoretical modelling of our broadband afterglow dataset (Ryan et al. 2015; Aksulu et al. 2020, 2022). `ScaleFit` is based on the `BoxFit` set of high-resolution hydrodynamic simulations of GRB explosions (van Eerten et al. 2012). `Boxfit` interpolates between a series of compressed data sets of hydrodynamical jet simulations and employs scale invariance between the blast wave energies and circumburst medium densities to cover the space of afterglow parameters, rapidly computing light curves and spectra using a linear radiative transfer module. `Scalefit` builds on this by making use of simple scaling laws between a set of scale-invariant characteristic quantities to derive the full set of spectral parameters that determine the observed emission (van Eerten & MacFadyen 2012a). The characteristic quantities are computed and tabulated directly from the `BoxFit` simulations, allowing for nearly instantaneous calculation of afterglow light curves and spectra given an arbitrary set of blast wave parameters. The initial conditions for the `BoxFit` simulations are the Blandford-McKee radial profile truncated to the opening angle of the jet θ_j. `ScaleFit` is therefore only suitable for the deceleration phase after reverse shock crossing and so cannot be used to model energy injection, plateaus or flares. The jet break and non-relativistic (Sedov-Taylor) transitions are both well-handled by `ScaleFit` (van Eerten & MacFadyen 2012a). `ScaleFit` can be used to model both an ISM or stellar wind medium, and accepts ten free parameters: explosion-related parameters including the isotropic-equivalent blast wave energy $E_{\mathrm{K,iso}}$, circumburst medium density n_0, and opening angle of the jet θ_j; shock microphysics parameters including the electron energy distribution spectral index p, the fraction of accelerated electrons within the shock ξ_N, and the fractions of shock internal energy partitioned to electrons and magnetic fields, ϵ_e and ϵ_B, respectively; and observer-related parameters including the burst redshift z, luminosity distance d_L, and observer angle with respect to the jet axis θ_{obs}.

We use the `emcee` Python package (Foreman-Mackey et al. 2013) to implement a Markov chain Monte Carlo (MCMC) exploration of our `ScaleFit` model parameter space. An MCMC analysis allows for correlations (and degeneracies) between parameters to be readily identified. Furthermore, the uncertainty on each parameter can be determined through marginalisation of the posterior distribution. `emcee` offers advantages over traditional MCMC samplers because its multiple 'walkers' moving through the parameter space make it affine-invariant, with the result that it is unaffected by covariances between parameters. For GRB afterglow modelling, if a large majority of the measured data points are in a single spectral regime (e.g. at optical and X-ray frequencies) the location of the spectral breaks will not be well constrained, and so there are likely to be strong correlations between the $E_{\mathrm{K,iso}}$, n_0, ϵ_e and ϵ_B parameters.

In order to reduce the number of free parameters when fitting, we fix the burst redshift at the MUSE value of $z = 3.08$ (Sect. 4.2.5) and the luminosity distance at 8.25×10^{28} cm, computed using our adopted cosmology (Sect. 5.1). The fraction of shock-accelerated electrons ξ_N is degenerate with respect to the parameters $\{E_{\mathrm{K,iso}}, n_0, \epsilon_e, \epsilon_B\}$ (Eichler & Waxman 2005), so we make the common assumption that $\xi_N = 1$. We further assume that the observer is looking directly down the axis of the jet ($\theta_{\mathrm{obs}} = 0$). We account for Galactic extinction using the Milky Way extinction curve from Fitzpatrick (1999) with $R_V = 3.1$ and $A_{\mathrm{V}} = 0.13$ mag for the GRB line of sight (Schlafly & Finkbeiner 2011). The host galaxy extinction is a free parameter in our modelling, where we employ the Small Magellanic Cloud (SMC) extinction curve from Pei (1992) at the burst redshift since the vast majority of GRB host galaxies are consistent with an SMC extinction law (Schady et al. 2010; Zafar et al. 2011). We assume that the flux blueward of the rest-frame Lyman limit (912 Å) is totally absorbed. For both Galactic and host extinction we employ the astropy-affiliated `dust_extinction`[6] Python package to redden our model SEDs.

In total we have seven free parameters denoted by the vector Θ:

$$\Theta \equiv \{p, E_{\mathrm{K,iso}}, n_0, \epsilon_e, \epsilon_B, \theta_j, A_{\mathrm{V,host}}\}. \tag{4.1}$$

Given a data set D of flux measurements at frequencies ν_i and times t_i, the posterior probability $p(\Theta|D)$ is proportional to the product of the likelihood $p(D|\Theta)$ and the prior $p(\Theta)$ via Bayes' Theorem

$$p(\Theta|D) \propto p(D|\Theta)p(\Theta). \tag{4.2}$$

To account for both detections and non-detections in our data, we employ the likelihood function for Gaussian errors used by Laskar et al. (2014)

$$p(D|\Theta) = \prod p(e_i)^{\delta_i} F(e_i)^{1-\delta_i}, \tag{4.3}$$

where δ_i is equal to one for a detection and zero for an upper limit, e_i are the residuals

$$e_i = F_i(\nu_i, t_i) - F_{\mathrm{model}}(\nu_i, t_i; \Theta), \tag{4.4}$$

$p(e_i)$ is the probability density function of the residuals, and $F(e_i)$ is the cumulative distribution function of the residuals. The two functions $p(e_i)$ and $F(e_i)$ take the form

$$p(e_i) = \frac{1}{\sqrt{2\pi}\sigma_i} e^{-e_i^2/2\sigma_i^2} \tag{4.5}$$

and

$$F(e_i) = \frac{1}{2}\left[1 + erf\left(\frac{e_i}{\sqrt{2}\sigma_i}\right)\right] \tag{4.6}$$

respectively, where σ_i are the errors on the flux measurements or upper limits. As in Laskar et al. (2014), we also enforce a floor of 5% on the measured flux errors so as not to give undue weight to very high S/N measurements (usually those at optical wavelengths).

`ScaleFit` requires certain parameters to be transformed into dimensionless values in log space in order to improve performance when fitting. The energy $E_{\mathrm{K,iso}}$ is transformed into dimensionless units of $\log 10^{53}$ erg, and the quantity $\log \bar{\epsilon_e}$ is used by `ScaleFit` rather than $\log \epsilon_e$. The two quantities are related via

$$\bar{\epsilon_e} = \frac{p-2}{p-1}\epsilon_e. \tag{4.7}$$

The circumburst medium density n_0 is defined as the number of particles per cm^3 at the reference distance of 10^{17} cm from the GRB central engine. In a stellar wind medium the circumburst medium has a density profile following $\rho(r) = Ar^{-2}$. Chevalier & Li (2000) define a dimensionless $A_\star$ parameter according to $A_\star = A/(5 \times 10^{11}\,\mathrm{g\,cm^{-1}})$. The n_0 parameter is therefore related to $A_\star$ via

$$n_0 = A_\star \times 29.89\,\mathrm{cm}^{-3}. \tag{4.8}$$

We employ wide, uninformative log-uniform priors on all parameters except for p and $A_{\mathrm{V,host}}$, for which we use uniform priors (see Table 4.3). The jet opening angle is restricted to a range varying from a very narrow jet ($\theta_j = 0.6°$) to a spherical jet ($\theta_j = 90°$). Our priors are equivalent to those used by Aksulu et al. (2022). During our `emcee` run we utilise 1000 walkers performing 2000 steps through the parameter space. The initial state of the walkers are clustered around the values from a Maximum-Likelihood fit performed using the `scipy` package. We discard the initial 200 steps as burn-in. We performed the MCMC analysis in both an ISM and stellar wind circumburst medium and calculated log likelihoods of $\ln P(\Theta_{\mathrm{ISM}}|D) = 124.9^{+1.6}_{-2.2}$ and $\ln P(\Theta_{\mathrm{Wind}}|D) = 120.0^{+2.5}_{-3.8}$ for

---

[6] https://dust-extinction.readthedocs.io/en/stable/

Table 4.3: Priors on parameters in Θ used in our MCMC analysis.

Parameter	Prior	Distribution
p	$[1.0, 3.0]$	uniform
$\log E_{\rm K,iso,53}$	$[-3, 3]$	log-uniform
$\log n_0$	$[-3, 3]$	log-uniform
$\log \bar{\epsilon}_e$	$[-10, 1]$	log-uniform
$\log \epsilon_B$	$[-10, 0]$	log-uniform
$\log \theta_j$	$[-2, 0.2]$	log-uniform
$A_{\rm V,host}$	$[0, 10]$	uniform

each medium, respectively. Assuming both an ISM and stellar wind medium have equal prior probabilities of fitting our data, the Bayes factor is simply the likelihood ratio between the two models. We therefore derive a Bayes factor of 134.29 in favour of an ISM environment. According to Kass & Raftery (1995) a Bayes factor > 100 provides decisive evidence in favour of one model over another, so we only show the results of our ISM modelling henceforth. For completeness we present the results of the wind modelling in Appendix 4.A.

4.4.2 Results

Figure 4.10 shows the marginalised distributions and correlations between pairs of parameters, and Table 4.4 presents the median values along with their 1σ uncertainties derived from the marginalised distributions. For the electron spectral index we derive a value of $p = 2.00^{+0.08}_{-0.06}$. This value is consistent within uncertainties with the value for p derived from the post-jet break decay index of $p = \alpha_2 = 2.17 \pm 0.14$ in Sect. 4.3.2. Furthermore, the model associated with the median values for each parameter (bold lines in Fig. 4.11) has ν_c below the optical and X-ray regimes during our observations, consistent with the argument in Sect. 4.3.3 based on the optical spectral index. This model has $\nu_a \approx 10^{12}$ Hz until ν_m crosses ν_a at 0.13 days, whereafter the afterglow spectral breaks are ordered $\nu_m < \nu_a < \nu_c$. The single radio detection at 17 GHz and MeerKAT non-detections at 1.4 GHz are unable to constrain the location of ν_m and ν_a precisely, and as a result there are strong degeneracies between $E_{\rm K,iso}$, n_0, $\bar{\epsilon}_e$ and ϵ_B, as expected. In contrast, the jet-opening angle is well-constrained to $4.5^{+1.2}_{-0.3}$ deg and is driven by the clear break in the optical light curves as discussed in Sect. 4.3.2. The corresponding beaming correction of $f_b = (1 - \cos\theta_j) = 3.1^{+1.8}_{-0.3} \times 10^{-3}$ results in a beaming-corrected prompt γ-ray energy of $E_\gamma = 1.5^{+0.9}_{-0.2} \times 10^{52}$ erg and kinetic energy of $E_{\rm K} = 3.1^{+20.3}_{-2.5} \times 10^{51}$ erg. The radiative efficiency of a GRB is defined as (Lloyd-Ronning & Zhang 2004)

$$\eta_\gamma = \frac{E_\gamma}{E_\gamma + E_K}, \tag{4.9}$$

from which we derive a high radiative efficiency of $\eta_\gamma \approx 84\%$. As mentioned in Sect. 4.4.1, assuming $\xi_N = 1$ means that our derived kinetic energy is actually a lower limit on the true energy, and therefore this calculated radiative efficiency is actually an upper limit. We note also that the uncertainty on E_K is rather large due to degeneracies in our theoretical modelling. Taking into account the uncertainties in E_K and E_γ, we derive a 1σ range of $39 - 97\%$ for η_γ. Wang et al. (2015) find that radiative efficiencies peak at ∼6% with the 1σ range extending up to ∼40%, though they still have a very wide distribution extending to almost 90%, fully consistent with our derived value.

Table 4.4: Parameter values derived from our theoretical modelling. We report the median values and 68% confidence intervals derived from our marginalised distributions in Fig. 4.10.

Parameter	value
p	$2.00^{+0.08}_{-0.06}$
$E_{\mathrm{K,iso}}$ (10^{53} erg)	$9.0^{+65.1}_{-7.4}$
n_0 (cm^{-3})	$1.9^{+13.3}_{-1.6} \times 10^{1}$
$\bar{\epsilon_e}$	$1.5^{+8.1}_{-1.3} \times 10^{-3}$
ϵ_B	$4.6^{+30.7}_{-4.3} \times 10^{-3}$
θ_j (deg)	$4.5^{+1.2}_{-0.3}$
$A_{\mathrm{V,host}}$ (mag)	0.09 ± 0.03

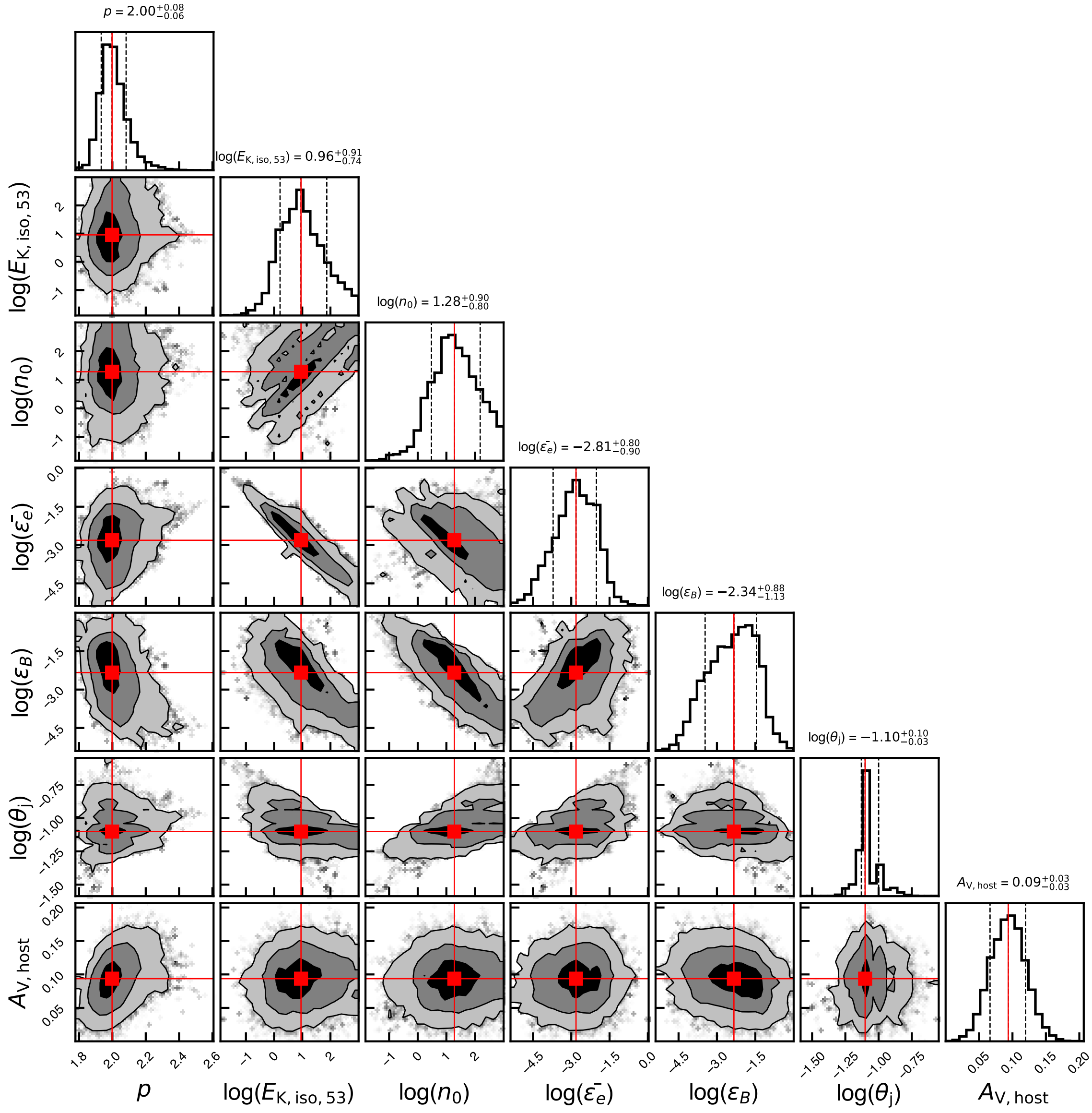

Figure 4.10: Corner plot from our MCMC implementation showing the 2-D marginalised distributions between pairs of model parameters along with the marginalised distributions for each individual model parameter. Contours denote the 1σ, 2σ and 3σ levels while the red lines denote the median values from the marginalised distributions for each model parameter. Uncertainties on each parameter are at the 16th and 84th (1σ) percentile.

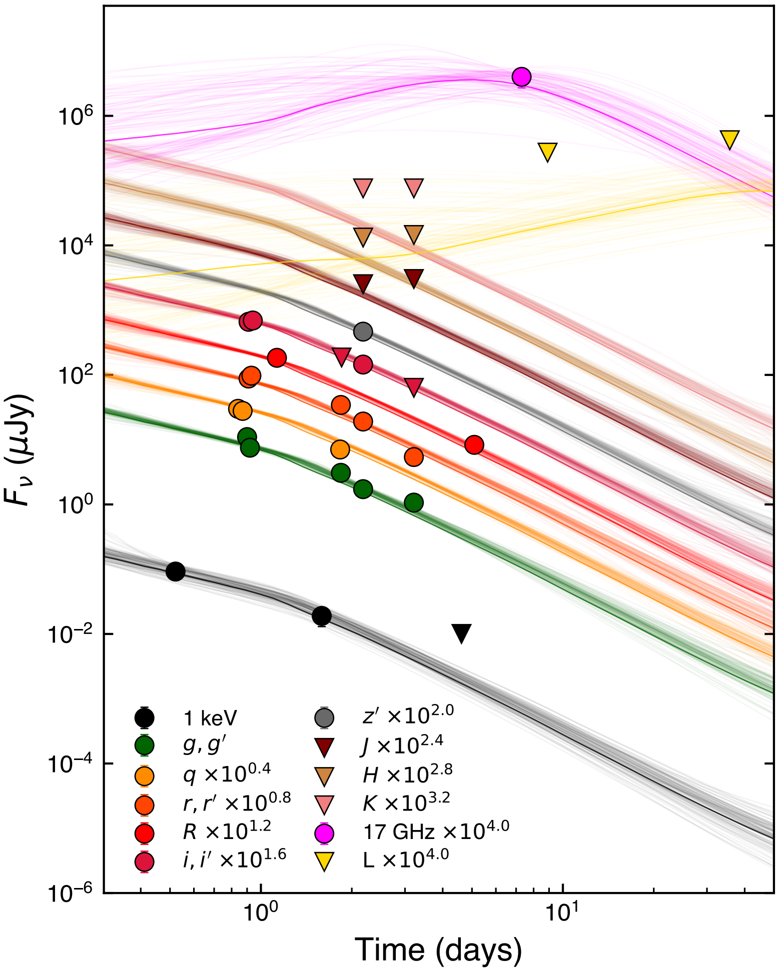

Figure 4.11: We show all afterglow flux measurements presented in Table 4.1 along with 100 random models drawn from our MCMC exploration of the parameter space. The bold lines represent the model associated with the median values from the marginalised posterior distributions in Fig. 4.10. Upper limits are shown as upside-down triangles.

4.5 Discussion

The defining feature of GRB 220627A is its two distinct prompt γ-ray emission episodes separated by ~600 s, resulting in a total burst duration of ~1090 s. At a redshift of $z = 3.08$, GRB 220627A is the most distant ultra-long GRB detected to date. We now discuss whether the prompt and afterglow emission are typical for normal long GRBs.

4.5.1 Prompt emission properties

Based on the sample of long GRBs fitted with cutoff power laws in the Fermi-GBM Gamma-Ray Burst Spectral Catalog, Poolakkil et al. (2021) find a distribution of low-energy photon indices of $\Gamma = 1.01^{+0.39}_{0.35}$ and peak energies of $E_p = 205^{+374}_{-109}$ keV. The prompt emission spectral parameters of GRB 220627A (see Sect. 4.2.2) are fully consistent with these distributions. For the first emission episode, an additional power law spectral component extending up to higher energies ($>$100 MeV) is needed to explain the LAT emission. Such a feature has been observed in several other long GRBs (e.g. GRBs 090902B, 090926A; Abdo et al. 2009; Ackermann et al. 2011). The spectral properties of GRB 220627A are therefore not unusual compared to the long GRB population. The temporal features, however, are rare though not unprecedented, and we discuss these further in Sect. 4.5.3 below.

4.5.2 Afterglow properties

Most of our model parameters derived from our theoretical modelling (Sect. 4.4.2) are typical values within the literature. Our value of p is within the 1σ range found by Wang et al. (2015) of $p = 2.33 \pm 0.48$. Wang et al. (2015) also find that the typical isotropic kinetic energy for GRBs without energy injection is $\log(E_{\rm K,iso}/{\rm erg}) = 54.66 \pm 1.18$. Our inferred kinetic energy of $E_{\rm K,iso} = 9.0 \times 10^{53}$ erg is well within their sample range. Our circumburst medium density of 19 cm^{-3} agrees within the range of $0.06 - 26$ cm^{-3} found by Aksulu et al. (2022) for long GRBs in ISM environments. Santana et al. (2014) found that ϵ_B spans almost five orders of magnitude from $10^{-5} - 10^{-1}$. Our value of $\epsilon_B \approx 5 \times 10^{-3}$ is close to their median value of 1.0×10^{-2}. We are unable to determine a physical value for ϵ_e using Eq. 4.7 since $p = 2$ results in $\bar{\epsilon_e} = 0$. Values of p less than two have been suggested in the literature (Panaitescu & Kumar 2002; Dai & Cheng 2001) and have been found through modelling of actual GRB datasets (Aksulu et al. 2022). As discussed in Granot & Sari (2002), using $\bar{\epsilon_e}$ is still valid when $p < 2$ as long as γ_m is proportional to the shock Lorentz factor; a high-energy cutoff in the electron energy distribution is then needed so that the total energy in electrons is bounded. Wang et al. (2015) found that the jet opening angle takes values of $\theta_j = 2.5 \pm 1.5$ deg. Our value of $4.5^{+1.2}_{-0.3}$ deg is just outside their 1σ range, but well within the range of the sample considered by Laskar et al. (2014) having $\theta_j = 7.4^{+11}_{-6.6}$ deg.

The afterglow properties derived from our theoretical modelling are fully consistent with long GRBs, and do not suggest a different or unusual progenitor. The large distance to GRB 220627A means that we are also unable to shed light on the progenitor through observations of a possible supernova (e.g. SN 2011kl accompanying the ultra-long GRB 111209A; Greiner et al. 2015) or another thermal transient. The findings presented here cannot exclude that GRB 220627A has a different progenitor compared to normal long GRBs.

4.5.3 GRBs with widely-spaced emission episodes

Among ultra-long GRBs, GRB 220627A is one of an even smaller subset of GRBs with distinct γ-ray emission episodes separated by long quiescent periods. Virgili et al. (2013) compared the ultra-long GRB 091024A with a sample of 11 other bursts having durations > 1000 s and divided ultra-long GRBs into those with continuous prompt γ-ray emission, and those with distinct emission episodes separated by long quiescent periods (so-called interrupted bursts). They pointed out that the total duration of interrupted bursts holds less significance than for continuous bursts, since long quiescent intervals between sub-bursts may not accurately reflect the duration of central engine activity. They identified four bursts with interrupted emission: GRBs 020410A, 080407A, 091024A, and 110709B. Since then, three GRBs have triggered *Fermi*/GBM twice as listed in the Fourth *Fermi*/GBM Gamma-Ray Burst Catalog (von Kienlin et al. 2020): GRB 130925A, GRB 150201A, and GRB 160625B. Although GRBs 110709B and 160625B are not strictly ultra-long due to having durations $<$1000 s, we still include them in this sample since they are close to 1000 s and have widely-spaced emission episodes. Some properties of these bursts including GRB 220627A are presented in Table 4.5, similar to Table 6 in Virgili et al. (2013). We now discuss the prompt and afterglow properties of these bursts in order to determine if they share any unifying characteristics.

The prompt emission light curves for all eight bursts are diverse in their morphology. Some bursts have weak precursor-like episodes preceding the main episode which contains the majority of the total fluence (GRBs 091024A, 130925A, 160625B), while others have brighter initial episodes (020410A, 080407A, 150201A, 220627A). GRB 110709B has two emission episodes of similar brightness. All bursts appear to show hard to soft evolution across the whole duration of γ-ray activity, a common trait for the wider GRB population. GRB 220627A is the most distant of all these bursts, and has the highest isotropic γ-ray energy. The bursts in Table 4.5 span almost two orders of magnitude in $E_{\gamma,\mathrm{iso}}$, comparable to the range of energies of the normal long GRB population (see Fig. 19 in Poolakkil et al. 2021). GRB 220627A is also one of only two bursts that has been detected at GeV γ-ray energies by *Fermi*/LAT.

The prompt emission light curve of GRB 220627A is most similar to that of GRB 110709B, a so-called double burst which triggered *Swift*/BAT twice separated by an interval of 11 minutes. Zhang et al. (2012) studied the prompt and X-ray emission in detail and ruled out a gravitational lensing and a giant X-ray flare origin for the second sub-burst. Their preferred physical explanation for the two sub-bursts with a long quiescent period in between was a magnetar to black hole (BH) scenario, where the first sub-burst is produced by a newly-formed magnetar releasing rotational energy via a magnetised jet, and the second, softer sub-burst is produced by a slower jet once the magnetar has collapsed to a BH. GRB 160625B was an extremely bright burst with three distinct emission episodes which were studied in great detail by Zhang et al. (2018). The first, short precursor episode was thermal-dominated, while the latter two episodes were consistent with synchrotron emission. This spectral transition was interpreted as direct evidence of the GRB jet changing its composition, with the first thermal component associated with the initial core collapse and break out of the ejecta from the surface of the Wolf-Rayet progenitor. For a black hole central engine the quiescent phase prior to the main emission was suggested to be a result of a magnetic barrier delaying accretion until enough material has built up (Proga & Zhang 2006), while for the magnetar engine the delay may be a result of the hot proto-magnetar taking time to dissipate energy before launching an outflow (Komissarov & Barkov 2007; Metzger et al. 2011). Thereafter, a Poynting-flux dominated outflow characterised by synchrotron emission would be launched. Due to the weakness and short duration ($T_{90}\sim$0.84 s) of the thermal precursor emission, the authors noted that such a feature would not have been observable had GRB 160625B been more distant. Such a feature may have been observed in GRB 220627A had it been closer. Based on 3D simulations, Gottlieb et al. (2022) proposed that the observed quiescent periods of $\sim$1$-$100 s in prompt emission light curves are naturally explained by a time-varying tilt of the central engine, such that quiescent periods correspond to times when the jet axis is pointed away from the observer. The much longer quiescent period of $\sim$600 s for GRB 220627A, however, may exclude this scenario.

In terms of afterglow emission, almost all of the bursts in Table 4.5 were detected in X-rays, and their X-ray luminosities are comparable to the majority of the GRB population (see Fig. 4.12). Levan et al. (2014) regarded the presence of X-ray flares as a defining feature of ultra-long GRBs. GRBs 110709B and 130925A show evidence for X-ray flares, though in the cases of GRBs 091024A and 160625B *Swift*/XRT was unable to observe at early times, so any flares may simply

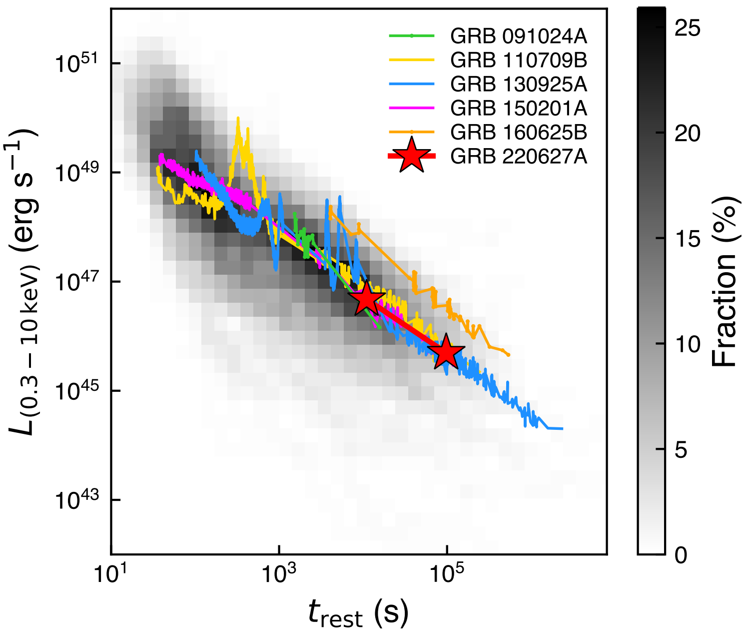

Figure 4.12: X-ray luminosities as a function of rest-frame time for all *Swift*/XRT-detected bursts in Table 4.5. For GRBs without redshifts (110709B and 150201A) we assume $z = 1$. The grey colour bar denotes the fraction of *Swift*/XRT-detected afterglows with known redshifts crossing each luminosity-time bin.

have been undetected (Fig. 4.12). GRB 150201A does not show any X-ray flares, despite there being early-time data. GRB 220627A was not localised until 0.84 days, so no search for flaring could be conducted. GRB 130925A is the nearest of the ultra-long GRBs in the sample and also has the longest duration measured in γ-rays. Its X-ray afterglow showed many large flares, similar to those of the ultra-long GRBs studied by Levan et al. (2014). Evidence for a thermal emission component was found in the X-ray spectra and was interpreted as photospheric emission from the GRB fireball (Piro et al. 2014). Such thermal emission has been observed in a number of other X-ray flares (Peng et al. 2014). Evans et al. (2014) suggested that the lack of external shock X-ray emission implied a low circumburst density, which could explain the ultra-long γ-ray duration since the deceleration time and radius would be larger, allowing more ejected shells to interact and produce prompt emission before reaching the external shock. The radio emission from GRB 130925A proved challenging to explain in a normal forward shock afterglow model (Horesh et al. 2015). GRBs 091024A, 130925A, and 160625B were all detected and localised by *Swift*/BAT and were therefore monitored from very early times at optical frequencies.

In summary, GRBs with widely-spaced emission episodes show a wide variety of prompt and afterglow features. More observations of such bursts are needed in order to determine if there are unifying characteristics that distinguish them from single-emission episode bursts.

4.6 Conclusion

GRB 220627A is an ultra-long GRB that triggered *Fermi*/GBM twice separated by a 956 s time interval. High-energy GeV γ-rays were detected by *Fermi*/LAT in coincidence with the first emission episode which led to the discovery of the optical afterglow with MeerLICHT at 0.84 days. Optical spectroscopic observations with MUSE were used to deduce the burst redshift of $z = 3.08$, making GRB 220627A the most distant ultra-long GRB observed to date. From our optical follow-up observations we identified a temporal break in the light curve at ~1.2 days which we interpret as a jet break. From our spectroscopic measurements we found that the environment

Table 4.5: Ultra-long GRBs with widely-spaced emission episodes.

GRB	Duration[a] (s)	z	Fluence[b] (10^{-5} erg cm^{-2})	Energy range[c] (keV)	$E_{\gamma,\mathrm{iso}}$[d] (10^{52} erg)	Episodes[e]	GeV[f]	Afterglow[g]	Refs.
020410A	1550	$\sim$0.5	2.8	15–1000	$\sim$1.8	4	-	X,O	1,2
080407A	2100	-	44	20–1000	$\sim$120	2	-	-	3
091024A	1300	1.092	1.5	10–10000	44	3	ND	X,O	4,5
110709B	900	-	0.22	15–150	$\sim$10	2	-	X,R	6
130925A	4500	0.347	62	20–10000	19	3	ND	X,O,R	7,8,9,10,11
150201A[h]	1400	-	6.8	10–1000	$\sim$36	2	-	X	12
160625B	800	1.406	66	10–1000	334	3	D	X,O,R	13,14
220627A	1200	3.08	4.5	10–1000	480	2	D	X,O,R	15, this work

[a] Approximate duration of γ-ray activity across all emission episodes.

[b] Fluence as measured across all emission episodes.

[c] Energy range over which reported fluence was measured.

[d] We assume $z = 1$ to calculate $E_{\gamma,\mathrm{iso}}$ for bursts without measured redshifts.

[e] Number of widely-spaced emission episodes present in prompt light curve.

[f] GeV γ-ray emission detected with *Fermi*/LAT. ND indicates a non detection, D indicates a detection.

[g] Afterglow detection in X-rays (X), optical (O) and radio (R).

[h] GRB 150201A triggered *Fermi*/GBM twice separated by 23 minutes. The burst position was earth-occulted during the second trigger, so the association between the two triggers is not beyond doubt.

References: (1) Nicastro et al. (2004); (2) Levan et al. (2005); (3) Pal'shin et al. (2012); (4) Gruber et al. (2011); (5) Virgili et al. (2013); (6) Zhang et al. (2012); (7) Golenetskii et al. (2013); (8) Evans et al. (2014); (9) Piro et al. (2014); (10) Greiner et al. (2014); (11) Horesh et al. (2015); (12) Yu & Pelassa (2015); (13) Zhang et al. (2018); (14) Alexander et al. (2017); (15) Huang et al. (2022).

of the burst is consistent with a sub-solar metallicity typical of DLA systems and other GRB afterglows. Combined with publicly-available X-ray and radio data, we performed broad-band theoretical modelling of the afterglow data and found preference for a homogeneous circumburst medium. Our most well-constrained parameter is the jet opening angle, which we constrain to $\theta_j = 4.5^{+1.2}_{-0.3}$ deg. All our parameters are typical for long GRB afterglows. Our observations of this ultra-long GRB do not require a different progenitor compared to normal long GRBs as suggested by some authors, though we cannot exclude this possibility. More observations of bursts with widely-spaced emission episodes are needed to determine if they form a separate population with distinct prompt and afterglow features.

Acknowledgements

The MeerLICHT consortium is a partnership between Radboud University, the University of Cape Town, the South African Astronomical Observatory (SAAO), the University of Oxford, the University of Manchester and the University of Amsterdam, in association with and, partly supported by, the South African Radio Astronomy Observatory (SARAO), the European Research Council and The Netherlands Research School for Astronomy (NOVA). We acknowledge the use of the Inter-University Institute for Data Intensive Astronomy (IDIA) data intensive research cloud for data processing. IDIA is a South African university partnership involving the University of Cape Town, the University of Pretoria and the University of the Western Cape. S.dW. and P.J.G. are supported by NRF SARChI Grant 111692. The research leading to these results has received funding from the European Union's Horizon 2020 Programme under the AHEAD2020 project (grant agreement number 871158). Part of the funding for GROND (both hardware and personnel) was generously granted from the Leibniz-Prize to G. Hasinger (DFG grant HA 1850/28-1) and by the Thüringer Landessternwarte Tautenburg. This work made use of data supplied by the UK Swift Science Data Centre at the University of Leicester.

Bibliography

Abdo, A. A., Ackermann, M., Ajello, M., et al. 2009, ApJ, 706, L138

Ackermann, M., Ajello, M., Asano, K., et al. 2011, ApJ, 729, 114

Aksulu, M. D., Wijers, R. A. M. J., van Eerten, H. J., & van der Horst, A. J. 2020, MNRAS, 497, 4672

Aksulu, M. D., Wijers, R. A. M. J., van Eerten, H. J., & van der Horst, A. J. 2022, MNRAS, 511, 2848

Alexander, K. D., Laskar, T., Berger, E., et al. 2017, ApJ, 848, 69

Aptekar, R. L., Frederiks, D. D., Golenetskii, S. V., et al. 1995, Space Sci. Rev., 71, 265

Asplund, M., Grevesse, N., Sauval, A. J., & Scott, P. 2009, ARA&A, 47, 481

Atwood, W. B., Abdo, A. A., Ackermann, M., et al. 2009, ApJ, 697, 1071

Bacon, R., Accardo, M., Adjali, L., et al. 2010, in Society of Photo-Optical Instrumentation Engineers (SPIE) Conference Series, Vol. 7735, Ground-based and Airborne Instrumentation for Astronomy III, ed. I. S. McLean, S. K. Ramsay, & H. Takami, 773508

Blandford, R. D. & McKee, C. F. 1976, Physics of Fluids, 19, 1130

Bloemen, S., Groot, P., Woudt, P., et al. 2016, in Society of Photo-Optical Instrumentation

Engineers (SPIE) Conference Series, Vol. 9906, Ground-based and Airborne Telescopes VI, ed. H. J. Hall, R. Gilmozzi, & H. K. Marshall, 990664

Bolmer, J., Ledoux, C., Wiseman, P., et al. 2019, A&A, 623, A43

Bromberg, O., Nakar, E., Piran, T., & Sari, R. 2013, ApJ, 764, 179

Burrows, D. N., Hill, J. E., Nousek, J. A., et al. 2005, Space Sci. Rev., 120, 165

Chambers, K. C., Magnier, E. A., Metcalfe, N., et al. 2016, arXiv e-prints, arXiv:1612.05560

Chevalier, R. A. & Li, Z.-Y. 2000, ApJ, 536, 195

Dai, Z. G. & Cheng, K. S. 2001, ApJ, 558, L109

De Cia, A., Ledoux, C., Mattsson, L., et al. 2016, A&A, 596, A97

de Wet, S., Groot, P. J., Malesani, D. B., et al. 2022, GRB Coordinates Network, 32289, 1

D'Elia, V., Campana, S., Covino, S., et al. 2011, MNRAS, 418, 680

D'Elia, V., Fiore, F., Meurs, E. J. A., et al. 2007, A&A, 467, 629

di Lalla, N., Axelsson, M., Arimoto, M., Omodei, N., & Crnogoreeviae, M. 2022, GRB Coordinates Network, 32283, 1

Drlica-Wagner, A., Ferguson, P. S., Adamów, M., et al. 2022, ApJS, 261, 38

Eichler, D. & Waxman, E. 2005, ApJ, 627, 861

Evans, P. A., Beardmore, A. P., Page, K. L., et al. 2009, MNRAS, 397, 1177

Evans, P. A., Beardmore, A. P., Page, K. L., et al. 2007, A&A, 469, 379

Evans, P. A. & Swift Team. 2022, GRB Coordinates Network, 32284, 1

Evans, P. A., Willingale, R., Osborne, J. P., et al. 2014, MNRAS, 444, 250

Fitzpatrick, E. L. 1999, PASP, 111, 63

Foreman-Mackey, D., Hogg, D. W., Lang, D., & Goodman, J. 2013, PASP, 125, 306

Frederiks, D., Lysenko, A., Ridnaya, A., et al. 2022, GRB Coordinates Network, 32295, 1

Fynbo, J. P. U., Watson, D., Thöne, C. C., et al. 2006, Nature, 444, 1047

Gao, H., Lei, W.-H., Zou, Y.-C., Wu, X.-F., & Zhang, B. 2013, New A Rev., 57, 141

Gendre, B., Stratta, G., Atteia, J. L., et al. 2013, ApJ, 766, 30

Giarratana, S., Leung, J., Wang, Z., et al. 2022, GRB Coordinates Network, 32454, 1

Golenetskii, S., Aptekar, R., Frederiks, D., et al. 2013, GRB Coordinates Network, 15260, 1

Gottlieb, O., Liska, M., Tchekhovskoy, A., et al. 2022, ApJ, 933, L9

Granot, J. & Piran, T. 2012, MNRAS, 421, 570

Granot, J. & Sari, R. 2002, ApJ, 568, 820

Greiner, J., Bornemann, W., Clemens, C., et al. 2008, PASP, 120, 405

Greiner, J., Mazzali, P. A., Kann, D. A., et al. 2015, Nature, 523, 189

Greiner, J., Yu, H. F., Krühler, T., et al. 2014, A&A, 568, A75

Groot, P. J., de Wet, S., Vreeswijk, P. M., & Meerlicht Consortium. 2022, GRB Coordinates Network, 32281, 1

Gruber, D., Krühler, T., Foley, S., et al. 2011, A&A, 528, A15

Heintz, K. E., Watson, D., Jakobsson, P., et al. 2018, MNRAS, 479, 3456

Horesh, A., Cenko, S. B., Perley, D. A., et al. 2015, ApJ, 812, 86

Huang, Y.-Y., Zhang, H.-M., Yan, K., Liu, R.-Y., & Wang, X.-Y. 2022, ApJ, 940, L36

Izzo, L., D'Elia, V., de Ugarte Postigo, A., et al. 2022, GRB Coordinates Network, 32291, 1

Jakobsson, P., Hjorth, J., Fynbo, J. P. U., et al. 2004, A&A, 427, 785

Jenkins, E. B. 2009, ApJ, 700, 1299

Kass, R. E. & Raftery, A. E. 1995, Journal of the American Statistical Association, 90, 773

Komissarov, S. S. & Barkov, M. V. 2007, MNRAS, 382, 1029

Kouveliotou, C., Meegan, C. A., Fishman, G. J., et al. 1993, ApJ, 413, L101

Krogager, J.-K. 2018, arXiv e-prints, arXiv:1803.01187

Laher, R. R., Gorjian, V., Rebull, L. M., et al. 2012, PASP, 124, 737

Laskar, T., Berger, E., Tanvir, N., et al. 2014, ApJ, 781, 1

Leung, J., Wang, Z., An, T., et al. 2022, GRB Coordinates Network, 32341, 1

Levan, A., Nugent, P., Fruchter, A., et al. 2005, ApJ, 624, 880

Levan, A. J., Tanvir, N. R., Starling, R. L. C., et al. 2014, ApJ, 781, 13

Lien, A., Sakamoto, T., Barthelmy, S. D., et al. 2016, ApJ, 829, 7

Lloyd-Ronning, N. M. & Zhang, B. 2004, ApJ, 613, 477

Meegan, C., Lichti, G., Bhat, P. N., et al. 2009, ApJ, 702, 791

Mészáros, P. & Rees, M. J. 1997, ApJ, 476, 232

Mészáros, P. & Rees, M. J. 2001, ApJ, 556, L37

Metzger, B. D., Giannios, D., Thompson, T. A., Bucciantini, N., & Quataert, E. 2011, MNRAS, 413, 2031

Nakauchi, D., Kashiyama, K., Suwa, Y., & Nakamura, T. 2013, ApJ, 778, 67

Nicastro, L., in't Zand, J. J. M., Amati, L., et al. 2004, A&A, 427, 445

Nicuesa Guelbenzu, A., Klose, S., & Rau, A. 2022, GRB Coordinates Network, 32304, 1

Pal'shin, V., Hurley, K., Goldsten, J., et al. 2012, in Gamma-Ray Bursts 2012 Conference (GRB 2012), 40

Panaitescu, A. & Kumar, P. 2002, ApJ, 571, 779

Pei, Y. C. 1992, ApJ, 395, 130

Peng, F.-K., Liang, E.-W., Wang, X.-Y., et al. 2014, ApJ, 795, 155

Péroux, C., Dessauges-Zavadsky, M., D'Odorico, S., Kim, T.-S., & McMahon, R. G. 2007, MNRAS, 382, 177

Piro, L., Troja, E., Gendre, B., et al. 2014, ApJ, 790, L15

Planck Collaboration, Ade, P. A. R., Aghanim, N., et al. 2016, A&A, 594, A13

Poolakkil, S., Preece, R., Fletcher, C., et al. 2021, ApJ, 913, 60

Prochaska, J. X. 2006, ApJ, 650, 272

Prochaska, J. X., Chen, H.-W., Dessauges-Zavadsky, M., & Bloom, J. S. 2007, ApJ, 666, 267

Proga, D. & Zhang, B. 2006, MNRAS, 370, L61

Qin, Y., Liang, E.-W., Liang, Y.-F., et al. 2013, ApJ, 763, 15

Rafelski, M., Wolfe, A. M., Prochaska, J. X., Neeleman, M., & Mendez, A. J. 2012, ApJ, 755, 89

Rastinejad, J. C., Gompertz, B. P., Levan, A. J., et al. 2022, Nature, 612, 223

Rhoads, J. E. 1999, ApJ, 525, 737

Roberts, O. J., Hristov, B., Meegan, C., & Fermi Gamma-ray Burst Monitor Team. 2022, GRB Coordinates Network, 32288, 1

Ryan, G., van Eerten, H., MacFadyen, A., & Zhang, B.-B. 2015, ApJ, 799, 3

Saccardi, A., Vergani, S. D., De Cia, A., et al. 2023, A&A, 671, A84

Santana, R., Barniol Duran, R., & Kumar, P. 2014, ApJ, 785, 29

Sari, R., Piran, T., & Halpern, J. P. 1999, ApJ, 519, L17

Sari, R., Piran, T., & Narayan, R. 1998, ApJ, 497, L17

Savaglio, S., Fall, S. M., & Fiore, F. 2003, ApJ, 585, 638

Savaglio, S., Rau, A., Greiner, J., et al. 2012, MNRAS, 420, 627

Schady, P., Page, M. J., Oates, S. R., et al. 2010, MNRAS, 401, 2773

Schlafly, E. F. & Finkbeiner, D. P. 2011, ApJ, 737, 103

Skrutskie, M. F., Cutri, R. M., Stiening, R., et al. 2006, AJ, 131, 1163

Soto, K. T., Lilly, S. J., Bacon, R., Richard, J., & Conseil, S. 2016, MNRAS, 458, 3210

Spitzer, L. 1998, Physical Processes in the Interstellar Medium

Stetson, P. B. 1987, PASP, 99, 191

Stratta, G., Gendre, B., Atteia, J. L., et al. 2013, ApJ, 779, 66

Thöne, C. C., de Ugarte Postigo, A., Fryer, C. L., et al. 2011, Nature, 480, 72

Thöne, C. C., Fynbo, J. P. U., Goldoni, P., et al. 2013, MNRAS, 428, 3590

Tody, D. 1993, in Astronomical Society of the Pacific Conference Series, Vol. 52, Astronomical Data Analysis Software and Systems II, ed. R. J. Hanisch, R. J. V. Brissenden, & J. Barnes, 173

van Eerten, H., van der Horst, A., & MacFadyen, A. 2012, ApJ, 749, 44

van Eerten, H. J. & MacFadyen, A. I. 2012a, ApJ, 747, L30

van Eerten, H. J. & MacFadyen, A. I. 2012b, ApJ, 751, 155

Virgili, F. J., Mundell, C. G., Pal'shin, V., et al. 2013, ApJ, 778, 54

von Kienlin, A., Meegan, C. A., Paciesas, W. S., et al. 2020, ApJ, 893, 46

Vreeswijk, P. M., Ledoux, C., Smette, A., et al. 2007, A&A, 468, 83

Wang, X.-G., Zhang, B., Liang, E.-W., et al. 2015, ApJS, 219, 9

Wang, X.-G., Zhang, B., Liang, E.-W., et al. 2018, ApJ, 859, 160

Willingale, R., Starling, R. L. C., Beardmore, A. P., Tanvir, N. R., & O'Brien, P. T. 2013, MNRAS, 431, 394

Woosley, S. E. & Bloom, J. S. 2006, ARA&A, 44, 507

Worters, H. L., O'Connor, J. E., Carter, D. B., et al. 2016, in Society of Photo-Optical Instrumentation Engineers (SPIE) Conference Series, Vol. 9908, Ground-based and Airborne Instrumentation for Astronomy VI, ed. C. J. Evans, L. Simard, & H. Takami, 99083Y

Yang, J., Ai, S., Zhang, B.-B., et al. 2022, Nature, 612, 232

Yu, H. F. & Pelassa, V. 2015, GRB Coordinates Network, 17370, 1

Zafar, T., Watson, D., Fynbo, J. P. U., et al. 2011, A&A, 532, A143

Zhang, B. 2018, The Physics of Gamma-Ray Bursts

Zhang, B., Fan, Y. Z., Dyks, J., et al. 2006, ApJ, 642, 354

Zhang, B. & Mészáros, P. 2004, International Journal of Modern Physics A, 19, 2385

Zhang, B.-B., Burrows, D. N., Zhang, B., et al. 2012, ApJ, 748, 132

Zhang, B. B., Zhang, B., Castro-Tirado, A. J., et al. 2018, Nature Astronomy, 2, 69

Zhang, B.-B., Zhang, B., Murase, K., Connaughton, V., & Briggs, M. S. 2014, ApJ, 787, 66

Zhang, W. & MacFadyen, A. 2009, ApJ, 698, 1261

Table 4.6: Same as Table 4.4, but for our modelling in a stellar wind medium.

Parameter	value
p	$2.12^{+0.19}_{-0.10}$
$E_{\mathrm{K,iso}}$ (10^{53} erg)	$3.7^{+16.1}_{-2.9}$
n_0 (cm^{-3})	$1.1^{+3.2}_{-0.8} \times 10^{2}$
$\bar{\epsilon}_e$	$4.2^{+16.3}_{-3.1} \times 10^{-3}$
ϵ_B	$1.9^{+11.8}_{-1.7} \times 10^{-3}$
θ_j (deg)	$5.7^{+2.9}_{-2.5}$
$A_{\mathrm{V,host}}$ (mag)	0.11 ± 0.03

4.A A wind model for GRB 220627A

We performed theoretical modelling as in Sect. 4.4, but for a stellar wind circumburst medium. The parameter values derived from of our MCMC analysis are presented in Table 4.6, and a sample of model light curves are shown in Fig. 4.13. Compared to the ISM case, we find that a slightly higher value of p is preferred (2.12 vs 2.00) along with a wider jet (5.7 vs 4.5 deg), though both parameters agree within uncertainties with the ISM values. The wider jet results in a jet break in the light curves at later times than in the ISM case (1.8 vs 1.2 days). The model associated with the median values from the marginalised posterior distributions (bold line in Fig. 4.13) undergoes fast cooling ($\nu_c < \nu_m$) until 0.06 days. The rising cooling frequency ($\nu_c \propto t^{1/2}$) is below the optical and X-ray bands until ~10 days, so that the light curves in both observing bands decline as $\alpha = (2-3p)/4 = -1.09$ prior to the jet break at ~1.8 days. The self-absorption frequency is at $\sim 10^{12}$ Hz at 0.01 days and declines as $t^{-3/5}$ until ν_m crosses ν_a at 0.18 days. All the radio observations are therefore in the self-absorbed regime, and the peak in the light curves are due to the passage of ν_m through the observing band in question. The jumps in the radio light curves are due to the fact that simulations in a wind environment struggle more than ISM simulations to numerically resolve the radial profile of a relativistic blast wave.

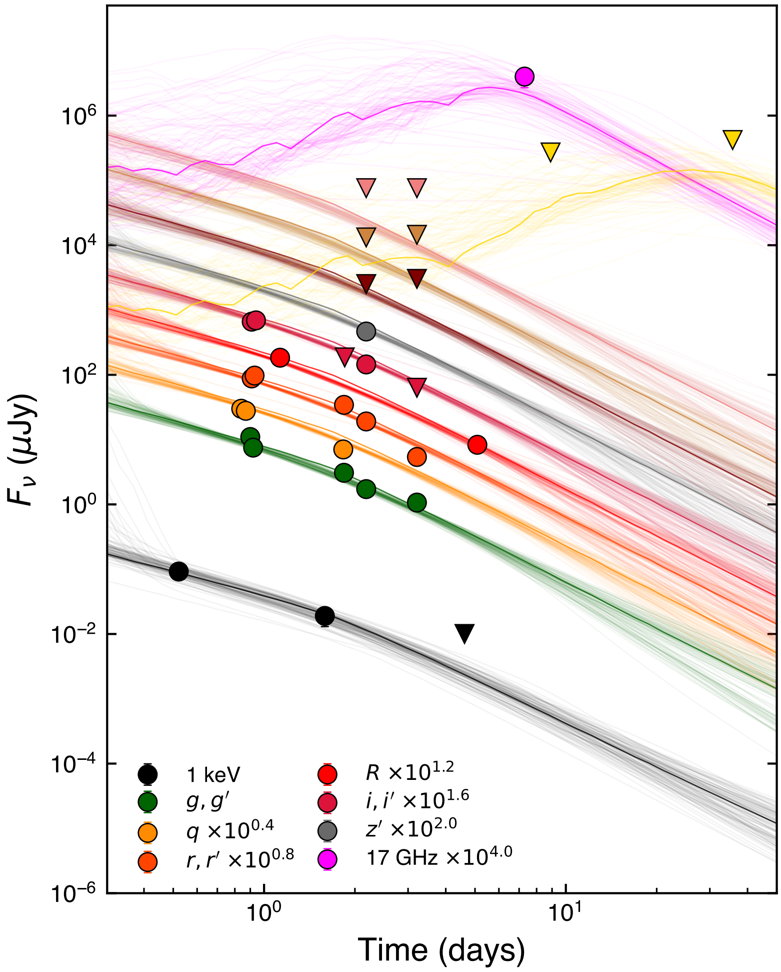

Figure 4.13: Same as Fig. 4.11, but for our modelling in a stellar wind medium.

Chapter 5

A millimeter rebrightening in GRB 210702A

S. de Wet[1], T. Laskar[2,3], P.J. Groot[1,3,4], E. Berger[5], C. Guidorzi[6,7,8], R. Barniol Duran[9], S. Kobayashi[10]

Based on the paper to be submitted to The Astrophysical Journal, February 2024

---

[1] Inter-University Institute for Data Intensive Astronomy & Department of Astronomy, University of Cape Town, Private Bag X3, Rondebosch, 7701, South Africa
[2] Department of Physics & Astronomy, University of Utah, Salt Lake City, UT 84112, USA
[3] Department of Astrophysics/IMAPP, Radboud University, P.O. Box 9010, 6500 GL, Nijmegen, The Netherlands
[4] South African Astronomical Observatory, P.O. Box 9, 7935, Observatory, South Africa
[5] Center for Astrophysics | Harvard & Smithsonian, 60 Garden St, Cambridge, MA 02138, USA
[6] Department of Physics and Earth Science, University of Ferrara, Via Saragat 1, I-44122 Ferrara, Italy
[7] INFN – Sezione di Ferrara, Via Saragat 1, 44122 Ferrara, Italy
[8] INAF – Osservatorio di Astrofisica e Scienza dello Spazio di Bologna, Via Piero Gobetti 101, 40129 Bologna, Italy
[9] Department of Physics and Astronomy, California State University, Sacramento, 6000 J Street, Sacramento, CA 95819-6041, USA
[10] Astrophysics Research Institute, Liverpool John Moores University, 146 Brownlow Hill, Liverpool L3 5RF, UK

Abstract

We present X-ray to radio frequency observations of the bright long gamma-ray burst GRB 210702A. Our ALMA 97.5 GHz observations show a significant rebrightening by a factor of ≈ 2 beginning at 8.2 days post-burst and rising to peak brightness at 18.1 days before declining again. This is the first such rebrightening seen in a millimeter afterglow light curve. A standard forward shock model in a stellar wind circumburst medium can explain most of our X-ray, optical and millimeter observations prior to the rebrightening, but fails to capture our self-absorbed radio emission and the millimeter rebrightening. We investigate possible explanations for the millimeter rebrightening and find that energy injection or a reverse shock from a late-time shell collision are plausible causes. Similar to other bursts, our radio data may require alternative scenarios such as a thermal electron population or a structured jet to explain the data. Our observations demonstrate that millimeter light curves can exhibit some of the rich features more commonly seen in optical and X-ray afterglow light curves, motivating further millimeter wavelength studies of GRB afterglows.

5.1 Introduction

The highly relativistic jets in long gamma-ray bursts (GRBs) are thought to be ejected by a black hole or a magnetar central engine that is formed following the catastrophic destruction of a massive Wolf-Rayet star due to their association with Type Ic supernovae (Woosley &

Bloom 2006). In the fireball model for GRBs, the GRB itself is produced via emission from internal dissipation processes within the expanding jet, while the longer-lived broadband afterglow emission is produced within an external forward shock created by the expanding jet as it sweeps up the surrounding medium (Mészáros & Rees 1997; Sari et al. 1998; Piran 1999, 2004; Kumar & Zhang 2015).

The forward shock model for GRB afterglows has been successful in explaining large swathes of observational data. In this basic picture, electrons are accelerated within the decelerating forward shock, which results in a power-law in energies that gives rise to a multi-segment broken power-law synchrotron emission spectrum characterised by a number of break frequencies whose evolution is dictated by the dynamics of the blast wave (Mészáros & Rees 1997; Sari et al. 1998). Optical and X-ray observations have shown widespread compatibility with the synchrotron forward shock model (Wang et al. 2015), though extensions from the simplest case have been required to account for less common features such as achromatic steepenings, flares and plateaus (Rhoads 1999; Sari et al. 1999; Zhang et al. 2006).

Compared to X-ray and optical observations, radio follow-up of GRBs has been more sparse, despite the key role that radio observations can play in elucidating the physics of GRB jets (Frail et al. 1997; Waxman et al. 1998; Berger et al. 2003; Chandra & Frail 2012; Granot & van der Horst 2014). Radio observations uniquely sample the peak of the synchrotron spectrum and the synchrotron self-absorption break, allowing for the GRB jet energy, external density, and microphysical parameters to be determined via broadband modelling. At later times once the blast wave has transitioned to a non-relativistic, spherical state, radio observations may be used to perform calorimetry and thereby constrain the jet energetics (Frail et al. 2000b; Berger et al. 2004; Frail et al. 2005; van der Horst et al. 2008). Very Long Baseline Interferometry observations have been used to constrain the source size and proper motion, for instance in GBR 030329 (Taylor et al. 2005; Pihlström et al. 2007; Mesler et al. 2012). Perhaps the most valuable contribution from studies at radio frequencies has been the detection of a second emission component due to reverse shock emission from a shock wave travelling back into the jet (Kulkarni et al. 1999; Frail et al. 2000a; Laskar et al. 2013; Perley et al. 2014; van der Horst et al. 2014), which has resulted in constraints on the jet's magnetization and initial bulk Lorentz factor (Sari & Piran 1999; Kobayashi & Zhang 2003; Zhang & Kobayashi 2005; Laskar et al. 2018b,a).

Observationally, radio light curves often rise at early times and peak at a few days post-burst before declining (at 8.5 GHz; Chandra & Frail 2012), which is in contrast to X-ray and optical light curves which are generally decaying at all times. Lower frequency radio light curves may even peak on longer timescales of months to years (e.g. GRB 030329; van der Horst et al. 2008). These peaks are commonly interpreted as the passage of the synchrotron peak frequency through the observing band, with lower frequencies peaking later than higher frequencies. Radio light curves show a diversity of behaviour, with some showing smooth light curves and others showing flares (Kulkarni et al. 1999; Soderberg et al. 2007; Schroeder et al. 2023). At early times, diffractive and refractive interstellar scintillation can severely affect centimeter-band observations, hampering physical interpretation. In contrast, millimeter observations are not subject to scintillation and therefore any observed light curve feature must be intrinsic to the source. Despite its value, millimeter follow-up efforts have been more limited compared to the centimeter bands, particularly in the pre-ALMA era when existing observatories had limited sensitivity (de Ugarte Postigo et al. 2012).

Here we present X-ray, optical, millimeter and radio observations of the long GRB 210702A spanning 8 orders of magnitude in frequency (1 keV to 700 MHz) and almost 5 orders of magnitude in time (0.001 to 86 days). Our ALMA 97.5 GHz (≈ 3 mm) light curve shows an unpredecedented rebrightening beginning at 8.2 days and increasing by a factor of ≈ 2 in brightness to reach a peak at 18.1 days before declining again. We find that a standard forward shock model can explain most of our multi-wavelength data prior to the millimeter rebrightening, but cannot explain the low frequency radio data and early X-ray light curve. We investigate a number of common explanations for rebrightenings in GRB afterglows and find that energy injection or a reverse shock from a late-time shell collision are plausible explanations, although we are unable to conclusively favour one scenario.

We report all uncertainties at the 1σ level unless stated otherwise, and all magnitudes are in the AB system. We adopt a ΛCDM cosmology with $\Omega_m = 0.315$ and $H_0 = 67.4$ km s^{-1} Mpc^{-1} (Planck Collaboration et al. 2020).

5.2 Observations

5.2.1 Prompt emission

The *Swift* Burst Alert Telescope (BAT; Barthelmy et al. 2005) was triggered by GRB 210702A at 19:07:13 UT on 2021 July 2 (Lien et al. 2021). Refined BAT analysis indicated that the γ-ray mask-weighted light curve showed a single-peaked fast rise exponential decay-like structure with a measured duration of $T_{90} = 138.2 \pm 47.6$ s. GRB 210702A was also detected by the CALET, AGILE, and Konus-Wind γ-ray detectors (Yamaoka et al. 2021; Ursi et al. 2021; Frederiks et al. 2021). The Konus Wind fluence in the 20 keV – 20 MeV range was $(2.5 \pm 0.2) \times 10^{-4}$ erg cm^{-2}. The burst redshift of $z = 1.160$ (Xu et al. 2021) corresponds to a luminosity distance of $D_L = 2.53 \times 10^{28}$ cm, from which we calculate a burst isotropic γ-ray energy of $E_{\gamma,\mathrm{iso}} = (9.3 \pm 0.7) \times 10^{53}$ erg. We take the BAT trigger time as T_0 and reference all other times with respect to this time.

5.2.2 X-ray

The X-Ray Telescope aboard *Swift* (XRT; Burrows et al. 2005) began observing the field of the GRB 95.5 s after the BAT trigger and identified a bright new X-ray source consistent with the BAT position (Lien et al. 2021). The first 310 s of data were taken in windowed timing (WT) mode while BAT was also capturing data, after which *Swift* had to slew away. Observations began again in photon counting (PC) mode at 3561 s post-trigger. We downloaded the X-ray count-rate light curve and time-averaged WT and PC spectra from the online *Swift*/XRT GRB Catalogue[1]. We fitted the WT and PC mode spectra in Xspec version 12.13.0 with a photoelectrically absorbed power-law model (`tbabs*ztbabs*pow`) taking into account Galactic and host galaxy absorption. The Galactic column density was fixed at $N_{\mathrm{H,Gal}} = 1.19 \times 10^{21}$ cm^{-2} (Willingale et al. 2013) and the burst redshift at $z = 1.160$. For the PC mode spectrum we derived a host galaxy column density of $N_{\mathrm{H,host}} = (2.3 \pm 0.6) \times 10^{21}$ cm^{-2} with a C-stat of 522 for 561 degrees of freedom. We obtained photon indices of $\Gamma = 1.54 \pm 0.01$ and $\Gamma = 1.95 \pm 0.03$ for the WT and PC mode spectra, respectively. The resulting spectral indices[2] are therefore $\beta_{\mathrm{X,WT}} = -0.54 \pm 0.01$ and $\beta_{\mathrm{X,PC}} = -0.95 \pm 0.03$. Using the photon indices from our fits along with respective unabsorbed counts-to-flux conversion factors of 4.86×10^{-11} erg cm^{-2} count^{-1} and 4.54×10^{-11} erg cm^{-2} count^{-1} from our fits, we converted the 0.3–10 keV count-rate light curve into a 1 keV flux density light curve.

5.2.3 UV/Optical

The *Swift* Ultra-Violet Optical Telescope (UVOT; Roming et al. 2005) started observing the BAT error region 104 s after the BAT trigger in the *white* filter. A bright optical source consistent with the XRT position was identified at coordinates $\alpha = 11^{\mathrm{h}}14^{\mathrm{m}}18.70^{\mathrm{s}}$, $\delta = -36°44'50.0''$ (J2000) with an uncertainty of $0.42''$ (Kuin et al. 2021). The first 147 s *white* filter exposure was saturated, along with a 44 s u-band exposure that began at 316 s post-trigger. UVOT recommenced observations just under one hour post-trigger, detecting the afterglow with a brightness of $b = 15.15 \pm 0.03$ mag. Observations continued intermittently in all filters until 8.08 days post-trigger. We obtained the

---

[1] https://www.swift.ac.uk/xrt_live_cat/01058804/

[2] Using $\beta_{\mathrm{X}} \equiv 1 - \Gamma$.

UVOT data from the *Swift* Archive Download Portal[3] hosted on the UK *Swift* Science Data Centre website, and extracted magnitudes using the `uvotproduct` tool from the HEASoft[4] *Swift* FTOOLS software package, version 6.31.1. We employed a $5''$ aperture for the source region and a $10''$ aperture for the background region. For the saturated u-band exposure we adopt the AB magnitude measurement of $u = 12.34 \pm 0.18$ mag calculated by Zhou et al. (2023) using their method for measuring photometries of moderately saturated UVOT sources. We do not include the *white* filter exposures since the *white* filter is too broad for our purposes.

The MeerLICHT optical telescope (Bloemen et al. 2016) was automatically triggered by the *Swift* detection of GRB 210702A and began observing the BAT errorbox at 19:22:54 UT, just under 16 minutes after the BAT trigger time. Observations consisted of 60 s exposures in six optical filters following the filter sequence $quqgqrqiqz$, where the q band is a wide filter spanning 440–720 nm and the $ugriz$ bands are standard SDSS filters. The optical afterglow was detected with a brightness of $q = 12.84 \pm 0.02$ mag in our first exposure (Groot et al. 2021). A total of 15 exposures were obtained over 25 minutes of observing before strong winds forced the telescope to close. We used the MeerLICHT pipeline (Vreeswijk et al., in prep.) to reduce the data, implementing standard CCD reduction tasks including astrometry and PSF photometry. The afterglow was well detected in all images.

We additionally make use of optical photometry made public through Gamma-Ray Coordinates Network (GCN) Circulars: the X-Shooter acquisition camera on the Very Large Telescope (VLT) detected the afterglow in a 20 s exposure at 0.18 days post-trigger with a brightness of $r' = 16.91 \pm 0.01$ mag (Xu et al. 2021), and the Chilescope RC-1000 telescope detected the afterglow at 0.19 days with a brightness of $r' = 17.01 \pm 0.05$ mag (Belkin et al. 2021).

5.2.4 Radio

ALMA

We obtained nine epochs of observations with the Atacama Large Millimeter/submillimeter Array (ALMA) in Band 3 (97.5 GHz) and three epochs of observations in Band 7 (343.5 GHz), through programs 2019.1.01484.T (PI Laskar) and 2019.1.01032.T (PI Perley). The Band 3 and Band 7 observations both employed two 4 GHz base-bands centred on 91.5 and 103.5 GHz, and 337.5 and 349.5 GHz, respectively. We downloaded the pipeline-generated images from the ALMA archive and measured the source flux using the Common Astronomy Software Application (CASA; McMullin et al. 2007) `imfit` task.

ATCA

We observed GRB 210702A at seven epochs with the Australia Telescope Compact Array (ATCA) beginning at 3.50 days post-trigger. The first epoch consisted of observations in the 16.7, 21.2, 33 and 35 GHz bands, while all subsequent epochs consisted of observations at these same frequencies along with the 5.5 and 9 GHz bands. We used PKS 1934−638 as the flux and bandpass calibrator and PKS 1144−379 as the complex gain calibrator. At 33 and 35 GHz the flux calibrator was significantly fainter than the gain calibrator, so in these two bands we used the gain calibrator as our bandpass calibrator (after first deriving its intrinsic spectral index using PKS 1934−638) in order to derive an accurate bandpass solution.

We used the `MIRIAD` software package[5] (Sault et al. 1995) for calibration and the CASA `tclean` task for imaging the calibrated target visibilities. We combined the 33 and 35 GHz measurement sets prior to imaging in order to obtain a single 34 GHz flux measurement. At 5.5 GHz we combined the target visibilities from all epochs and imaged the resulting data set in order to create a sky model for the other sources in the field. We then performed imaging on the

---

[3] https://www.swift.ac.uk/swift_portal/

[4] https://heasarc.gsfc.nasa.gov/docs/software/lheasoft/

[5] https://www.atnf.csiro.au/computing/software/miriad/

UV-subtracted target visibilities in order to measure the source flux. During epochs four through six the Array was in a configuration in which antenna CA06 was located far away compared to the other antennas. We excluded antenna CA06 while imaging the fifth epoch data as it produced better results. The epoch three and seven high frequency (16.7–35 GHz) gain calibrator phases varied wildly as a result of poor weather. We therefore exclude these data from subsequent analysis.

We measured the flux of the afterglow using two methods: using the CASA `imfit` task on the target images; and UV-fitting the calibrated measurement sets with a point source model with the CASA `uvmodelfit` task. The fluxes measured with both methods were generally found to agree within errors. We employ the UV fitting fluxes henceforth.

Additionally, Anderson et al. (2023) obtained early ($t < 1$ day) radio observations of GRB 210702A with ATCA and found rapid variability in the radio light curves which they attribute to interstellar scintillation. Since short time-scale variability is not the focus of this paper, we take the average of the 3σ fluxes per observing band from their Table A1 which results in a single flux measurement in each of the 5.5, 9, 16.7 and 21.2 GHz bands at ≈ 0.53 days.

MeerKAT

We observed the radio afterglow with the MeerKAT radio telescope in the L band (1.28 GHz) at five epochs through observing program SCI-20210212-TL-01 (PI Laskar). We used J0408−6545 as the flux and bandpass calibrator for the first and last epochs and J1939−6342 as the flux and bandpass calibrator for the intervening epochs, while J1154−3505 was used as the complex gain calibrator for all epochs. The total integration time on source was 0.65 hr per epoch. We flagged, calibrated and imaged the data using the `oxkat` pipeline[6] (Heywood 2020), and measured the flux of the afterglow with the `imfit` task in CASA.

GMRT

We obtained five epochs of observations with the Giant Metrewave Radio Telescope (GMRT) through program 40_084 (PI Laskar) beginning at 8.6 days post-trigger. Observations were carried out in Band 4 (700 MHz) with a 400 MHz bandwidth, employing 3C286 as the flux and bandpass calibrator, and J1154−350 as the complex gain calibrator. We flagged and calibrated the data using standard reduction techniques in CASA, and thereafter used the Inter-University Institute for Data Intensive Astronomy (IDIA) `processMeerKAT` software pipeline[7] (Collier, Sekhar, Frank, Taylor, et al., in prep.) to perform imaging and two rounds of phase self-calibration followed by one round of amplitude and phase self-calibration. No radio source was visible at the GRB position in the images from the first four epochs, so we report upper limits as three times the RMS noise at the afterglow position, calculated using the CASA task `imstat`. We detected the afterglow in our fifth and final epoch image and measured the flux density using `imfit`.

We report all X-ray, optical and radio flux measurements in Table 5.3, and we present examples of our radio images in Figure 5.1.

5.3 Multi-wavelength modelling

We interpret our observations within the synchrotron forward shock model of GRB afterglows. In this model, a collimated relativistic blast wave sweeps up the surrounding circumburst medium forming a shock front in which electrons are accelerated into a power-law distribution in energies characterised by a spectral index p. The electron distribution gives rise to a multi-segment broken power-law emission spectrum consisting of spectral breaks at three frequencies: ν_m is the frequency of the spectral break corresponding to electrons with the minimum energy in the

---

[6] https://github.com/IanHeywood/oxkat

[7] https://idia-pipelines.github.io/docs/processMeerKAT

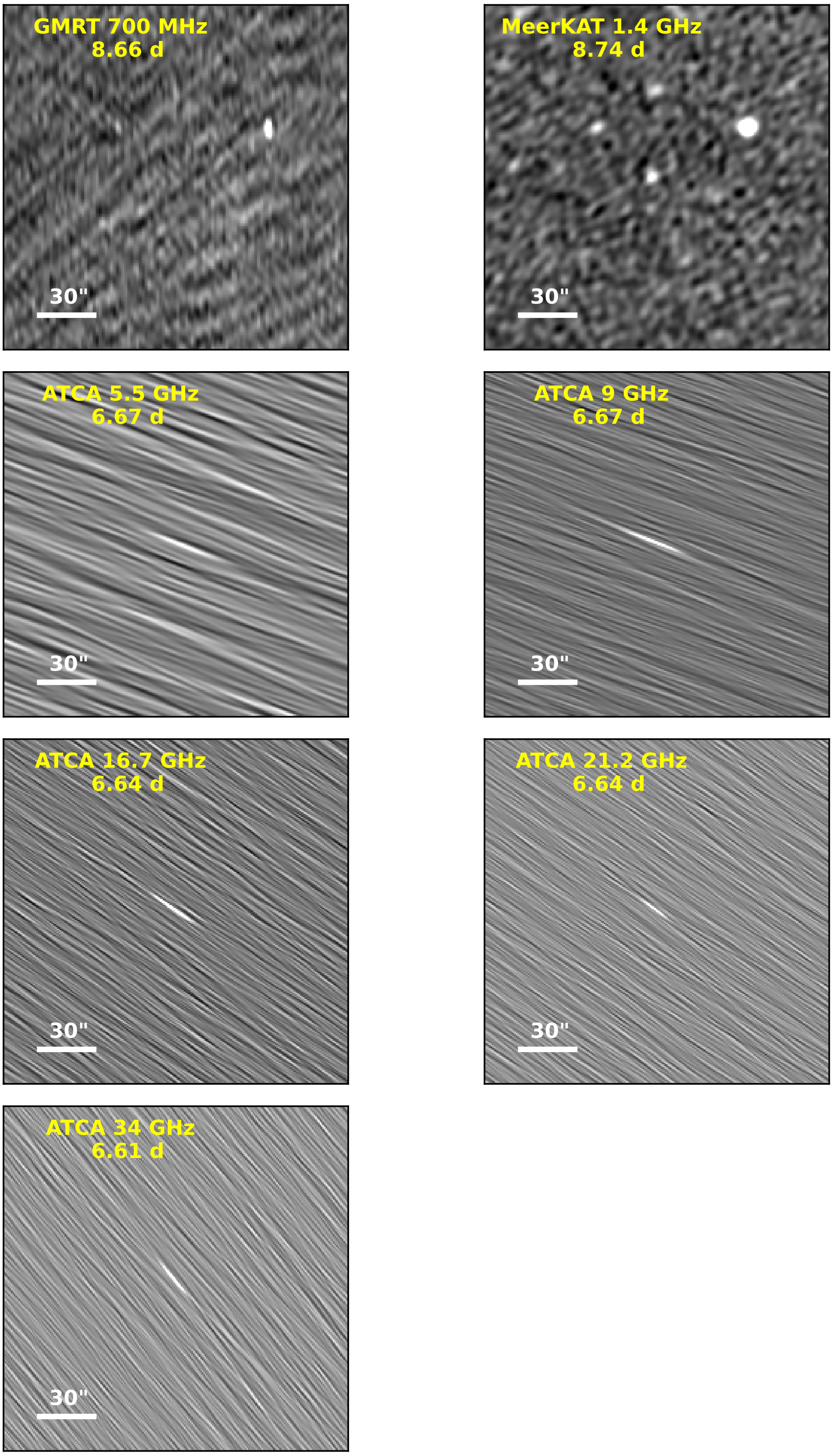

Figure 5.1: Example radio images obtained with the GMRT, MeerKAT, and ATCA radio telescopes spanning 700 MHz to 34 GHz. Each image is a $3' \times 3'$ cutout centred on the afterglow position. The afterglow is visible in all images other than the GMRT 700 MHz image, for which we derived an upper limit. The ATCA 5.5 GHz image is derived from sky-UV-subtracted data.

Parameter	Value
PL α	-1.03 ± 0.02
BPL α_1	3.04 ± 0.78
BPL α_2	-3.41 ± 1.60
BPL t_b (days)	19.50 ± 4.33

Table 5.1: ALMA 97.5 GHz light curve fit parameters

distribution; ν_c is that of the break above which electrons are undergoing cooling; and ν_a is the frequency of the break below which synchrotron radiation is self-absorbed. The evolution of the spectral breaks is dictated by the dynamics of the blast wave, for which we assume the Blandford & McKee (1976) solution for a relativistic explosion. The synchrotron forward shock model is described in detail in Sari et al. (1998) and Granot & Sari (2002). We follow the convention with $F_\nu \propto t^\alpha \nu^\beta$ henceforth.

5.3.1 The millimeter rebrightening

The most striking feature of our multi-wavelength data set is the ALMA 97.5 GHz light curve, as shown in Figure 5.2. After five epochs of clear fading behaviour the light curve begins to rebrighten at 8.2 days post-trigger, rising to a peak at 18.1 days before declining again. This rebrightening by a factor of ≈ 2 in flux is, to our knowledge, the first such rebrightening seen in a millimeter afterglow light curve. Although the light curve behaviour is unusual, the 3 millimeter luminosity of GRB 210702A is typical when compared to other long GRB millimeter light curves (Figure 5.3).

To characterise this light curve further, we fit a model comprising the sum of a power-law (PL) and a smoothly broken power-law (BPL), where the BPL follows the functional form

$$F(t) = F_0 \left[\left(\frac{t}{t_b} \right)^{-\alpha_1 \omega} + \left(\frac{t}{t_b} \right)^{-\alpha_2 \omega} \right]^{-1/\omega}, \tag{5.1}$$

with F_0 as a normalising flux, α_1 and α_2 as the pre- and post-break temporal indices, t_b as the break time, and ω as a smoothness parameter which sets the sharpness of the break. Larger values of ω (> 1) correspond to a sharper break in the light curve. The results of our light curve fit in Table 5.1 show that the power-law component decays with $\alpha_{97.5\ \mathrm{GHz}} = -1.03 \pm 0.02$. For the broken power-law component we find that a smoother break with $\omega = 1$ results in a better fit than sharper breaks. The rising and decaying indices for this component are $\alpha_1 = 3.04 \pm 0.78$ and $\alpha_2 = -3.41 \pm 1.60$ with a break time of $t_b = 19.5 \pm 4.3$ days. On the other hand, direct fits to the rising and decaying segments (Figure 5.2) result in $\alpha_{97.5\mathrm{GHz,rise}} = 0.95$ and $\alpha_{97.5\mathrm{GHz,decay}} = -1.67 \pm 0.17$, respectively, while the 343.5 GHz light curve decays with $\alpha = -1.31$. We return to this in our investigation of the millimeter rebrightening in Section 5.5.

5.3.2 X-ray and UV/optical temporal evolution

The X-ray and UV/optical band data show declining light curves throughout our observations. Fitting the MeerLICHT and *Swift* UV/optical data separately with power-laws in time, we find that the optical temporal decay rate during the MeerLICHT observations is $\alpha = -1.23 \pm 0.02$ while the decay rate during the *Swift* UV/optical observations is $\alpha = -1.37 \pm 0.02$ (see Figure 5.4), indicating a steepening in the optical decay rate between the two sets of observations. The residuals from the power-law fit to the MeerLICHT observations show evidence for the steepening occurring at ≈ 0.016 days, which we return to when fitting the combined optical light curve below.

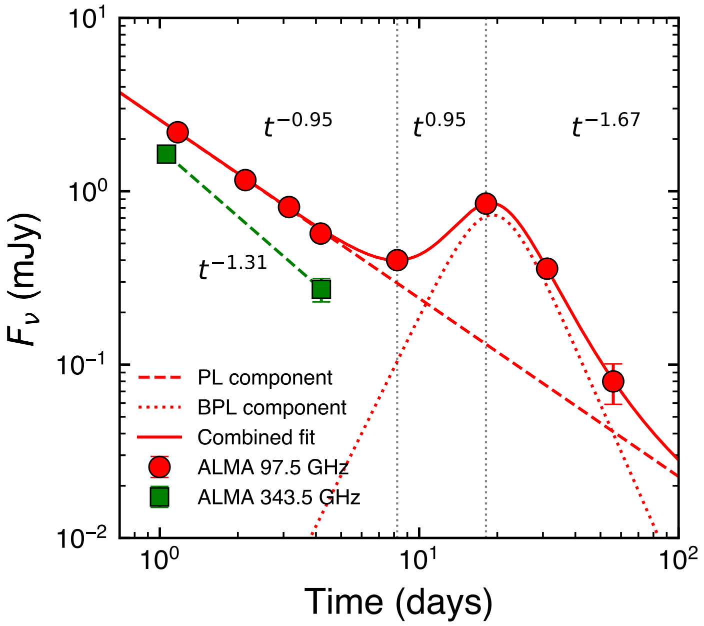

Figure 5.2: ALMA 97.5 GHz and 343.5 GHz light curves for GRB 210702A. The ALMA 97.5 GHz light curve shows a clear rebrightening peaking at ≈ 18 days. We show the combined PL+BPL fit to the 97.5 GHz light curve as well as each model component. The results of our fit are presented in Table 5.1. The decay rates from direct fits to each light curve segment are indicated above (below) the 97.5 GHz (343.5 GHz) light curve.

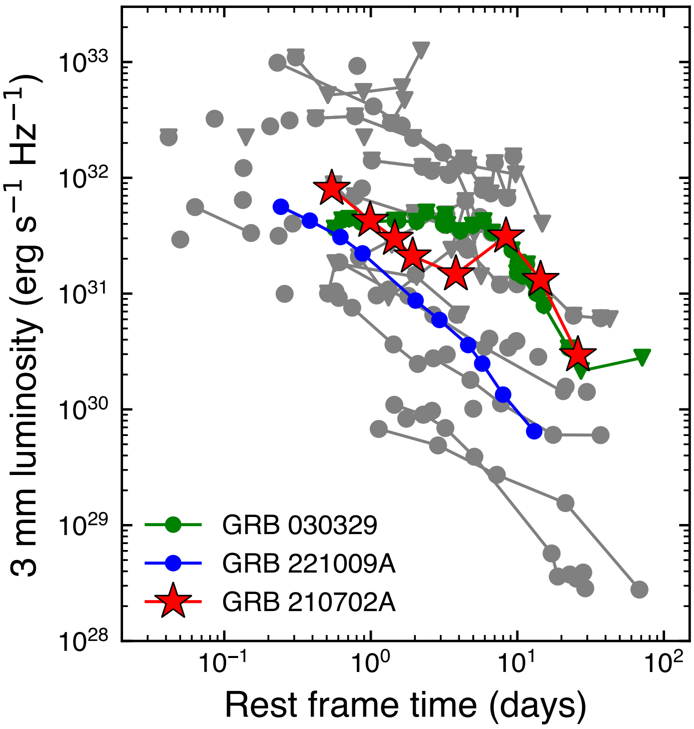

Figure 5.3: Spectral luminosity at a wavelength of 3 mm for GRB 210702A and a sample of long GRBs (gray) from Eftekhari et al. (2022). We highlight GRB 030329 and GRB 221009A, two nearby ($z = 0.1685$ and $z = 0.151$) and extremely bright bursts. GRB 210702A is the first GRB with a clear rebrightening at millimeter wavelengths, though its luminosity is at all times by no means exceptional.

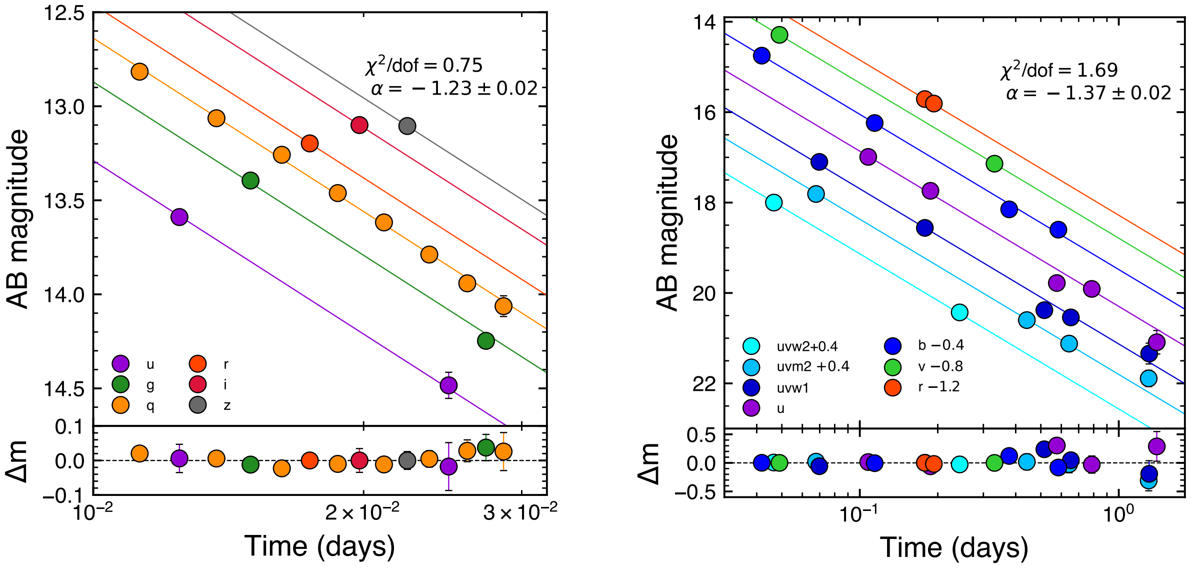

(a) (b)

Figure 5.4: Power-law light curve fits to the MeerLICHT photometry (a) and *Swift*/UVOT photometry including the X-Shooter and Chilescope r-band measurements (b). The power-law decay rate was constrained to be the same across each band during fitting. The MeerLICHT residuals show evidence for a steepening in the light curve at ≈ 0.016 days

We measure the u- to v-band spectral index during each set of observations by interpolating our light curve fits in Figure 5.4 to a common time, and find that the MeerLICHT in-band spectral index of $\beta_{\mathrm{MeerLICHT}} = -1.42 \pm 0.15$ is consistent with the UVOT in-band spectral index of $\beta_{\mathrm{UVOT}} = -1.46 \pm 0.11$. To characterise the optical temporal evolution further, we create a composite b-band light curve by transforming the UVOT u, b and v bands along with the MeerLICHT u, g and q bands to a common observing frequency equivalent to the UVOT b-band using a spectral index of $\beta = -1.44$, the average spectral index from our spectral fits to the MeerLICHT and UVOT data. Since the optical light curve steepens between the MeerLICHT and UVOT observations, we fit the light curve with a smoothly broken power-law following Equation 5.1. The best-fit light curve (see Figure 5.5) has pre- and post-break temporal indices of $\alpha_1 = -1.05 \pm 0.16$ and $\alpha_2 = -1.42 \pm 0.01$, respectively, favouring a sharper break ($\omega \approx 29$) with a break time of $t_b = 0.017 \pm 0.002$ days which is consistent with the evidence for a break seen in our residuals from the power-law fit to the MeerLICHT data. The steepening of the light curve to $\alpha = -1.42 \pm 0.01$ is unlikely to be due to a jet break since post-jet break decay is predicted to decay as t^{-p} with p between 2 and 3 (Sari et al. 1999). If lateral spreading of the jet is not significant, the predicted steepening is $\Delta\alpha = -0.75$ in an interstellar medium-like (ISM) circumburst medium or $\Delta\alpha = -0.5$ in a stellar-wind medium. Both of these cases are still steeper than the measured $\Delta\alpha = -0.37 \pm 0.16$, though the wind case does agree within the errors. If the temporal steepening is due to the passage of the cooling break we would expect a change of $\Delta\alpha = -0.25$ which is shallower than the measured $\Delta\alpha = -0.37 \pm 0.16$, but also consistent within the errors. We return to this in Section 5.3.3.

The X-ray light curve consists of two segments separated by a period during which *Swift* had to slew away. Fitting each segment with a simple power-law (see Figure 5.5), we find that the early WT-mode decay rate of $\alpha_{\mathrm{WT}} = -1.00 \pm 0.02$ is consistent with the early optical evolution, while the later PC-mode decay rate of $\alpha_{\mathrm{PC}} = -1.44 \pm 0.01$ is in very close agreement with the post-break optical decay rate of $\alpha_2 = -1.42 \pm 0.01$. Although the pre- and post-break X-ray and optical decay rates are very similar and may suggest achromatic X-ray to optical evolution, we note that the X-ray to optical b-band spectral index was $\beta_{\mathrm{O-X}} = -0.91$ at 0.004 days and

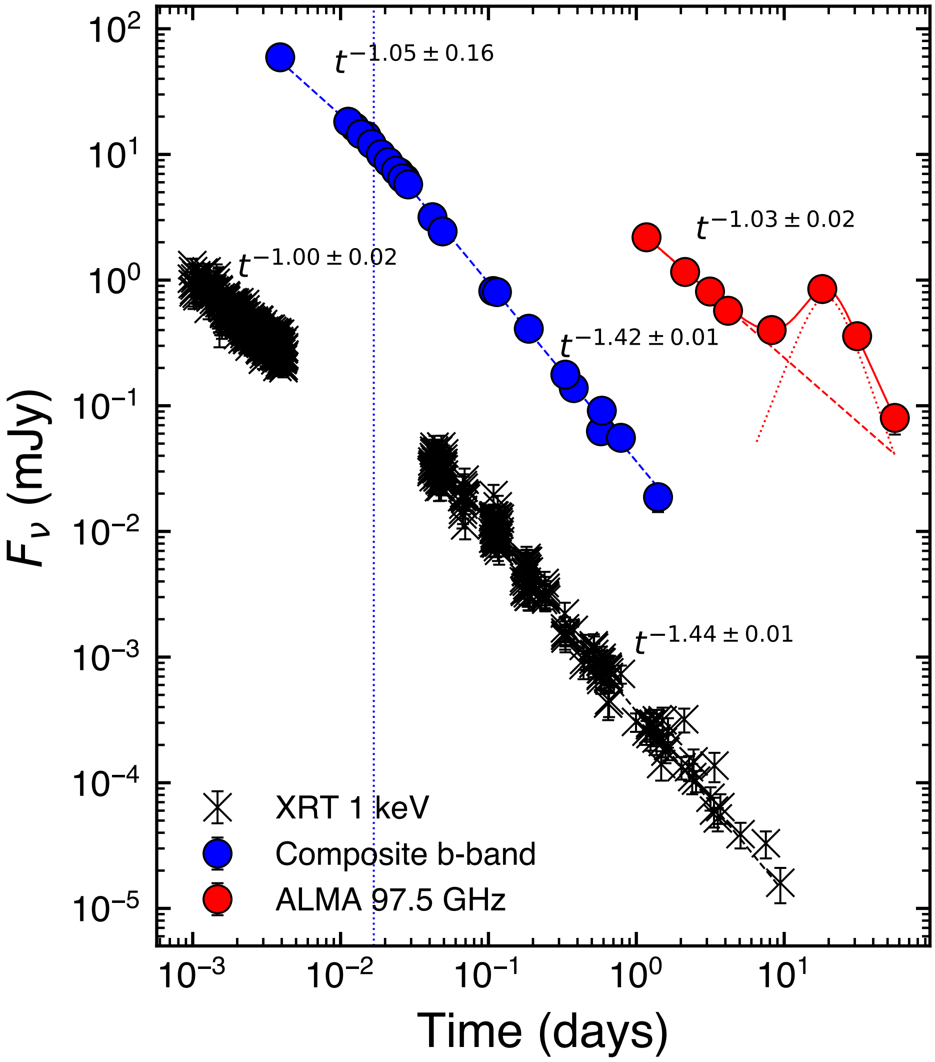

Figure 5.5: X-ray, composite b-band and ALMA 97.5 GHz light curves. We show the power-law fits to the WT-mode and PC-mode X-ray light curve segments (black dashed lines), and the broken power-law fit to the optical light curve (blue dashed line). The vertical dotted line denotes the break time of the optical light curve fit, $t_b = 0.017 \pm 0.002$ days. We show the light curve fit from Figure 5.2.

$\beta_{\mathrm{O-X}} = -0.77$ at 0.1 days, therefore ruling out achromatic evolution between the two bands. We return to this in Section 5.3.3 below.

5.3.3 Stellar wind medium

We now investigate whether a standard forward shock model can explain the observed spectral and temporal characteristics of our X-ray, UV/optical and early millimeter data. From 0.2–10 days our X-ray and UV/optical light curves decline as power-laws with similar indices of $\alpha \approx -1.43$, suggestive of a 'normal' afterglow decay and that both bands may lie within the same spectral regime. During slow-cooling ($\nu_m < \nu_c$) there are two spectral regimes to consider for our declining X-ray and optical light curves: either $\nu_m < \nu_c < \nu_{\mathrm{O}} < \nu_{\mathrm{X}}$ or $\nu_m < \nu_{\mathrm{O}} < \nu_{\mathrm{X}} < \nu_c$.

In the regime with $\nu_m < \nu_c < \nu_{\mathrm{O}} < \nu_{\mathrm{X}}$ we expect a spectral index of $\beta = -p/2$ and a temporal decay rate of $\alpha = (2 - 3p)/4$, regardless of the circumburst medium. Using the average of the observed optical and X-ray temporal indices of $\alpha = -1.43 \pm 0.01$ results in $p = 2.57 \pm 0.01$ and a spectral index of $\beta = -1.28 \pm 0.01$. Correcting our optical SED derived from the *Swift*/UVOT light curve for a Galactic extinction of $A_V = 0.3271$ mag along the line of sight (Schlafly & Finkbeiner 2011), the b- to r-band spectral index of $\beta_\mathrm{O} = -0.63 \pm 0.08$ is clearly in disagreement with the predicted spectral index of $\beta = -1.28 \pm 0.01$, ruling out this scenario.

In the regime with $\nu_m < \nu_\mathrm{O} < \nu_\mathrm{X} < \nu_c$ we expect a spectral index of $\beta = (1-p)/2$ and temporal indices of $\alpha_\mathrm{ISM} = 3(1-p)/4$ for an ISM-like circumburst medium or $\alpha_\mathrm{wind} = (1-3p)/4$ for a stellar wind medium. For the ISM case we derive $p = 2.91 \pm 0.01$ and a spectral index of $\beta = -0.96 \pm 0.01$ from our temporal index of $\alpha = -1.43 \pm 0.01$. This was the scenario favoured by Anderson et al. (2023). Although this spectrum agrees with the PC-mode X-ray spectral index of $\beta_\mathrm{X} = -0.95 \pm 0.03$ (Section 5.2.2), it is steeper than the optical index of $\beta_\mathrm{O} = -0.63 \pm 0.08$ and the optical-to-X-ray index of $\beta_\mathrm{O-X} = -0.77$ calculated at 0.1 days. For the stellar wind case we derive $p = 2.24 \pm 0.01$ from our observed light curve evolution and an expected spectral index of $\beta = -0.62 \pm 0.01$, which is in close agreement with the optical spectral index of $\beta_\mathrm{O} = -0.63 \pm 0.08$ and therefore our preferred scenario. With $p = 2.24 \pm 0.01$ the predicted spectral index above the cooling break is $\beta = -1.12 \pm 0.01$, which is slightly steeper than our X-ray spectral index of $\beta_\mathrm{X} = -0.95 \pm 0.03$. In a stellar wind medium, the frequency of the cooling break, ν_c, rises as $t^{1/2}$. A smooth cooling break (Uhm & Zhang 2014) with ν_c close to the X-ray band is a possible explanation for the similar temporal indices of the X-ray and optical bands, but steeper X-ray spectrum compared to the optical.

Further support for a stellar wind medium is found when considering the early millimeter data. At the time of the first ALMA 97.5 GHz detection at 1.17 days, we measure a 97.5 GHz to optical r-band spectral index of $\beta_\mathrm{97.5GHz-O} = -0.47$, which is shallower than the optical in-band spectral index $\beta_\mathrm{O} = -0.63 \pm 0.08$ and optical-to-X-ray index of $\beta_\mathrm{O-X} = -0.77$. Moreover, extrapolating our 97.5 GHz light curve fit to the time of the first 343.5 GHz detection at 1.06 days yields a 97.5 GHz to 343.5 GHz spectral index of $\beta_\mathrm{97.5-343.5GHz} = -0.31$, indicating that the spectrum is flattening off towards lower frequencies and that ν_m lies below the millimeter bands. In an ISM medium the peak flux of the synchrotron spectrum remains constant with time, whereas in a stellar wind medium the peak flux declines as $t^{-1/2}$. Assuming that ν_m is within the 97.5 GHz band at the time of our first detection at 1.17 days, the corresponding peak flux is $F_{\nu_m} \approx 2$ mJy. Our u-band detection at 0.004 days has a flux density of $F_u \approx 42$ mJy, which is more than an order of magnitude larger than our constraint on the peak flux from our millimeter data at 1.17 days and therefore clearly rules out an ISM medium.

The peak frequency for both an ISM and wind medium evolves as $t^{-3/2}$. If we assume a stellar wind medium in which ν_m is close to the 97.5 GHz band with a flux of $F_{\nu_m} \approx 2$ mJy at 1.17 days, we expect the peak flux to be $F_{\nu_m} \approx 34$ mJy at 0.004 days and ν_m to be at a frequency $\nu_m \approx 4.9 \times 10^{14}$ Hz, which corresponds to the optical r-band. Since the u band must be above ν_m due to the declining optical light curve and negative spectral slope observed in the MeerLICHT data, ν_m in the r-band at 0.004 days is consistent with our observations. The expected peak flux of $F_{\nu_m} \approx 34$ mJy is only a factor 1.2 smaller than our u-band detection of $F_u \approx 42$ mJy at this time, and so we still regard a stellar wind medium as being consistent with our observations.

The UV/optical and millimeter light curves initially have temporal decay rates with $\alpha \approx -1$ compared to the later decay rate of $\alpha \approx -1.43$ observed in the optical and X-rays. This shallower decay might be due to the proximity of ν_m to the observing band, causing the light curve to decay less steeply initially before transitioning to the expected decay rate. The shallow decay with $\alpha = -1.00 \pm 0.02$ observed in the X-rays prior to 0.01 days, however, cannot be explained via this interpretation since ν_m should be far below the X-ray band at this time. An explanation for the shallower X-ray decline could be continuous energy injection into the GRB blast wave which results in an observed plateau or shallow decay, an effect which has been observed extensively in X-ray light curves (Zhang et al. 2006; Nousek et al. 2006).

5.3.4 Radio evolution

We have shown in the previous section that the optical, X-ray data after 0.01 days, and millimeter data prior to the millimeter wavelength rebrightening can be explained with a standard forward shock model in a stellar wind medium with $p \approx 2.2$. We now consider the implications of our lower frequency radio data.

Figure 5.6 shows our radio light curves separated by observing band and instrument. We have extracted SEDs at seven epochs indicated by the vertical grey regions, which are shown in Figure 5.7. The ALMA 97.5 GHz rebrightening begins at 8.2 days and rises to a peak at 18.1 days. Prior to the start of the rebrightening at 8.2 days we assume that the rebrightening does not have a significant effect on the light curves nor SEDs. The early ATCA observations obtained by Anderson et al. (2023) allow us to construct an SED at the time of our first ALMA observations by interpolating the light curves using their power-law behvaiour. The Epoch 1 SED shows a clearly rising spectrum from 5.5 GHz to 97.5 GHz measurement with a spectral index of $\beta_{5.5-97.5\mathrm{GHz}} = 0.93 \pm 0.06$. Such a rising spectrum is suggestive of optically thick synchrotron emission, which we use to place a tentative constraint on the self-absorption break of $\nu_a \approx 97.5$ GHz at 1.17 days. From our arguments in Section 5.3.3, this places ν_a very close to ν_m at this time. In Section 5.4 below we will demonstrate that no standard forward shock model can accommodate such a high self absorption frequency.

Although $\beta_{5.5-97.5\mathrm{GHz}} = 0.93 \pm 0.06$ is not as steep as the theoretically-predicted slope of ν^2 for synchrotron self-absorbed emission, a smooth self-absorption break may account for the shallower measured slope. The rising ATCA light curves at $t < 8$ days (see Figure 5.6) with $\alpha \approx 1$ are also suggestive of optically thick emission, since the predicted temporal evolution below ν_a is t^1 in a stellar wind medium. By the time of our Epoch 2 SED at 3.5 days we see a flat spectrum from 16.7 to 97.5 GHz. This allows us to place a constraint on the self-absorption break of $\nu_a < 16.7$ GHz, and that ν_a must have evolved faster than $t^{-1.6}$ between these two epochs. Such a fast evolution of the self-absorption break is inconsistent with any known evolution. The declining spectrum from 97.5 to 343.5 GHz appears to be consistent with ν_m having passed through the millimeter bands as demonstrated in Section 5.3.3 above. The Epoch 3 SED at 6.6 days provides a second clear case of a self-absorbed spectrum with a spectral index $\beta = 1.03 \pm 0.16$ measured from 5.5 to 16.7 GHz, and a self-absorption break at $\nu_a \approx 16.7$ GHz. The fact that the self-absorption break evolved as $t^{-1.6}$ between Epochs 1 and 2 and not at all between Epoch 2 and 3 demonstrates that the optically-thick radio data cannot be reconciled within any standard forward shock model.

Throughout the millimeter rebrightening, our radio light curves do not show obviously achromatic behaviour. The low frequency 1.4, 5.5 and 9 GHz bands rise and even peak when the 97.5 GHz light curve is rising and peaks, whereas the higher frequency bands at 16.7, 21.2 and 34 GHz do not show clear rises despite being closer to the 97.5 GHz band in frequency. We note that the omission of higher frequency data from our third epoch of ATCA data at 10.4 days (Section 5.2.4) leads to a loss of possibly valuable temporal information. Following the 97.5 GHz peak, all of the radio light curves besides the 1.4 GHz MeerKAT light curve decline. Since the MeerKAT band is in the optically thick regime throughout our observations (see Figure 5.7), the rising light curve appears consistent with rising self-absorbed synchrotron emission (Granot & Sari 2002).

Before, during, and after the rebrightening, our radio SEDs show complex behaviour. Epoch 4 coincides in time with the 97.5 GHz peak and the fluxes measured in that epoch show tentative evidence for an additional spectral component peaking at 97.5 GHz as seen in the rising spectrum from 16.7 to 97.5 GHz. The Epoch 5 and 6 SEDs show similar peaks at 34 GHz and 21.2 GHz, respectively. However, our radio SEDs are characterised by a number of sharp jumps which may not be intrinsic to the source since we do not expect synchrotron radiation from a relativistic blast wave – even with additional spectral components – to result in such sharp jumps in the spectrum. It may be the case that the small scale features in our light curves and SEDs are a

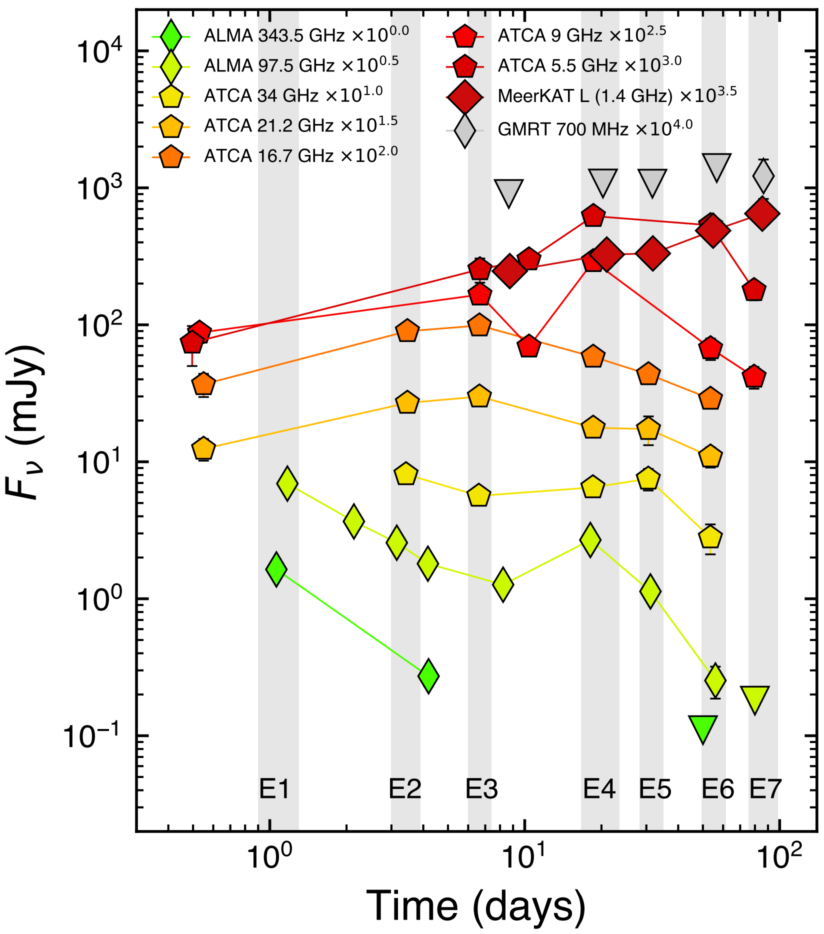

Figure 5.6: Radio light curves separated by observing band. The vertical grey columns indicate the epochs for which we show the corresponding radio SEDs in Figure 5.7. We shift each light curve vertically in flux for clarity, while upper limits are shown as upside down triangles. We advise caution in interpreting the significant dip seen in the 9 GHz light curve at 10.4 days since this epoch of ATCA data was strongly affected by phase instabilities (see Section 5.2.4).

result of interstellar scintillation or unaccounted-for systematic uncertainties from the calibration of our ATCA data. The unusual SEDs call us to question We discuss our radio data taken during and after the rebrightening further in Section 5.5.

5.4 Afterglow modelling with ScaleFit

Constraints on the three spectral break frequencies (ν_a, ν_m, ν_c) and the peak flux of the synchrotron spectrum can be used to derive intrinsic blast wave parameters of the forward shock and may also be used to test whether a standard forward shock model is compatible with our data. In Section 5.3.3 we constrained the peak flux to $F_{\nu_m} \approx 2$ mJy at 1.17 days, the time of our first 97.5 GHz observation. We also have ν_m close to the 97.5 GHz band at this time, so $\nu_m \approx 90$ GHz. We expect the cooling break to cross the X-ray band during our PC-mode observations, so $\nu_c \approx 2.4 \times 10^{17}$ Hz at 0.5 days. Our Epoch 1 radio SED places a constraint on the self-absorption frequency of $\nu_a \approx 97.5$ GHz at 1.17 days. Solving the system of four equations describing the locations of the spectral breaks and their flux densities in a wind medium (see Table 2 in Granot & Sari (2002)) results in an unphysical value for the fraction of shock internal energy partitioned to electrons of $\epsilon_e > 1$, which is driven primarily by our constraint on the self-absorption break.

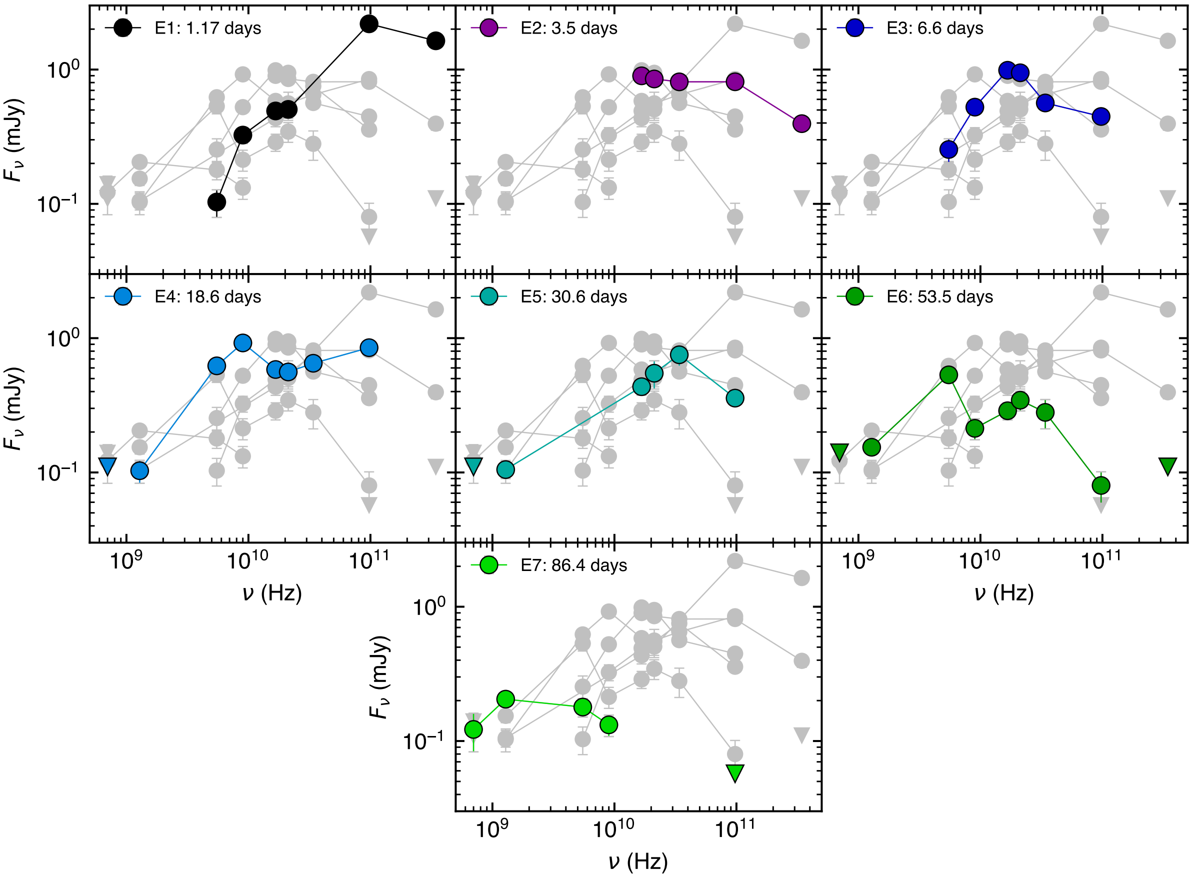

Figure 5.7: SEDs at the epochs indicated in Figure 5.6. Epochs 1 through 7 correspond to approximate times of 1.17, 3.5, 6.6, 18.6, 30.6, 53.5 and 86.4 days post-trigger. For Epoch 1 we interpolate the ATCA fluxes to a time of 1.17 days, while for Epochs 2 and 3 we interpolate the 97.5 GHz and 343.5 GHz flux to their respective times. Upper limits are shown as upside down triangles. The rising segment in the Epoch 1 SED has a spectral slope of $\beta = 0.93 \pm 0.06$.

We therefore do not expect a standard wind-medium forward shock model to be able to account for the observed optically thick radio emission prior to the 97.5 GHz rebrightening at 8.2 days. We note that similar incompatibilities with standard forward shock models resulting from radio observations have been observed in other GRB afterglows (Marongiu et al. 2022; de Wet et al. 2023b; Laskar et al. 2023; Schroeder et al. 2023). We discuss this further in Section 5.6.2.

We perform theoretical modelling using the `ScaleFit` software package (Ryan et al. 2015; Aksulu et al. 2020, 2022), which is based on the `BoxFit` set of high-resolution hydrodynamic simulations of GRB explosions (van Eerten et al. 2012). `ScaleFit` generates afterglow spectra and light curves of forward shock emission in both ISM or stellar wind environments during the deceleration phase after reverse shock crossing, and can take into account the jet break effect as well as the non-relativistic transition. Non-standard effects such as reverse shock emission, energy injection, plateaus, or flares, however, are not included. `ScaleFit` accepts 10 free parameters: the isotropic-equivalent energy of the blast wave $E_{\mathrm{K,iso}}$, circumburst density n_0[8], opening angle of the jet θ_j, electron energy distribution spectral index p, fraction of accelerated electrons within the shock ξ_N, fractions of shock internal energy distributed to electrons and magnetic fields ϵ_e and ϵ_B, burst redshift z, luminosity distance d_L, and observer angle relative to the jet axis θ_{obs}.

We fix the burst redshift to $z = 1.160$ and the luminosity distance to the value computed using our adopted cosmology, $d_L = 2.52 \times 10^{28}$ cm. We assume that the observer is looking directly down the axis of the jet ($\theta_{\mathrm{obs}} = 0$) and that the fraction of shock-accelerated electrons is unity despite the fact that ξ_N is degenerate with respect to the parameters $\{E_{\mathrm{K,iso}}, n_0, \epsilon_e, \epsilon_B\}$, as shown by Eichler & Waxman (2005). To account for Galactic dust extinction we correct our UV/optical data using the Fitzpatrick (1999) Milky Way extinction law with $R_V = 3.1$ and $A_V = 0.3271$ mag. Furthermore, we adopt the Small Magellanic Cloud (SMC) extinction curve from Pei (1992) to account for possible host galaxy extinction, which is a free parameter in our modelling.

We conduct a Markov Chain Monte Carlo (MCMC) exploration of our `ScaleFit` parameter space using the `emcee` Python package (Foreman-Mackey et al. 2013) following the implementation described in detail in de Wet et al. (2023a). The Lyman limit of 912 Å at the host redshift lies squarely within the $uvw2$ ultraviolet band so these flux measurements are likely to be severely affected by photoelectric absorption. We therefore exclude these data from our modelling, along with the radio observations following the start of the 97.5 GHz rebrightening at 8.2 days. We also exclude the early-time X-ray data ($t < 0.01$ days), the first epoch of ATCA data ($t \approx 0.5$ days), and the lower frequency (< 16.7 GHz) radio data at 6.6 days since we do not expect our model to be able to account for these data following the arguments in Sections 5.3.3 and 5.3.4. We assume a spherical jet ($\theta = \pi/2$) since our observations show no clear evidence for a jet break.

The results of our modelling are presented in Table 5.2 and Figure 5.8, while the light curves corresponding to the highest-likelihood model are shown in Figure 5.9. This model has $p = 2.27$ which is close to the value of $p = 2.24$ derived from our late-time optical and X-ray light curves in Section 5.3.3. The spectrum is in fast cooling with $\nu_c < \nu_m$ until ν_m crosses ν_c at 0.0011 days at a frequency of $\nu \approx 10^{16}$ Hz which is between the optical and X-ray bands. The cooling break ν_c begins crossing the X-ray band midway through our PC-mode observations which explains the steeper observed X-ray spectral index of $\beta_{\mathrm{X}} = -0.95 \pm 0.03$ compared to the optical index of $\beta_{\mathrm{O}} = -0.63 \pm 0.08$, while the similar temporal decay observed in both bands is a result of the smooth cooling break. By ≈ 0.01 days ν_m has passed through all of the optical bands, consistent with the observed steepening of the optical light curve from $\alpha_{\mathrm{O}} = -1.05$ to $\alpha_{\mathrm{O}} = -1.44$ at 0.017 days as seen in Figure 5.5. At the time of our first ALMA observations we have $\nu_m \approx 330$ GHz which is close to the 343.5 GHz ALMA band. The shallow decay observed in the early optical and millimeter light curves is a result of the proximity of ν_m to the observing band, consistent with our arguments in Section 5.3.3. As we expected, the optically thick spectra observed in

---

[8] In a wind medium the $A_\star$ parameter is commonly used as a measure of the density, as defined in Chevalier & Li (2000). The n_0 parameter is related to the $A_\star$ parameter via $n_0 = A_\star \times 29.89$ cm^{-3}.

Paramater	Highest-likelihood model	MCMC results
p	2.27	$2.28^{+0.01}_{-0.01}$
$E_{\mathrm{K,iso}}$ (10^{53} erg)	29.0	$30.7^{+4.5}_{-3.1}$
$A_\star$	6.3×10^{-3}	$4.7^{+1.6}_{-2.1} \times 10^{-3}$
ϵ_e	9.7×10^{-3}	$8.7^{+1.3}_{-2.1} \times 10^{-3}$
ϵ_B	1.5×10^{-1}	$2.4^{+3.7}_{-1.0} \times 10^{-1}$
$A_{V,\mathrm{host}}$ (mag)	0.009	$0.011^{+0.010}_{-0.007}$
t_j (days)	$\gtrsim 8.2$	-
θ_j (deg)	$\gtrsim 1.1$	-
E_{K} (10^{50} erg)	$\gtrsim 5.2$	-
E_γ (10^{50} erg)	$\gtrsim 1.7$	-

Table 5.2: Forward shock parameters

the Epoch 1 and 3 radio SEDs are incompatible with our highest-likelihood model, as shown in Figure 5.10. At 6.6 days the self-absorption frequency is at $\nu_a \approx 110$ MHz, an order of magnitude below the observed break at 16.7 GHz. We return to this in Section 5.6.2.

No jet break is seen in our data prior to the start of the millimeter rebrightening at 8.2 days, so we can place a lower limit on the opening angle using the inverted form of Equation 31 from Chevalier & Li (2000):

$$\theta_j = 5.9^{-1} \left(\frac{1+z}{2}\right)^{-1/4} E_{52}^{-1/4} A_\star^{1/4} t_j^{1/4}, \tag{5.2}$$

where θ_j is in radians, E_{52} is the isotropic-equivalent kinetic energy in units of 10^{52} erg, and t_j is the jet break time in days. We calculate a lower limit of $\theta_j \gtrsim 1.1$ deg, which is consistent with the sample range of $\theta_j = 2.5 \pm 1.5$ degrees found by Wang et al. (2015). The corresponding lower limit on the beaming correction is $f_b = (1 - \cos\theta_j) \gtrsim 1.8 \times 10^{-4}$, resulting in a beaming-corrected γ-ray energy of $E_\gamma \gtrsim 1.7 \times 10^{50}$ erg and a kinetic energy of $E_{\mathrm{K}} \gtrsim 5.2 \times 10^{50}$ erg. We calculate the radiative efficiency using $\eta_\gamma = E_{\gamma,\mathrm{iso}}/(E_{\gamma,\mathrm{iso}} + E_{\mathrm{K,iso}})$ and find $\eta_\gamma = 24.6\%$.

5.5 Explanations for the millimeter rebrightening

We consider a number of mechanisms that may give rise to a rebrightening at radio frequencies, including supernova emission, a counter jet, a density enhancement of the surrounding medium, interstellar scintillation, a two-component jet, energy injection, and reverse shock emission.

5.5.1 Supernova emission

Barniol Duran & Giannios (2015) investigated the possibility of detecting radio emission from the highly-energetic Type Ic supernovae that are expected to accompany most long GRBs, and found that the emission from the shocked external medium swept up by the supernova blast wave should peak a few tens of years after the explosion, much later than our observed peak at 18.1 days. Furthermore, the luminosities of supernovae observed at millimeter wavelengths are generally 2–4 orders of magnitude fainter than those of GRB afterglows (Eftekhari et al. 2022). We therefore rule out supernova emission as a possible cause for the rebrightening in GRB 210702A.

5.5.2 Counter jet

Once the GRB blast wave transitions into the non-relativistic regime a bump in radio light curves may be expected from the receding counter jet, with simulations showing that the emission should peak more than ~ 1000 days after the GRB (Zhang & MacFadyen 2009). The decelerating jet

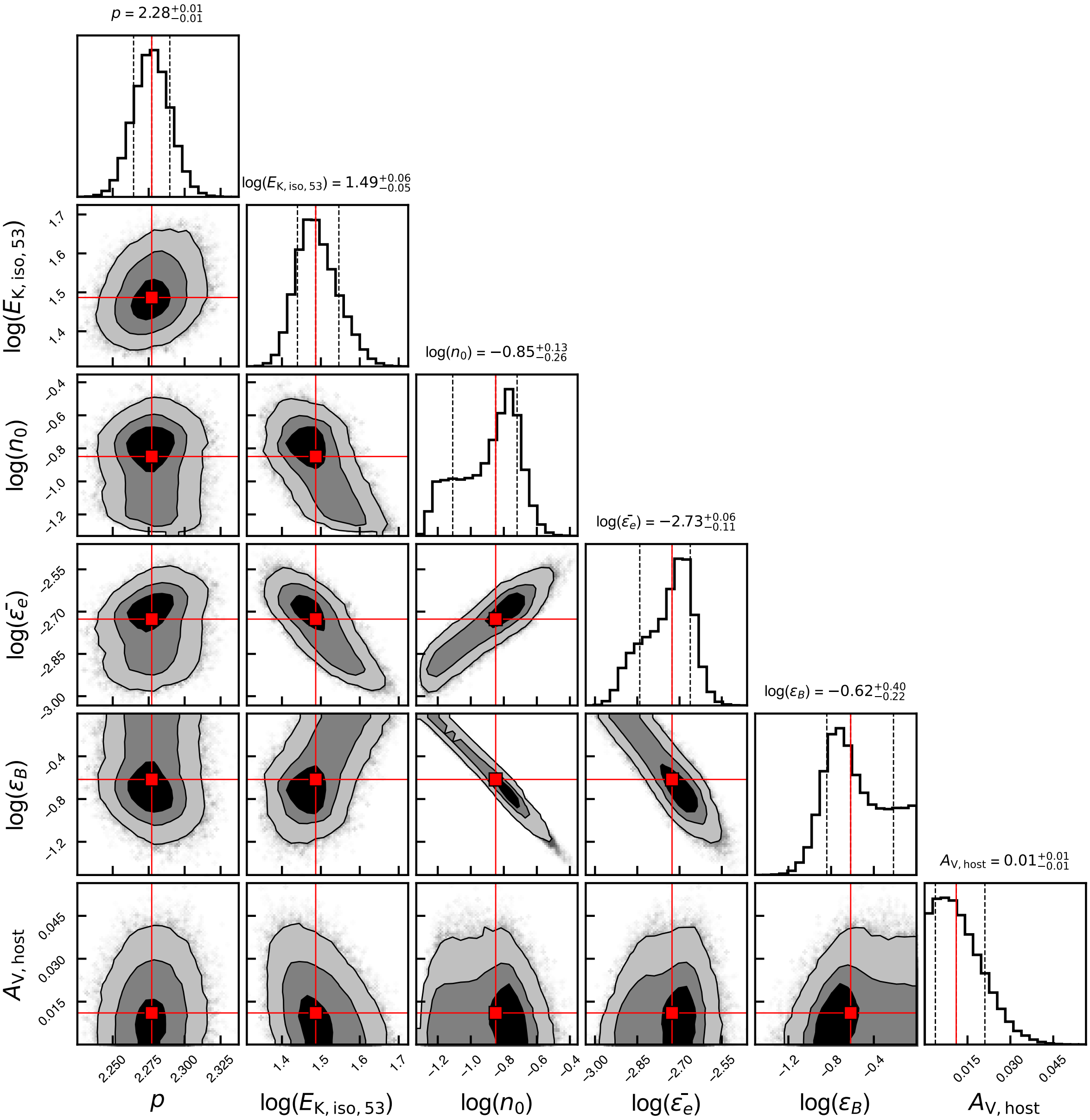

Figure 5.8: Corner plot from our MCMC analysis. Contours denote the 1σ, 2σ and 3σ levels. Red lines correspond to the median values in the marginalised distributions.

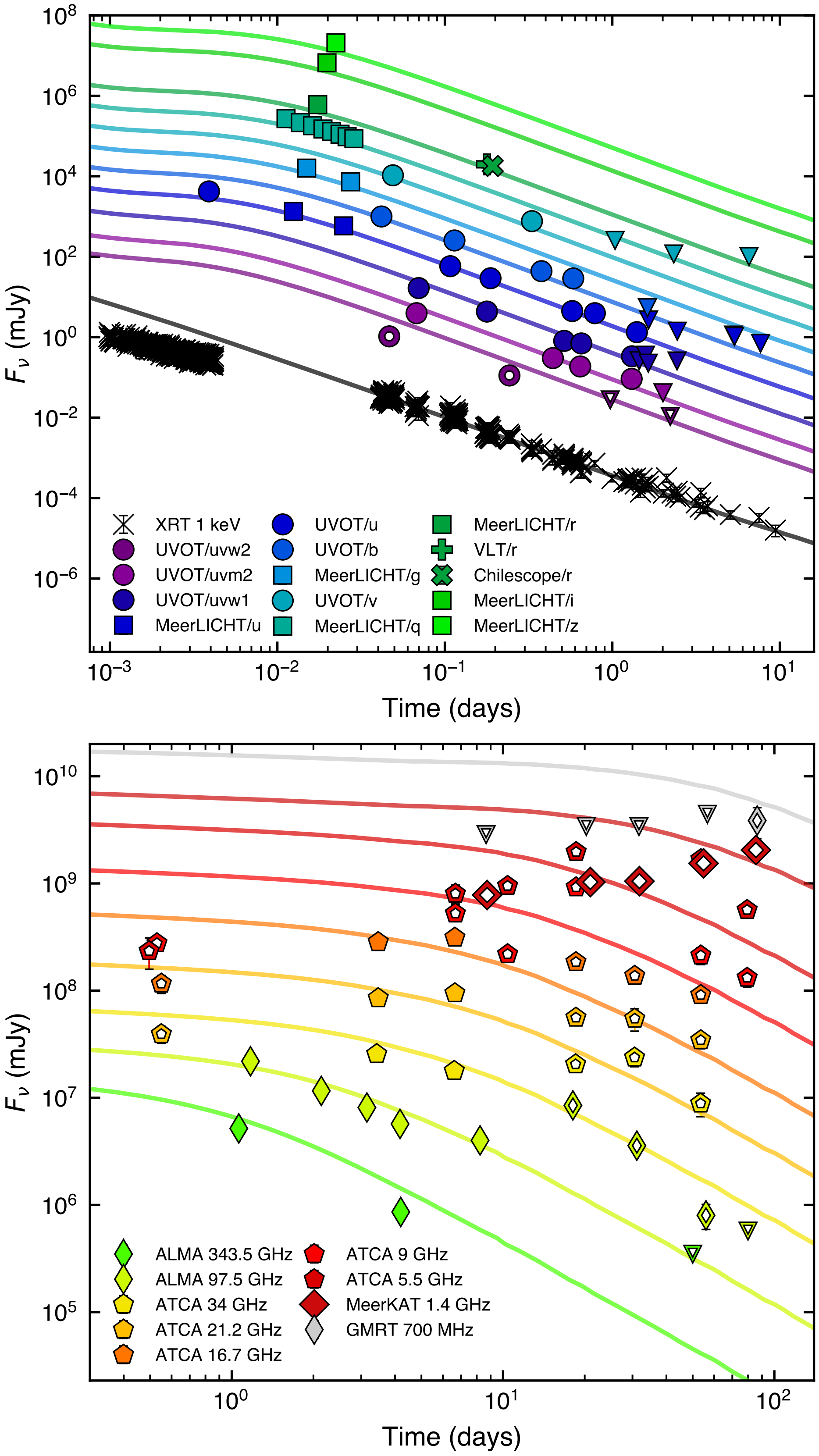

Figure 5.9: Model light curves associated with the highest-likelihood forward shock model from our MCMC analysis. We separate the data by observing band and instrument, and shift each light curve by a factor of $10^{0.5n}$ in flux, where n is an integer. Open symbols denote those data which were not included when fitting the model. Upside-down triangles indicate upper limits.

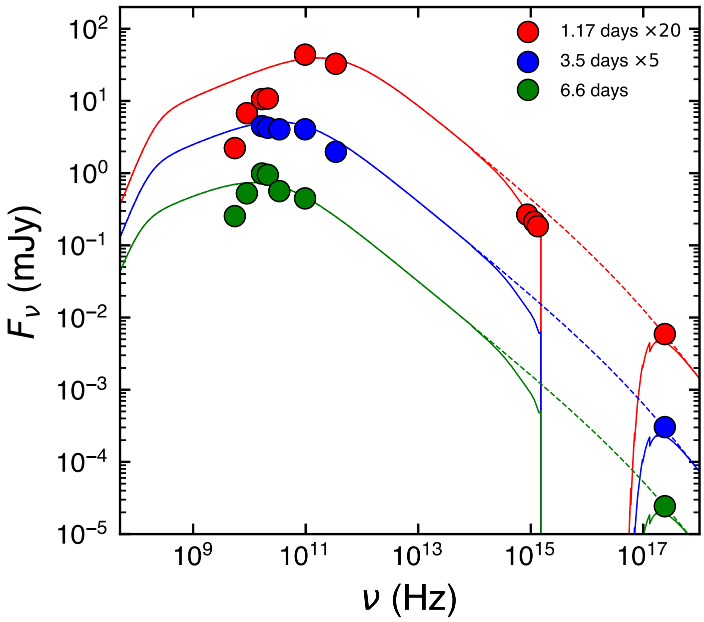

Figure 5.10: Broadband SEDs at three epochs along with model SEDs corresponding to our highest-likelihood model. Dashed lines indicate the unabsorbed synchrotron spectrum, while solid lines take into account photoelectric absorption and Galactic and host galaxy extinction. The radio data correspond to the first three SEDs in Figure 5.7, respectively.

will experience a jet break prior to the non-relativistic transition. The lack of a jet break observed in our data therefore rules out a counter jet as a viable explanation.

5.5.3 Density enhancement

Long GRBs offer a natural mechanism for producing a variable circumburst density since their progenitors are massive stars which produce stellar winds and undergo significant mass loss preceding their death. Several analytic and simulation-based studies, however, have shown that even large density variations cannot produce sharp features in afterglow light curves (Nakar & Granot 2007; van Eerten et al. 2009; Gat et al. 2013; Geng et al. 2014).

5.5.4 Interstellar scintillation

Interstellar scintillation (ISS) due to inhomogeneities in the Galactic free electron density have been observed at radio wavelengths in a number of GRB afterglows (Goodman 1997; Chandra et al. 2008; van der Horst et al. 2014; Greiner et al. 2018; Alexander et al. 2019). Anderson et al. (2023) explored ISS as an explanation for the early, rapid variability in the radio light curves of GRB 210702A and found a transition frequency of $\nu_0 = 7.66$ GHz for the GRB line of sight. Our millimeter observations are more than an order of magnitude higher in frequency than this transition frequency and at a much later time so that the effects of ISS should be negligible. We therefore rule out ISS as a viable explanation.

5.5.5 Two-component jet

A two-component jet has been invoked to explain the afterglows of several GRBs where a standard forward shock model does not suffice (Berger et al. 2003; Racusin et al. 2008; van der Horst et al. 2014; Sato et al. 2023). A faster, more narrowly-collimated inner jet gives rise to the early optical and X-ray emission while a slower, wider jet gives rise to later emission. If the rebrightening is due to forward shock emission from a wider jet, we would require a jet break from the inner jet near the start of the rebrightening around 8.1 days, otherwise a very steep rise of $\alpha \approx 3$ (from our light curve fit in Section 5.3.2) would be required which is not possible from standard forward shock emission. No jet break is seen our X-ray light curve, so this model appears to be disfavoured.

5.5.6 Energy injection

There are two physical forms of energy injection that may give rise to a rebrightening in afterglow light curves. The first involves a long-lasting central engine which injects a Poynting flux into the blast wave, such as a spinning-down millisecond magnetar (Dai & Lu 1998; Zhang & Mészáros 2001). The luminosity of the central engine is usually given as a power-law in time beginning at a time t_0 and defined by the power-law index q: $L(t) = L_0(t/t_0)^{-q}$. The blast wave energy will only increase substantially when $q < 1$, with the total energy increasing as $E_{\rm tot} \propto t^{1-q}$. The second form of energy injection invokes an impulsive central engine injection of a stratified ejecta with a power-law distribution in the bulk Lorentz factor: $M(>\gamma) \propto \gamma^{-s}$ (Rees & Mészáros 1998; Sari & Mészáros 2000). It is impossible to physically distinguish the two scenarios from afterglow observations since both forms can be made equivalent through a relationship between the q and s parameters (Zhang et al. 2006). During the period of energy injection the light curves within each spectral regime will be altered according to the value of q or s. Thereafter, the afterglow will evolve as a blast wave with the new, increased kinetic energy.

We test the energy injection scenario by making use of the closure relations for energy injection within the q-formalism from Zhang et al. (2006). At the start of the rebrightening the 97.5 GHz band is within the spectral regime with $\nu_m < \nu_{97.5\rm GHz} < \nu_c$. The appropriate closure relation in a wind medium is $\alpha = \frac{(2-2p)-(p+1)q}{4}$. Using our light curve rising index of $\alpha_{97.5\rm GHz,rise} = 0.95$ and a value of $p = 2.28 \pm 0.01$ derived from our theoretical modelling, we calculate a value of $q = -1.88$. The blast wave energy increases as $E_{\rm K,iso,1} = E_{\rm K,iso,0}\,(t_1/t_0)^{1-q}$ over the period of energy injection. We take t_0 and t_1 as the times corresponding to the start and peak of the rebrightening at 8.2 and 18.1 days, respectively. We find that the blast wave energy increases by a factor of ≈ 10 over the course of the rebrightening.

Taking our forward shock model from Section 5.4 as the starting point, we introduce a period of energy injection in which the kinetic energy of the blast wave increases as t^{1-q} between 8.2 and 18.1 days. We keep all other forward shock parameters the same. We exclude the lower frequency radio bands since there is no standard forward shock model prior to the rebrightening that can accommodate these data. The resulting model results in an achromatic rebrightening across all bands. The model can adequately capture the 97.5 GHz rebrightening, but does not fully capture the behaviour in the higher frequency bands (Figure 5.11). As discussed in Section 5.3.4, however, possible unaccounted-for systematic uncertainties from the calibration of our ATCA data prevents us from completely excluding this scenario.

5.5.7 Reverse shock

We now consider whether the 97.5 GHz rebrightening is caused by emission from a reverse shock (RS). There are two physical mechanisms that can produce RS emission: the first is a standard RS related to the forward shock (FS) that is produced by a shock wave moving back through the jet ejecta; the second is a RS produced by the late-time collision of a shell ejected by the GRB central engine. For both cases, the RS will emit synchrotron radiation characterised by its own set of spectral break frequencies and peak flux: $\nu_{a,\rm r}$, $\nu_{m,\rm r}$, $\nu_{c,\rm r}$, and $F_{\nu_{m,\rm r}}$. For a standard RS, the RS and FS parameters are related at the deceleration (or shock crossing) time $t_{\rm dec}$, and can therefore be used to derive the ejecta Lorentz factor and magnetization. After the deceleration time, the flux above $\nu_{c,\rm r}$ is negligible since electrons are no longer accelerated within the ejecta. The evolution of the RS spectral breaks depends on whether the shock is relativistic or Newtonian

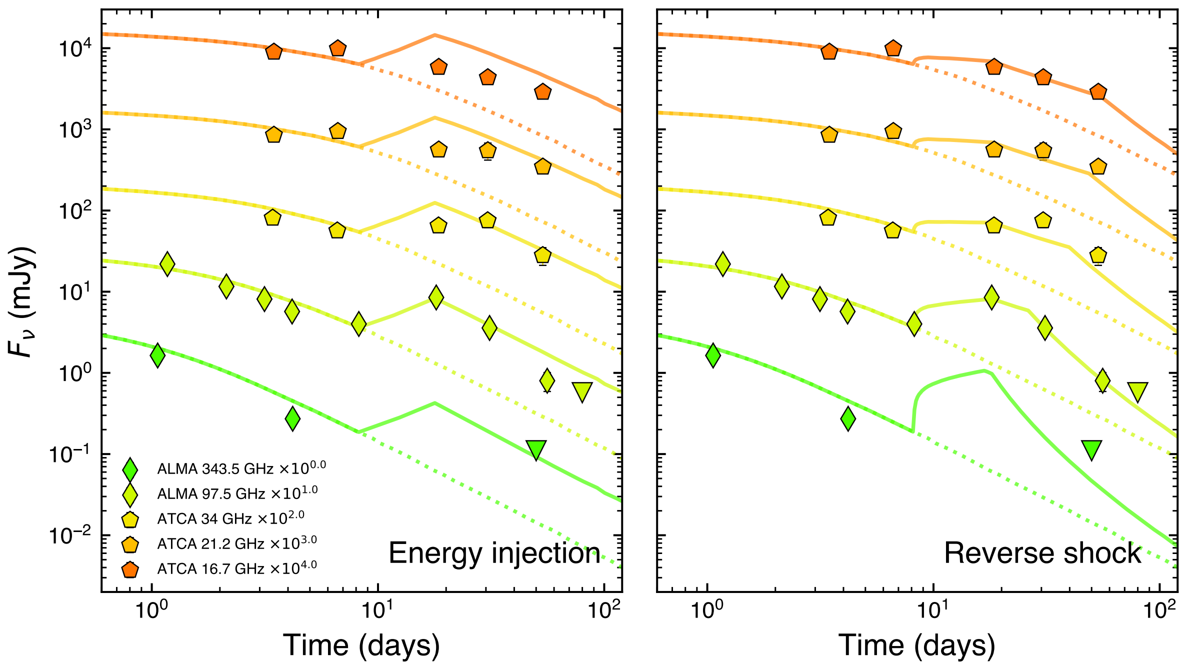

Figure 5.11: Higher frequency ($\nu \geq 16.7$ GHz) radio light curves with our energy injection (left) and reverse shock (right) models. The initial model (dotted line) is our highest-likelihood forward shock model from Section 5.4. We note that the energy injection and reverse shock models presented here have not been fitted to the data, but are rather meant to demonstrate that such models can accommodate the data.

in the frame of the unshocked ejecta. In the Newtonian case the spectral evolution depends on an additional parameter g which dictates the profile of the shocked ejecta with $\gamma \propto r^{-g}$, and where we expect $1/2 \lesssim g \lesssim 3/2$ from theoretical arguments (Mészáros & Rees 1999; Kobayashi & Sari 2000).

If the 97.5 GHz rebrightening is caused by a standard RS related to the FS, our first optical detection at 0.004 days allows us set an upper limit on the deceleration time of $t_{\rm dec} < 0.004$ days since we were able to model all of the optical emission with a FS (Section 5.4) which must have decelerated prior to this time. After shock crossing it is only possible to obtain a rising and falling light curve through the passage of a spectral break, which must be $\nu_{a,\rm r}$ for a RS in a wind medium (Zou et al. 2005). Regardless of the ordering of the spectral breaks, we find that the RS emission in this case would outshine the detected optical emission at 0.004 days by several orders of magnitude, ruling out a standard RS scenario.

Next we consider RS emission from the violent collision of two ejecta shells (Zhang & Mészáros 2002; Lyutikov 2017; Lamberts & Daigne 2018). Such a scenario has been used to model GRBs 140304A and 210672A (Laskar et al. 2018b; Schroeder et al. 2023). A requirement for a violent collision is that the second shell is moving much faster than the initial shell (which is responsible for the observed FS emission) at the collision time ($t_{\rm col}$), so that $\Gamma_2 \gg \Gamma_1$. Furthermore, we rely on the assumptions that the energy of the initial shell does not increase enough to cause an increase in the FS emission and that FS emission from the second shell is negligible compared to the RS emission (Zhang & Mészáros 2002). The RS emission from the second shell begins forming when the two shells collide at $t_{\rm col}$, and peaks once the RS has crossed the ejecta and fully decelerated at the deceleration time $t_{\rm dec}$. We choose to associate the collision time with the beginning of the rise in the 97.5 GHz light curve at 8.2 days, and the deceleration time with the peak in the light curve at 18.1 days. For a standard ordering of spectral breaks ($\nu_{a,\rm r} < \nu_{m,\rm r} < \nu_{c,\rm r}$), we find that a relativistic RS in which $\nu_{m,\rm r}$ crosses the 97.5 GHz band shortly after shock crossing can provide an adequate fit to our higher frequency radio data (Figure 5.11). At the shock crossing time, this model has $\nu_{m,\mathrm{r}} \approx 300$ GHz, $\nu_{a,\mathrm{r}} \lesssim 16.7$ GHz, $\nu_{c,\mathrm{r}} \gtrsim 10^{14}$ Hz, and $F_{\nu_{m,\mathrm{r}}} \approx 1$ mJy. We note, however, that this is not a unique model since two of the break frequencies ($\nu_{a,\mathrm{r}}$, and $\nu_{c,\mathrm{r}}$) are not well-constrained. Futhermore, Newtonian RS models with both standard and non-standard orderings of spectral breaks can also accommodate the data.

5.6 Discussion

5.6.1 Radio rebrightenings

Similar radio rebrightenings to the one observed in GRB 210702A have been observed in XRF 050416A and GRB 210726A (Soderberg et al. 2007; Schroeder et al. 2023). Radio observations of XRF 050416A at 1.43, 4.86 and 8.46 GHz showed an unusual flare peaking at $t \sim 40$ days which was followed by rapid fading (t^{-2}), with the radio spectrum remaining optically thin throughout the observations. Soderberg et al. (2007) regarded a large circumburst density jump or late-time energy injection from a slow-moving shell as the most plausible explanation for the rebrightening. In the energy injection scenario, the decay following the peak should be the same as the asymptotic temporal decay prior to the injection. The fact that the post-peak decay rate of $\alpha \gtrsim -2$ was steeper than the predicted decay led Soderberg et al. (2007) to suggest that a jet break may have occurred on a similar timescale to the energy injection, a trend found by Laskar et al. (2015) in their study of energy injection in GRB afterglows. This scenario is in fact consistent with the post-peak decay rate in GRB 210702A of $\alpha_{\mathrm{mm,decay}} = -1.67 \pm 0.17$ being steeper than the predicted decay of $\alpha \approx -1.4$.

More recently, Schroeder et al. (2023) studied the short GRB 210726A and found a radio flare at 6 GHz with a rapid rise between $\approx 10 - 19$ days followed by a rapid decline at 3, 6 and 10 GHz. Energy injection and a reverse shock from a shell collision were regarded as plausible explanations to explain the late-time radio flare. Similar to the energy injection scenario for XRF 050416A, a jet break at the time of the peak of the flare was invoked to explain the steep post-peak temporal index of $\alpha = -2.1 \pm 0.4$. For the reverse shock shell collision scenario, an X-ray rebrightening at 4.6 days was attributed to the ejection of the shell while the peak of the radio flare was attributed to the deceleration time of the reverse shock.

The most noteworthy difference between these previous studies and ours is that the observed rebrightening in these bursts occurred at centimeter wavelengths whereas the rebrightening in GRB 210702A occurred in the millimeter regime, where scintillation is virtually guaranteed not to play a role (Section 5.5.4). Had millimeter data been obtained for these other bursts, it is possible that they may also have shown a rebrightening at millimeter wavelengths. Our observations demonstrate that millimeter light curves can exhibit some of the more complex features commonly seen at higher frequency optical and X-ray bands, and that these features may actually be more widespread than previous observations suggest, given that only a small number of bursts with have millimeter follow-up.

5.6.2 Failure of forward shock model

Prior to the millimeter rebrightening, a standard forward shock model within a stellar wind medium was sufficient to account for the optical, early millimeter and late-time X-ray data in GRB 210702A. The early X-ray data was not accounted for by our model, so we attributed the shallower early X-ray decline with $\alpha = -1.00 \pm 0.02$ to a period of energy injection. The greatest challenge to our model, however, was posed by the lower frequency ($\nu \leq 21.2$ GHz) radio data. In particular, our first SED at 1.17 days showed a steep drop at frequencies below the millimeter band (Figures 5.7 and 5.10) which we attributed to self-absorbed emission. If the broadband multi-wavelength afterglow is all from a single forward shock emission component, no standard model can accommodate such a high self-absorption frequency (Section 5.4). One means of suppressing the radio emission is to invoke a population of thermal, non-accelerated electrons within the shocked region which may lead to an increase in the self-absorption frequency by a factor of $\approx 10 - 100$ (Ressler & Laskar 2017; Warren et al. 2018). Such an argument was made for GRB 210731A and GRB 210726A (de Wet et al. 2023b; Schroeder et al. 2023).

Past sample studies of radio afterglows have shown that standard forward shock models are often incompatible with observations, which contrasts with observations at optical and X-ray afterglows that show general agreement with the forward shock models. Kangas et al. (2020) studied 21 GRBs with multi-wavelength data showing clear evidence for a jet break in their X-ray light curves and found that only half of the bursts had radio afterglows consistent with standard models. Most of the radio light curves were consistent with a single power-law, even after a jet break observed at higher frequencies. Levine et al. (2023) used standard afterglow closure relations to test whether radio observations of 84 GRBs were consistent with predicted temporal and spectral behaviour and, similar to Kangas et al. (2020), found that only roughly half of the sample agreed with expectations. More recently, difficulties in modelling radio data have been encountered in the all time brightest GRB 221009A. Laskar et al. (2023) found that the data could only partially be explained by a forward shock model, with additional emission components needed to explain the radio and millimeter emission, or nonstandard assumptions regarding the basic analytic models of relativistic synchrotron emission such as evolving microphysics parameters or an atypical electron energy distribution. Gill & Granot (2023) instead modelled the broadband afterglow with a shallow angular structured jet in which all of the radio emission arises from a reverse shock rather than forward shock emission component. A two-component jet was proposed by other authors (Sato et al. 2023; Zhang et al. 2023). In summary, radio observations of GRB afterglows are highlighting the need for additional theoretical and modelling efforts in order to explain the data. We leave it to future work to test these alternative scenarios for GRB 210702A.

5.7 Conclusions

We have presented the results of our extensive multi-wavelength follow-up campaign of GRB 210702A, a bright long-duration GRB at $z = 1.160$. Our 97.5 GHz ALMA light curve shows a rebrightening beginning at 8.2 days and peaking at 18.1 days, the first such rebrightening seen in a GRB millimeter light curve. Our X-ray, optical and millimeter data taken prior to the rebrightening can be explained by a standard forward shock model in a stellar wind medium with an electron energy spectral index of $p \approx 2.27$. The shallow decay with $\alpha \approx -1$ seen in the optical light curve prior to 0.017 days and in the 97.5 GHz light curve prior to the rebrightening we attribute to the proximity of ν_m to the observing band. The shallow decay with $\alpha \approx -1$ in the X-rays, however, we attribute to a period of energy injection. Our radio light curves from 700 MHz to 34 GHz do not appear to evolve achromatically along with the millimeter rebrightening, though we cannot exclude this for the higher-frequency ATCA data due to inherent uncertainties arising from radio data calibration. Our radio SEDs show clear evidence for synchrotron self-absorbed emission, though we are unable to reconcile our constraints on the self-absorption break with any standard forward shock model. Our radio observations show similar incompatibilities found in modelling other GRBs, such as GRB 221009A, and may require alternative scenarios such as a structured jet or thermal electron population.

We considered a number of scenarios to explain the millimeter rebrightening in GRB 210702A and found that a period of energy injection into the forward shock or a reverse shock from a late-time shell collision are the most plausible mechanisms, yet both scenarios are unable to capture the behaviour seen in the other radio bands. Our observations demonstrate that millimeter light curves can display some of the more complex features seen in X-ray and optical light curves, such as rebrightenings or flares. Further millimeter observations will be required to determine the frequency of such features.

Acknowledgements

The MeerLICHT consortium is a partnership between Radboud University, the University of Cape Town, the South African Astronomical Observatory (SAAO), the University of Oxford, the University of Manchester and the University of Amsterdam, in association with and, partly supported by, the South African Radio Astronomy Observatory (SARAO), the European Research Council and The Netherlands Research School for Astronomy (NOVA). We acknowledge the use of the Inter-University Institute for Data Intensive Astronomy (IDIA) data intensive research cloud for data processing. IDIA is a South African university partnership involving the University of Cape Town, the University of Pretoria and the University of the Western Cape. S.dW. and P.J.G. are supported by NRF SARChI Grant 111692. This work made use of data supplied by the UK Swift Science Data Centre at the University of Leicester. The research leading to these results has received funding from the European Union's Horizon 2020 Programme under the AHEAD2020 project (grant agreement number 871158). The Australia Telescope Compact Array is part of the Australia Telescope National Facility[9] which is funded by the Australian Government for operation as a National Facility managed by CSIRO. We acknowledge the Gomeroi people as the Traditional Owners of the Observatory site. We thank the staff of the GMRT that made these observations possible. The MeerKAT telescope is operated by the South African Radio Astronomy Observatory, which is a facility of the National Research Foundation, an agency of the Department of Science and Innovation. GMRT is run by the National Centre for Radio Astrophysics of the Tata Institute of Fundamental Research. RBD acknowledges support from the National Science Foundation under grant 2107932.

Bibliography

Aksulu, M. D., Wijers, R. A. M. J., van Eerten, H. J., & van der Horst, A. J. 2020, MNRAS, 497, 4672

Aksulu, M. D., Wijers, R. A. M. J., van Eerten, H. J., & van der Horst, A. J. 2022, MNRAS, 511, 2848

Alexander, K. D., Laskar, T., Berger, E., et al. 2019, ApJ, 870, 67

Anderson, G. E., Russell, T. D., Fausey, H. M., et al. 2023, MNRAS, 523, 4992

Barniol Duran, R. & Giannios, D. 2015, MNRAS, 454, 1711

Barthelmy, S. D., Barbier, L. M., Cummings, J. R., et al. 2005, Space Sci. Rev., 120, 143

Belkin, S., Pozanenko, A., Pankov, N., Krugov, M., & GRB IKI FuN Collaboration. 2021, GRB Coordinates Network, 30365, 1

Berger, E., Kulkarni, S. R., & Frail, D. A. 2004, ApJ, 612, 966

Berger, E., Kulkarni, S. R., Pooley, G., et al. 2003, Nature, 426, 154

Blandford, R. D. & McKee, C. F. 1976, Physics of Fluids, 19, 1130

Bloemen, S., Groot, P., Woudt, P., et al. 2016, in Society of Photo-Optical Instrumentation Engineers (SPIE) Conference Series, Vol. 9906, Ground-based and Airborne Telescopes VI, ed. H. J. Hall, R. Gilmozzi, & H. K. Marshall, 990664

Burrows, D. N., Hill, J. E., Nousek, J. A., et al. 2005, Space Sci. Rev., 120, 165

---

[9] https://ror.org/05qajvd42

Chandra, P., Cenko, S. B., Frail, D. A., et al. 2008, ApJ, 683, 924

Chandra, P. & Frail, D. A. 2012, ApJ, 746, 156

Chevalier, R. A. & Li, Z.-Y. 2000, ApJ, 536, 195

Dai, Z. G. & Lu, T. 1998, Phys. Rev. Lett., 81, 4301

de Ugarte Postigo, A., Lundgren, A., Martín, S., et al. 2012, A&A, 538, A44

de Wet, S., Izzo, L., Groot, P. J., et al. 2023a, A&A, 677, A32

de Wet, S., Laskar, T., Groot, P. J., et al. 2023b, A&A, 671, A116

Eftekhari, T., Berger, E., Metzger, B. D., et al. 2022, ApJ, 935, 16

Eichler, D. & Waxman, E. 2005, ApJ, 627, 861

Fitzpatrick, E. L. 1999, PASP, 111, 63

Foreman-Mackey, D., Hogg, D. W., Lang, D., & Goodman, J. 2013, PASP, 125, 306

Frail, D. A., Berger, E., Galama, T., et al. 2000a, ApJ, 538, L129

Frail, D. A., Kulkarni, S. R., Nicastro, L., Feroci, M., & Taylor, G. B. 1997, Nature, 389, 261

Frail, D. A., Soderberg, A. M., Kulkarni, S. R., et al. 2005, ApJ, 619, 994

Frail, D. A., Waxman, E., & Kulkarni, S. R. 2000b, ApJ, 537, 191

Frederiks, D., Golenetskii, S., Lysenko, A., et al. 2021, GRB Coordinates Network, 30366, 1

Gat, I., van Eerten, H., & MacFadyen, A. 2013, ApJ, 773, 2

Geng, J. J., Wu, X. F., Li, L., Huang, Y. F., & Dai, Z. G. 2014, ApJ, 792, 31

Gill, R. & Granot, J. 2023, MNRAS, 524, L78

Goodman, J. 1997, New A, 2, 449

Granot, J. & Sari, R. 2002, ApJ, 568, 820

Granot, J. & van der Horst, A. J. 2014, PASA, 31, e008

Greiner, J., Bolmer, J., Wieringa, M., et al. 2018, A&A, 614, A29

Groot, P. J., de Wet, S., Vreeswijk, P. M., Levan, A. J., & Meerlicht Consortium. 2021, GRB Coordinates Network, 30354, 1

Heywood, I. 2020, oxkat: Semi-automated imaging of MeerKAT observations, Astrophysics Source Code Library, record ascl:2009.003

Kangas, T., Fruchter, A. S., Cenko, S. B., et al. 2020, ApJ, 894, 43

Kobayashi, S. & Sari, R. 2000, ApJ, 542, 819

Kobayashi, S. & Zhang, B. 2003, ApJ, 597, 455

Kuin, N. P. M., Lien, A. Y., & Swift/UVOT Team. 2021, GRB Coordinates Network, 30356, 1

Kulkarni, S. R., Frail, D. A., Sari, R., et al. 1999, ApJ, 522, L97

Kumar, P. & Zhang, B. 2015, Phys. Rep., 561, 1

Lamberts, A. & Daigne, F. 2018, MNRAS, 474, 2813

Laskar, T., Alexander, K. D., Berger, E., et al. 2018a, ApJ, 862, 94

Laskar, T., Alexander, K. D., Margutti, R., et al. 2023, ApJ, 946, L23

Laskar, T., Berger, E., Margutti, R., et al. 2015, ApJ, 814, 1

Laskar, T., Berger, E., Margutti, R., et al. 2018b, ApJ, 859, 134

Laskar, T., Berger, E., Zauderer, B. A., et al. 2013, ApJ, 776, 119

Levine, D., Dainotti, M., Fraija, N., et al. 2023, MNRAS, 519, 4670

Lien, A. Y., Barthelmy, S. D., Kennea, J. A., et al. 2021, GRB Coordinates Network, 30351, 1

Lyutikov, M. 2017, Physics of Fluids, 29, 047101

Marongiu, M., Guidorzi, C., Stratta, G., et al. 2022, A&A, 658, A11

McMullin, J. P., Waters, B., Schiebel, D., Young, W., & Golap, K. 2007, in Astronomical Society of the Pacific Conference Series, Vol. 376, Astronomical Data Analysis Software and Systems XVI, ed. R. A. Shaw, F. Hill, & D. J. Bell, 127

Mesler, R. A., Pihlström, Y. M., Taylor, G. B., & Granot, J. 2012, ApJ, 759, 4

Mészáros, P. & Rees, M. J. 1997, ApJ, 476, 232

Mészáros, P. & Rees, M. J. 1999, MNRAS, 306, L39

Nakar, E. & Granot, J. 2007, MNRAS, 380, 1744

Nousek, J. A., Kouveliotou, C., Grupe, D., et al. 2006, ApJ, 642, 389

Pei, Y. C. 1992, ApJ, 395, 130

Perley, D. A., Cenko, S. B., Corsi, A., et al. 2014, ApJ, 781, 37

Pihlström, Y. M., Taylor, G. B., Granot, J., & Doeleman, S. 2007, ApJ, 664, 411

Piran, T. 1999, Phys. Rep., 314, 575

Piran, T. 2004, Reviews of Modern Physics, 76, 1143

Planck Collaboration, Aghanim, N., Akrami, Y., et al. 2020, A&A, 641, A6

Racusin, J. L., Karpov, S. V., Sokolowski, M., et al. 2008, Nature, 455, 183

Rees, M. J. & Mészáros, P. 1998, ApJ, 496, L1

Ressler, S. M. & Laskar, T. 2017, ApJ, 845, 150

Rhoads, J. E. 1999, ApJ, 525, 737

Roming, P. W. A., Kennedy, T. E., Mason, K. O., et al. 2005, Space Sci. Rev., 120, 95

Ryan, G., van Eerten, H., MacFadyen, A., & Zhang, B.-B. 2015, ApJ, 799, 3

Sari, R. & Mészáros, P. 2000, ApJ, 535, L33

Sari, R. & Piran, T. 1999, ApJ, 520, 641

Sari, R., Piran, T., & Halpern, J. P. 1999, ApJ, 519, L17

Sari, R., Piran, T., & Narayan, R. 1998, ApJ, 497, L17

Sato, Y., Murase, K., Ohira, Y., & Yamazaki, R. 2023, MNRAS, 522, L56

Sault, R. J., Teuben, P. J., & Wright, M. C. H. 1995, in Astronomical Society of the Pacific Conference Series, Vol. 77, Astronomical Data Analysis Software and Systems IV, ed. R. A. Shaw, H. E. Payne, & J. J. E. Hayes, 433

Schlafly, E. F. & Finkbeiner, D. P. 2011, ApJ, 737, 103

Schroeder, G., Rhodes, L., Laskar, T., et al. 2023, arXiv e-prints, arXiv:2308.10936

Soderberg, A. M., Nakar, E., Cenko, S. B., et al. 2007, ApJ, 661, 982

Taylor, G. B., Momjian, E., Pihlström, Y., Ghosh, T., & Salter, C. 2005, ApJ, 622, 986

Uhm, Z. L. & Zhang, B. 2014, ApJ, 780, 82

Ursi, A., Pittori, C., Verrecchia, F., et al. 2021, GRB Coordinates Network, 30363, 1

van der Horst, A. J., Kamble, A., Resmi, L., et al. 2008, A&A, 480, 35

van der Horst, A. J., Paragi, Z., de Bruyn, A. G., et al. 2014, MNRAS, 444, 3151

van Eerten, H., van der Horst, A., & MacFadyen, A. 2012, ApJ, 749, 44

van Eerten, H. J., Meliani, Z., Wijers, R. A. M. J., & Keppens, R. 2009, MNRAS, 398, L63

Wang, X.-G., Zhang, B., Liang, E.-W., et al. 2015, ApJS, 219, 9

Warren, D. C., Barkov, M. V., Ito, H., Nagataki, S., & Laskar, T. 2018, MNRAS, 480, 4060

Waxman, E., Kulkarni, S. R., & Frail, D. A. 1998, ApJ, 497, 288

Willingale, R., Starling, R. L. C., Beardmore, A. P., Tanvir, N. R., & O'Brien, P. T. 2013, MNRAS, 431, 394

Woosley, S. E. & Bloom, J. S. 2006, ARA&A, 44, 507

Xu, D., Izzo, L., de Ugarte Postigo, A., et al. 2021, GRB Coordinates Network, 30357, 1

Yamaoka, K., Yoshida, A., Sakamoto, T., et al. 2021, GRB Coordinates Network, 30362, 1

Zhang, B., Fan, Y. Z., Dyks, J., et al. 2006, ApJ, 642, 354

Zhang, B. & Kobayashi, S. 2005, ApJ, 628, 315

Zhang, B. & Mészáros, P. 2001, ApJ, 552, L35

Zhang, B. & Mészáros, P. 2002, ApJ, 566, 712

Zhang, B., Wang, X.-Y., & Zheng, J.-H. 2023, arXiv e-prints, arXiv:2311.14180

Zhang, W. & MacFadyen, A. 2009, ApJ, 698, 1261

Zhou, H., Jin, Z.-P., Covino, S., Fan, Y.-Z., & Wei, D.-M. 2023, ApJS, 268, 65

Zou, Y. C., Wu, X. F., & Dai, Z. G. 2005, MNRAS, 363, 93

5.A Table of flux measurements

Table 5.3: GRB 210702A flux measurements

Δt (days)	Telescope	Band/Filter	Frequency (Hz)	Flux (μJy)	Uncertainty (μJy)	Detection? (1 = yes)
0.00099	*Swift*/XRT	1 keV	2.42e+17	1.026390	0.129683	1
0.00099	*Swift*/XRT	1 keV	2.42e+17	1.316908	0.163709	1
0.00100	*Swift*/XRT	1 keV	2.42e+17	0.928455	0.114673	1
0.00101	*Swift*/XRT	1 keV	2.42e+17	1.179080	0.160764	1
0.00101	*Swift*/XRT	1 keV	2.42e+17	0.798587	0.209709	1
0.00102	*Swift*/XRT	1 keV	2.42e+17	0.833583	0.217465	1
0.00103	*Swift*/XRT	1 keV	2.42e+17	0.906841	0.253542	1
0.00104	*Swift*/XRT	1 keV	2.42e+17	1.031328	0.268417	1
0.00105	*Swift*/XRT	1 keV	2.42e+17	0.946370	0.187503	1
0.00106	*Swift*/XRT	1 keV	2.42e+17	1.093325	0.193594	1
0.00106	*Swift*/XRT	1 keV	2.42e+17	0.781019	0.130834	1
0.00108	*Swift*/XRT	1 keV	2.42e+17	0.743697	0.097786	1
0.00109	*Swift*/XRT	1 keV	2.42e+17	0.879087	0.094013	1
0.00118	*Swift*/XRT	1 keV	2.42e+17	1.148642	0.146396	1
0.00119	*Swift*/XRT	1 keV	2.42e+17	0.930707	0.119872	1
0.00121	*Swift*/XRT	1 keV	2.42e+17	0.900970	0.114238	1
0.00122	*Swift*/XRT	1 keV	2.42e+17	0.919412	0.118184	1
0.00123	*Swift*/XRT	1 keV	2.42e+17	0.919277	0.123524	1
0.00124	*Swift*/XRT	1 keV	2.42e+17	1.173663	0.170917	1
0.00125	*Swift*/XRT	1 keV	2.42e+17	0.839406	0.119394	1
0.00127	*Swift*/XRT	1 keV	2.42e+17	0.745867	0.111995	1
0.00128	*Swift*/XRT	1 keV	2.42e+17	0.590101	0.102562	1
0.00130	*Swift*/XRT	1 keV	2.42e+17	0.809004	0.148220	1
0.00131	*Swift*/XRT	1 keV	2.42e+17	0.994474	0.185441	1
0.00132	*Swift*/XRT	1 keV	2.42e+17	0.726628	0.137475	1
0.00134	*Swift*/XRT	1 keV	2.42e+17	0.820200	0.175176	1
0.00135	*Swift*/XRT	1 keV	2.42e+17	0.845963	0.192069	1
0.00136	*Swift*/XRT	1 keV	2.42e+17	0.769093	0.184788	1
0.00138	*Swift*/XRT	1 keV	2.42e+17	0.784391	0.200434	1
0.00139	*Swift*/XRT	1 keV	2.42e+17	0.697939	0.179588	1
0.00140	*Swift*/XRT	1 keV	2.42e+17	0.826119	0.193322	1
0.00142	*Swift*/XRT	1 keV	2.42e+17	0.769060	0.171199	1
0.00143	*Swift*/XRT	1 keV	2.42e+17	0.951239	0.216245	1
0.00144	*Swift*/XRT	1 keV	2.42e+17	0.730799	0.167392	1
0.00145	*Swift*/XRT	1 keV	2.42e+17	1.078969	0.253739	1
0.00147	*Swift*/XRT	1 keV	2.42e+17	0.675967	0.248109	1
0.00148	*Swift*/XRT	1 keV	2.42e+17	0.702335	0.291182	1
0.00149	*Swift*/XRT	1 keV	2.42e+17	0.844056	0.384854	1
0.00151	*Swift*/XRT	1 keV	2.42e+17	0.824112	0.439800	1
0.00152	*Swift*/XRT	1 keV	2.42e+17	0.655351	0.363423	1
0.00153	*Swift*/XRT	1 keV	2.42e+17	0.698792	0.332566	1
0.00155	*Swift*/XRT	1 keV	2.42e+17	0.728875	0.363314	1
0.00156	*Swift*/XRT	1 keV	2.42e+17	0.684224	0.321776	1
0.00158	*Swift*/XRT	1 keV	2.42e+17	0.647168	0.306587	1
0.00159	*Swift*/XRT	1 keV	2.42e+17	0.604577	0.090373	1

Table 5.3: Continued.

Δt (days)	Telescope	Band/Filter	Frequency (Hz)	Flux (μJy)	Uncertainty (μJy)	Detection? (1 = yes)
0.00159	*Swift*/XRT	1 keV	2.42e+17	0.644169	0.092341	1
0.00160	*Swift*/XRT	1 keV	2.42e+17	0.677758	0.097137	1
0.00161	*Swift*/XRT	1 keV	2.42e+17	0.608942	0.084982	1
0.00161	*Swift*/XRT	1 keV	2.42e+17	0.659907	0.092948	1
0.00162	*Swift*/XRT	1 keV	2.42e+17	0.597896	0.084880	1
0.00163	*Swift*/XRT	1 keV	2.42e+17	0.539127	0.079852	1
0.00164	*Swift*/XRT	1 keV	2.42e+17	0.553372	0.079364	1
0.00164	*Swift*/XRT	1 keV	2.42e+17	0.608929	0.086179	1
0.00165	*Swift*/XRT	1 keV	2.42e+17	0.568453	0.081257	1
0.00166	*Swift*/XRT	1 keV	2.42e+17	0.710534	0.101760	1
0.00166	*Swift*/XRT	1 keV	2.42e+17	0.632413	0.089693	1
0.00167	*Swift*/XRT	1 keV	2.42e+17	0.756924	0.108093	1
0.00168	*Swift*/XRT	1 keV	2.42e+17	0.693560	0.099368	1
0.00168	*Swift*/XRT	1 keV	2.42e+17	0.683385	0.096901	1
0.00169	*Swift*/XRT	1 keV	2.42e+17	0.739721	0.106331	1
0.00169	*Swift*/XRT	1 keV	2.42e+17	0.621540	0.088934	1
0.00170	*Swift*/XRT	1 keV	2.42e+17	0.570790	0.082906	1
0.00171	*Swift*/XRT	1 keV	2.42e+17	0.591708	0.084752	1
0.00172	*Swift*/XRT	1 keV	2.42e+17	0.484003	0.070324	1
0.00173	*Swift*/XRT	1 keV	2.42e+17	0.599618	0.086385	1
0.00173	*Swift*/XRT	1 keV	2.42e+17	0.626977	0.089344	1
0.00174	*Swift*/XRT	1 keV	2.42e+17	0.533853	0.075600	1
0.00175	*Swift*/XRT	1 keV	2.42e+17	0.628433	0.089598	1
0.00175	*Swift*/XRT	1 keV	2.42e+17	0.582068	0.083262	1
0.00176	*Swift*/XRT	1 keV	2.42e+17	0.560113	0.080966	1
0.00177	*Swift*/XRT	1 keV	2.42e+17	0.636068	0.089521	1
0.00178	*Swift*/XRT	1 keV	2.42e+17	0.593353	0.082380	1
0.00178	*Swift*/XRT	1 keV	2.42e+17	0.544564	0.075648	1
0.00179	*Swift*/XRT	1 keV	2.42e+17	0.587087	0.083516	1
0.00180	*Swift*/XRT	1 keV	2.42e+17	0.626109	0.088615	1
0.00181	*Swift*/XRT	1 keV	2.42e+17	0.600258	0.082564	1
0.00181	*Swift*/XRT	1 keV	2.42e+17	0.660285	0.090965	1
0.00182	*Swift*/XRT	1 keV	2.42e+17	0.642221	0.089014	1
0.00183	*Swift*/XRT	1 keV	2.42e+17	0.480116	0.070199	1
0.00184	*Swift*/XRT	1 keV	2.42e+17	0.476678	0.067417	1
0.00184	*Swift*/XRT	1 keV	2.42e+17	0.493895	0.067903	1
0.00185	*Swift*/XRT	1 keV	2.42e+17	0.591916	0.082364	1
0.00186	*Swift*/XRT	1 keV	2.42e+17	0.577151	0.078858	1
0.00187	*Swift*/XRT	1 keV	2.42e+17	0.666677	0.092305	1
0.00187	*Swift*/XRT	1 keV	2.42e+17	0.615325	0.086049	1
0.00188	*Swift*/XRT	1 keV	2.42e+17	0.548853	0.076633	1
0.00189	*Swift*/XRT	1 keV	2.42e+17	0.562683	0.077085	1
0.00189	*Swift*/XRT	1 keV	2.42e+17	0.588930	0.079886	1
0.00190	*Swift*/XRT	1 keV	2.42e+17	0.532990	0.072324	1
0.00191	*Swift*/XRT	1 keV	2.42e+17	0.639250	0.086788	1
0.00192	*Swift*/XRT	1 keV	2.42e+17	0.471743	0.065631	1
0.00192	*Swift*/XRT	1 keV	2.42e+17	0.663490	0.090099	1

Table 5.3: Continued.

Δt (days)	Telescope	Band/Filter	Frequency (Hz)	Flux (μJy)	Uncertainty (μJy)	Detection? (1 = yes)
0.00193	*Swift*/XRT	1 keV	2.42e+17	0.469774	0.063304	1
0.00194	*Swift*/XRT	1 keV	2.42e+17	0.530683	0.071943	1
0.00195	*Swift*/XRT	1 keV	2.42e+17	0.554204	0.075394	1
0.00195	*Swift*/XRT	1 keV	2.42e+17	0.578733	0.077509	1
0.00196	*Swift*/XRT	1 keV	2.42e+17	0.483138	0.065482	1
0.00197	*Swift*/XRT	1 keV	2.42e+17	0.591388	0.077983	1
0.00198	*Swift*/XRT	1 keV	2.42e+17	0.643650	0.086912	1
0.00198	*Swift*/XRT	1 keV	2.42e+17	0.527049	0.071753	1
0.00199	*Swift*/XRT	1 keV	2.42e+17	0.524480	0.069945	1
0.00200	*Swift*/XRT	1 keV	2.42e+17	0.516177	0.068899	1
0.00201	*Swift*/XRT	1 keV	2.42e+17	0.464518	0.063610	1
0.00201	*Swift*/XRT	1 keV	2.42e+17	0.603678	0.081090	1
0.00202	*Swift*/XRT	1 keV	2.42e+17	0.365099	0.059419	1
0.00203	*Swift*/XRT	1 keV	2.42e+17	0.489170	0.065036	1
0.00204	*Swift*/XRT	1 keV	2.42e+17	0.584390	0.077204	1
0.00204	*Swift*/XRT	1 keV	2.42e+17	0.530977	0.070299	1
0.00205	*Swift*/XRT	1 keV	2.42e+17	0.442878	0.058379	1
0.00206	*Swift*/XRT	1 keV	2.42e+17	0.451804	0.059758	1
0.00207	*Swift*/XRT	1 keV	2.42e+17	0.667309	0.087479	1
0.00208	*Swift*/XRT	1 keV	2.42e+17	0.460310	0.061925	1
0.00208	*Swift*/XRT	1 keV	2.42e+17	0.465874	0.062455	1
0.00209	*Swift*/XRT	1 keV	2.42e+17	0.436363	0.057329	1
0.00210	*Swift*/XRT	1 keV	2.42e+17	0.439585	0.056852	1
0.00211	*Swift*/XRT	1 keV	2.42e+17	0.492272	0.064972	1
0.00212	*Swift*/XRT	1 keV	2.42e+17	0.483553	0.064007	1
0.00213	*Swift*/XRT	1 keV	2.42e+17	0.556185	0.072146	1
0.00213	*Swift*/XRT	1 keV	2.42e+17	0.463632	0.060386	1
0.00214	*Swift*/XRT	1 keV	2.42e+17	0.527637	0.069847	1
0.00215	*Swift*/XRT	1 keV	2.42e+17	0.606657	0.078661	1
0.00216	*Swift*/XRT	1 keV	2.42e+17	0.417960	0.055287	1
0.00217	*Swift*/XRT	1 keV	2.42e+17	0.488286	0.063963	1
0.00217	*Swift*/XRT	1 keV	2.42e+17	0.337033	0.054225	1
0.00218	*Swift*/XRT	1 keV	2.42e+17	0.443592	0.057514	1
0.00219	*Swift*/XRT	1 keV	2.42e+17	0.439341	0.057441	1
0.00220	*Swift*/XRT	1 keV	2.42e+17	0.543179	0.069630	1
0.00221	*Swift*/XRT	1 keV	2.42e+17	0.427373	0.056346	1
0.00222	*Swift*/XRT	1 keV	2.42e+17	0.519389	0.068511	1
0.00222	*Swift*/XRT	1 keV	2.42e+17	0.517134	0.067561	1
0.00223	*Swift*/XRT	1 keV	2.42e+17	0.440861	0.056491	1
0.00224	*Swift*/XRT	1 keV	2.42e+17	0.372589	0.058460	1
0.00225	*Swift*/XRT	1 keV	2.42e+17	0.394801	0.060893	1
0.00225	*Swift*/XRT	1 keV	2.42e+17	0.397422	0.058138	1
0.00226	*Swift*/XRT	1 keV	2.42e+17	0.644557	0.082083	1
0.00227	*Swift*/XRT	1 keV	2.42e+17	0.477146	0.061554	1
0.00227	*Swift*/XRT	1 keV	2.42e+17	0.583910	0.076354	1
0.00228	*Swift*/XRT	1 keV	2.42e+17	0.353452	0.057246	1
0.00229	*Swift*/XRT	1 keV	2.42e+17	0.471310	0.061370	1

Table 5.3: Continued.

Δt (days)	Telescope	Band/Filter	Frequency (Hz)	Flux (μJy)	Uncertainty (μJy)	Detection? (1 = yes)
0.00230	*Swift*/XRT	1 keV	2.42e+17	0.390272	0.057251	1
0.00230	*Swift*/XRT	1 keV	2.42e+17	0.435726	0.055360	1
0.00231	*Swift*/XRT	1 keV	2.42e+17	0.399750	0.059381	1
0.00232	*Swift*/XRT	1 keV	2.42e+17	0.522137	0.066500	1
0.00233	*Swift*/XRT	1 keV	2.42e+17	0.396758	0.059508	1
0.00233	*Swift*/XRT	1 keV	2.42e+17	0.334576	0.052545	1
0.00234	*Swift*/XRT	1 keV	2.42e+17	0.345842	0.054018	1
0.00235	*Swift*/XRT	1 keV	2.42e+17	0.334595	0.052258	1
0.00236	*Swift*/XRT	1 keV	2.42e+17	0.453809	0.058206	1
0.00236	*Swift*/XRT	1 keV	2.42e+17	0.390208	0.059508	1
0.00237	*Swift*/XRT	1 keV	2.42e+17	0.391414	0.059828	1
0.00238	*Swift*/XRT	1 keV	2.42e+17	0.397626	0.056093	1
0.00238	*Swift*/XRT	1 keV	2.42e+17	0.397626	0.060756	1
0.00239	*Swift*/XRT	1 keV	2.42e+17	0.442962	0.056349	1
0.00240	*Swift*/XRT	1 keV	2.42e+17	0.371116	0.053415	1
0.00241	*Swift*/XRT	1 keV	2.42e+17	0.409526	0.052970	1
0.00242	*Swift*/XRT	1 keV	2.42e+17	0.362069	0.056507	1
0.00243	*Swift*/XRT	1 keV	2.42e+17	0.295408	0.045260	1
0.00243	*Swift*/XRT	1 keV	2.42e+17	0.490348	0.062035	1
0.00244	*Swift*/XRT	1 keV	2.42e+17	0.370767	0.057925	1
0.00245	*Swift*/XRT	1 keV	2.42e+17	0.508746	0.064892	1
0.00246	*Swift*/XRT	1 keV	2.42e+17	0.396116	0.050919	1
0.00247	*Swift*/XRT	1 keV	2.42e+17	0.509134	0.065487	1
0.00247	*Swift*/XRT	1 keV	2.42e+17	0.366921	0.058258	1
0.00248	*Swift*/XRT	1 keV	2.42e+17	0.469690	0.059097	1
0.00249	*Swift*/XRT	1 keV	2.42e+17	0.478288	0.060303	1
0.00250	*Swift*/XRT	1 keV	2.42e+17	0.442885	0.056885	1
0.00250	*Swift*/XRT	1 keV	2.42e+17	0.352048	0.054905	1
0.00251	*Swift*/XRT	1 keV	2.42e+17	0.360237	0.055018	1
0.00252	*Swift*/XRT	1 keV	2.42e+17	0.393562	0.055551	1
0.00253	*Swift*/XRT	1 keV	2.42e+17	0.395151	0.056774	1
0.00253	*Swift*/XRT	1 keV	2.42e+17	0.334156	0.051323	1
0.00254	*Swift*/XRT	1 keV	2.42e+17	0.373168	0.057164	1
0.00255	*Swift*/XRT	1 keV	2.42e+17	0.378840	0.057904	1
0.00255	*Swift*/XRT	1 keV	2.42e+17	0.359247	0.055926	1
0.00256	*Swift*/XRT	1 keV	2.42e+17	0.457208	0.058580	1
0.00257	*Swift*/XRT	1 keV	2.42e+17	0.385991	0.058461	1
0.00258	*Swift*/XRT	1 keV	2.42e+17	0.326148	0.050101	1
0.00258	*Swift*/XRT	1 keV	2.42e+17	0.388752	0.059567	1
0.00259	*Swift*/XRT	1 keV	2.42e+17	0.476001	0.061427	1
0.00260	*Swift*/XRT	1 keV	2.42e+17	0.393245	0.054433	1
0.00261	*Swift*/XRT	1 keV	2.42e+17	0.399895	0.061391	1
0.00262	*Swift*/XRT	1 keV	2.42e+17	0.459465	0.059308	1
0.00262	*Swift*/XRT	1 keV	2.42e+17	0.351635	0.055020	1
0.00263	*Swift*/XRT	1 keV	2.42e+17	0.391846	0.060678	1
0.00264	*Swift*/XRT	1 keV	2.42e+17	0.381578	0.059889	1
0.00264	*Swift*/XRT	1 keV	2.42e+17	0.438785	0.056113	1

Table 5.3: Continued.

Δt (days)	Telescope	Band/Filter	Frequency (Hz)	Flux (μJy)	Uncertainty (μJy)	Detection? (1 = yes)
0.00265	*Swift*/XRT	1 keV	2.42e+17	0.347685	0.053859	1
0.00266	*Swift*/XRT	1 keV	2.42e+17	0.394926	0.052235	1
0.00267	*Swift*/XRT	1 keV	2.42e+17	0.454948	0.058533	1
0.00268	*Swift*/XRT	1 keV	2.42e+17	0.395357	0.053105	1
0.00269	*Swift*/XRT	1 keV	2.42e+17	0.386360	0.059202	1
0.00269	*Swift*/XRT	1 keV	2.42e+17	0.405257	0.051684	1
0.00270	*Swift*/XRT	1 keV	2.42e+17	0.436522	0.055996	1
0.00271	*Swift*/XRT	1 keV	2.42e+17	0.372218	0.058576	1
0.00272	*Swift*/XRT	1 keV	2.42e+17	0.419305	0.053774	1
0.00273	*Swift*/XRT	1 keV	2.42e+17	0.423354	0.053717	1
0.00274	*Swift*/XRT	1 keV	2.42e+17	0.332741	0.051110	1
0.00274	*Swift*/XRT	1 keV	2.42e+17	0.444556	0.057464	1
0.00275	*Swift*/XRT	1 keV	2.42e+17	0.367972	0.056486	1
0.00276	*Swift*/XRT	1 keV	2.42e+17	0.384735	0.058817	1
0.00277	*Swift*/XRT	1 keV	2.42e+17	0.387340	0.059298	1
0.00277	*Swift*/XRT	1 keV	2.42e+17	0.371688	0.059011	1
0.00278	*Swift*/XRT	1 keV	2.42e+17	0.375715	0.057484	1
0.00279	*Swift*/XRT	1 keV	2.42e+17	0.388020	0.059726	1
0.00279	*Swift*/XRT	1 keV	2.42e+17	0.485093	0.061918	1
0.00280	*Swift*/XRT	1 keV	2.42e+17	0.326259	0.051029	1
0.00281	*Swift*/XRT	1 keV	2.42e+17	0.326659	0.050233	1
0.00282	*Swift*/XRT	1 keV	2.42e+17	0.355432	0.054495	1
0.00282	*Swift*/XRT	1 keV	2.42e+17	0.479148	0.060806	1
0.00283	*Swift*/XRT	1 keV	2.42e+17	0.342778	0.053428	1
0.00284	*Swift*/XRT	1 keV	2.42e+17	0.282381	0.043948	1
0.00285	*Swift*/XRT	1 keV	2.42e+17	0.335951	0.053251	1
0.00286	*Swift*/XRT	1 keV	2.42e+17	0.320520	0.050012	1
0.00286	*Swift*/XRT	1 keV	2.42e+17	0.405720	0.052652	1
0.00287	*Swift*/XRT	1 keV	2.42e+17	0.275741	0.042476	1
0.00288	*Swift*/XRT	1 keV	2.42e+17	0.311408	0.047762	1
0.00289	*Swift*/XRT	1 keV	2.42e+17	0.394229	0.055938	1
0.00290	*Swift*/XRT	1 keV	2.42e+17	0.352573	0.055133	1
0.00291	*Swift*/XRT	1 keV	2.42e+17	0.373050	0.059346	1
0.00291	*Swift*/XRT	1 keV	2.42e+17	0.425352	0.054850	1
0.00292	*Swift*/XRT	1 keV	2.42e+17	0.366753	0.061544	1
0.00293	*Swift*/XRT	1 keV	2.42e+17	0.295924	0.046059	1
0.00294	*Swift*/XRT	1 keV	2.42e+17	0.316927	0.048450	1
0.00294	*Swift*/XRT	1 keV	2.42e+17	0.338195	0.051616	1
0.00295	*Swift*/XRT	1 keV	2.42e+17	0.331322	0.050608	1
0.00296	*Swift*/XRT	1 keV	2.42e+17	0.374106	0.057081	1
0.00297	*Swift*/XRT	1 keV	2.42e+17	0.388545	0.057622	1
0.00297	*Swift*/XRT	1 keV	2.42e+17	0.377847	0.058826	1
0.00298	*Swift*/XRT	1 keV	2.42e+17	0.232578	0.036228	1
0.00299	*Swift*/XRT	1 keV	2.42e+17	0.447003	0.058318	1
0.00300	*Swift*/XRT	1 keV	2.42e+17	0.315682	0.049163	1
0.00301	*Swift*/XRT	1 keV	2.42e+17	0.306231	0.047743	1
0.00302	*Swift*/XRT	1 keV	2.42e+17	0.389296	0.059668	1

Table 5.3: Continued.

Δt (days)	Telescope	Band/Filter	Frequency (Hz)	Flux (μJy)	Uncertainty (μJy)	Detection? (1 = yes)
0.00302	*Swift*/XRT	1 keV	2.42e+17	0.287708	0.044220	1
0.00303	*Swift*/XRT	1 keV	2.42e+17	0.256904	0.040175	1
0.00304	*Swift*/XRT	1 keV	2.42e+17	0.334885	0.051316	1
0.00305	*Swift*/XRT	1 keV	2.42e+17	0.394952	0.056993	1
0.00306	*Swift*/XRT	1 keV	2.42e+17	0.300189	0.046051	1
0.00306	*Swift*/XRT	1 keV	2.42e+17	0.384044	0.057112	1
0.00307	*Swift*/XRT	1 keV	2.42e+17	0.333577	0.051907	1
0.00308	*Swift*/XRT	1 keV	2.42e+17	0.327718	0.050260	1
0.00309	*Swift*/XRT	1 keV	2.42e+17	0.349812	0.053671	1
0.00310	*Swift*/XRT	1 keV	2.42e+17	0.360058	0.057311	1
0.00310	*Swift*/XRT	1 keV	2.42e+17	0.314477	0.048242	1
0.00311	*Swift*/XRT	1 keV	2.42e+17	0.243704	0.037367	1
0.00312	*Swift*/XRT	1 keV	2.42e+17	0.277356	0.042380	1
0.00313	*Swift*/XRT	1 keV	2.42e+17	0.394867	0.054213	1
0.00314	*Swift*/XRT	1 keV	2.42e+17	0.295101	0.045167	1
0.00315	*Swift*/XRT	1 keV	2.42e+17	0.390385	0.059817	1
0.00315	*Swift*/XRT	1 keV	2.42e+17	0.329645	0.052287	1
0.00316	*Swift*/XRT	1 keV	2.42e+17	0.348832	0.053193	1
0.00317	*Swift*/XRT	1 keV	2.42e+17	0.291642	0.044458	1
0.00318	*Swift*/XRT	1 keV	2.42e+17	0.288658	0.043590	1
0.00319	*Swift*/XRT	1 keV	2.42e+17	0.399735	0.057009	1
0.00319	*Swift*/XRT	1 keV	2.42e+17	0.317072	0.048417	1
0.00320	*Swift*/XRT	1 keV	2.42e+17	0.366363	0.057081	1
0.00321	*Swift*/XRT	1 keV	2.42e+17	0.358312	0.054817	1
0.00322	*Swift*/XRT	1 keV	2.42e+17	0.348680	0.053297	1
0.00322	*Swift*/XRT	1 keV	2.42e+17	0.367448	0.056235	1
0.00323	*Swift*/XRT	1 keV	2.42e+17	0.332964	0.051770	1
0.00324	*Swift*/XRT	1 keV	2.42e+17	0.269665	0.041194	1
0.00325	*Swift*/XRT	1 keV	2.42e+17	0.294793	0.045187	1
0.00326	*Swift*/XRT	1 keV	2.42e+17	0.409577	0.053483	1
0.00327	*Swift*/XRT	1 keV	2.42e+17	0.256853	0.039243	1
0.00328	*Swift*/XRT	1 keV	2.42e+17	0.301556	0.047049	1
0.00329	*Swift*/XRT	1 keV	2.42e+17	0.274964	0.042892	1
0.00330	*Swift*/XRT	1 keV	2.42e+17	0.329211	0.050400	1
0.00331	*Swift*/XRT	1 keV	2.42e+17	0.354396	0.054111	1
0.00331	*Swift*/XRT	1 keV	2.42e+17	0.343076	0.053516	1
0.00332	*Swift*/XRT	1 keV	2.42e+17	0.300966	0.046046	1
0.00333	*Swift*/XRT	1 keV	2.42e+17	0.359947	0.054988	1
0.00334	*Swift*/XRT	1 keV	2.42e+17	0.292325	0.047186	1
0.00334	*Swift*/XRT	1 keV	2.42e+17	0.347801	0.054132	1
0.00335	*Swift*/XRT	1 keV	2.42e+17	0.322747	0.049238	1
0.00336	*Swift*/XRT	1 keV	2.42e+17	0.317643	0.050251	1
0.00337	*Swift*/XRT	1 keV	2.42e+17	0.345992	0.052824	1
0.00338	*Swift*/XRT	1 keV	2.42e+17	0.410212	0.052678	1
0.00338	*Swift*/XRT	1 keV	2.42e+17	0.308403	0.047357	1
0.00339	*Swift*/XRT	1 keV	2.42e+17	0.307035	0.047842	1
0.00340	*Swift*/XRT	1 keV	2.42e+17	0.355850	0.054285	1

Table 5.3: Continued.

Δt (days)	Telescope	Band/Filter	Frequency (Hz)	Flux (μJy)	Uncertainty (μJy)	Detection? (1 = yes)
0.00341	*Swift*/XRT	1 keV	2.42e+17	0.321548	0.050408	1
0.00342	*Swift*/XRT	1 keV	2.42e+17	0.287797	0.044003	1
0.00342	*Swift*/XRT	1 keV	2.42e+17	0.320264	0.048982	1
0.00343	*Swift*/XRT	1 keV	2.42e+17	0.269271	0.041091	1
0.00344	*Swift*/XRT	1 keV	2.42e+17	0.275486	0.042812	1
0.00345	*Swift*/XRT	1 keV	2.42e+17	0.394683	0.059895	1
0.00346	*Swift*/XRT	1 keV	2.42e+17	0.244607	0.037386	1
0.00347	*Swift*/XRT	1 keV	2.42e+17	0.292419	0.045638	1
0.00348	*Swift*/XRT	1 keV	2.42e+17	0.317977	0.049614	1
0.00349	*Swift*/XRT	1 keV	2.42e+17	0.274581	0.041998	1
0.00350	*Swift*/XRT	1 keV	2.42e+17	0.278852	0.042730	1
0.00351	*Swift*/XRT	1 keV	2.42e+17	0.275486	0.043012	1
0.00351	*Swift*/XRT	1 keV	2.42e+17	0.314741	0.049165	1
0.00352	*Swift*/XRT	1 keV	2.42e+17	0.250466	0.038346	1
0.00353	*Swift*/XRT	1 keV	2.42e+17	0.323351	0.051171	1
0.00354	*Swift*/XRT	1 keV	2.42e+17	0.287659	0.044875	1
0.00355	*Swift*/XRT	1 keV	2.42e+17	0.356498	0.054602	1
0.00356	*Swift*/XRT	1 keV	2.42e+17	0.385201	0.058227	1
0.00356	*Swift*/XRT	1 keV	2.42e+17	0.258564	0.040222	1
0.00357	*Swift*/XRT	1 keV	2.42e+17	0.303368	0.046615	1
0.00358	*Swift*/XRT	1 keV	2.42e+17	0.286013	0.043827	1
0.00359	*Swift*/XRT	1 keV	2.42e+17	0.306342	0.046934	1
0.00360	*Swift*/XRT	1 keV	2.42e+17	0.294748	0.045967	1
0.00361	*Swift*/XRT	1 keV	2.42e+17	0.259378	0.040475	1
0.00362	*Swift*/XRT	1 keV	2.42e+17	0.229798	0.034919	1
0.00363	*Swift*/XRT	1 keV	2.42e+17	0.246039	0.037828	1
0.00364	*Swift*/XRT	1 keV	2.42e+17	0.324219	0.050889	1
0.00365	*Swift*/XRT	1 keV	2.42e+17	0.377598	0.058110	1
0.00365	*Swift*/XRT	1 keV	2.42e+17	0.313253	0.048188	1
0.00366	*Swift*/XRT	1 keV	2.42e+17	0.329951	0.046377	1
0.00367	*Swift*/XRT	1 keV	2.42e+17	0.347188	0.053203	1
0.00368	*Swift*/XRT	1 keV	2.42e+17	0.276522	0.042334	1
0.00369	*Swift*/XRT	1 keV	2.42e+17	0.323302	0.049486	1
0.00370	*Swift*/XRT	1 keV	2.42e+17	0.299434	0.045868	1
0.00370	*Swift*/XRT	1 keV	2.42e+17	0.320053	0.049014	1
0.00371	*Swift*/XRT	1 keV	2.42e+17	0.239476	0.039427	1
0.00372	*Swift*/XRT	1 keV	2.42e+17	0.385402	0.057802	1
0.00373	*Swift*/XRT	1 keV	2.42e+17	0.297286	0.046538	1
0.00374	*Swift*/XRT	1 keV	2.42e+17	0.203740	0.031852	1
0.00375	*Swift*/XRT	1 keV	2.42e+17	0.318542	0.049185	1
0.00376	*Swift*/XRT	1 keV	2.42e+17	0.255472	0.040151	1
0.00377	*Swift*/XRT	1 keV	2.42e+17	0.373395	0.057281	1
0.00378	*Swift*/XRT	1 keV	2.42e+17	0.300865	0.046255	1
0.00378	*Swift*/XRT	1 keV	2.42e+17	0.299429	0.046030	1
0.00379	*Swift*/XRT	1 keV	2.42e+17	0.321695	0.049293	1
0.00380	*Swift*/XRT	1 keV	2.42e+17	0.250341	0.039042	1
0.00381	*Swift*/XRT	1 keV	2.42e+17	0.287389	0.044866	1

Table 5.3: Continued.

Δt (days)	Telescope	Band/Filter	Frequency (Hz)	Flux (μJy)	Uncertainty (μJy)	Detection? (1 = yes)
0.00382	*Swift*/XRT	1 keV	2.42e+17	0.307165	0.047127	1
0.00383	*Swift*/XRT	1 keV	2.42e+17	0.287399	0.044161	1
0.00384	*Swift*/XRT	1 keV	2.42e+17	0.327266	0.050350	1
0.00385	*Swift*/XRT	1 keV	2.42e+17	0.239494	0.036738	1
0.00386	*Swift*/XRT	1 keV	2.42e+17	0.275365	0.042332	1
0.00387	*Swift*/XRT	1 keV	2.42e+17	0.286733	0.044022	1
0.00388	*Swift*/XRT	1 keV	2.42e+17	0.213945	0.033322	1
0.00389	*Swift*/XRT	1 keV	2.42e+17	0.220486	0.033757	1
0.00390	*Swift*/XRT	1 keV	2.42e+17	0.374311	0.057257	1
0.00390	*Swift*/XRT	1 keV	2.42e+17	0.316273	0.050125	1
0.00391	*Swift*/XRT	1 keV	2.42e+17	0.269655	0.042029	1
0.00392	*Swift*/XRT	1 keV	2.42e+17	0.301301	0.047063	1
0.00393	*Swift*/XRT	1 keV	2.42e+17	0.273627	0.042749	1
0.00394	*Swift*/XRT	1 keV	2.42e+17	0.209941	0.032076	1
0.00395	*Swift*/XRT	1 keV	2.42e+17	0.295309	0.046757	1
0.00396	*Swift*/XRT	1 keV	2.42e+17	0.295313	0.046894	1
0.00397	*Swift*/XRT	1 keV	2.42e+17	0.260535	0.040610	1
0.00398	*Swift*/XRT	1 keV	2.42e+17	0.216827	0.033159	1
0.00399	*Swift*/XRT	1 keV	2.42e+17	0.210465	0.032964	1
0.00401	*Swift*/XRT	1 keV	2.42e+17	0.233354	0.035899	1
0.00401	*Swift*/XRT	1 keV	2.42e+17	0.232310	0.036999	1
0.00403	*Swift*/XRT	1 keV	2.42e+17	0.314648	0.048291	1
0.00403	*Swift*/XRT	1 keV	2.42e+17	0.232063	0.035634	1
0.00405	*Swift*/XRT	1 keV	2.42e+17	0.237283	0.037738	1
0.00406	*Swift*/XRT	1 keV	2.42e+17	0.246113	0.037829	1
0.00407	*Swift*/XRT	1 keV	2.42e+17	0.232466	0.035703	1
0.00408	*Swift*/XRT	1 keV	2.42e+17	0.240980	0.036865	1
0.00409	*Swift*/XRT	1 keV	2.42e+17	0.239136	0.036683	1
0.00410	*Swift*/XRT	1 keV	2.42e+17	0.280830	0.043941	1
0.00411	*Swift*/XRT	1 keV	2.42e+17	0.198840	0.030479	1
0.00412	*Swift*/XRT	1 keV	2.42e+17	0.207549	0.032390	1
0.00413	*Swift*/XRT	1 keV	2.42e+17	0.282115	0.044147	1
0.00414	*Swift*/XRT	1 keV	2.42e+17	0.247557	0.038754	1
0.00415	*Swift*/XRT	1 keV	2.42e+17	0.291446	0.045472	1
0.00416	*Swift*/XRT	1 keV	2.42e+17	0.333201	0.051953	1
0.00417	*Swift*/XRT	1 keV	2.42e+17	0.255244	0.039024	1
0.04123	*Swift*/XRT	1 keV	2.42e+17	0.029681	0.006665	1
0.04140	*Swift*/XRT	1 keV	2.42e+17	0.030895	0.006328	1
0.04159	*Swift*/XRT	1 keV	2.42e+17	0.032870	0.007026	1
0.04173	*Swift*/XRT	1 keV	2.42e+17	0.035990	0.008104	1
0.04190	*Swift*/XRT	1 keV	2.42e+17	0.034078	0.007132	1
0.04209	*Swift*/XRT	1 keV	2.42e+17	0.031206	0.006837	1
0.04227	*Swift*/XRT	1 keV	2.42e+17	0.030777	0.006930	1
0.04242	*Swift*/XRT	1 keV	2.42e+17	0.033576	0.007177	1
0.04262	*Swift*/XRT	1 keV	2.42e+17	0.027015	0.005943	1
0.04279	*Swift*/XRT	1 keV	2.42e+17	0.039075	0.008416	1
0.04292	*Swift*/XRT	1 keV	2.42e+17	0.043915	0.009861	1

Table 5.3: Continued.

Δt (days)	Telescope	Band/Filter	Frequency (Hz)	Flux (μJy)	Uncertainty (μJy)	Detection? (1 = yes)
0.04305	*Swift*/XRT	1 keV	2.42e+17	0.041890	0.008777	1
0.04317	*Swift*/XRT	1 keV	2.42e+17	0.047194	0.010354	1
0.04334	*Swift*/XRT	1 keV	2.42e+17	0.037516	0.007537	1
0.04351	*Swift*/XRT	1 keV	2.42e+17	0.031467	0.006885	1
0.04368	*Swift*/XRT	1 keV	2.42e+17	0.032735	0.007024	1
0.04382	*Swift*/XRT	1 keV	2.42e+17	0.031504	0.006884	1
0.04407	*Swift*/XRT	1 keV	2.42e+17	0.031922	0.006435	1
0.04421	*Swift*/XRT	1 keV	2.42e+17	0.035948	0.008072	1
0.04438	*Swift*/XRT	1 keV	2.42e+17	0.033016	0.007084	1
0.04456	*Swift*/XRT	1 keV	2.42e+17	0.031258	0.006894	1
0.04474	*Swift*/XRT	1 keV	2.42e+17	0.028283	0.006076	1
0.04493	*Swift*/XRT	1 keV	2.42e+17	0.035896	0.007379	1
0.04508	*Swift*/XRT	1 keV	2.42e+17	0.043445	0.008899	1
0.04527	*Swift*/XRT	1 keV	2.42e+17	0.026909	0.005935	1
0.04544	*Swift*/XRT	1 keV	2.42e+17	0.029922	0.006747	1
0.04562	*Swift*/XRT	1 keV	2.42e+17	0.044066	0.009005	1
0.04575	*Swift*/XRT	1 keV	2.42e+17	0.032813	0.007023	1
0.04592	*Swift*/XRT	1 keV	2.42e+17	0.035545	0.008004	1
0.04608	*Swift*/XRT	1 keV	2.42e+17	0.027366	0.005996	1
0.04630	*Swift*/XRT	1 keV	2.42e+17	0.022520	0.005078	1
0.04652	*Swift*/XRT	1 keV	2.42e+17	0.029748	0.006680	1
0.04670	*Swift*/XRT	1 keV	2.42e+17	0.025818	0.005789	1
0.04693	*Swift*/XRT	1 keV	2.42e+17	0.025421	0.005732	1
0.04712	*Swift*/XRT	1 keV	2.42e+17	0.030865	0.006322	1
0.04730	*Swift*/XRT	1 keV	2.42e+17	0.032941	0.007050	1
0.04748	*Swift*/XRT	1 keV	2.42e+17	0.033420	0.007152	1
0.04766	*Swift*/XRT	1 keV	2.42e+17	0.036364	0.008165	1
0.04782	*Swift*/XRT	1 keV	2.42e+17	0.022668	0.005104	1
0.04800	*Swift*/XRT	1 keV	2.42e+17	0.047409	0.010359	1
0.04817	*Swift*/XRT	1 keV	2.42e+17	0.024614	0.005281	1
0.04838	*Swift*/XRT	1 keV	2.42e+17	0.026062	0.005844	1
0.04860	*Swift*/XRT	1 keV	2.42e+17	0.034549	0.007239	1
0.04876	*Swift*/XRT	1 keV	2.42e+17	0.031194	0.006843	1
0.04895	*Swift*/XRT	1 keV	2.42e+17	0.025491	0.005724	1
0.04914	*Swift*/XRT	1 keV	2.42e+17	0.033480	0.007147	1
0.04931	*Swift*/XRT	1 keV	2.42e+17	0.032817	0.007023	1
0.04946	*Swift*/XRT	1 keV	2.42e+17	0.037950	0.008359	1
0.04964	*Swift*/XRT	1 keV	2.42e+17	0.035026	0.007330	1
0.04982	*Swift*/XRT	1 keV	2.42e+17	0.031201	0.006429	1
0.05002	*Swift*/XRT	1 keV	2.42e+17	0.028303	0.006096	1
0.05024	*Swift*/XRT	1 keV	2.42e+17	0.041755	0.006538	1
0.06640	*Swift*/XRT	1 keV	2.42e+17	0.018734	0.004116	1
0.06673	*Swift*/XRT	1 keV	2.42e+17	0.013662	0.003116	1
0.06706	*Swift*/XRT	1 keV	2.42e+17	0.023354	0.005124	1
0.06731	*Swift*/XRT	1 keV	2.42e+17	0.014806	0.003358	1
0.06769	*Swift*/XRT	1 keV	2.42e+17	0.016358	0.003699	1
0.06795	*Swift*/XRT	1 keV	2.42e+17	0.022298	0.004993	1

Table 5.3: Continued.

Δt (days)	Telescope	Band/Filter	Frequency (Hz)	Flux (μJy)	Uncertainty (μJy)	Detection? (1 = yes)
0.06822	*Swift*/XRT	1 keV	2.42e+17	0.018968	0.004167	1
0.06845	*Swift*/XRT	1 keV	2.42e+17	0.020066	0.004512	1
0.06876	*Swift*/XRT	1 keV	2.42e+17	0.019587	0.004203	1
0.06898	*Swift*/XRT	1 keV	2.42e+17	0.025806	0.005803	1
0.06923	*Swift*/XRT	1 keV	2.42e+17	0.018764	0.004117	1
0.06960	*Swift*/XRT	1 keV	2.42e+17	0.011168	0.002518	1
0.06998	*Swift*/XRT	1 keV	2.42e+17	0.019050	0.004168	1
0.07033	*Swift*/XRT	1 keV	2.42e+17	0.018272	0.003747	1
0.10670	*Swift*/XRT	1 keV	2.42e+17	0.011851	0.002604	1
0.10700	*Swift*/XRT	1 keV	2.42e+17	0.011411	0.002555	1
0.10731	*Swift*/XRT	1 keV	2.42e+17	0.012963	0.002856	1
0.10767	*Swift*/XRT	1 keV	2.42e+17	0.008751	0.001880	1
0.10794	*Swift*/XRT	1 keV	2.42e+17	0.013403	0.002933	1
0.10821	*Swift*/XRT	1 keV	2.42e+17	0.019461	0.003992	1
0.10845	*Swift*/XRT	1 keV	2.42e+17	0.010316	0.002313	1
0.10880	*Swift*/XRT	1 keV	2.42e+17	0.010719	0.002349	1
0.10908	*Swift*/XRT	1 keV	2.42e+17	0.012478	0.002810	1
0.10944	*Swift*/XRT	1 keV	2.42e+17	0.008074	0.001816	1
0.10974	*Swift*/XRT	1 keV	2.42e+17	0.013388	0.002925	1
0.11006	*Swift*/XRT	1 keV	2.42e+17	0.009611	0.002060	1
0.11047	*Swift*/XRT	1 keV	2.42e+17	0.009279	0.002093	1
0.11073	*Swift*/XRT	1 keV	2.42e+17	0.010266	0.002302	1
0.11106	*Swift*/XRT	1 keV	2.42e+17	0.011774	0.002583	1
0.11137	*Swift*/XRT	1 keV	2.42e+17	0.010291	0.002211	1
0.11171	*Swift*/XRT	1 keV	2.42e+17	0.011302	0.002542	1
0.11204	*Swift*/XRT	1 keV	2.42e+17	0.008756	0.001969	1
0.11238	*Swift*/XRT	1 keV	2.42e+17	0.010388	0.002226	1
0.11281	*Swift*/XRT	1 keV	2.42e+17	0.007993	0.001759	1
0.11319	*Swift*/XRT	1 keV	2.42e+17	0.008163	0.001844	1
0.11362	*Swift*/XRT	1 keV	2.42e+17	0.010667	0.002241	1
0.11396	*Swift*/XRT	1 keV	2.42e+17	0.010774	0.002371	1
0.11432	*Swift*/XRT	1 keV	2.42e+17	0.008750	0.001974	1
0.11459	*Swift*/XRT	1 keV	2.42e+17	0.013123	0.002875	1
0.11493	*Swift*/XRT	1 keV	2.42e+17	0.009413	0.002108	1
0.11530	*Swift*/XRT	1 keV	2.42e+17	0.010776	0.002364	1
0.11554	*Swift*/XRT	1 keV	2.42e+17	0.015826	0.003374	1
0.11587	*Swift*/XRT	1 keV	2.42e+17	0.007503	0.001690	1
0.11623	*Swift*/XRT	1 keV	2.42e+17	0.012971	0.002722	1
0.11656	*Swift*/XRT	1 keV	2.42e+17	0.008879	0.001910	1
0.11697	*Swift*/XRT	1 keV	2.42e+17	0.011860	0.002485	1
0.11730	*Swift*/XRT	1 keV	2.42e+17	0.009558	0.002143	1
0.11769	*Swift*/XRT	1 keV	2.42e+17	0.008159	0.001830	1
0.11809	*Swift*/XRT	1 keV	2.42e+17	0.007013	0.001577	1
0.11842	*Swift*/XRT	1 keV	2.42e+17	0.011341	0.002547	1
0.11879	*Swift*/XRT	1 keV	2.42e+17	0.009389	0.002118	1
0.11912	*Swift*/XRT	1 keV	2.42e+17	0.009985	0.002191	1
0.11941	*Swift*/XRT	1 keV	2.42e+17	0.012645	0.002840	1

Table 5.3: Continued.

Δt (days)	Telescope	Band/Filter	Frequency (Hz)	Flux (μJy)	Uncertainty (μJy)	Detection? (1 = yes)
0.11997	*Swift*/XRT	1 keV	2.42e+17	0.008369	0.001331	1
0.17345	*Swift*/XRT	1 keV	2.42e+17	0.004005	0.000899	1
0.17424	*Swift*/XRT	1 keV	2.42e+17	0.004259	0.000958	1
0.17493	*Swift*/XRT	1 keV	2.42e+17	0.005500	0.001239	1
0.17568	*Swift*/XRT	1 keV	2.42e+17	0.003390	0.000774	1
0.17662	*Swift*/XRT	1 keV	2.42e+17	0.003309	0.000729	1
0.17737	*Swift*/XRT	1 keV	2.42e+17	0.005559	0.001220	1
0.17798	*Swift*/XRT	1 keV	2.42e+17	0.005815	0.001279	1
0.17838	*Swift*/XRT	1 keV	2.42e+17	0.005274	0.001183	1
0.17915	*Swift*/XRT	1 keV	2.42e+17	0.004804	0.001027	1
0.17976	*Swift*/XRT	1 keV	2.42e+17	0.005173	0.001170	1
0.18038	*Swift*/XRT	1 keV	2.42e+17	0.004737	0.001067	1
0.18092	*Swift*/XRT	1 keV	2.42e+17	0.006155	0.001386	1
0.18160	*Swift*/XRT	1 keV	2.42e+17	0.003977	0.000897	1
0.18211	*Swift*/XRT	1 keV	2.42e+17	0.005830	0.001311	1
0.18288	*Swift*/XRT	1 keV	2.42e+17	0.003724	0.000819	1
0.18362	*Swift*/XRT	1 keV	2.42e+17	0.005038	0.001135	1
0.18440	*Swift*/XRT	1 keV	2.42e+17	0.003219	0.000709	1
0.18520	*Swift*/XRT	1 keV	2.42e+17	0.005811	0.001279	1
0.18597	*Swift*/XRT	1 keV	2.42e+17	0.003480	0.000785	1
0.18689	*Swift*/XRT	1 keV	2.42e+17	0.003021	0.000665	1
0.18765	*Swift*/XRT	1 keV	2.42e+17	0.004799	0.001081	1
0.18860	*Swift*/XRT	1 keV	2.42e+17	0.003025	0.000687	1
0.18963	*Swift*/XRT	1 keV	2.42e+17	0.003038	0.000682	1
0.19064	*Swift*/XRT	1 keV	2.42e+17	0.003509	0.000711	1
0.23969	*Swift*/XRT	1 keV	2.42e+17	0.003889	0.000876	1
0.24046	*Swift*/XRT	1 keV	2.42e+17	0.003148	0.000694	1
0.24146	*Swift*/XRT	1 keV	2.42e+17	0.003068	0.000692	1
0.24245	*Swift*/XRT	1 keV	2.42e+17	0.002979	0.000668	1
0.24344	*Swift*/XRT	1 keV	2.42e+17	0.003565	0.000780	1
0.24447	*Swift*/XRT	1 keV	2.42e+17	0.003302	0.000724	1
0.24581	*Swift*/XRT	1 keV	2.42e+17	0.002867	0.000475	1
0.328	*Swift*/XRT	1 keV	2.42e+17	0.002222	0.000485	1
0.329	*Swift*/XRT	1 keV	2.42e+17	0.001693	0.000380	1
0.330	*Swift*/XRT	1 keV	2.42e+17	0.001479	0.000333	1
0.331	*Swift*/XRT	1 keV	2.42e+17	0.001570	0.000354	1
0.332	*Swift*/XRT	1 keV	2.42e+17	0.001406	0.000315	1
0.333	*Swift*/XRT	1 keV	2.42e+17	0.001513	0.000265	1
0.378	*Swift*/XRT	1 keV	2.42e+17	0.001646	0.000337	1
0.439	*Swift*/XRT	1 keV	2.42e+17	0.000862	0.000195	1
0.441	*Swift*/XRT	1 keV	2.42e+17	0.001227	0.000276	1
0.443	*Swift*/XRT	1 keV	2.42e+17	0.000951	0.000160	1
0.512	*Swift*/XRT	1 keV	2.42e+17	0.000888	0.000200	1
0.514	*Swift*/XRT	1 keV	2.42e+17	0.000953	0.000211	1
0.515	*Swift*/XRT	1 keV	2.42e+17	0.001240	0.000279	1
0.517	*Swift*/XRT	1 keV	2.42e+17	0.000894	0.000201	1
0.518	*Swift*/XRT	1 keV	2.42e+17	0.001190	0.000270	1

Table 5.3: Continued.

Δt (days)	Telescope	Band/Filter	Frequency (Hz)	Flux (μJy)	Uncertainty (μJy)	Detection? (1 = yes)
0.520	*Swift*/XRT	1 keV	2.42e+17	0.001060	0.000214	1
0.572	*Swift*/XRT	1 keV	2.42e+17	0.000918	0.000207	1
0.574	*Swift*/XRT	1 keV	2.42e+17	0.000707	0.000160	1
0.576	*Swift*/XRT	1 keV	2.42e+17	0.000801	0.000180	1
0.578	*Swift*/XRT	1 keV	2.42e+17	0.000727	0.000165	1
0.580	*Swift*/XRT	1 keV	2.42e+17	0.000658	0.000149	1
0.582	*Swift*/XRT	1 keV	2.42e+17	0.000909	0.000206	1
0.583	*Swift*/XRT	1 keV	2.42e+17	0.000988	0.000222	1
0.585	*Swift*/XRT	1 keV	2.42e+17	0.000799	0.000139	1
0.639	*Swift*/XRT	1 keV	2.42e+17	0.000839	0.000190	1
0.640	*Swift*/XRT	1 keV	2.42e+17	0.000813	0.000184	1
0.643	*Swift*/XRT	1 keV	2.42e+17	0.000794	0.000179	1
0.645	*Swift*/XRT	1 keV	2.42e+17	0.000427	0.000112	1
0.647	*Swift*/XRT	1 keV	2.42e+17	0.000674	0.000153	1
0.650	*Swift*/XRT	1 keV	2.42e+17	0.000668	0.000151	1
0.652	*Swift*/XRT	1 keV	2.42e+17	0.000694	0.000157	1
0.654	*Swift*/XRT	1 keV	2.42e+17	0.000453	0.000120	1
0.656	*Swift*/XRT	1 keV	2.42e+17	0.000756	0.000161	1
0.786	*Swift*/XRT	1 keV	2.42e+17	0.000735	0.000121	1
0.995	*Swift*/XRT	1 keV	2.42e+17	0.000305	0.000051	1
1.172	*Swift*/XRT	1 keV	2.42e+17	0.000255	0.000055	1
1.237	*Swift*/XRT	1 keV	2.42e+17	0.000287	0.000075	1
1.241	*Swift*/XRT	1 keV	2.42e+17	0.000299	0.000078	1
1.246	*Swift*/XRT	1 keV	2.42e+17	0.000244	0.000064	1
1.251	*Swift*/XRT	1 keV	2.42e+17	0.000296	0.000059	1
1.304	*Swift*/XRT	1 keV	2.42e+17	0.000264	0.000069	1
1.309	*Swift*/XRT	1 keV	2.42e+17	0.000295	0.000058	1
1.370	*Swift*/XRT	1 keV	2.42e+17	0.000225	0.000059	1
1.376	*Swift*/XRT	1 keV	2.42e+17	0.000314	0.000066	1
1.472	*Swift*/XRT	1 keV	2.42e+17	0.000141	0.000037	1
1.51	*Swift*/XRT	1 keV	2.42e+17	0.000314	0.000082	1
1.51	*Swift*/XRT	1 keV	2.42e+17	0.000211	0.000052	1
1.57	*Swift*/XRT	1 keV	2.42e+17	0.000177	0.000034	1
1.64	*Swift*/XRT	1 keV	2.42e+17	0.000258	0.000068	1
1.64	*Swift*/XRT	1 keV	2.42e+17	0.000196	0.000045	1
2.02	*Swift*/XRT	1 keV	2.42e+17	0.000133	0.000027	1
2.11	*Swift*/XRT	1 keV	2.42e+17	0.000320	0.000069	1
2.27	*Swift*/XRT	1 keV	2.42e+17	0.000133	0.000030	1
2.39	*Swift*/XRT	1 keV	2.42e+17	0.000111	0.000030	1
2.44	*Swift*/XRT	1 keV	2.42e+17	0.000148	0.000036	1
2.53	*Swift*/XRT	1 keV	2.42e+17	0.000104	0.000020	1
3.17	*Swift*/XRT	1 keV	2.42e+17	0.000076	0.000016	1
3.35	*Swift*/XRT	1 keV	2.42e+17	0.000060	0.000016	1
3.38	*Swift*/XRT	1 keV	2.42e+17	0.000137	0.000036	1
3.55	*Swift*/XRT	1 keV	2.42e+17	0.000052	0.000011	1
3.70	*Swift*/XRT	1 keV	2.42e+17	0.000064	0.000017	1
5.07	*Swift*/XRT	1 keV	2.42e+17	0.000039	0.000009	1

Table 5.3: Continued.

Δt (days)	Telescope	Band/Filter	Frequency (Hz)	Flux (μJy)	Uncertainty (μJy)	Detection? (1 = yes)
7.51	*Swift*/XRT	1 keV	2.42e+17	0.000033	0.000008	1
9.42	*Swift*/XRT	1 keV	2.42e+17	0.000016	0.000005	1
0.01126	MeerLICHT	q	5.169e+14	26.434	0.444	1
0.01247	MeerLICHT	u	7.889e+14	12.560	0.474	1
0.01372	MeerLICHT	q	5.169e+14	21.088	0.406	1
0.01497	MeerLICHT	g	6.246e+14	15.457	0.297	1
0.01622	MeerLICHT	q	5.169e+14	17.439	0.282	1
0.01742	MeerLICHT	r	4.789e+14	18.484	0.254	1
0.01872	MeerLICHT	q	5.169e+14	14.399	0.301	1
0.01979	MeerLICHT	i	3.919e+14	19.776	0.629	1
0.02107	MeerLICHT	q	5.169e+14	12.482	0.220	1
0.02237	MeerLICHT	z	3.276e+14	18.998	0.452	1
0.02367	MeerLICHT	q	5.169e+14	10.642	0.232	1
0.02488	MeerLICHT	u	7.889e+14	5.391	0.345	1
0.02609	MeerLICHT	q	5.169e+14	9.180	0.267	1
0.02737	MeerLICHT	g	6.246e+14	6.965	0.245	1
0.02863	MeerLICHT	q	5.169e+14	8.141	0.413	1
0.04183	*Swift*/UVOT	b	6.848e+14	3.162	0.087	1
0.04659	*Swift*/UVOT	$uvw2$	1.401e+15	0.331	0.015	1
0.04896	*Swift*/UVOT	v	5.511e+14	3.342	0.123	1
0.06778	*Swift*/UVOT	$uvm2$	1.319e+15	0.394	0.022	1
0.06976	*Swift*/UVOT	$uvw1$	1.115e+15	0.525	0.024	1
0.10778	*Swift*/UVOT	u	8.583e+14	0.581	0.021	1
0.11414	*Swift*/UVOT	b	6.848e+14	0.802	0.022	1
0.17832	VLT	r	4.812e+14	0.625	0.006	1
0.17833	*Swift*/UVOT	$uvw1$	1.115e+15	0.137	0.005	1
0.18741	*Swift*/UVOT	u	8.583e+14	0.291	0.008	1
0.19320	Chilescope	r	4.812e+14	0.570	0.026	1
0.24302	*Swift*/UVOT	$uvw2$	1.401e+15	0.035	0.003	1
0.331	*Swift*/UVOT	v	5.511e+14	0.242	0.020	1
0.377	*Swift*/UVOT	b	6.848e+14	0.138	0.015	1
0.442	*Swift*/UVOT	$uvm2$	1.319e+15	0.030	0.004	1
0.496	BOOTES-3	R	4.729e+14	0.229	0.021	1
0.516	*Swift*/UVOT	$uvw1$	1.115e+15	0.026	0.003	1
0.576	*Swift*/UVOT	u	8.583e+14	0.044	0.005	1
0.584	*Swift*/UVOT	b	6.848e+14	0.091	0.009	1
0.643	*Swift*/UVOT	$uvm2$	1.319e+15	0.019	0.003	1
0.653	*Swift*/UVOT	$uvw1$	1.115e+15	0.022	0.003	1
0.787	*Swift*/UVOT	u	8.583e+14	0.039	0.005	1
0.972	*Swift*/UVOT	$uvw2$	1.401e+15	0.009	0.000	0
1.038	*Swift*/UVOT	v	5.511e+14	0.080	0.000	0
1.305	*Swift*/UVOT	$uvm2$	1.319e+15	0.009	0.002	1
1.310	*Swift*/UVOT	$uvw1$	1.115e+15	0.011	0.002	1
1.402	*Swift*/UVOT	u	8.583e+14	0.013	0.003	1
1.447	*Swift*/UVOT	$uvw1$	1.115e+15	0.008	0.000	0
1.58	*Swift*/UVOT	$uvw1$	1.115e+15	0.011	0.000	0
1.62	*Swift*/UVOT	b	6.848e+14	0.017	0.000	0

Table 5.3: Continued.

Δt (days)	Telescope	Band/Filter	Frequency (Hz)	Flux (μJy)	Uncertainty (μJy)	Detection? (1 = yes)
1.64	*Swift*/UVOT	$uvw1$	1.115e+15	0.007	0.000	0
1.65	*Swift*/UVOT	u	8.583e+14	0.027	0.000	0
2.01	*Swift*/UVOT	$uvm2$	1.319e+15	0.004	0.000	0
2.22	*Swift*/UVOT	$uvw2$	1.401e+15	0.003	0.000	0
2.33	*Swift*/UVOT	v	5.511e+14	0.037	0.000	0
2.43	*Swift*/UVOT	$uvw1$	1.115e+15	0.008	0.000	0
2.44	*Swift*/UVOT	u	8.583e+14	0.014	0.000	0
5.29	*Swift*/UVOT	u	8.583e+14	0.011	0.000	0
5.37	*Swift*/UVOT	u	8.583e+14	0.010	0.000	0
6.55	*Swift*/UVOT	v	5.511e+14	0.032	0.000	0
7.67	*Swift*/UVOT	u	8.583e+14	0.007	0.000	0
0.496	ATCA	5.5 GHz	5.50e+09	0.074	0.024	1
0.530	ATCA	9 GHz	9.00e+09	0.277	0.044	1
0.550	ATCA	21.2 GHz	2.12e+10	0.393	0.071	1
0.550	ATCA	16.7 GHz	1.67e+10	0.368	0.071	1
1.061	ALMA	343.5 GHz	3.44e+11	1.637	0.053	1
1.172	ALMA	97.5 GHz	9.75e+10	2.190	0.009	1
2.14	ALMA	97.5 GHz	9.75e+10	1.160	0.018	1
3.15	ALMA	97.5 GHz	9.75e+10	0.811	0.010	1
3.42	ATCA	34 GHz	3.40e+10	0.810	0.047	1
3.47	ATCA	21.2 GHz	2.12e+10	0.851	0.035	1
3.47	ATCA	16.7 GHz	1.67e+10	0.898	0.044	1
4.17	ALMA	97.5 GHz	9.75e+10	0.570	0.022	1
4.20	ALMA	343.5 GHz	3.44e+11	0.272	0.042	1
6.61	ATCA	34 GHz	3.40e+10	0.564	0.053	1
6.64	ATCA	21.2 GHz	2.12e+10	0.946	0.085	1
6.64	ATCA	16.7 GHz	1.67e+10	0.988	0.047	1
6.67	ATCA	9 GHz	9.00e+09	0.525	0.033	1
6.67	ATCA	5.5 GHz	5.50e+09	0.254	0.051	1
8.23	ALMA	97.5 GHz	9.75e+10	0.400	0.008	1
8.66	GMRT	700 MHz	7.00e+08	0.090	0.030	0
8.74	MeerKAT	L	1.28e+09	0.078	0.015	1
10.39	ATCA	9 GHz	9.00e+09	0.219	0.030	1
10.39	ATCA	5.5 GHz	5.50e+09	0.300	0.030	1
18.09	ALMA	97.5 GHz	9.75e+10	0.849	0.016	1
18.51	ATCA	34 GHz	3.40e+10	0.650	0.050	1
18.56	ATCA	21.2 GHz	2.12e+10	0.560	0.042	1
18.56	ATCA	16.7 GHz	1.67e+10	0.584	0.031	1
18.59	ATCA	9 GHz	9.00e+09	0.921	0.026	1
18.59	ATCA	5.5 GHz	5.50e+09	0.622	0.033	1
20.27	GMRT	700 MHz	7.00e+08	0.108	0.036	0
20.98	MeerKAT	L	1.28e+09	0.103	0.020	1
30.53	ATCA	34 GHz	3.40e+10	0.752	0.135	1
30.58	ATCA	21.2 GHz	2.12e+10	0.548	0.130	1
30.58	ATCA	16.7 GHz	1.67e+10	0.435	0.060	1
31.13	ALMA	97.5 GHz	9.75e+10	0.358	0.012	1
31.69	GMRT	700 MHz	7.00e+08	0.107	0.037	0

Table 5.3: Continued.

Δt (days)	Telescope	Band/Filter	Frequency (Hz)	Flux (μJy)	Uncertainty (μJy)	Detection? (1 = yes)
31.82	MeerKAT	L	1.28e+09	0.105	0.015	1
50.02	ALMA	343.5 GHz	3.44e+11	0.110	0.037	0
53.50	ATCA	34 GHz	3.40e+10	0.280	0.069	1
53.55	ATCA	21.2 GHz	2.12e+10	0.345	0.058	1
53.55	ATCA	16.7 GHz	1.67e+10	0.288	0.042	1
53.59	ATCA	9 GHz	9.00e+09	0.213	0.038	1
53.59	ATCA	5.5 GHz	5.50e+09	0.533	0.065	1
54.83	MeerKAT	L	1.28e+09	0.154	0.017	1
55.98	ALMA	97.5 GHz	9.75e+10	0.080	0.021	1
56.66	GMRT	700 MHz	7.00e+08	0.140	0.046	0
79.37	ATCA	9 GHz	9.00e+09	0.132	0.024	1
79.37	ATCA	5.5 GHz	5.50e+09	0.179	0.028	1
79.98	ALMA	97.5 GHz	9.75e+10	0.057	0.019	0
85.53	MeerKAT	L	1.28e+09	0.205	0.015	1
86.44	GMRT	700 MHz	7.00e+08	0.122	0.039	1

Chapter 6

Summary and future work

In this thesis I presented the GRB follow-up campaign we implemented with the fully-robotic MeerLICHT optical telescope. The observing programme was originally intended to focus on the follow-up of *Fermi*/GBM bursts as their large error boxes require tiled observations, making them an ideal testing-ground for the follow-up of gravitational wave events. We decided to include the follow-up of *Swift* bursts in our programme due to their scientific potential. Here I present some of the highlights from this thesis.

6.1 Thesis highlights

Our GRB follow-up campaign started off on a strong footing with the detection of *two* optical afterglows on the same night in June 2021. Less than a month later we had our first autonomous response to a GRB with observations of GRB 210702A beginning 15 minutes post-trigger, which was followed a month later by our discovery of the afterglow to GRB 210731A along with its highly unusual light curve. GRB 211130A was our first *Fermi*-triggered burst. We managed to observe the entire error box and identify an afterglow candidate, however, we were not able to confirm whether this was indeed the afterglow since we only reported our results after 10 days. Over the almost 2.5 years of our campaign we followed-up a total of 29 GRBs, for an average rate ~ 0.9 GRBs per month. We responded to 15 *Swift* triggers and 10 *Fermi* triggers, and were able to start observing within 1 hour for 10 of the GRBs in our sample, with our fastest response time being 129 seconds for GRB 220715B.

Among the three published bursts, GRB 210731A (Chapter 3) was the burst which most clearly demonstrated MeerLICHT's capabilities: the telescope responded fully-autonomously and began observations a mere 286 s after the *Swift* trigger; MeerLICHT's sensitivity led to the discovery of the optical afterglow in our first q-band image where previously the *Swift*/UVOT telescope had not detected anything (Troja et al. 2021); and our multi-filter observations allowed us to establish that the complex triply-peaked light curve likely had a hydrodynamical rather than spectral origin. Due to the unusual MeerLICHT light curve, we submitted director's discretionary time proposals to obtain radio follow-up of GRB 210731A with the MeerKAT telescope at 1.4 GHz, and with the Very Large Array at 6 and 10 GHz. Combined with optical data from GROND, UVOT, VLT, NOT and KAIT, and X-ray data from *Swift*/XRT, we performed spectral and temporal analyses which found a preference for a stellar-wind environment. This was further supported by our radio data, with ν_m transitioning through 10 GHz at 34.2 days. Through broadband theoretical afterglow modelling we were able to account for all of the data from the X-rays to 6 GHz, but not the MeerKAT data. Our MeerKAT non-detections were incompatible with any standard forward shock model, so we suggested that a thermal electron population might provide an additional source of opacity that would effectively 'lower' the self-absorption frequency. For the complex triple-peaked MeerLICHT light curve, we suggested that energy injection was the most plausible explanation. In this case, the GRB blast wave energy would have increased by a factor ~ 1000

over the course of energy injection. We additionally identified the first peak in the light curve as an afterglow onset peak and used it to constrain the initial Lorentz factor of the jet to $\Gamma_0 \approx 24$.

There was initially much excitement associated with GRB 220627A (Chapter 4) due to the fact that the two *Fermi* triggers separated by almost 1000 s might have been caused by gravitational lensing (Roberts et al. 2022). The gravitational-lensing claim was later dropped once it was established that the spectra of the two γ-ray emission episodes were quite different. Although MeerLICHT responded quickly to the GBM trigger - it began tiled observations of the GBM error box within 22 minutes - due to observing constraints we did not observe the field containing the eventual afterglow during these observations. The *Fermi*/LAT localisation of the burst led us to schedule 2×300 s observations in the q-band for the following night. Through these deep observations we were able to identify the optical afterglow to GRB 220627A coincident with an X-ray candidate. After reporting our detection (de Wet et al. 2022), follow-up observations with MUSE on the VLT established that the redshift of the burst was $z = 3.08$, making GRB 220627A the most distant ultra-long GRB to date. Ultra-long GRBs were suggested by Levan et al. (2014) to form a distinct population compared to long and short GRBs, with possibly a different progenitor too. In our afterglow analysis of GRB 220627A, we found that the observed properties of GRB 220627A were typical for the broader long GRB population and were not suggestive of a different progenitor, though we could not exclude such a scenario. We also compared GRB 220627A with a small sample of GRBs showing multiple widely-spaced emission episodes in their γ-ray light curve.

GRB 210702A (Chapter 5) was unique for being the first GRB with a clear rebrightening in its millimeter light curve. MeerLICHT started observing GRB 210702A $\sim$ 16 minutes after the *Swift* trigger and obtained sufficient data for us to constrain the early-time optical decay rate. Combined with UVOT photometry, we found that the optical light curve steepened from $\alpha \approx -1$ to $\alpha \approx -1.4$. Prior to the millimeter rebrightening, the X-ray, optical and millimeter light curves could be reconciled within a standard forward shock model in a stellar wind medium, where the shallower early decline in the optical and millimeter light curves was due to the proximity of ν_m to the observing band. Our lower frequency $\nu < 16$ GHz radio light curves, however, could not be modelled by any standard forward shock model. Similar problems have been seen in other bursts with comprehensive radio datasets (e.g. GRB 221009A; Laskar et al. 2023), and may require non-standard scenarios such as a thermal electron population or structured jet to explain the data. We found that the millimeter rebrightening could be explained by energy injection into the forward shock or a reverse shock from the late-time collision of a shell ejected by the GRB central engine. The detection of such a rebrightening demonstrates that the millimeter band can show some of the complex features seen more often in X-ray and optical light curves.

6.2 Future work

Our programme has demonstrated its worth: we have had the opportunity to test our systems for GW follow-up while following-up on *Fermi* triggers; we have made our presence known in the GRB community through submitting 22 GCN circulars, most of them with a short time-delay; and three bursts have resulted in publications. Going forward, I propose continuing the programme with MeerLICHT, with the following remarks:

- The time commitment for MeerLICHT has been small. A total of 29 triggers over 2.5 years has not been disruptive to 'normal' scheduling.

- I suggest continuing the follow-up of *Fermi*/GBM bursts, but only as a further means of preparing for GW follow-up since the science returns were not found to be high. We targeted the brightest, and therefore best localised, GRBs with our criteria being that a total of 80 fields or fewer encompassing a probability of at least 70% must be visible within 5 hours of a trigger. Even for a telescope with a large field-of-view like MeerLICHT, this was a challenging task. The number of *Fermi* triggers was rather small (15 triggers in 25.5 months) over this period, so I suggest adjusting the triggering criteria by removing the 5 hour time constraint, which would have doubled the number of triggers from 15 to 31.

- *Swift* follow-up has proven to be fruitful. MeerLICHT's multi-filter capabilities are a real asset and are still rather rare compared to other facilities conducting optical follow-up. However, MeerLICHT's field of view is unnecessarily large for *Swift* follow-up, so it may be worthwhile investigating the use of the SAAO Lesedi telescope equipped with the Mookodi low-resolution spectrograph and imager. Mookodi has a $10' \times 10'$ field of view and five SDSS filters (*ugriz*), which would allow us to maintain a multi-colour approach.
- For *Swift* GRBs where we can observe very soon after a trigger ($<$ 10 minutes), it is worth considering reducing our exposure time from the nominal 60 s at the very earliest times. GRB afterglows evolve on logarithmic timescales, and $\Delta t/t$ is rather large at early times for 60 s exposures, meaning that we might miss out on temporal variability.
- The flexibility to manually schedule the telescope should be maintained. This is vital for special cases such as when an IPN localisation or *Fermi*/LAT detection is announced.
- To maximise science returns, it is necessary to foster scientific collaborations and ties within the GRB community. An interesting optical light curve alone is not enough to put together a paper. Data sharing is essential.
- The radio regime is less well studied than in the optical and X-rays and is still an exciting frontier. To obtain high quality radio datasets will require collaboration with others who have existing programmes (e.g. Dr Laskar), or submitting our own proposals.
- *Swift* is reaching the end of its life. The Chinese-French SVOM (Space-based multi-band astronomical Variable Objects Monitor) mission is scheduled to launch in June 2024, and will be the successor to *Swift*. The positions of bursts detected by SVOM will be made public to the GRB community. Although MeerLICHT could follow-up on SVOM GRBs, it would make more sense to utilise the smaller field of view Lesedi telescope equipped with Mookodi to do so, as noted above.
- The Chinese-European Einstein Probe (EP) mission was launched on 2024 January 9. EP has a Wide-field X-ray Telescope (WXT) and Follow-up X-ray Telescope (FXT) on board, and will search for new X-ray transients. A number of EP transients have already been discovered, some of which have been confirmed as X-ray afterglows to GRBs, and others which may fall within an entirely different population of X-ray transients. The WXT localisation error boxes are typically 3 arcminutes in radius (6 arcminutes in diameter), which is small enough for Lesedi's field of view. Again, I recommend using Lesedi rather than MeerLICHT to follow-up on EP transients.

Bibliography

de Wet, S., Groot, P. J., Malesani, D. B., et al. 2022, GRB Coordinates Network, 32289, 1

Laskar, T., Alexander, K. D., Margutti, R., et al. 2023, ApJ, 946, L23

Levan, A. J., Tanvir, N. R., Starling, R. L. C., et al. 2014, ApJ, 781, 13

Roberts, O. J., Hristov, B., Meegan, C., & Fermi Gamma-ray Burst Monitor Team. 2022, GRB Coordinates Network, 32288, 1

Troja, E., Ambrosi, E., D'Elia, V., et al. 2021, GRB Coordinates Network, 30568, 1

Acknowledgements

This PhD has certainly been the most challenging and most rewarding undertaking of my life. I would not have been able to make it without the help and guidance of many people, so I will express my gratitude to them here.

I will start with Paul. I remember my first zoom call with you in 2019 as a prospective master's student with little idea of the astronomy research landscape. All I knew was that I had a vague interest in transient astronomy as a result of the exciting joint gravitational wave and electromagnetic detection of GW 170817. Starting my master's degree, I was very uncertain whether I should pursue a career in science. The biggest thing I want to thank you for is the self-belief you gave me. You made me believe that I have potential as a scientist, and you made me seriously consider science as a career. I hugely admire your can-do attitude and enthusiasm you bring to your work. You have been a great mentor and I especially appreciate the way you have supported me throughout my PhD journey.

Tanmoy. You have been my closest scientific collaborator over the course of my PhD. The two research visits I undertook - first to Radboud to work on GRB 210731A, then to Salt Lake City to work on GRB 210702A - played a huge role in developing my skills and approach to doing science. Although these trips were incredibly intense, I felt as if I learnt more in the two weeks of those trips than I learnt in the following two months. Your hands-on help and especially the time you devoted to teaching me radio techniques and afterglow physics is greatly appreciated. The attention to detail you showed when reviewing my papers strengthened them immensely and taught me how to put together a convincing scientific argument. I feel that I am a much better scientific writer due to your input.

Hendrik van Eerten, I'd like to thank you for the week-long afterglow modelling workshop you led and hosted at the University of Bath in October 2022. You were a tremendous teacher and I learnt a great deal about afterglow physics and modelling from you. I especially appreciated the way you fielded all of my questions. You have also been very helpful in responding to my questions via email. Andrew Levan, thank you for getting me going within the GRB field and mentoring me in the early stages of my PhD. Your guidance and help in writing the radio DDT proposals for GRB 210731A were essential at the time since I knew so little about afterglow studies. Thank you for putting me in touch with Tanmoy. Paul Vreewijk, thank you for helping me with everything MeerLICHT- and pipeline-related. Your prompt response to my emails made working with you a breeze. I admire and respect you as an astronomer. Patrick, it was you who put me in touch with Paul Groot in my gap year when I was looking to do a Master's degree. Thank you for guiding and supporting me along the way. I especially appreciate the way you showed me the magic of observing during my first week-long observing run on the SAAO 40-inch telescope in April 2021. From that week onwards, I have tried to grab almost every opportunity I can to go observing, particularly in Sutherland. David Buckley, I thoroughly enjoyed the week-long HIPPO observing run we had in Sutherland in July 2022. I enjoyed our conversations about astronomy and beyond, and was constantly entertained by your stories. I hugely admire your passion and enthusiasm for astronomy and for forming collaborations with scientists from all over the world, especially those from the global south. Daniel Egbo, I admire your work ethic and passion for science. I've enjoyed getting to know you over the past few years. The challenges you've faced and the way you've gone about them is inspiring. I look forward to seeing you graduate with your PhD too.

Among the UCT office people, I would like to single out Jordan, Krishna, Francesco, and Lennart. Jordan, Krishna and Francesco, I really love your sense of humour and relaxed attitude when it comes work. You are all great scientists, but I appreciate the fact that you never took work *too* seriously. The banter we had during the 3 weeks that Francesco helped me with VLA calibration made the whole process much more entertaining than it might have been. I greatly miss your presence in the department at UCT. Lennart, I love your sense of wonder and fascination when it comes to science. You are a true idealist (particularly when it comes to data privacy!), and I think the world needs more people like you. Thank you for the many in-depth discussions we've had on all topics from science to politics.

On a more personal note, I want to thank my family for the incredible support you have given me over all of the years leading up to today. Mom, thank you for being my number one fan and for being such a towering rock through all of my endeavours. You've always been there to provide a listening and understanding ear when I've been going through difficulties. Nicky, your passion and enthusiasm for everything you do is a great inspiration, particularly when it comes to wine. Timothy, thank you for leading the way on the PhD journey. I don't think you know how much I admire you as a scientist. Your ability to rapidly hone in on important scientific questions and your sharpness of mind are qualities I aspire to. Our discussions on the philosophy of science and the broader scientific landscape have been enlightening. I am excited to watch your career progress. Frances, thank you for being the person who helps me unwind and come back down to earth at the end of each day. I appreciate all of the support you've given me along the way. Bruce, your zest for life and willingness to follow your dreams are a great inspiration to me. I cherish all of the adventures we've had together over the years. To my dad, I know that you would be incredibly proud of me and would be completely fascinated by my work. Thank you for making me the person I am today. I miss you greatly.